



**ΔΙΔΡΥΜΑΤΙΚΟ ΔΙΑΤΜΗΜΑΤΙΚΟ
ΠΡΟΓΡΑΜΜΑ ΜΕΤΑΠΤΥΧΙΑΚΩΝ
ΣΠΟΥΔΩΝ
“ΣΧΕΔΙΑΣΗ ΚΑΙ ΕΠΕΞΕΡΓΑΣΙΑ
ΣΥΣΤΗΜΑΤΩΝ”**



**ΣΤΡΑΤΙΩΤΙΚΗ ΣΧΟΛΗ
ΕΥΕΛΠΙΔΩΝ**
Τμήμα Στρατιωτικών
Επιστημών

ΠΟΛΥΤΕΧΝΕΙΟ ΚΡΗΤΗΣ
Σχολή Μηχανικών
Παραγωγής & Διοίκησης

HELLENIC ARMY ACADEMY
Department of Military Sciences

TECHNICAL UNIVERSITY OF CRETE
School of Production Engineering & Management

**INTERAFACULTY POSTGRADUATE PROGRAM
“SYSTEMS ENGINEERING”**

MASTER THESIS

“Small size 3D printed hydraulic components with integrated fluid sensing capabilities: A proof of concept”

CHRYSOULA MANOLI

AM: 2017018010

Supervisor: Dionysios E. Mouzakis, *Professor Dr-Ing. Mech. & Aeronaut. Engng. Director, Mechanics Laboratory, Hellenic Army Academy*

Co-Supervisor: Paolo Petagna, *Project Leader, CERN, Physics Department, Genève, Switzerland*

Vari-Attika, 2021

THIS PAGE INTENTIONALLY LEFT BLANK

Η μεταπτυχιακή διατριβή της Χρυσούλας Μανώλη εγκρίνεται:

ΤΡΙΜΕΛΗΣ ΕΞΕΤΑΣΤΙΚΗ ΕΠΙΤΡΟΠΗ

Καθηγητής Διονύσιος Μουζάκης (Επιβλέπων) ,

Καθηγητής Νικόλαος Δάρας ,

Καθηγητής Νικόλαος Τσουρβελούδης ,

THIS PAGE INTENTIONALLY LEFT BLANK

© Copyright Chrysoula Manoli

Year 2021

THIS PAGE INTENTIONALLY LEFT BLANK

ACKNOWLEDGEMENT

I would like to thank everyone that supported me and contributed to the completion of this work. I would like to start with my supervisor Dr. Dionysios Mouzakis, *Director at Mechanics of Materials Laboratory at the Hellenic Army Academy*. Many thanks for the assignment of the thesis subject, the guidance and his trust on me. In particular, I appreciate the valuable help that he has offered me, all these years, from the beginning of my studies until today.

I would like to express my warm thanks to the European Organization for Nuclear Research “CERN”, where I had the chance to conduct my technical studentship with a financial support, in the frame of my postgraduate studies in the interfaculty program “Systems Engineering”.

Especially, I would like to thank my supervisor Mr. Paolo Petagna, *Project Leader at Detector Cooling Project of the CERN Physics Department*. He gave me the opportunity to work as a member of his team and gain a significant experience at CERN, accomplishing one of my biggest goals. Many thanks for his support and contribution to theoretical scientific background, his guidance in the laboratory, in the execution of experiments and results processing, as well as, the fact that he gave me the chance to develop my ideas and skills.

In addition, I would like to thank Dr. Sébastien Lani, *Project Manager and Activity Manager at CSEM* and Dr. Nicholas Hendricks, *Senior Research and Development Engineer at CSEM* for the impeccable cooperation, in the frame of SWaP project. They gave me the chance to visit the advanced facilities at CSEM and gain a new experience in Additive Manufacturing technologies. Many thanks for their response and feedback, regarding problems that I faced during the project by providing help, based on their scientific and technical background.

I would like to express my thanks to the EP-DT team at CERN that support my experimental work by giving me access to laboratories and workshops. Special thanks to Jerome Noel for his valuable help in the technical domain and the time that he has spent to guide me to test facilities of the Crystal Palace laboratory, as well as, for his useful tips, regarding “hands-on” work. Many thanks to Alessandro La Rosa and his team for scheduling and performing tests on time, in the facilities of QART Lab.

Last but not least, many thanks to the team of IdeaSquare at CERN, headed by Dr. Markus Nordberg, *Head of Resources Development of the Development and Innovation Unit (IPT-DI) at CERN*. Dr. Nordberg and his team supported my work, in order to find sustainable applications of SWaP technology and potential companies and industries that would be interested in this technology. Many thanks for the collaboration with the Aalto University of Helsinki, where I had the chance to visit a team of postgraduate students and work together on sustainable solutions of SWaP project. I would also like to thank him for his useful advices in several stages of the project and the chance to participate in many activities with his team at IdeaSquare.

THIS PAGE INTENTIONALLY LEFT BLANK

ABSTRACT

The field of thermal management is becoming more and more important due to the increased demands in application fields such as aerospace (engines, shielding), automotive (batteries, electric motors), particle detectors (silicon tracker cooling) and manufacturing (injection molds, tooling stamps). Sensing and monitoring fluid parameters of circulating fluids, used in thermal management systems is essential to the control and efficiency of a process system. Complex hydraulic circuits with a number of integrated sensors are required, to meet the increased demands of such applications. As systems become more complex so too does the measurement of fluid properties.

SWaP (Smart Wall Pipes and ducts) is a project that has been developed, in the frame of the ATTRACT project, funded by Horizon 2020. Two large Organizations, based in Switzerland, CERN (European Organization for Nuclear Research) and CSEM (Swiss Centre for Electronics and Microtechnology) collaborated and worked on the development of revolutionary components for the next generation of cooling systems, directly embedding sensors in a hydraulic circuit element by the combination of Additive Manufacturing (AM) technologies. SWaP addresses the limitations of conventional methods by combining AM techniques for the fabrication of smart structures (Selective Laser Melting and Aerosol Jet Printing). This project has received funding from the ATTRACT project funded by the EC under Grant Agreement 777222.

The subject of this Master Thesis is combined with the work on SWaP, in the frame of the candidate's technical studentship at CERN (Sep19 – Oct20). An overview on the Additive Manufacturing technology, commonly known as “3D-printing”, including the methods, the used materials and the key advantages over conventional manufacturing (freedom of design, complex shapes, and on demand production) are presented in the first part of this work. Then, the thesis concentrates on the different methods of metal AM for the production of structural components, with an emphasis on the SLM method. The innovative technology of AJP is analyzed, presenting the state-of-the-art fields of application.

The second part of the thesis concentrates on the fabrication and evaluation of the SWaP prototype, including the used methods of AM, the materials, the laboratory equipment and the test methods. Finally, the test results for the evaluation of the SWaP prototype sensor are presented and discussed.

ΠΕΡΙΛΗΨΗ

Το πεδίο της θερμικής διαχείρισης γίνεται όλο και πιο σημαντικό λόγω των αυξημένων απαιτήσεων σε τομείς όπως η αεροδιαστημική (κινητήρες, θωράκιση), η αυτοκινητοβιομηχανία (μπαταρίες, ηλεκτρικοί κινητήρες), οι ανιχνευτές σωματιδίων (silicon tracker detectors) και η κατασκευή (καλούπια έγχυσης). Η ανίχνευση και παρακολούθηση των ιδιοτήτων των ρευστών, που χρησιμοποιούνται σε συστήματα θερμικής διαχείρισης είναι απαραίτητη για τον έλεγχο και την απόδοση συστημάτων διεργασίας. Σύνθετα υδραυλικά κυκλώματα με έναν αριθμό ενσωματωμένων αισθητήρων, είναι απαραίτητα για την κάλυψη των αυξημένων απαιτήσεων τέτοιων εφαρμογών. Καθώς τα συστήματα γίνονται πιο περίπλοκα, το ίδιο γίνεται και η μέτρηση των ιδιοτήτων των ρευστών.

Το SWaP (Smart Wall Pipes and ducts) είναι ένα project που αναπτύχθηκε στα πλαίσια του ATTRACT project, Horizon 2020. Δύο μεγάλοι οργανισμοί, το CERN (Ευρωπαϊκός Οργανισμός Πυρηνικής Έρευνας) και το CSEM (Ελβετικό Κέντρο Ηλεκτρονικής και Μικροτεχνολογίας) συνεργάστηκαν για την ανάπτυξη επαναστατικών εξαρτημάτων, για την επόμενη γενιά συστημάτων ψύξης, ενσωματώνοντας απευθείας αισθητήρες στο εσωτερικό τοίχωμα υδραυλικών κυκλωμάτων, με τον συνδυασμό τεχνολογιών Additive Manufacturing (AM). Το SWaP αντιμετωπίζει τους περιορισμούς των συμβατικών μεθόδων συνδυάζοντας τεχνικές AM (SLM και AJP) για την ανάπτυξη έξυπνων κατασκευών. Αυτό το έργο έλαβε χρηματοδότηση από το ATTRACT project που χρηματοδοτήθηκε από την EC βάσει της συμφωνίας επιχορήγησης 777222.

Το θέμα της Μεταπτυχιακής Διατριβής βασίζεται στο SWaP, στα πλαίσια της πρακτικής άσκησης της υποψήφιας στο CERN. Στο πρώτο μέρος της εργασίας γίνεται μια επισκόπηση στην τεχνολογία Additive Manufacturing (ή 3D printing), συμπεριλαμβάνοντας τις μεθόδους, τα υλικά και τα κύρια πλεονεκτήματα σε σχέση με τις συμβατικές μεθόδους κατασκευής. Στη συνέχεια, η εργασία επικεντρώνεται στις διαφορετικές μεθόδους του AM μετάλλων για την παραγωγή δομικών στοιχείων, με έμφαση στη μέθοδο SLM. Η καινοτόμος τεχνολογία του AJP αναλύεται λεπτομερώς, παρουσιάζοντας τα υπερσύγχρονα πεδία εφαρμογής της.

Το δεύτερο μέρος της διατριβής επικεντρώνεται στην κατασκευή και την αξιολόγηση του πρωτοτύπου SWaP, παρουσιάζοντας τις συνδυαστικές μεθόδους AM, τα υλικά, τον εργαστηριακό εξοπλισμό, καθώς και τις πειραματικές μεθόδους. Τέλος, παρουσιάζονται και αναλύονται τα αποτελέσματα των δοκιμών για την αξιολόγηση του αισθητήρα του SWaP πρωτοτύπου.

TABLE OF CONTENTS

AKNOWLEDGEMENT	5
ABSTRACT	8
ΠΕΡΙΛΗΨΗ	9
CHAPTER 1 INTRODUCTION TO SWaP	13
1.1 Introduction	13
1.2 The ATTRACT Project.....	18
1.3 The involved parties of SWaP	21
1.3.1 CSEM.....	22
1.3.2 CERN	24
1.3.3 IdeaSquare	28
1.4 SWaP' scope.....	32
CHAPTER 2 ADDITIVE MANUFACTURING (AM)	34
2.1 Introduction to the AM Process.....	34
2.2 AM Methods.....	38
2.2.1 VAT Photopolymerization	39
2.2.2 Material Extrusion	41
2.2.3 Jetting	44
2.2.4 Sheet Lamination	47
2.3 Additive Manufacturing vs Traditional Manufacturing	48
CHAPTER 3 METAL ADDITIVE MANUFACTURING	51
3.1 Introduction	51
3.2 Powder Bed Fusion (PBF).....	53
3.2.1 Selective Laser Sintering (SLS).....	54
3.2.2 Direct Metal Laser Sintering (DMLS)	56
3.2.3 Selective Laser Melting (SLM)	56
3.2.4 Electron Beam Melting (EBM)	58
3.2.5 SLM compared to EBM.....	59
3.3 Direct Energy Deposition (DED)	61
3.4 Process parameters & metallurgical defects.....	64
3.5 Post-processing	69
3.6 Applications.....	72
3.6.1 Aerospace	72
3.6.2 Automotive.....	75

3.6.3	Oil and gas.....	77
CHAPTER 4	AEROSOL JET PRINTING.....	79
4.1	Introduction	79
4.2	The Aerosol Jet System.....	81
4.3	Inks and substrates	87
4.4	Post – processing	90
4.5	Parameters	92
4.6	Applications.....	98
4.6.1	Passive devices	98
4.6.2	Active devices.....	101
4.6.3	Sensors	104
CHAPTER 5	DESIGN & FABRICATION OF THE SWaP PROTOTYPE.....	111
5.1	Introduction	111
5.2	The smart pipe – SLM.....	113
5.3	The embedded sensors – AJP	117
5.3.1	Introduction to temperature sensing.....	117
5.3.2	Resistance Temperature Detectors (RTDs).....	119
5.3.3	The embedded RTDs	125
5.4	Fluid temperature sensing	129
5.4.1	Immersed sensors and thermowells	129
5.4.2	Surface sensors	131
5.5	Applications of SWaP	136
CHAPTER 6	LABORATORY TEST SETUP	137
6.1	Laboratory test-setup upgrade	137
6.2	Integration of the prototype to the test setup.....	143
6.3	Calibration of the AJP sensor	146
CHAPTER 7	EVALUATION OF THE SWaP PROTOTYPE SENSOR.....	149
7.1	Tests under vacuum	149
7.1.1	TEST 1: Temperature Groups	149
7.1.2	TEST 2: Constant Temperature	152
7.1.3	TEST 3: Fast Cycling.....	159
7.2	Tests under real conditions	162
7.2.1	Insulated test section	163
7.2.2	Uninsulated test section.....	166
7.3	Discussion - Obtained Results & Comments	170

7.4	Conclusions and future work.....	172
REFERENCES	173

CHAPTER 1

INTRODUCTION TO SWaP

1.1 Introduction

Smart Wall Pipes and ducts (SWaP) is one of the “ATTRACT” projects, a European Union project funded by Horizon 2020 [1]. The participants of this project are two Research & Technology Organizations in Switzerland; the *Centre Suisse d’Electronique et Microtechnique (CSEM)* in a collaboration with the *European Organization for Nuclear Research (CERN)*. This project has received funding from the ATTRACT project funded by the EC under Grant Agreement 777222.

The idea of SWaP has derived from the limitations and difficulties of measuring directly the properties of a fluid in a hydraulic circuit of a cooling system by current and existing methods. Sensing local and integrated properties of circulating fluids is of utmost importance for the control and efficiency of a process system. Measuring fluid properties by placing sensors along a pipeline provides useful information, regarding the system’s operation and it could also indicate early-stage failures. The measured properties of interest are commonly temperature, pressure and flow rate of fluids. This work focuses on fluid temperature sensing by developing a non-invasive method for direct measurements, eliminating difficulties that the current methods present.

A variety of methods has been developed to measure the fluid temperature in a circulating system and they can be categorized in invasive and non-invasive [2]. Both of them are using either resistance temperature detectors (RTDs) or thermocouples (TCs) to detect the fluid temperature. Invasive methods require modification and preparation of piping, to integrate sensing devices in the fluid stream, contrary to non-invasive, where no intrusiveness is needed. In the case of invasive methods, the sensing element is either integrated directly in the stream flow or it is placed inside a thermowell, which touches the fluid. The sensing element is placed and attached on the outer pipe’ surface, in the case of non-invasive.

The integration of sensing elements in a system requires either drilling of the pipe or connecting the sensor to the pipe by placing an extra element (elbow, tee union, etc.).

Immersing sensors in the flow stream is pretty invasive and it requires a well-defined planning before the installation, since several factors can affect the system's operation and increase the risk of failures. In addition, the replacement of immersed sensors is a time consuming process that requires draining the system and reintroducing the fluid into the piping system. To simplify the process of replacing immersed sensors, thermowells are established as the main method of fluid temperature measuring in pipe systems (**Figure 1.1.a**). Since, only the thermowell is connected to the pipe and immersed in the flow, the sensor that is placed inside the thermowell can be easily removed and replaced in its sheath (thermowell). Fluid properties, pipe's material and diameter, and immersion depth are common factors that should be wisely considered before the integration of sensing devices in a pipe. Another factor that has been studied in the literature [3] concerns the method of inserting the thermowell in a pipeline, perpendicular or with an angle to the flow or at a pipe elbow (**Figure 1.1.b**). The volume and the size of sensors or thermowells limits the number of sensors that can be installed in a pipeline.

Due to the complicated installation and the limitations of immersed sensors and thermowells, a simplest approach of mounting a sensor on the outside surface of a pipe is used as a faster and cheapest approach. This method assumes that the temperature reading at the outer surface is the same as the fluid temperature, based on the fact that heat conducts through a surface to the ambient air. Gluing or clamping temperature sensors on the outer surface of the pipe by adding a layer of thermal paste between two surfaces is a simpler and low-cost method of installation. Insulation of the pipeline and the sensor is required to eliminate heat losses. Compared to immersed sensors, the accuracy and the response time of surface sensors are usually lower, because of temperature differences between the measured and the real fluid values as well as of heat losses [4]. Common readout errors are caused by lack of contact between the sensor and the pipe surface due to bad mounting of the sensor on the pipe. A more professional solution to surface sensors uses instruments, which optimize surface contact by spring-loaded sensor and calculate the fluid temperature via a thermal conductivity algorithm [5] (**Figure 1.1.c**). The accuracy and response time are comparable to those of thermowells [6], however such devices are pretty massive and their usage is limited to applications where space and weight is not an issue.

The aim of SWaP's developed prototype is to exceed the limitations that the current methods present by utilizing combined Additive Manufacturing (AM) techniques to produce innovative devices for efficient systems operation. Instead of mounting a sensor on the outside

pipe surface, the idea is to integrate, a sensor in the inside wall pipe, providing direct, accurate and fast response fluid temperature measurements. The center of interest of SWaP's technology is that hydraulic elements and sensors can be fabricated as a single component (**Figure 1.1.d**) with a total size, comparable or even smaller than typical sensors and thermowells, due to AM technology. SWaP revolutionary components for the next generation of cooling systems are pipes with directly embedded sensors developed by a combination of AM techniques; Selective Laser Melting (SLM) to produce the metal parts (pipe, embedded wiring, and external electrical connectors) and Aerosol Jet Printing (AJP) to deposit the temperature sensor. Producing sensors via AJP in the inner wall pipe can be very advantageous, since it increases the number and possible position of sensors within a structure, providing accurate and direct fluid measurements.

An example application, where SWaP's technology can be used and contribute to the optimization of a system, is the thermal management of silicon detectors for High Energy Physics at CERN (**Figure 1.2**). All particle detectors are using millions of silicon electronic sensors. These electronics and their read-out generate significant heat, which must be reduced in order to avoid thermal runaway and uncontrolled annealing. Different cooling methods have been used for the thermal management of tracker detectors, such as forced air convection, direct cooling of heat sinks with pipe flow and microchannel cooling [7]. However, the high demands and specific constrains of silicon Trackers requires the development of low mass integrated cooling solutions, which minimize the temperature difference between the cooling fluid and the sensor' surface and they will also provide good temperature uniformity over the detection area. Modern trends on local thermal management of silicon detectors introduce a new design of cooling systems, which was developed and installed first in the ATLAS experiment, in the frame of detector upgrade in 2014 [8]. A thin-wall, small diameter (ID < 2mm) cooling pipe of Titanium was integrated in highly conductive carbon foam, supporting the electronic elements (**Figure 1.3**). SWaP's technology could contribute in the new design of cooling solutions for the thermal management of tracker detectors by adding sensing capabilities (fluid temperature and pressure), providing monitoring of the cooling system.

This chapter presents the frame in which SWaP has been developed, including the general idea and the aim of the ATTRACT program, as well as the role of all involved parties working on this project. A summary of SWaP's scope, idea and technology will be presented

in the end of this chapter including a brief introduction to the AM applied methods that they will be therefore further analysed in next chapters of this thesis.

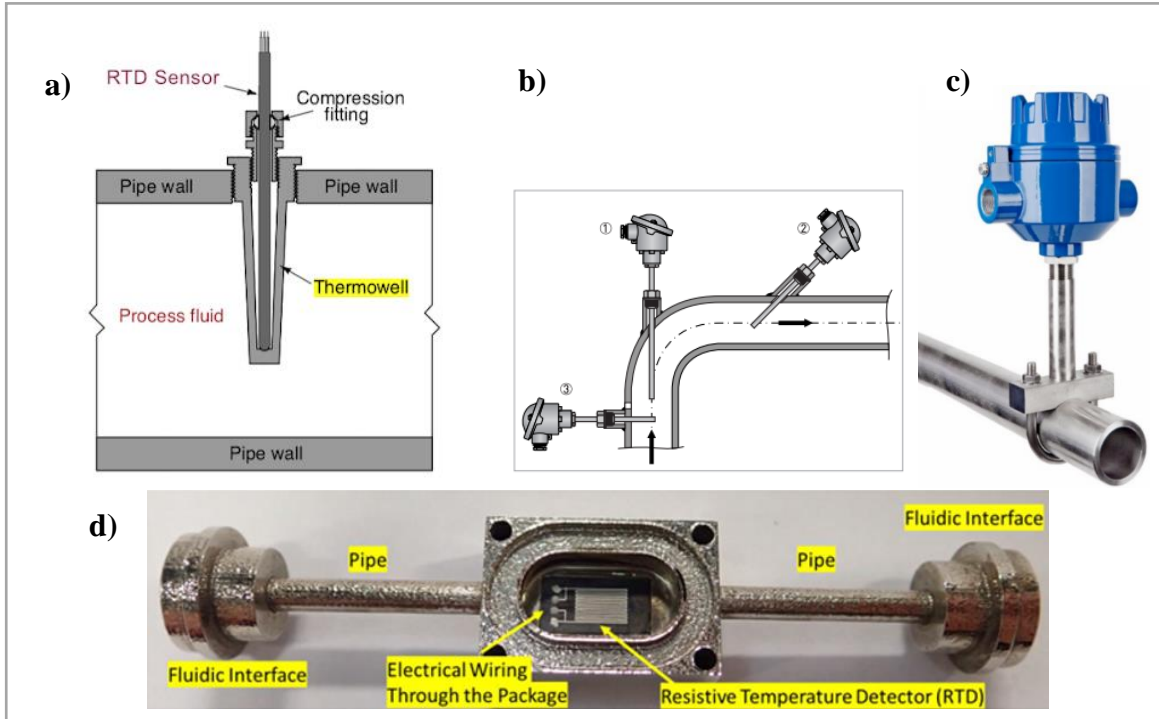


Figure 1.1. a) Sensor placed inside an immersed to the flow thermowell [9], b) three different possible options of integrating thermowells in a pipe [10], c) spring-loaded surface sensor [11] and d) SWaP's prototype with embedded sensor in the inner wall of the pipe [12].

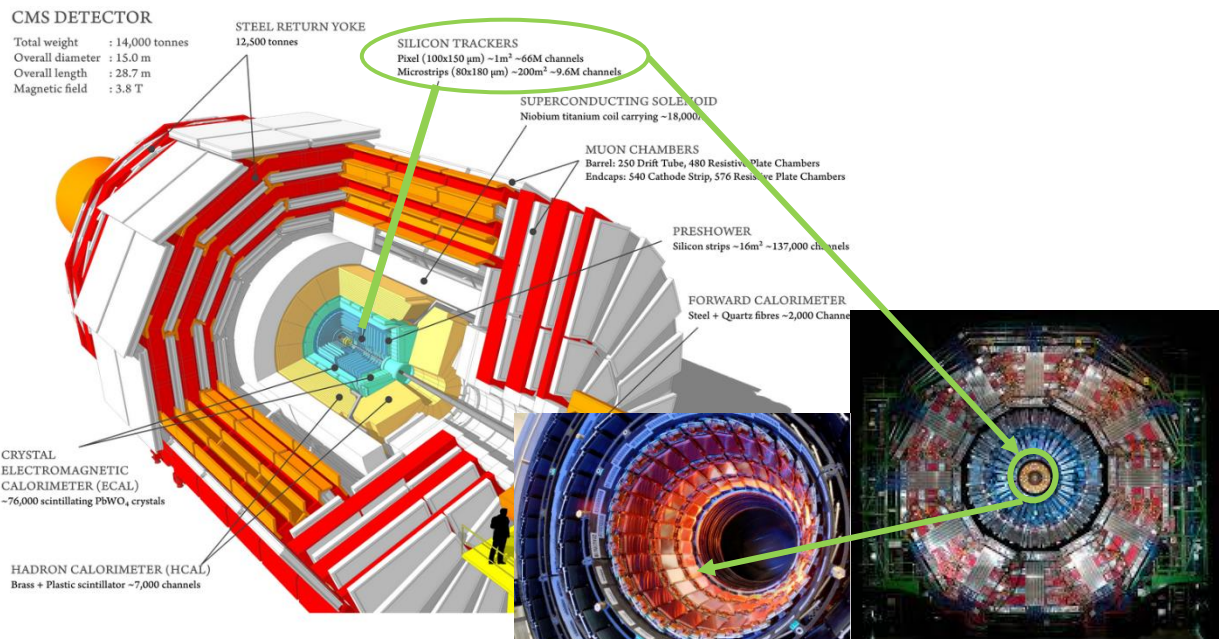


Figure 1.2. Position of the silicon trackers with millions of electronics inside the CMS detector.

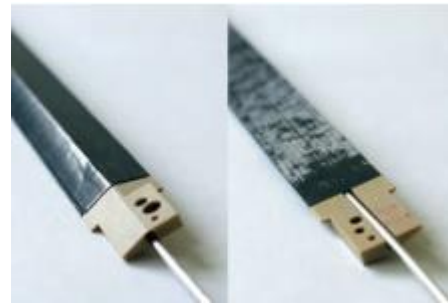
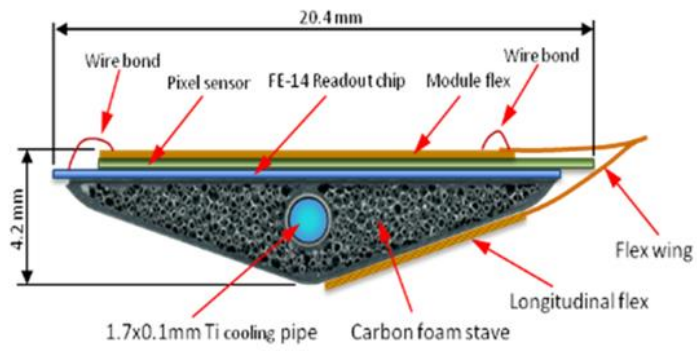


Figure 1.3. Low mass integrated thermal management solutions in the ATLAS IBL stave [13].

1.2 The ATTRACT Project

ATTRACT is funded by the European Union's Horizon 2020 program and its aim is the development of breakthrough next generation of Detection & Imaging technologies, in order to improve Europe's economy by creating products, services, companies and job opportunities [14]. This could be achieved by designing a new model based on Open Innovation and Open Science, which will help in filling the gap between research and real market needs.

The program is divided in two phases (**Figure 1.4**). ATTRACT Phase-1 started in 2019 and 17 million euros have been invested for 170 breakthrough technology projects. Each project has received the amount of 100,000 euros in order to develop a proof of concept during one year. Phase-1 focuses on the idea of transforming science into products and services that will meet societal needs. During Phase-1 the project partners should develop an idea, create a demonstrator and present a final prototype. In Phase-2, new funds will be given to the selected projects, to improve the prototype and create a final product, which will be released to the market.

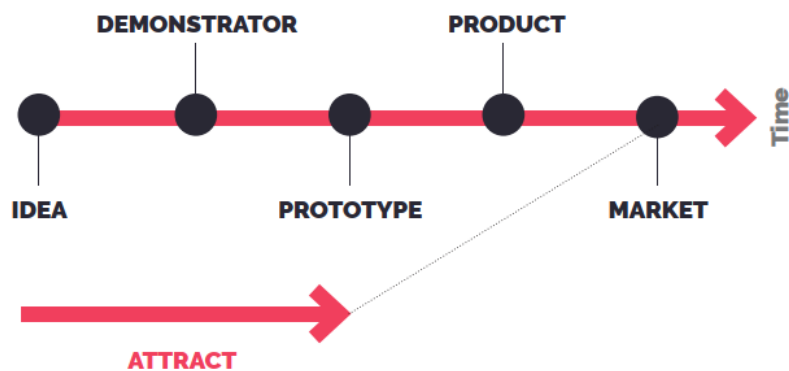


Figure 1.4. Illustration of ATTRACT Phase-1 and Phase-2.

Every project develops an idea in the field of Detection and Imaging technologies, which affect all major technology areas. It is of great significance that future scientific applications with societal character will be almost enabled by those technologies. Manufacturing, sensing, medicine, biotechnology and energy are main areas (**Figure 1.5**) of interest that ATTRACT concentrates on and develops innovative, smart solutions, friendly to the environment and humans. To understand better the importance of developing such systems

and their contribution to real-life problems, ATTRACT strategic program summary presents some example applications [15] and two of them are described below here.

The high rise of cancer cases in Europe have caused the need of developing imaging medical devices such as chips applied in X-ray CT, in prototype systems for digital mammography and in CT imagers for mammography. However, the aim is to develop more personalized treatment options and to improve the identification of tumors. Faster scanners with better resolution are required, in order to test faster more patients and to identify clearly the type of tumors. Another example focuses on the forecasted increase of air mobility of passengers and cargo. This situation requires a significant growth of fleets, which however will increase the costs of staff, equipment and maintenance. The biggest challenge for Europe will be to maintain its technology leadership. Real-time monitoring of the technical health status of airplanes via opto-electronic sensing technology could reduce or even cut the costs of airlines. There are several examples of each technology area where detection and imaging is involved and can be found in many research publications.

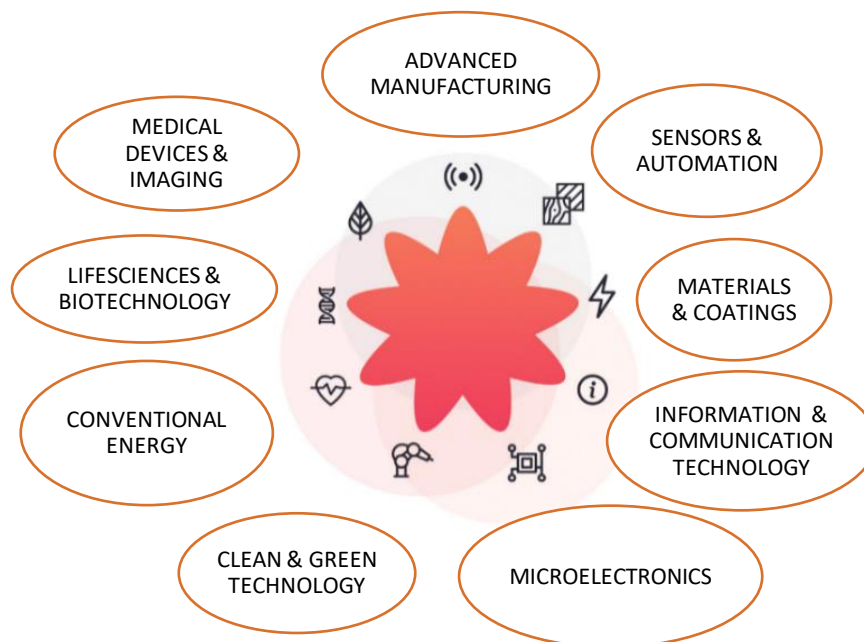


Figure 1.5. Areas where Detection & Imaging technologies are applied in ATTRACT.

SWaP's technology belongs to the area of advanced manufacturing and sensors & automations. Advanced manufacturing is a term used to describe the integration of new, modern and innovative methods in products and processes. This field includes all the

techniques of Additive Manufacturing (AM), intelligent robots in production systems and micro & nano manufacturing that can provide high level of design and excellent accuracy of fabrication. Sensors are devices used to detect events in a system's environment, in order to measure and identify a variety of parameters depending on the application of a system. The existence of sensors is not something new but it is growing up a technology that nowadays uses smart sensors in wireless networks, 3D printed sensors and energy harvesting. The developed technology of SWaP applies a combination of AM methods to produce a device with embedded sensing capabilities. Potential applications of SWaP could contribute in several of the above technology areas, such as medicine, biotechnology and energy.

1.3 The involved parties of SWaP

It has been already noted that CSEM and CERN are the Organizations working on SWaP, in frame of ATTRACT. Proof of concept's goals are several, apart from the ones of research and science and they have been discussed previously as part of the ATTRACT scope, which concentrates on building the bridge between science and society. To fulfill those goals, connections and collaborations with other parties other than scientific researchers are required.

CERN, as partner of this project has taken advantage of the organization's facilities and groups by contacting IdeaSquare and Knowledge Transfer (KT) group. Both could contribute in the process of developing potential applications of SWaP by searching and indicating industries and companies that may be interested in the final product of this project. In particular, during ATTRACT Phase-1, IdeaSquare contributed to the project by introducing SWaP to Aalto University, where a team of postgraduate students worked on searching fields of applications with a positive impact on the society. In this section, the profile of all the involved in SWaP parties (**Figure 1.6**) will be presented with an emphasis to their role and contribution to this project.

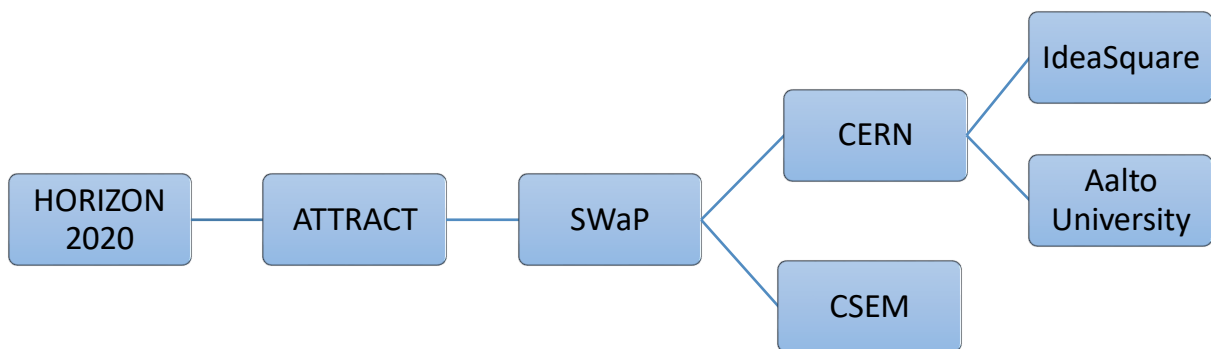


Figure 1.6. Involved parties of the SWaP project.

1.3.1 CSEM

CSEM, the Swiss Center for Electronics and Microtechnology is a private non-profit research and technology organization, located in Neuchâtel, Switzerland. CSEM has been established in 1984 as a merge among three microtechnology intuitions, the Centre Electronique Horloger (CEH), the Fondation Suisse pour la Recherche en Microtechnique (FSRM), and the Laboratoire Suisse de Recherches Horlogères (LSRH) [16]. CSEM focuses on three main strategic research areas and provides expertise, technologies, processes and services that can add value to research, industry and R&D. The research areas include:

- **Digitalization:** Internet of Things (IoT), wearables, edge computing, artificial intelligence, and data science
- **Precision manufacturing:** digital manufacturing, micro and nano manufacturing, additive manufacturing, material design, surface coatings, sensors
- **Renewable energy:** building-integrated photovoltaics (BIPV), energy harvesting powering wireless sensors, energy saving control devices

The combination of main research areas leads to the development of innovative and smart systems that attract the interest of today's technological applications. The total areas of expertise [17] are presented in **Figure 1.7**. CSEM supplies a broad range of markets, including automotive, medical, machine tools, space exploration, etc. In particular, the industries [18] in which CSEM operates are shown in **Figure 1.8**.

CSEM has a major and leading role in the SWaP project. A range of manufacturing fields, especially micro and nanotechnology (printed electronics, MEMS) are areas that CSEM has been active for many years. A combination of micro and nano-scale fabrication with AM methods aims at the miniaturization of 3D structures made from functional materials (mechanical, electrical, optical) and the development of 3D structures with sensing capabilities (sensors, MEMS, CMOS). CSEM has recently developed a method to produce 3D metal parts with embedded electrical wires, which is opening a new approach to add sensors and actuators to demanding systems. The advanced equipment of CSEM laboratories has been used for the entire fabrication of SWaP's prototype.

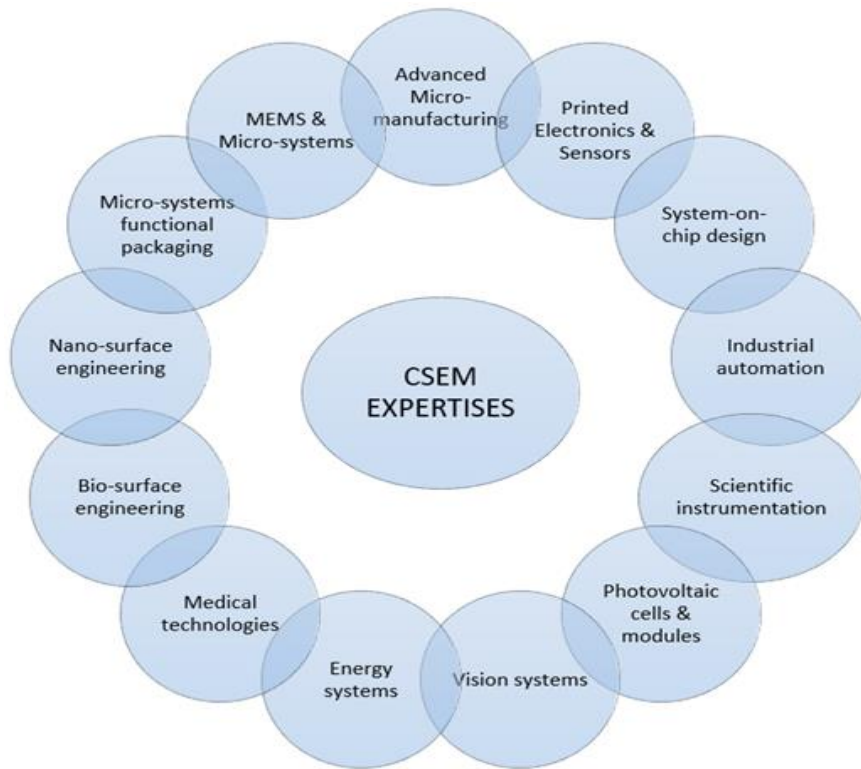


Figure 1.7. CSEM areas of expertise.



Figure 1.8. CSEM areas of industry.

1.3.2 CERN

CERN (Conseil Européen pour la Recherche Nucléaire) is the European Organization for Nuclear Research and the world's largest particle physics laboratory, established in 1954. Fundamental physics is CERN's core business and its mission is to uncover what the Universe is made of and how it works. This mission requires unique range of equipment, laboratories and facilities as well as staff members from all expertise. CERN's staff members, numbering around 2500, take part in the design, construction and operation of the research infrastructure [19]. CERN has changed the world of science by well-known key achievements, such as the birth of web in 1989, the antimatter by developing the Antiproton Decelerator in 2000, the Large Hardon Collider in 2008, which has been followed by the High-Luminosity LHC in 2011 and the most recent one in 2012, The Higgs Boson [20].

CERN is worldwide well known for the most powerful accelerator (**Figure 1.9**) that has been ever built in the world, the Large Hardon Collider (LHC). It boosts the particles in a loop 27 kilometres in circumference at an energy of 6.5 TeV (teraelectronvolts), generating collisions at an energy of 13 TeV [21]. However, CERN operates a complex of eight accelerators including LHC and two decelerators (**Figure 1.10**). These accelerators either supply experiments or are used as injectors, accelerating particles for larger accelerators. The LHC uses detectors to analyse the myriad of particles produced by collisions in the accelerator. There are seven experiments at the LHC, using detectors with the biggest to be four of them, ATLAS, CMS, ALICE and LHCb.



Figure 1.9. The LHC tunnel and a zoom of the accelerator.

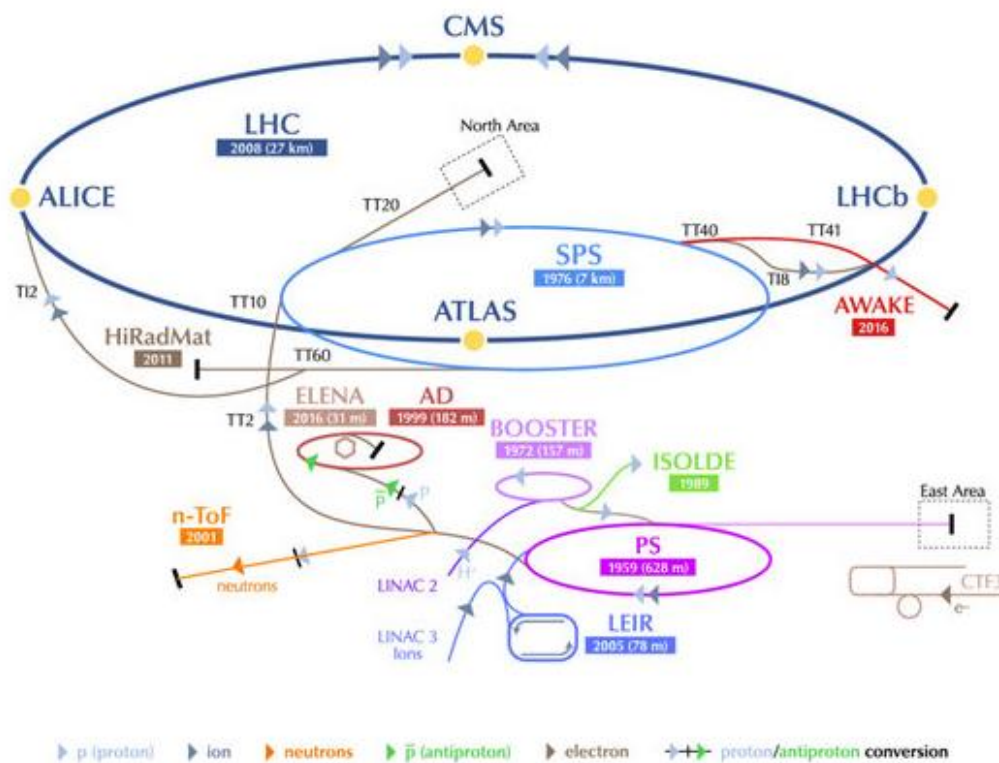


Figure 1.10. The position of the experiments on the LHC tunnel.

ATLAS and **CMS** (Compact Muon Solenoid) are the largest experiments and they are using general-purpose detectors (**Figure 1.11**). The 7000-tonne ATLAS detector is probing for fundamental particles [22] while the CMS detector uses a huge solenoid magnet to bend the paths of particles from collisions in the LHC [23]. **ALICE** (A Large Ion Collider Experiment) and **LHCb** (Large Hadron Collider beauty) using detectors specialised for focussing on specific phenomena (**Figure 1.12**). ALICE detects quark-gluon plasma, a state of matter thought to have formed just after the big bang [24] while the LHCb experiment will shed light on why we live in a universe that appears to be composed almost entirely of matter, but no antimatter [25].

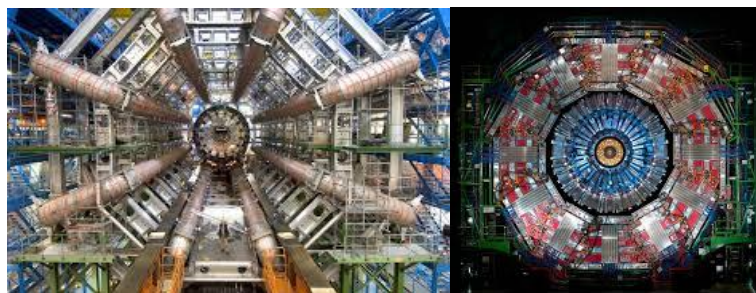


Figure 1.11. Left: The detector of ATLAS experiment, Right: CMS detector.

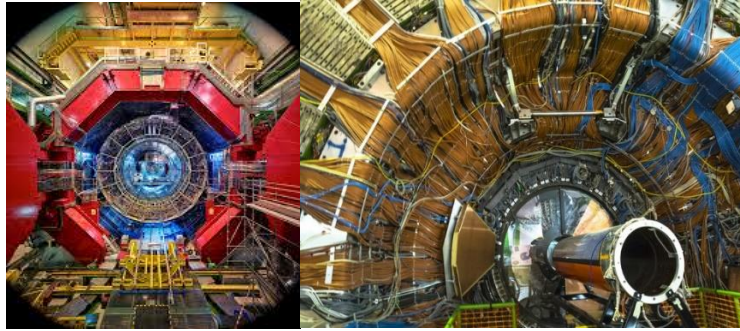


Figure 1.12. Left: ALICE detector, Right: LHCb detector.

CERN research focuses mainly on the experiments at LHC that were presented above. However, there are plenty other experiments at accelerators other than LHC, which remain an important part of the laboratory's activities. In addition, CERN is running collaborations with many universities and organizations, participating in several European programs and developing R&D technologies with a value to the society. The work that is being held at CERN is a result of many teams, from different expertise and backgrounds, the main are physics, engineering, computing and accounting. For the good operation of such a large organization, CERN is divided in four main sectors of expertise and each one of them is separated in departments, according to the research field (**Figure 1.13**).

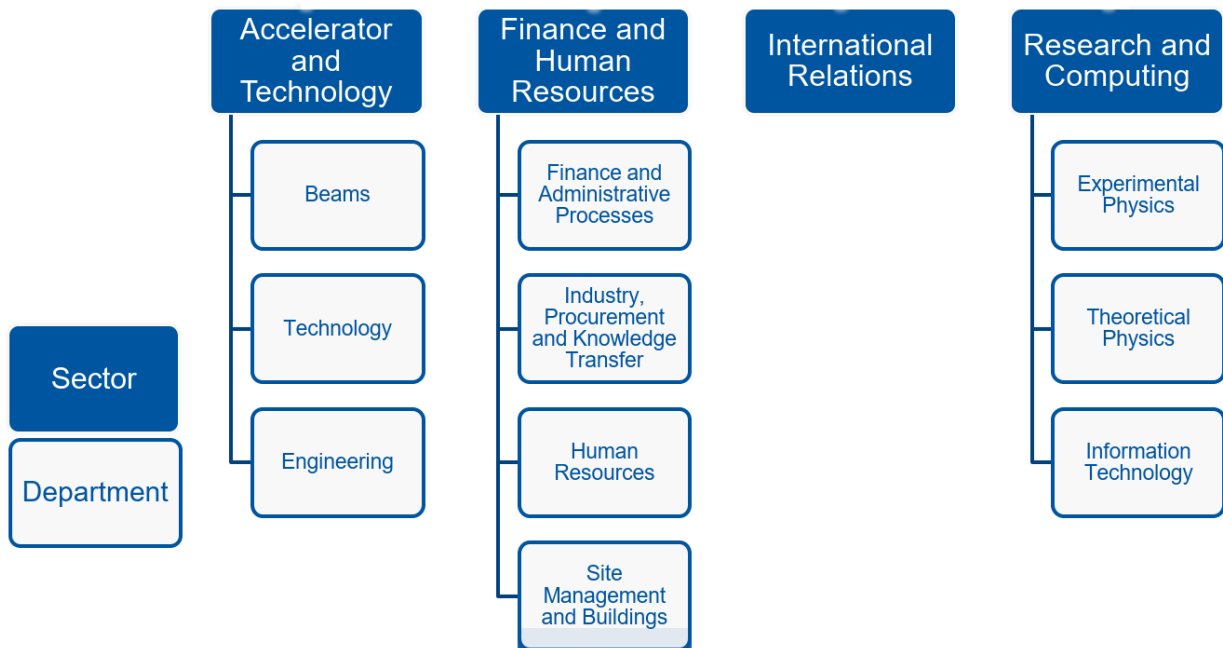


Figure 1.13. Sectors and departments of CERN.

The SWaP project belongs to the section of Fluidic Systems (FS) of Detector Technologies (DT) group in the Experimental Physics (EP) department at CERN (**Figure 1.14**). The Detector Technologies (DT) group participates in the development, construction and operation of particle detectors for experiments at CERN [26]. The Fluidic Systems (FS) is a section of the DT group that develops, maintain and operates infrastructure for detector operation. FS is divided in two subsections; The Detector Cooling Systems and the Gas Systems.

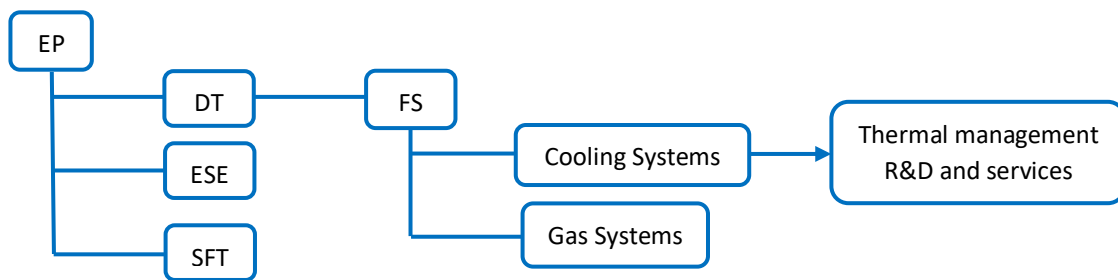


Figure 1.14. Groups and sections of Experimental Physics (EP) department at CERN.

The key activity of Detector Cooling Systems is the innovative thermal management of detectors by focusing on the high level of engineering optimization, to achieve the required physics performance. Thermal management solutions concentrate on the design and construction of cooling plants, the highly efficient local cooling, and the environmental monitoring for cold operations. The team of Detector Cooling Systems participates in R&D projects, in order to study innovative technologies that could solve or improve issues in existing or future detectors with respect to feasibility, performance and reliability. This is exactly where the SWaP project belongs and it is introducing a new generation of hydraulic components with a different approach of sensing fluid properties, circulating in cooling systems of detectors.

The infrastructure, the equipment and the laboratories provided by the FS section are proper to cover the needs of SWaP's prototype, in terms of testing. Basically, the role of CERN to this project is to test and evaluate the prototype after fabrication, as wells to test the compatibility to detector's cooling systems. The infrastructure, the equipment and the work that have been held at CERN's facilities, in frame of SWaP will be further presented in the following chapters of this thesis.

1.3.3 IdeaSquare

IdeaSquare is a place, a facility that has been established in December 2014 at CERN [27] to generate new ideas in a collaborative environment and to promote rapid prototyping and experimental innovations (**Figure 1.15**). Its aim is to connect Research & Development (R&D) to societal needs and explore future solutions for humans. Its work concentrates on the spread of CERN technologies to the world, in order to face societal challenges. Curious minds from all over the world, inside or outside CERN are working together on building a bridge between science and society. The accomplishment of this goal is based on three main ingredients, which are the motto of IdeaSquare; Think, Do and Collaborate [27].

Think is the first step of developing any model, process or application. This place due to its unique environment and infrastructure can be the inspiration of thinking outside of the box by giving the opportunity to everybody to meet other people, discuss and generate new ideas. The ideas concern subjects such as development of next generation detection and imaging technologies, solutions to global challenging that our planet faces and implantation of innovative methodologies that can support multi-faceted research, problem reframing and iterative testing.

Do is what follows thinking. After thinking and generating an idea, it would be a privilege to be able to try and test this idea. This means to create an illustration of the idea by building prototypes. However, this process requires tools, facilities, and equipment; IdeaSquare is a well-equipped place that provides such facilities to everyone. The facilities (**Figure 1.16**) include a variety of workshops, which are the 3D printing room for rapid prototyping, the Electro Shop for building and testing electronic devices, the Machine Shop for mechanical engineering processes (drilling, cutting, gluing) and last but not least the Light Lab which is basically a cleanroom designed for detector assembly and testing.

Collaborate is a step of high importance since it is the way of bringing these ideas in form of applications to the world. IdeaSquare applies methods of open science and open innovation to create new collaborative processes that enable rethinking and redesigning of research, developing and testing new methods for integrating the principle of open science & innovation and establishing new forms of stakeholder interactions and collaborations. The above can be performed by the participation of people to IdeaSquare's collaborative activities [27] like hackathons, workshops, Challenge Based Innovation (CBI) student programmes and plenty of innovation and entrepreneurship-driven events (**Figure 1.17**).

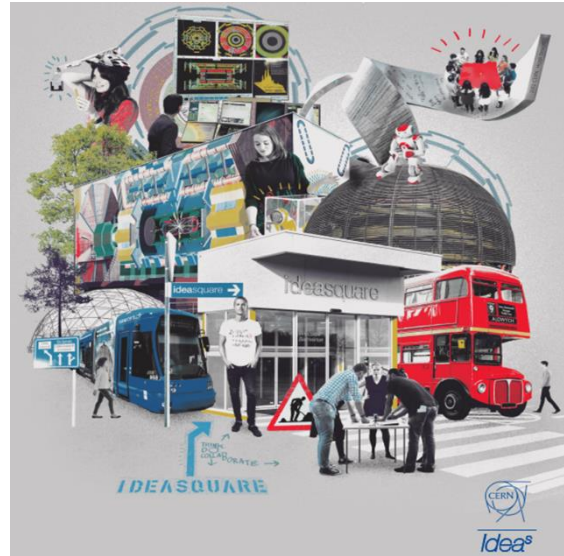
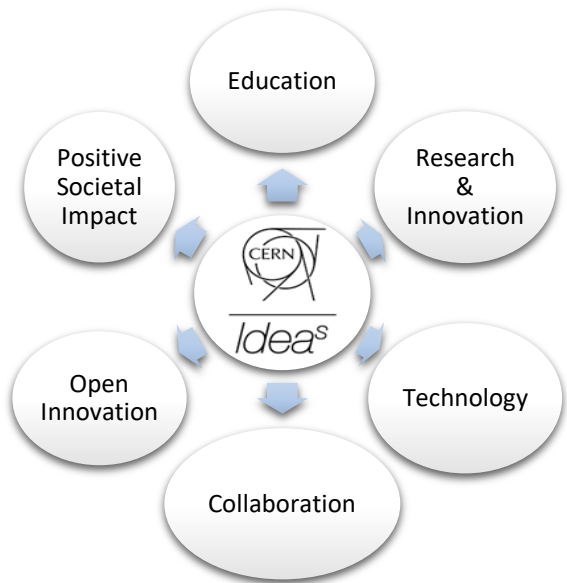


Figure 1.15. IdeaSquare in one picture.

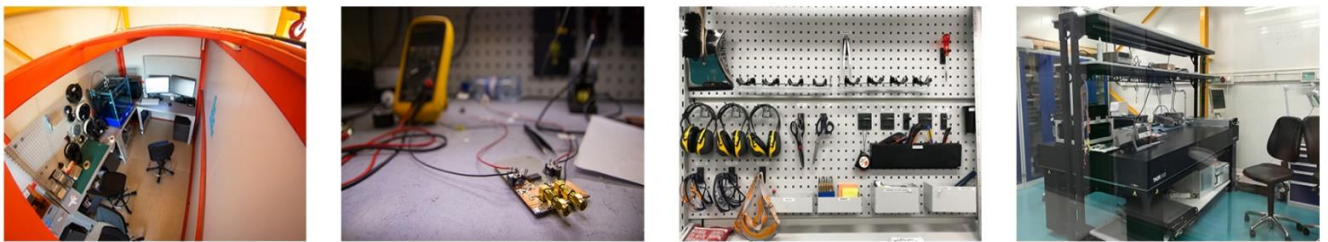


Figure 1.16. IdeaSquare facilities.



Figure 1.17. Events and hackathons at IdeaSquare, CERN.

IdeaSquare could not be away from R&D projects. In particular, R&D project, funded by the European Union, which are related to CERN detector's upgrades, ATLAS and CMS are hosted by IdeaSquare. In this frame, it participates in ATTRACT, where Phase-1 has been

successfully launched there [27]. Future plans include the integration of student programs in the selected projects in Phase-2. IdeaSquare team is working on ATTRACT, as members of the Project Consortium Board as well as the Project Administrative Office (PAO), which is the administrative body for the delivery of the ATTRACT Project.

In this respect, IdeaSquare and its team is an important contributor for the project SWaP. PAO provided always sufficient and useful information for the preparation of reports and presentations, required in ATTRACT Phase 1 and also a plan for Phase-2. In addition, the opportunity to participate in innovated activities, which enable brainstorming, has been an important factor for SWaP applications. IdeaSquare has a close contact with the Knowledge Transfer (KT) group, which provides a list of companies and industries with profiles that match with SWaP, in order to promote our work in real-world applications.

In frame of SWaP, IdeaSquare has built a contact between CERN and a team from Aalto University in Finland. One of the several University's projects is called Capstone in Sustainability course, in which postgraduate students work in multidisciplinary teams towards finding creative solutions to real-life social and environmental challenges brought by partner companies or organizations. SWaP was selected by a student team with a background in business, design and built environment, with an emphasis on sustainability areas. The key role of the team working on SWaP was to analyse the project, bring new fresh ideas and describe possible business and sustainable solutions. Their work concentrated on finding real life applications of SWaP, which are aligned to Sustainable Development Goals (SDGs) (**Figure 1.18**) and evaluating the societal impact of this technology.

Brainstorming, workshops and presentations (**Figure 1.19**) has been held in the facilities of Aalto University and IdeaSquare, aiming at SWaP sustainable applications. The team's work concentrated on exploring SWaP applications with a positive impact to society. Another role of this team was to search for industries and companies that are interested in SWaP's technology. The duration of the Capstone project and our collaboration was limited to three months. However, the team managed to bring some example applications of SWaP, which include fields such as hydroponics, aquaculture systems, pipe leakage detection and concentration of trace gases in the atmosphere. They also proposed a list of companies based in Finland that their work concentrates on the above mentioned fields.



Figure 1.18. The 17 Sustainable Development Goals (SDGs), which are an urgent call for action.



Figure 1.19. Left: The team from Aalto visited the CMS experiment, Right: The presentation of SWaP sustainable applications at IdeaSquare, CERN.

1.4 SWaP' scope

The **initial idea** of SWaP concentrates on the use of Additive Manufacturing (AM) techniques for the production of hydraulic components with embedded sensors inside their structures. AM technology, well known as 3D printing is very popular nowadays due to the fact that compared to traditional manufacturing methods, it has plenty of advantages and it is opening new possibilities to the world of fabrication and production. AM principle is based on the layer by layer or point by point additive fabrication to create objects of any requested complex shape and geometry. Taking advantage of AM operation, SWaP studies new AM processes capable of directly printing specific sensing functionalities together with the hydraulic part, in order to create 3D printed smart devices as a single components.

The **scope** of SWaP is to deliver a proof concept and the feasibility of its principle, to combine different AM techniques and methods. In other words, it is aiming to prove that first the combination of different AM methods is feasible and effective and second that the final prototype can be customized, reliable, relatively low cost and adopted in future cooling systems. The potential combinations of AM methods and the different used materials are plenty and require a lot of time for testing. In order to decide a first approach, a plan has been set with respect to the available time and budget that has been invested for this project. Thus, this work is divided in stages, considering that the primary stage should concentrate on how to create a functional component.

A **plan** has been launched to determine the design of both the pipe and the sensor, the AM methods and materials, and the type of the sensor, which is the most challenging part. Every proof of concept that is being in an initial phase is challenging, because many parameters that may not be already well defined should be considered. However, our idea was to start from the very basics and design components in a simplest way. In this sense, a straight pipe of stainless steel was fabricated using the Selective Laser Melting (SLM) technique and the type of the embedded sensor has the form of a straight line resistor for temperature fluid measurements. Temperature sensors are the simplest, in terms of production, calibration and data processing. The type of temperature sensor is an RTD (Resistance Temperature Detectors) that changes the resistance with respect to temperature changes. A silver-based straight line was deposited on the inner wall of the 3D printed SLM pipe via Aerosol Jet Printing (AJP) method.

The next plan of the project is to study how to expand SWaP for the detection of other fluid parameters such as pressure and flow. The design and fabrication of such sensors is not as simple as in the case of temperature. The integration of such sensors in a pipe, requires Therefore, more time and funds are required and should be invested in the research of design, fabrication, materials and integration of such sensors in a pipe, so that a functional device with proper electrical and mechanical properties could be produced.

To summarize, the aim of the project's initial phase concentrates on how to combine advanced manufacturing methods, in order to create a new generation of smart fluidic elements, compatible with existing standard hydraulic circuits and capable of providing measurements of fundamental fluidic parameters, with negligible addition of mass and volume and at an affordable cost. On this point, worth noting that SWaP's prototype will be the first demonstrator of its kind worldwide, and the technological platform will have a large positive impact not only on the future cooling systems of High Energy Physics detectors, but also on the field of scientific research on heat and mass transfer at small scales, and on several industrial fields.

SWaP's technology will be further analyzed in the next chapters, beginning with an introduction to Additive Manufacturing technology, including the principle, methods, materials and applications. The third chapter concentrates on metal 3D printing with an emphasis on SLM and the fourth chapter presents the Aerosol Jet technology that has been employed for the fabrication of the temperature sensor.

CHAPTER 2

ADDITIVE MANUFACTURING (AM)

2.1 Introduction to the AM Process

Additive Manufacturing (AM), commonly known as 3D printing or Rapid Prototyping is very popular nowadays but its story began back in 1980. AM is a fabrication technique that belongs to the technology of Rapid Prototyping (RP), which was developed during 1980s [28]. The term RP is used to describe the fast process of creating a physical model, called prototype, based on a Computer Aided Design (CAD) model. The produced prototype is not the final product but a fast and low cost representation of the final one. However, the development of RP techniques during the past years proved that AM is capable of manufacturing end products.

The first patent for a rapid prototyping system was applied by Hideo Kodama, back in 1980 in Japan [28]. He invented a system that employs UV light to harden photopolymer materials and it builds up a model layer by layer. This process is well known today, as Stereolithography. However, Hideo is not the inventor of Stereolithography because the patent was not filled within the deadline, due to funding issues that he faced.

Rapid Prototyping is also known as Solid Freedom Fabrication (SFF) or Layered Manufacturing (LM) or Additive Manufacturing (AM). These terms are synonymous, since they are based on the same principle and they follow a common process. The idea is to design a digital model, using a Computer Aided Design (CAD) system and to build this model by adding multiple layers of material. The process of AM is quite simple, fast and low cost comparing to traditional manufacturing methods. The steps of AM process (**Figure 2.1**) are common for all different AM techniques and they are the following:

1. 3D model design (CAD)
2. Conversion of CAD model to STL file
3. Slicing and G-code generation
4. AM process
5. Post processing

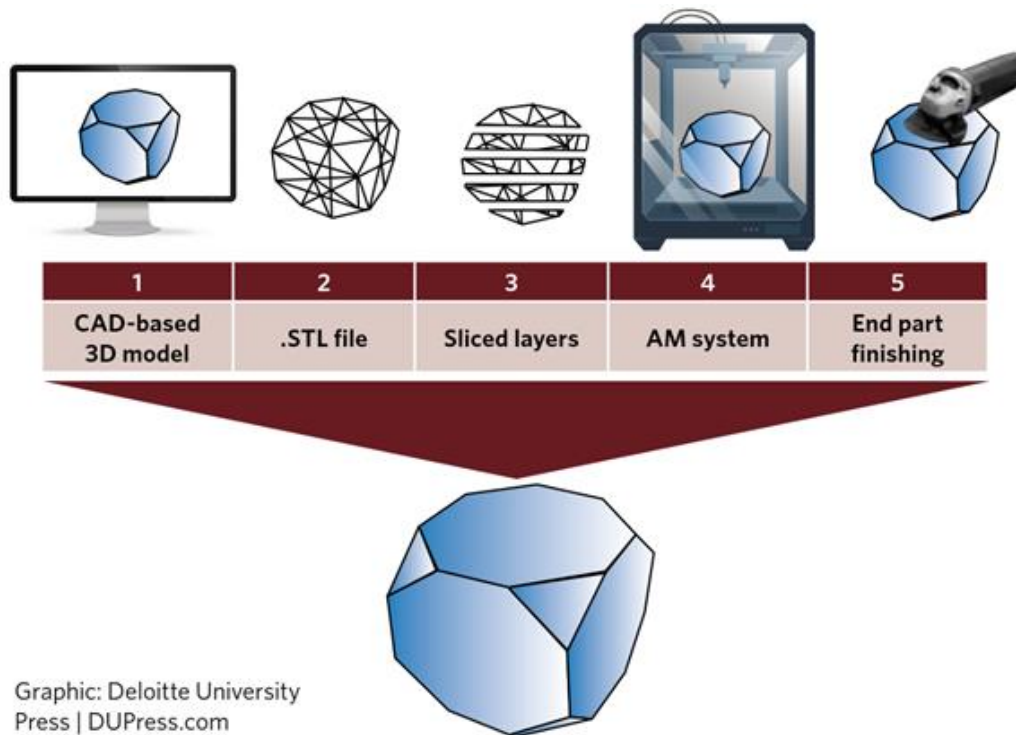


Figure 2.1. Steps of AM processes [29].

The first step includes the *creation and design of a virtual digital model*. The digital model can be created by many modelling Computer Aided Design (CAD) software such as AutoCAD, CATIA, Solidworks, etc. The CAD model is solid with clearly defined surface in terms of geometry, volume and topology. Another option of creating such models is based on the so called reverse engineering process that employs 3D scanners [30]. These machines use a scanning source, UV light, which is emitted from the source and received back after hitting the target object to be scanned. The use of 3D scanners finds applications in several fields, but mostly in prosthetic human parts [31].today, several websites provide already made digital models that can be easily downloaded (free or with charges) and used for 3D printing. However, this is a solution, suitable for users and hobbyists but not for industry or companies.

In the next stage, the *CAD model file is converted to an STL file format*. STL stands for STereoLithography, although it refers also as Standard Triangle Language or Standard Tessellation Language. Basically, this file converts the CAD model data into a triangulated surface by using 3D Cartesian co-ordinates [32]. It is the tessellated representation of the model's surface, consisting of many linked triangles. The STL file format is required for the slicing process and is readable by slicer software.

The *slicer software* is a tool that slices the 3D model, imported as an STL file, into uniform layers of a required thickness in horizontal orientation. The layer thickness depends on the geometry of the model and the printer's capability of setting parameters. In this stage, support structures can be added to the model, if it is necessary for the printing of the object. The support structure can be then separated from the final 3D printed object, usually manually. In addition, another role of slicing is to generate the *Geometric code (G-code)*. This code is a programming language that first has been developed and applied in Computer Numerical Control (CNC) machines. A code is generated and its commands (**Figure 2.2**) define and control the movement of the binding mechanism (extruder, laser, and print head) and of the platform direction [33]. Depending on the AM method, in some machines only the head moves in the three directions x,y,z and the platform is fixed, while in other printers only the platform moves.

```
G28 ; home all axes (X, Y, and Z)

G90 ; use absolute positioning for the XYZ axes

G1 X10 F3600 ; move to the X=10mm position on the bed

G1 X20 F3600 ; move to X=20mm
```

Figure 2.2. G-code commands [34]

Once the 3D model is ready and the G-code is generated, the *AM process* can almost begin. First, there are few parameters that should be defined before starting a printing. These are the printing parameters that can be defined and selected by the 3D printer's software, according to the printing method. These include, speed of printing, temperature of the print head or laser's intensity, temperature of the platform and other features such as the infill percentage (**Figure 2.3**) and geometry of the model (**Figure 2.4**). However, the industrial 3D printers require more parameters to be selected and also a preparation of the machine and the process chamber' environment should be applied. Then, the printing is ready to begin and the

machine follows the process of adding material layer by layer, until the completion of a 3D object.



Figure 2.3. Infill percentage of different ranges [35].

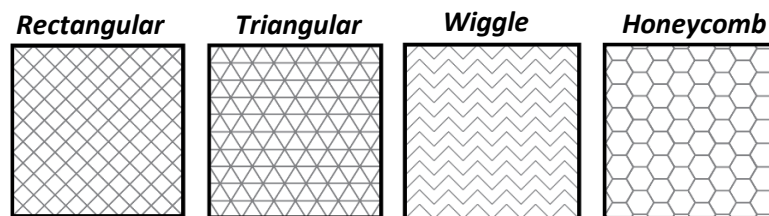


Figure 2.4. Common infill geometries in 3D printing [35].

The last stage refers to the *post processing* of the 3D printed object. This process needs to be performed, in order to further enhance the object. There are several tasks and techniques, which can be applied according to the AM technique that has been used for the fabrication of an object. These include support removal, resin removal, powder removal and surface finishing. Plenty of AM methods require support structures for creating complex geometries and shapes. These structures, whether use the same material as the printed object or different material, they should be in any case removed. Removing the support could be performed either by hand or by using sharp tools in a gentle way, in order to avoid damages of the 3D printed part. However, surface finishing is required. The resin removal refers to curing-based methods, where the post-processing step involves rinsing of the 3D printed part in a solvent bath and then UV curing. Rinsing removes all uncured resin residues and unclogs internal cavities, while UV curing it enhances the mechanical properties. On the other hand, Powder Bed Fusion AM techniques are using materials in a form of powder that after printing should be removed by suction, blowing, sweeping or blasting. In metal 3D printing, treatments such as machining, polishing or anodizing can reinforce the properties of metals.

2.2 AM Methods

Today, there are several methods of Additive Manufacturing (AM), which have been developed during the past 40 years to meet the demand of printing complex structures at fine resolutions. AM methods differ in terms of operating principle, materials and binding mechanism. AM processes are separated in seven categories (**Table 2.1**), defined by the American Society for Testing and Materials (ASTM) International Committee F42 [36]. This chapter reviews five out of seven categories, according to the categorization of the following table. Powder Bed Fusion (PBF) and Direct Energy Deposition (DED) are mostly used in metal AM and therefore will be presented on the next chapter.

Process	Method	Raw material	Type of material	Binding mechanism
VAT Photo polymerization	Stereo Lithography Apparatus (SLA)	Liquid resin	Photopolymer resin	UV laser
	Digital Light Processing (DLP)	Liquid resin	Photopolymer resin	UV projector
Material Extrusion	Fused Deposition Modelling (FDM)	Filament	Polymer/ Conductive/ Composite/ Wood	Thermal print head
Material Jetting (MJ)	Material Jetting	Ink	Polymer/ Wax	UV lamp
Binder Jetting (BJ)	Binder Jetting	Powder and binder	Ceramic/ Metal/ Polymer/ Composite	Binder material
Sheet Lamination	Laminated Object Manufacturing (LOM)	Sheet	Paper/ Plastic/ Metal laminate/ Ceramic/ Composite	Bonding
Powder Bed Fusion	Selective Laser Sintering (SLS)	Thermoplastic powder	Polymer/ Metal/ Ceramic/ Composite	Laser beam
	Selective Laser Melting (SLM)	Powder	Metal/ Alloy/ Ceramic	Laser beam
	Direct Metal Laser Sintering (DMLS)	Powder	Metal/ Alloy/ Ceramic	Laser beam
	Electron Beam Melting (EBM)	Powder	Metal/ Alloy	Electron beam

Direct Energy Deposition (DED)	Laser Engineered Net Shaping (LENS)	Powder	Metal/ Alloy	Laser beam
	Laser Metal Deposition (LMD)	Powder	Metal/ Alloy	Laser beam
	Wire and Arc Additive Manufacturing (WAAM)	Wire	Metal/ Alloy	Electric arc

Table 2.1. The seven categories of AM processes.

2.2.1 VAT Photopolymerization

VAT Photopolymerization is based on the principle of polymerization of resins that are cured under light irradiation. The resins have a liquid form and they are photosensitive. Today, there are several methods of additive manufacturing using photo-curing but the oldest and the most common method that has been developed is Stereolithography, well known as SLA. Digital Light Processing (DLP) also belongs to VAT Photopolymerization techniques and it is very similar to SLA. The difference between them is the light source. These methods are ideal for jewellery, low-run injection molding and many dental and medical applications, due to fine details produced parts. The main limitations of vat polymerization is the brittleness of the produced parts. Both methods are presented below.

Stereo Lithography Apparatus (SLA)

Stereolithography is the first developed method of additive manufacturing and it was invented by Charles Hull in 1984 [30]. Charles started his own company “3D Systems” in 1986, when the patent of stereolithography was issued. Some years later in 1988, the first Stereo Lithography Apparatus SLA-1 (**Figure 2.5**) was released to the market as a commercial product. 3D Systems is one of the biggest 3D printing companies until today.

Stereolithography belongs to the photo-curing AM methods, in which solid objects are built by the polymerization of specific materials; the photo polymer resins. The light source is a focused laser beam, which scans an area of the liquid photosensitive resin, in order to induce polymerization/ solidification and build up a layer. Today, an SLA printer (**Figure 2.6**) consists of a tank filled with resin, a build platform and a UV laser. The process starts when the build platform emerges inside the resin tank or vat and the UV laser, which is driven and focused by mirrors, is scanning a cross-section, and causing polymerization to the first layer. In the next

step, the build platform is being lifted up by the elevator and the UV laser solidifies the new layer upon the previous one. This process is repeated layer-by-layer until the entire part is being produced.

Stereolithography is a method that provides high quality surfaces of a printed object and post processing is not always required. Thermal post processing such as heating or photo curing is required for parts with high demands on mechanical properties. The printing resolution is also high within a range of 10 μm [37] and therefore the method is proper for applications where complex and detailed geometries are required. On the other hand, SLA is a slow and expensive printing method and materials are limited to photopolymer resins. The printing parameters that could affect and control the layer thickness is the energy of the light source and exposure [30].

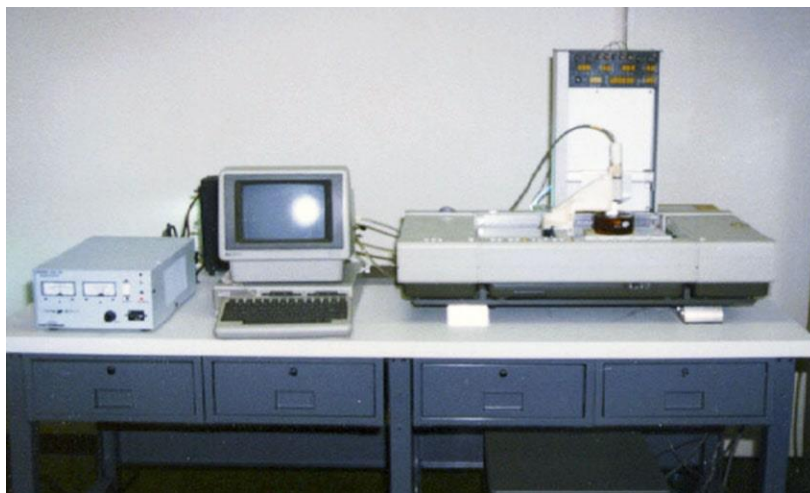


Figure 2.5. SLA 1, the first Stereo Lithography Apparatus [38].

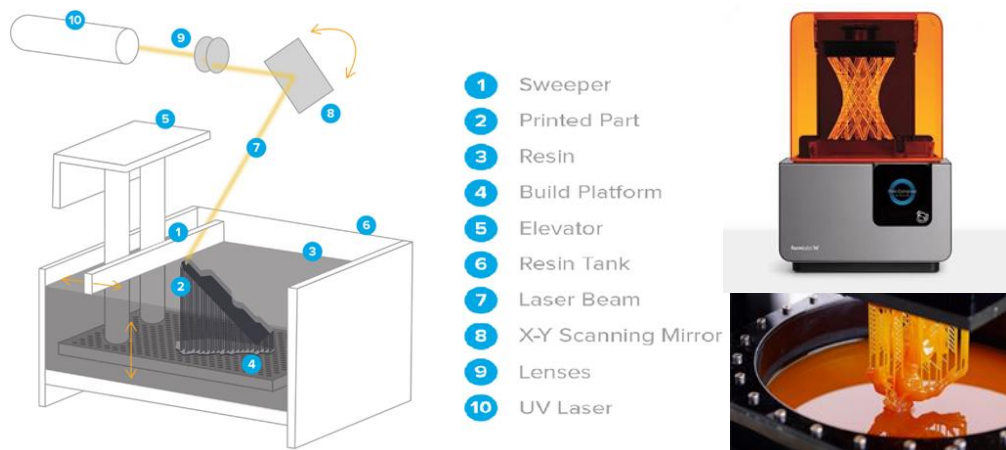


Figure 2.6. Stereolithography process and Formlabs SLA printer [39].

Digital Light Processing (DLP)

Digital Light Processing (DLP) is another photo-curing method of AM, very similar to SLA that is using photopolymers resins and a light source to build objects layer by layer (**Figure 2.7**). The main difference between SLA and DLP is the light source. SLA is using a laser beam that hits the photopolymer resin point-by-point to form a cross section of each layer, while DLP builds the entire cross section of a layer at once, using a DLP light engine or projector. A key factor of DLP is the use of an additional component, called Digital Micromirror Device (DMD), which is inserted between the path of light source and the tank of resin. DMDs are optical semiconductors, invented in 1977 by Dr. Larry Hornback and commercialized by Texas instruments in 1996 [40]. The DMD is composed of an array of rotating mirrors that reflect the light into or away from the resin. Every mirror represents a single pixel and every tilting of a mirror enables the switching of pixels. [40]. The DLP method achieves entire and uniform curing, with no difference between the inner areas and the outline, which means that post processing is an optional step. In addition, the printing speed is faster and the cost is lower comparing to SLA. However, the surface of a printed object is rougher and the resolution is lower.

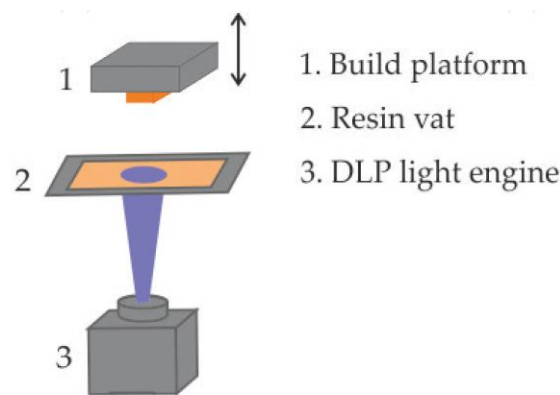


Figure 2.7. Digital Light Processing (DLP) process [41].

2.2.2 Material Extrusion

Material extrusion is a thermal process, where thermoplastic materials are heated or melted via a heated extruder. The melted material passes through a heated nozzle, which deposits the material layer by layer on a printer's bed. In this method, materials are provided in the form of wire. The most popular and widely used method of material extrusion is the fused deposition modelling (FDM).

Fused Deposition Modeling (FDM)

Fused Deposition Modeling belongs to the material extrusion 3D-printing methods. It has been developed after SLA and SLS, in 1988 by Scott Crump, the co-founder of the company “Stratasys”, one of the market leaders for high precision 3D printers [42]. One of the first industries to take on the technology in the early 90s was medicine. This method has become very popular nowadays, due to the fact that is commercially available, providing 3D desktop printers in affordable cost. A key factor that has contributed in the spread of FDM is the RepRap code. The RepRap is an open-source code that has been developed in 2005, accessible to everyone that was interested in printing parts of a 3D printer and assembling them, to build their own 3D printer. Back then, users of this code were obliged to print parts for three more printers that will be used afterwards by other people. Nevertheless, the real “boom” in FDM printing started in 2009, the year of patent’s expiration. This fact has led to the commercialization of such printers, the development of new companies, start-ups, services and jobs.

The principle of FDM method is based on the heating or melting of thermoplastic materials and their deposition in layer-by-layer fashion [43]. An FDM printer consists of a heated platform usually called bed and a heated head, which consists of the extruder and the heated nozzle. The materials are mostly plastics in a solid state and in a form of string, called filament. The process starts when the filament is pulled of a coil reel to the heated extruder’s nozzle driven by stepper motors (**Figure 2.8**). The extruder’s nozzle heats the material to its melting point, which is then extruded and deposited on the printer’s bed in a predetermined path, in order to form the first layer. The layer cools down and solidifies instantly with the help of a small fan placed next to the nozzle. The first layer is the solid base for the next layer. In most of the printers the extruder moves in x, y direction and the bed in z direction. However, few printers provide motion in z direction by the extruder. Once the first layer has been formed, the bed rises in a height equal to the previous layer’s thickness and the extruder starts the deposition of the next layer. The process is repeated until the entire object is fabricated.

FDM uses thermoplastic filaments of either 1.75mm or 3mm diameter and provides a very wide range of materials such as PLA, ABS, PETG, PEEK, Nylon, etc. [44]. The most commonly used materials are ABS and PLA, however the method offers more exotic materials such as carbon fibre, wood and conductive plastic. Every material has different properties and therefore the nozzle and bed temperature should be selected with respect to the specifications.

PLA (Polylactic Acid) is a biodegradable plastic, environmental friendly and finds applications in food packaging. However, PLA is brittle with low mechanical properties and cannot be used for items that bend, twist and are exposed in high temperatures. On the other hand, ABS (Acrylonitrile Butadiene Styrene) is a polymer with good mechanical properties, and resistant to high temperatures and chemical. It is often used for rapid prototyping and due to its high strength finds applications in industry. Both PLA and ABS are the most commonly used materials in FDM, due their low cost and ease of printing.

FDM is a method that everybody can use, since it offers desktop 3D printers (**Figure 2.9**) that are easy to use, they do not require particular environmental conditions and the cost is affordable. However, the rapid development of materials than can be used in a form of filament makes this method particular attractive for research and industry applications. There are several publications, focusing on the synthesis and fabrication of composite filaments with specific material properties. Although, there are several filaments already available on the market other than the common ones that show very good mechanical properties and can be used in applications, where structural demands are high. A good example is the carbon fiber filament, which is a filament like PLA, ABS, PETG, and nylon reinforced with short carbon fiber strands. Produced components are extremely stiff and rigid with relatively little weight. Therefore, carbon fiber filament is particular attractive for the production of components or devices that require structural strength, low density and good mechanical properties. One project, in frame of my postgraduate studies at the Hellenic Army Academy, utilized FDM with carbon fiber filament to print a drone for defence and army applications (**Figure 2.10**).

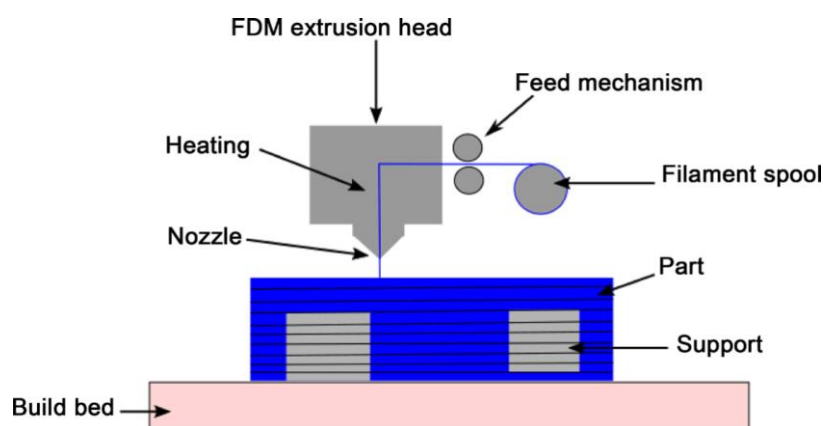


Figure 2.8. Fused Deposition Modelling (FDM) process [45].

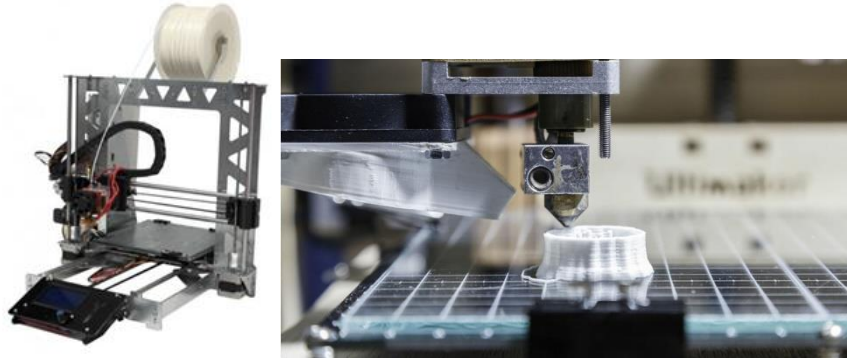


Figure 2.9. FDM desktop 3D printer.



Figure 2.10. 3D printed drone via FDM with carbon fiber filament for defence applications at the Lab of Mechanics of the Hellenic Army Academy.

2.2.3 Jetting

Material Jetting

Material jetting is a very common method of AM that builds objects in a similar way as two dimensional ink jet printers. In this technique, ink droplets are pumped and deposited on a surface via the injection nozzle, using thermal or piezoelectric method (**Figure 2.11**). The first layer solidifies and further layers are deposited on top of the previous. Then, the material layers are either cured or hardened by ultraviolet (UV) light. Post processing is required to remove the support material by using a sodium hydroxide solution or water jet. Due to the curing of the materials layers with UV light, further post treatment is not required.

The printing process can be either continuous or Drop on Demand (DOD) [46]. In the first approach, material droplets are formed via an oscillating nozzle and are deposited on the build surface. Then, droplets are charged and positioned onto the surface using charged

deflection plates. Droplets that are not used, they can be recycled back into the printing system. This approach provides high level of droplet control. DOD approach is used to deposit material onto a required surface. Droplets are formed and dispensed only when needed, controlled by thermal or piezoelectric actuators in the nozzle. Thermal actuators consist of a thin film resistor that forms the droplets and deposit them at a very fast rate. Piezoelectric actuators are preferable, in terms of materials range. Materials used in material jetting are limited to the ones that are able to form droplets. Commonly used materials are polymers and waxes, due to their viscosity.

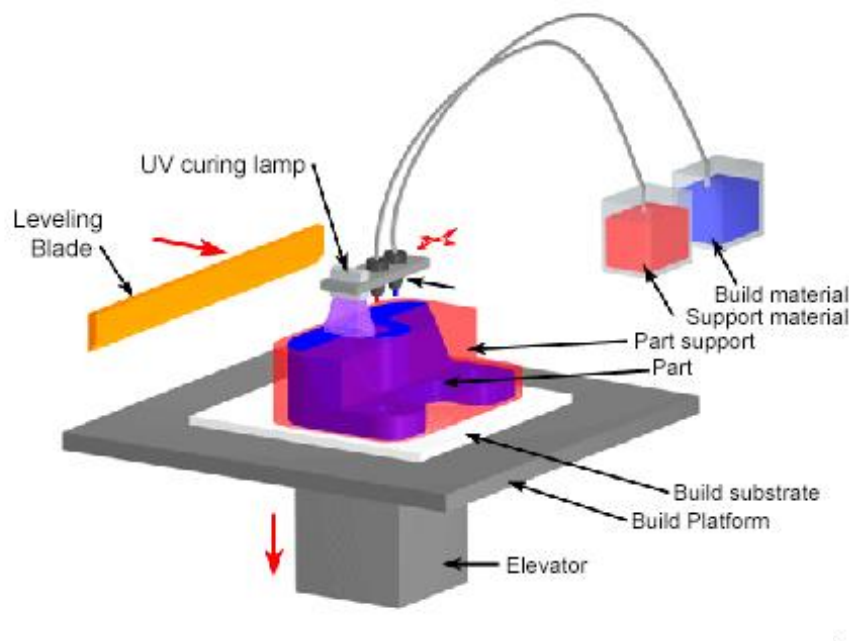


Figure 2.11. Material Jetting process

Binder Jetting

Binder jetting was developed at Massachusetts Institute of Technology (MIT) in the early 1990s but it was commercialized in 2010 [47, 48]. This method employs two materials, a powder-based material and a binder material (adhesive). The binder material is usually liquid and acts as an adhesive between powder layers. In this process, first powder is supplied via a piston and is spread in a thin layer over the build platform via a roller (**Figure 2.12**). The binder material is deposited via the print head on top of the powder and selectively binds powder particles. Then, the build platform is lowered at a height equal to the thickness of the first layer and a new layer of powder is spread over the previous layer. The process is repeated until the

entire part has been made. Support structure is not required, since the part is being printed within the powder. After printing, the unbound excess powder can be removed and reused for another printing. To achieve high quality finish, time is required for the binder to set and for the part to cool down and solidify. To enhance mechanical properties, post processing, such as curing, de-powdering, sintering, infiltration, annealing, and finishing is a mandatory step [49, 50].

A wide range of materials can be handled by this method, such as ceramics, metals/alloys (Al-based, Cu-based, Fe-based, Ni-based, and Co-based alloys) and composites. This method is well known for ceramic printing, since it was the first AM technique that achieved the fabrication of ceramic parts, and pioneered the direct fabrication of ceramic molds for casting. A key advantage of this method is the use of two materials, which provides different binder-powder combinations, which can adjust the mechanical properties by changing the ratio of the two materials. However, the use of binder materials may lead to porosity as in the conventional sintering process and therefore the material properties of the produced parts are not always suitable for structural parts, used mainly in aerospace and automotive applications [51].

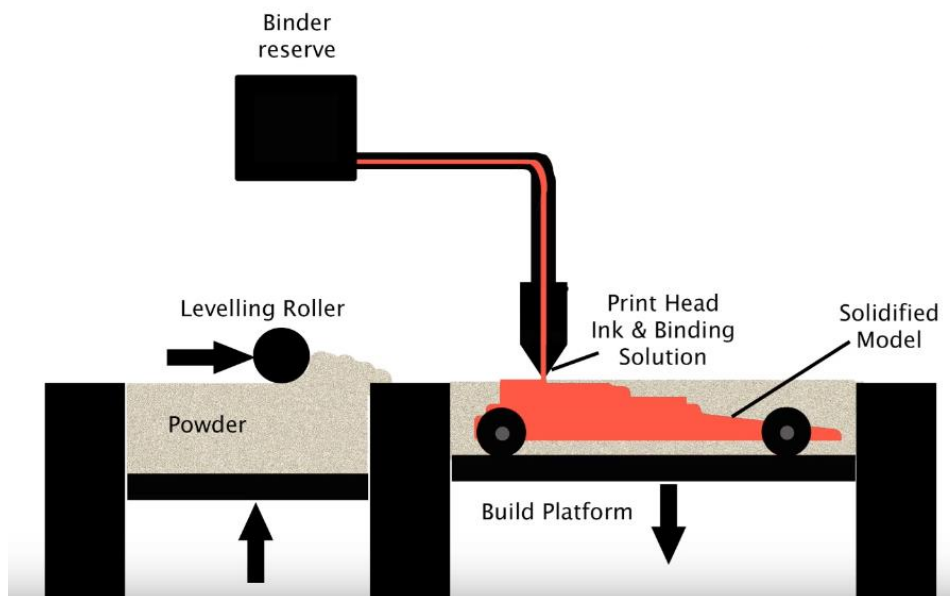


Figure 2.12. Binder Jetting process.

2.2.4 Sheet Lamination

Laminated Object Manufacturing (LOM) is an AM method that was developed by Helisys Inc (now Cubic Technologies). LOM is based on cutting and lamination of sheets or rolls of materials in layer by layer fashion. Sheets of material are laminated together by applied heat and pressure and are cut by a mechanical cutter or a laser, in order to form a geometry according to the 3D model (**Figure 2.13**). The process starts either by cutting and afterwards bonding (form-then-bond) or by bonding and then cutting (bond-then-form) [52]. The first approach provides removing of excess material before bonding and is usually applied for ceramic and metallic sheets. After cutting, the excess materials can be removed and recycled [52]. A wide range of materials can be used in LOM method, such as paper, wood, ceramics, polymer composites and metals. Depending on the type of material and demanded material properties, thermal post processing may be required. LOM is a simple, cheap and fast manufacturing method which is proper for the production of larger structures. Compared to other AM methods is less precise and accurate and therefore its usage is limited to simple geometries, where complexity is not required. LOM fields of applications are mainly food industry, paper manufacturing and electronics.

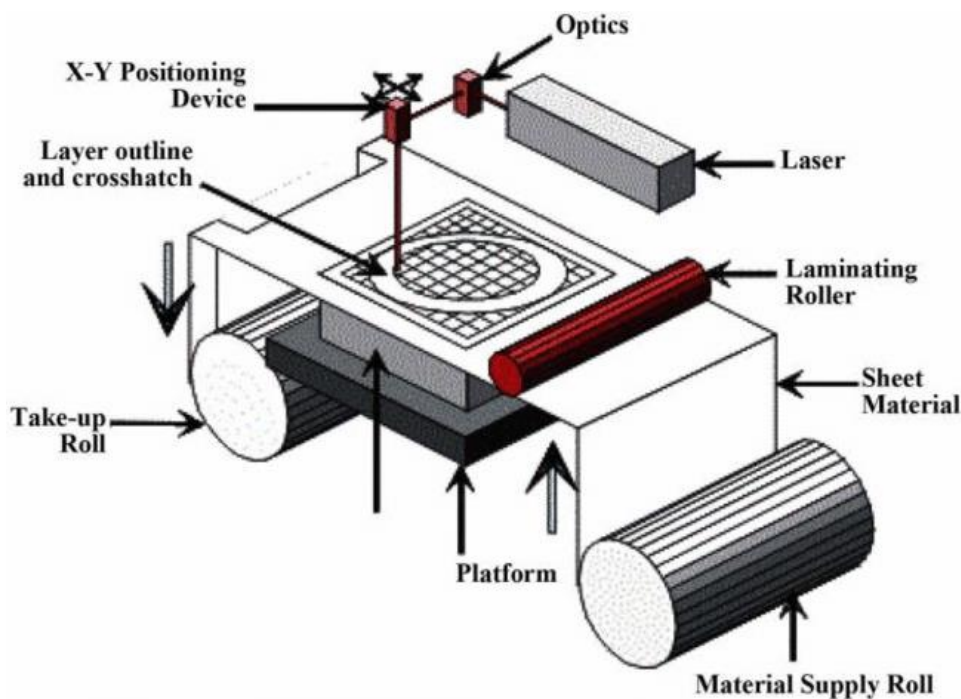


Figure 2.13. Laminated Object Manufacturing (LOM) process [53].

2.3 Additive Manufacturing vs Traditional Manufacturing

Additive Manufacturing is a continuously developed technology that is able of both prototyping and manufacturing of end-use products. AM does not replace other manufacturing technologies but it provides significant advantages over traditional manufacturing processes [54, 55]. Traditional manufacturing refers to processes that has been first developed and established in the world of industry, to create end-use products. The main processes of standard manufacturing include CNC Machining, Injection Molding, Plastic Forming and Joining. However, these processes have some limitations, in terms of complex shapes production and they are expensive due to costs of tooling, equipment, and labour for assembly and production. In order to even out these costs, traditional manufacturing requires mass production and therefore is not a proper method for prototyping or small scale production.

AM is a powerful tool that mainly reduces the complexity in the supply chain, for a variety of reasons. The key advantage of AM lies on the freedom of part design, which does not depend on any tool or mold. The main benefits of AM over traditional manufacturing include enabling mass customization, increasing design freedom, allowing for the reduction of assembly, and can serve as a cost-effective low volume production process. In particular, the key advantages of AM are the following [56, 57]:

- Design freedom
- Reduction of assembly
- Less material waste
- Less environment harmful
- On-demand manufacturing
- Less labour
- Singe step process

AM provides maximum *geometric design freedom* due to its operating principle of adding material selectively and fully controlled by software system. Any shape that can be designed in a 3D CAD program, can be entirely produced by AM. Complex geometries refer to three dimensional structures with many cavities or undercuts that their production by conventional technologies was either impossible or significantly expensive and time consuming. The developed methods of AM achieve not only complexity of structures but also

high accuracy and resolution of such parts in a reduced cost, due to lower material consumption.

Another benefit of AM is the **reduction of assembly**. Assembling is a very important stage in any production chain. Usually, components are produced and post processed individually and then assembled together, in order to obtain the end-use product. This is a process that consumes time and money, mainly due to labour work. Furthermore, this process rises the risk of errors or even damages of individual components. On the other hand, the binding mechanism of assembling often includes, welding and soldering that induces future potential failures of the seams. AM enables functional integration of less components by producing all required parts in one step and replacing or reducing binding mechanisms. Instead of multiple individual components, single components that consist of many parts can be produced at once by AM. Less assembled parts means lower cost, time reduction and errors elimination; factors that improve the efficiency of production.

Material consumption is a very important factor for product development and production. Traditional methods, such as CNC machining using subtractive manufacturing to create the desired shape of an object. This technology is efficient for creating large size components for mass production; however, the level of material waste is very high. Contrariwise, AM operates exactly in the opposite way. Instead of removing material, AM is adding material in selected areas, where it is absolutely necessary to build an entire object. This technology considers that products should consume resources that are required only for the functionality of a product.

Apart from the reduction of material waste, which consumes less resources, AM has further features that can contribute to **environmental protection**. The plastic materials used in AM are entirely recyclable and parts of metal powders that have not been melted during SLS/SLM process can be totally reused for another printing. AM builds solid parts with the option of selecting the infill percentage and geometry. Thus, it enables producing of lighter components that have however excellent strength to weight ratio. Weight is a very critical factor for vehicles and aircrafts, in terms of fuel consumption. The reduction of weight and mass, leads to less fuel consumption, mitigating harmful fuel emissions.

Various requirements and high demands appear increasingly in many industries, such as automotive and medical technology to produce custom products that fulfil the customer's needs. The design and fabrication freedom provided by AM, enables **production on demand**

with almost no limitation of product customization. AM contributes in medical technology, providing individual solutions with tailored shapes, functions and material strengths of the produced components.

Additive Manufacturing technology as compared to conventional manufacturing is capable of reducing the energy consumption, required in the fabrication process, due to the elimination of material waste. According to a study from Michigan Technological University [58], the production of parts via 3D printing technology requires 41% to 74% less energy than large-scale manufactured goods. Another study [59] by Digital Alloys, metal 3D printer manufacturer, compares the energy consumption, required in different metal AM technologies with the CNC machining. The first point of this study concludes that the energy consumption, required in the manufacturing process is larger in the case of metal AM and especially with Powder Bed Fusion (PBF) methods, compared to CNC processes. Taking into account other factors, which are essential to a manufacturing process, such as material waste, material recycling and post-processing, the results proved that AM is the less energy consuming process. The amount of material waste in CNC machining is the critical factor that increases the energy consumption in such processes (more than 90%).

CHAPTER 3

METAL ADDITIVE MANUFACTURING

3.1 Introduction

Additive manufacturing, has been first developed to produce prototypes. Nowadays, AM is capable of producing not even prototypes but also final products. In the beginning, AM processes were strictly limited to polymer materials. The advancement in laser and electron beam technologies contributed to the development of AM machines, capable of processing other than polymer materials, such as metals. Metal AM have several advantages when compared to conventional manufacturing, in terms of low volume production of complex geometries and mass customization. Metal AM features and capabilities are particularly attractive for various fields, such as aerospace, automotive and biomedical industries.

Several methods of additive manufacturing have been developed and classified in categories, as presented in the previous chapter. Some of these methods have been established and used almost only for metal production, although they are capable of processing a wide range of materials. However, other methods are developed particularly for metal processing. The major methods of metal AM are two and are classified in Powder Bed Fusion (PBF) and Direct Energy Deposition (DED). Both of them employ a heat source (laser, electron beam, arc) to sinter or melt a cross section of powder. The key difference between those methods is the way of introducing the material to the system (feeding mechanism). In PBF systems, powder is supplied through a tank and is spread via a roller or a rake in the powder bed, where a laser or electron beam scans and fuses selectively a surface. In DED, powder or wire is fed through a deposition nozzle directly on the surface, where an energy source simultaneously melts the powder. PBF and DED methods are presented in **Table 3.1**.

Other than PBF and DED, metals can be utilized in almost every of the seven categories of AM processes. Some of them are more promising and attractive, depending on the field of application. However, metal AM is a powerful tool for industry and is adopted in several industrial fields such as aerospace, automotive and defense. A recent study by Chedro [60] presents the distribution of metal AM process used in industry for 2020. According to the data, PBF is the mostly used method in metal AM for industrial applications and covers more than

50%, as compared to the rest. This chapter focuses on PBF processes, materials, challenges and fields of application. An introduction to DED processes is also presented here.

Process	Method	Raw material	Type of materials	Binding mechanism
Powder Bed Fusion	Selective Laser Sintering (SLS)	Thermoplastic powder	Polymers/ Metals/ Ceramics/ Composites	Laser beam
	Selective Laser Melting (SLM)	Powder	Metals/ Alloys/ Ceramics	Laser beam
	Direct Metal Laser Sintering (DMLS)	Powder	Metals/ Alloys/ Ceramics	Laser beam
	Electron Beam Melting (EBM)	Powder	Metals/ Alloys	Electron beam
Direct Energy Deposition (DED)	Laser Engineered Net Shaping (LENS)	Powder	Metals/ Alloys	Laser beam
	Laser Metal Deposition (LMD)	Powder	Metals/ Alloys	Laser beam
	Wire and Arc Additive Manufacturing (WAAM)	Wire	Metals/ Alloys	Electric arc

Table 3.1. The metal Additive Manufacturing methods.

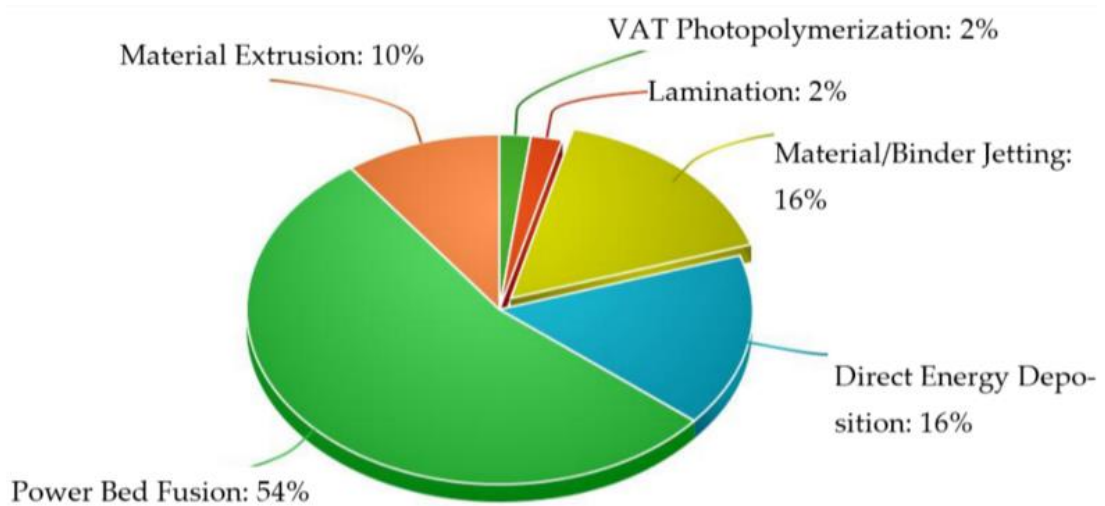


Figure 3.1. Metal Additive Manufacturing Market in 2020. [61]

3.2 Powder Bed Fusion (PBF)

Powder Bed Fusion (PBF) methods of additive manufacturing are using materials in a powder form and a thermal source (laser or electron beam), which induces fusion (sintering or melting) between the particles of powder in layer-by-layer fashion, according to the CAD model. A mechanism (roller/ rake) is used to spread a thin layer of powder on the build platform, where the thermal source is applied to a defined cross section of powder, forming the first layer (**Figure 3.2**). Then, the platform is lowered by one layer and a new layer of powder is spread to be fused. The process is repeated by adding several layers until the completion of the 3D printed part. The PBF processes of metals require a closed chamber with inert gases such as Argon (Ar) or Nitrogen (Ni) to prevent oxidation [62].

PBF systems are capable of processing a variety of materials such as metals, ceramics, polymers and composites. Nevertheless, it is the most popular technique for the production of metal parts. PBF processes are distinguished in Selective Laser Sintering (SLS), Direct Metal Laser Sintering (DMLS), Selective Laser Melting (SLM) and Electron Beam Melting (EBM). The key difference between sintering and melting is that in sintering, a material is heated up just below its melting point, while in melting just above its melting point. Therefore, the melting process requires higher laser power to melt metal powders and purer substance rather than an alloy, due to different melting points in alloys that could make the process difficult. Melting compared to sintering, produces parts with lower porosity, due to the fact that materials can consolidate before reforming and hardening to create a new solid structure.

All of the above methods utilize a laser beam to sinter or melt powder particles. Electron Beam Melting (EBM) also belongs to PBF methods but instead of laser, it uses an electron beam. A laser beam is focused and controlled by a system of lenses and scanning mirrors, while an electron beam uses magnetic coils to collimate and deflect the position of the beam and requires an electron beam column (**Figure 3.2**). Another difference of EBM with the other methods (SLS, DMLS, and SLM) is that EBM process is performed in vacuum. Among the above methods, SLM and EBM are considered to be the key players, in terms of metal AM, due to the fact that melting compared to sintering process provides finer and less porous end surfaces. However, SLS remains a powerful method for polymer processing. This section presents the operating principle and process of each PBF method.

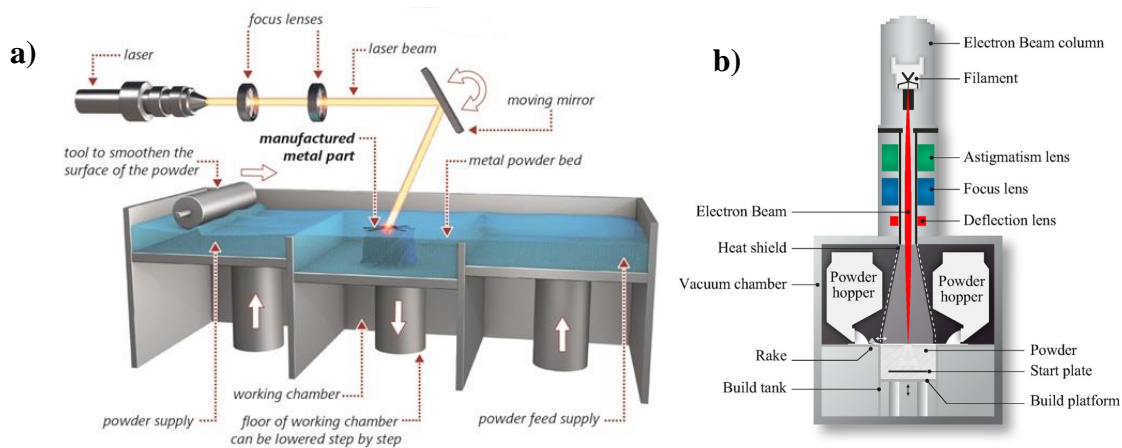


Figure 3.2. a) PBF system with laser beam (SLS, DMLS, SLM) [63] and b) PBF system with electron beam (EBM) [64].

3.2.1 Selective Laser Sintering (SLS)

Selective Laser Sintering was the first method of powder bed fusion techniques of AM that was invented in 1988 by Carl Deckard, an undergraduate student at the University of Texas [65]. The first SLS machine was called Betsy and was able to print only simple plastic parts. In the beginning, SLS used only polymers and nylon to create prototypes. However, as the method was further developed, a wide range of materials such as metals, ceramics and composites in form of thermoplastic powders can be applied to produce functional end products.

SLS is based on sintering, a process of fusing particles together into one solid mass by heating but not melting to the point of liquefaction [66]. Sintering occurs at lower temperatures and less energy is required to cause the solidification, comparing to melting. The process begins when the roller spreads a thin layer of powder over the preheated build platform (**Figure 3.3**). Then the laser beam, usually CO₂ laser scans a cross-section and sinters selectively the powder particles to form the first layer. The build platform is then lowered by one layer thickness and a new layer of powder is spread and sintered upon the previous layer. The process is repeated until the entire solid part is being produced. The 3D printed part is fully encapsulated in powder, which has not been sintered and should be removed by compressed air or blasting. However, the unused powder can be collected and reused for another printing.

SLS does not require support structures, since the object is produced in the platform where powder is only supplied but not removed. This fact, makes the method proper for

producing complex geometries and shapes. However, SLS parts have a grainy finish and post processing is required. First, compressed air is applied to the SLS part to remove all the excess powder. Then, the part's surface is further cleaned via bead blasting to remove powder that is not sintered but it is stacked to the surface. Sometimes, polishing can be applied for a smoother and excellent finish surface.

This method is capable of producing functional parts from a wide range of materials such as Nylon, carbon-fiber filled nylon, PEEK, TPU. The most commonly used material of this method is Polyamide 12 also known as Nylon 12. This material can be filled with carbon fibers, glass fibers and aluminum to improve the mechanical and thermal properties of SLS produced parts. SLS parts exhibit good mechanical properties and isotropic behavior. However, internal porosity is a common feature of this method and special post treatment is required to enhance humidity resistant.

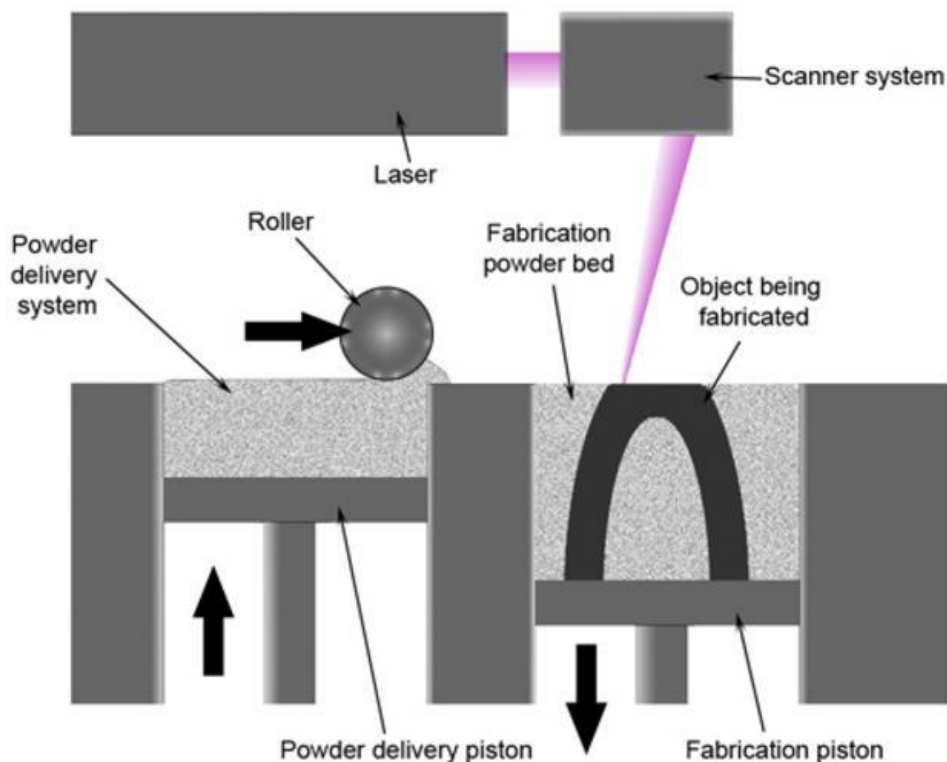


Figure 3.3. Selective Laser Sintering (SLS) process.

3.2.2 Direct Metal Laser Sintering (DMLS)

Direct Metal Laser Sintering (DMLS) was developed jointly by the Rapid Product Innovations (ElectroluxRapid Development, Finland) and EOS GmbH (Germany) [67]. DMLS is essentially the same process as SLS; both employ a laser source to sinter selectively a cross section of powder. However, this method differs from SLS, in terms of material powders. DMLS can process only metallic powders, while SLS process metals, ceramics, polymers and composites. A variety of metal powders free of binder can be used in DMLS, with the most common to be bronze-based and stainless steel-based powders. Stainless steel requires Nitrogen atmosphere, while bronze can be processed in regular atmosphere environment.

3.2.3 Selective Laser Melting (SLM)

Selective Laser Melting (SLM) is the second method after SLS that has been developed in 1995 at the Fraunhofer Institute ILT in Aachen, Germany [68]. This method is very similar to SLS and is based on the same principle, using a laser source to fuse selectively a cross section of each layer of powder. The key difference is that SLS sinters the powder, while SLM melts it. Therefore, they differ, in terms of laser power and material powders that can be used.

Typically, a SLM system consists of an enclosed process chamber with three cylinders, a roller and a laser source. The process chamber is filled with an inert gas, typically Nitrogen or Argon, to prevent oxidation of metals during thermal processing. The powder is placed on the supply cylinder and the process starts when the roller shifts a very thin layer of powder, with a thickness of 10-100 μm [69] from the supply to the build cylinder, where the laser scans and melts a cross section of powder, according to the processed data (**Figure 3.4**). Then, the excess powder is being delivered to the third cylinder; the build cylinder is lowered and the next layer of powder is deposited and melted by the laser. This process is repeated until the entire component is built. Unlike SLS, in this method support structure is required, since the excess powder is being removed from the build cylinder. The excess powder that has not been used can be reused for another printing. Once the component is complete, it can be separated from the substrate cylinder manually or by electrical discharge machining. The support structure can be easily removed manually but post processing, such as polishing is required to

obtain a perfect surface. Additional post processing could be performed, if it is needed to improve porosity and surface roughness.

SLM employs high power lasers of 200 to 1000 W [69], commonly carbon dioxide (CO₂) or fiber. An impressive feature of SLM is that some machines have the option to work with more than one laser beams (**Figure 3.5**), producing a batch of the same components at the same time. When the laser beam heats the material, this expands and after it shrinks during solidification. Therefore, residual stresses are observed, due to shrinkage and the rapid heating and cooling of the powder layer. To reduce the development of residual stresses, preheating of the powder is required. Some SLM systems provide the option of preheated build platform or even of the entire process chamber. Thus, the fusion of the particles is smoother and faster, and internal stresses are reduced.

Materials used in SLM are mostly metal and metal alloy powders without thermoplastic coating, such as stainless steel, titanium, aluminum, cobalt-chrome, and nickel. In addition, SLM is capable of processing ceramics. Due to higher melting point of metals and ceramics and absence of binder material, higher laser power is required. Post processing, such as material infiltration or heat processes commonly used in SLS, here are not required. SLM is a highly accurate process that produces very dense parts. It is particularly attractive for the aerospace and automotive industry, due to dense but lightweight produced components.

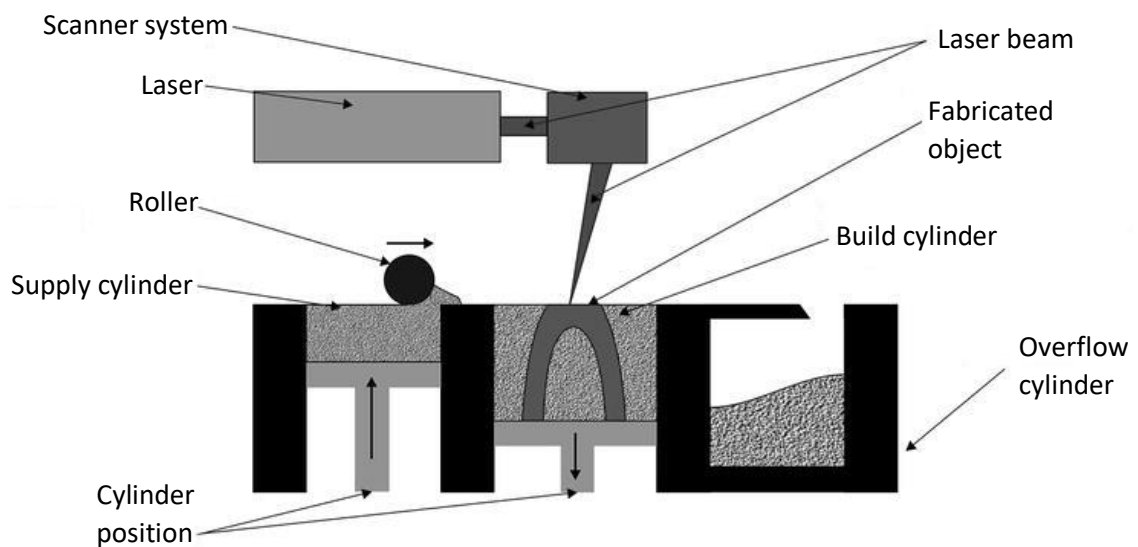


Figure 3.4. Selective Laser Melting (SLM) process.

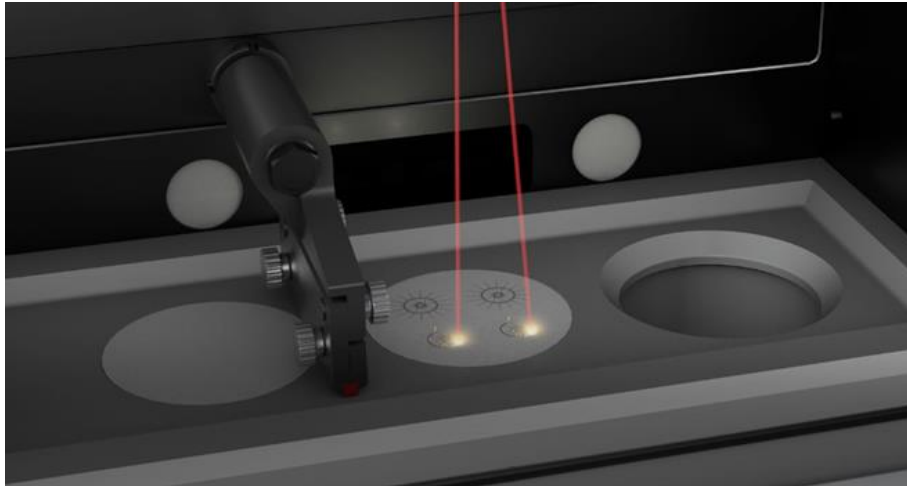


Figure 3.5. SLM machine with two laser beams [70].

3.2.4 Electron Beam Melting (EBM)

Electron Beam Melting (EBM) is a PBF method that was developed in 1997 by the company “Arcam” in Sweden [71]. It is based on the same principle as other PBF methods that use materials in the form of powders and an energy source to produce layer by layer 3D components. EBM is capable of producing fully dense components, as SLM. The key difference between them is the energy source. EBM uses an electron beam instead of laser, which means that energy is carried by electrons and not by photons, as it is in lasers. The reaction between powder and electron beam induces the solidification of particles, due to electrical charges. Materials used in EBM are limited to conductive metal and metal alloy powders but no polymers or ceramics can be applied.

An EBM machine consists of the electron gun, the process chamber under vacuum of 10^{-4} – 10^{-5} mbar [72], two hoppers filled with powder and the rake (**Figure 3.6**). The electron gun operates at a power of 60kW [69] and generates an electron beam, which is focused by focus lenses and controlled by deflection lenses. Focus lenses are electromagnetic lenses that focus the beam in a desired diameter, while deflection lenses control the deflection of the focused beam at points of the powder layer that need to be scanned. EBM process includes two stages, the preheating and melting [73]. First, a thin layer of powder with a thickness of 50-150 μm [69] is spread by the rake on the preheated build plate and the electron beam is used to scan the layer several times, in order to heat and sinter the powder particles. After preheating, the

current and the scanning speed of the electron beam are lowered and the beam scans the same cross section of powder, in order to melt the particles and form a solid material. Once the printing process is completed, support structures are removed and post processing is applied to enhance material properties, similar to SLM. Materials used in EBM are limited to conductive metals, such as titanium alloys, titanium aluminide, stainless steel, copper, Inconel and others.

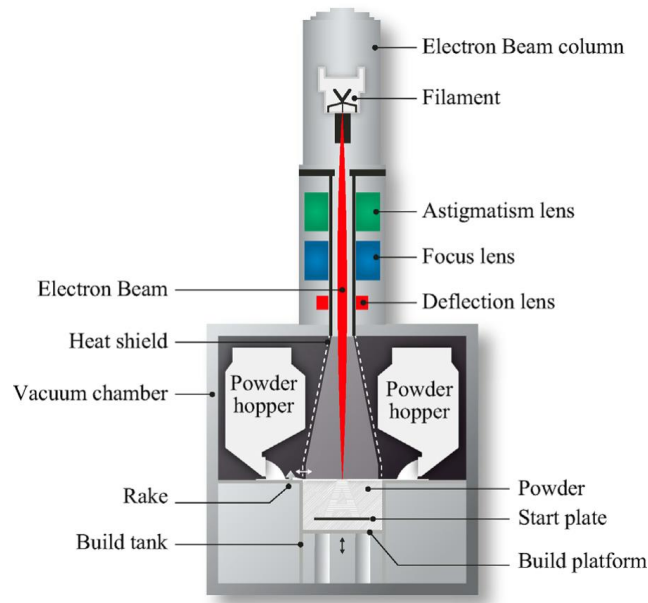


Figure 3.6. Components of an EBM machine by Arcam.

3.2.5 SLM compared to EBM

SLM and EBM are the most commonly used methods of metal AM. Both processes are very similar and they are based on the same principle of melting powder materials by an energy source. The key difference between them is the type of energy source, which is a laser beam for SLM and electron beam for EBM. Since, laser sources are carried by photons, while electron beams by electrons, the solidification in EBM is induced by the reaction of electrons with powder particles, due to electrical charges. Therefore, the range of materials used in EBM is limited to conductive metals, contrary to SLM that is capable of processing a wide range of metals and ceramics.

Unlike SLM, EBM transfers energy at very high speed via the kinetic collisions between accelerated electrons and powder particles. This means that the electron beam is so powerful that induces negative charges, other than melting of the powder. As a result, powders repel some of the electrons and the beam becomes more diffused. However, the electron beam penetration is higher than the laser's beam, reducing the process time compared to SLM.

In both processes residual stresses are observed, due to the rapid heating and cooling of the powder layer. Preheating of the powder, prior to melting is required to reduce the thermal gradients and therefore the development of residual stresses. In SLM systems the preheating of the powder is made via the heating of the build platform. On the other hand, EBM systems use the electron beam to scan and heat the powder before melting. Preheating is an important stage in the process that can result in variations in the morphology of the printed part, if it is not applicable. It is advisable to read the machine's technical features and specifications because this feature is not available in all of the PBF systems.

Another difference between the two methods is the process environmental conditions. The EBM process is performed under vacuum, which is required for the quality of the electron beam. In addition, vacuum acts as an insulator and reduces thermal convection and gradients, and oxidation of metals (e.g. titanium alloys). On the other hand, SLM process uses Argon to prevent oxidation of some sensitive to it metals or Nitrogen for non-reactive materials. The different conditions of environment, result in lower oxygen content in EBM produced parts than in SLM parts.

In general, EBM is a high-cost process with smaller available build volume and lower accuracy, as compared to SLM. Many industrial applications have adopted SLM to their production, in particular in aerospace field, as it is presented in section 3.4. SWaP prototype also used successfully SLM to produce the pipe, the hydraulic interfaces and the electrical connectors of stainless-steel powder.

3.3 Direct Energy Deposition (DED)

Direct Energy Deposition (DED) principle derives from welding technology, where material is deposited by focusing a shielded gas over the molten pool [74]. Typical DED systems consists of an energy source, a deposition nozzle and a substrate plate, which can be either stationary or rotated, enabling movement in more than 3-axis. During the process, inert gas (Argon or Nitrogen) is supplied to prevent oxidation of metals, such as titanium alloys. Moreover, purge cycling can be performed, to reduce the content of oxygen in the environment. DED methods use feedstock material in the form of powder or wire and an energy source that can be either laser, electron beam or electric arc. In DED process, as the material is deposited through the nozzle, material is being melted simultaneously by the heat source beam. DED methods are distinguished either according to the type of material feedstock or the energy source (**Figure 3.7**). According to the type of material feedstock, they are divided in powder-fed systems and wire-fed systems (**Figure 3.8**).

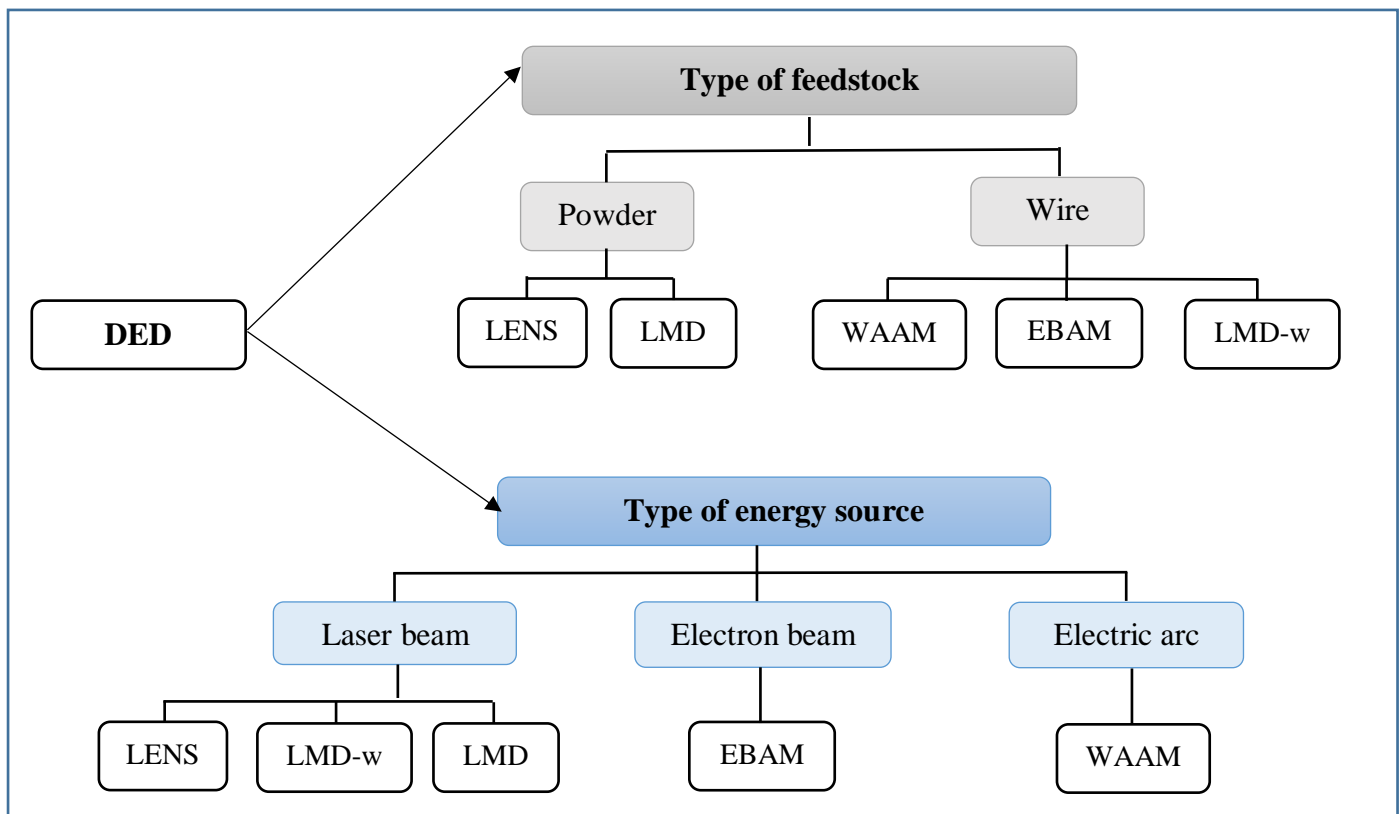


Figure 3.7. Classification of Directed Energy Deposition (DED) systems.

In powder-fed systems, powder is supplied through a nozzle and is melted by a laser or an electron beam. Laser Engineering Net Shape (LENS) developed by Sandia National Laboratories and commercialized by Optomec, employs a laser beam to melt a stream of powder. Another common method that uses powder, is called Laser Metal Deposition (LMD), in which powder is melted by a laser or electron beam.

In wire-fed systems, wire is deposited through a nozzle and melted by the energy source (laser, electron beam, electric arc), which is surrounded and focused by inert gas. Compared to powder-fed systems, this method provides higher deposition rates. Such methods include Wire Arc Additive Manufacturing (WAAM), in which the wire is melted by an electric arc and Laser Metal Deposition- wire (LMD-w) that employs a laser beam. Similar to WAAM and LMD-w, Electron Beam Additive Manufacturing (EBAM) also uses wire but utilizes an electron beam to melt the wire, producing near-net shape parts inside a vacuum chamber.

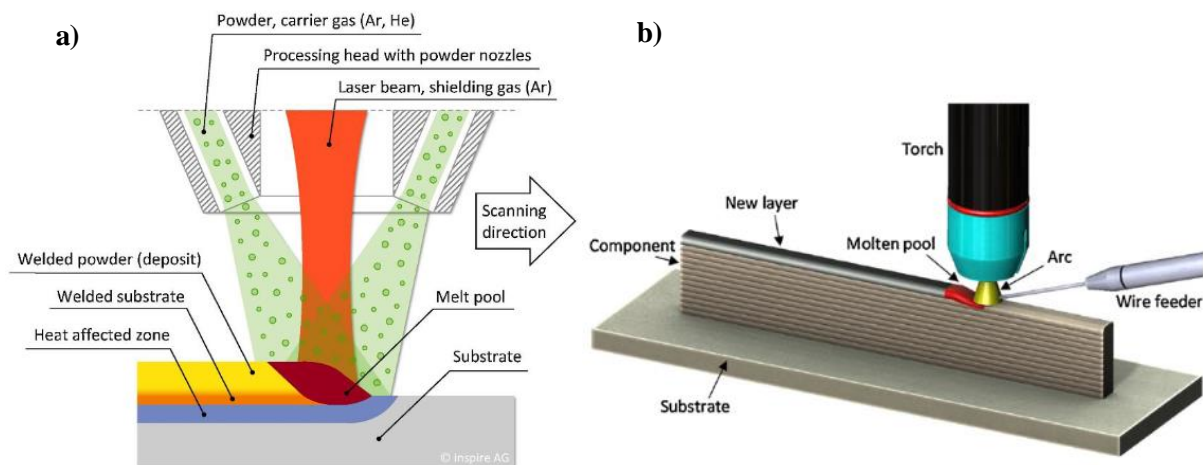


Figure 3.8. Schematic of **a)** powder-fed DED process [75] and **b)** wire-fed DED process [76].

The main differences between DED and PBF systems derive from material feed and material melting. In PBF systems the material (powder) is spread on the bed via a roller, while in DED systems the material (powder or wire) is deposited through the nozzle on the build substrate. Additionally, the material is being melted at the same time as it is being deposited, unlike PBF that the material is first spread and then selectively melted. Due to the deposition nozzle, DED methods can be used not only for manufacturing but also for repairing and coatings. DED has been successfully employed to repair large-scale metal components and to deposit coatings. Worth noted is the ability of DED systems to switch the input material feedstock, providing layers with different composition.

A key advantage of DED methods is the high deposition rates, which reach an average of 1 Kg/h, instead of 0.1 Kg/h that is reached by PBF. Due to this fact, DED are proper for the production of large components with high ratios. However, such higher deposition rates lead to increased layer thickness, which results in rougher surfaces of lowered accuracy. In DED systems, the material, the produced heat by the laser and the shield gas are transferred from the nozzle directly to the build platform, achieving more efficient heat conduction, compared to PBF systems. Another observation focuses on the laser or electron beam movement, which is faster in PBF systems compared to the movement of DED nozzles. Faster movement induces porosity, due to sharp thermal cycles.

3.4 Process parameters & metallurgical defects

Metal AM is a heat transfer process that uses an energy source to cause solidification of metal particles. A single scan forms a solidified material line, which's quality depends on heat source power and scan speed. A single layer is formed by multiple scanned lines and is defined by hatch/scan line spacing. The thickness of each layer should be determined so that multiple layers can be consolidated and form the required solidified part. These parameters (**Figure 3.9**) are essential, since they have an impact on the final part, in terms of surface roughness and defects (porosity, balling, etc.) and they should be wisely considerate. These parameters introduce the term of energy density that is defined, according to metal AM used method.

In PBF processes that work with laser beam, such as SLM, energy density is expressed as [77]:

$$E = \frac{nP}{vhd} \quad (3.1)$$

Where, E is the energy density (J/mm^3), n the number of repeated scanning, P the laser beam power, v the scanning speed, h and d the energy absorption thickness and width, respectively. In DED processes or electron beam-based PBF processes, such as EBM, the energy density is represented as [78]:

$$E = \frac{4UI}{\pi vs} \quad (3.2)$$

Where, U is the acceleration voltage, I the current of the electron beam and s the scan line spacing. Considering material feed rate in DED process, the energy density can be expressed as [78]:

$$E = \frac{PF}{s} \quad (3.3)$$

Where, P is the laser beam power, F the material feed rate and s here is similar to scan speed in PBF processes.

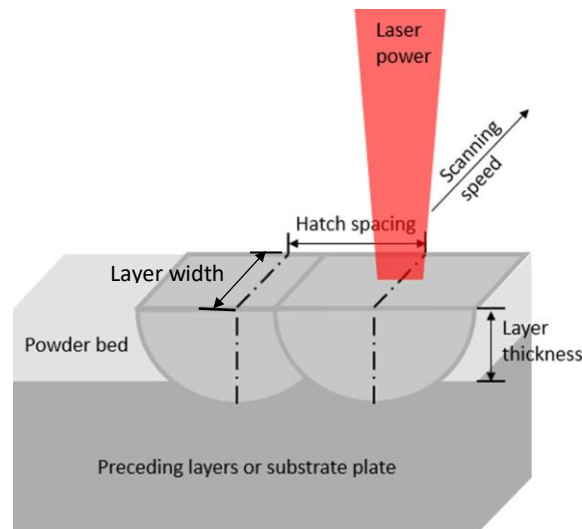


Figure 3.9. Process parameters: laser power, scanning speed, hatch spacing, and layer thickness and width [79].

Process parameters is the key factor, in order to produce dense parts with homogenous melting and consolidated layers. It is essential, to find out a proper combination of energy power and scan speed so that process parameters are optimum, obtaining structures with eliminated defects. Several phenomena, such as defects, cracks, balling, and porosity are observed, due to non-optimum parameters and are presented in this section.

Porosity and balling

Porosity is a very common attribute in parts, produced by metal AM that affects negatively and can reduce the mechanical properties of a produced part. Two are the main factors that can induce porosity [80]; gas pores in powder, called *powder-induced porosity* and non-optimum process parameters, called *process-induced porosity* (**Figure 3.10**).

Powder-induced porosity is caused by trapped gas in powder materials. Gas pores are internal pores that are caused by gas entrapment during metal powder production. These pores are spherical and can be transferred to the fabricated parts. However, porosity formation is mainly caused by process parameters.

The main parameter that is linked with process-induced porosity is the energy power, which causes either lack-of-fusion [81, 82] or shrinkage [83, 84] porosity. If the applied power is insufficient, residual un-melted powder particles with poor metallurgical bonds, causing lack-of-fusion pores in the produced part. On the other hand, if the applied power is too high causes spatter ejection, which means that temperature exceeds the boiling point and the

evaporative material creates melt pool with trapped vapor bubbles, causing shrinkage porosity. Regions of molten pool with incomplete solidification are observed and induce irregular-shaped pores in the entire produced part.

Energy density is the key parameter in porosity formation. Adjustment of the main parameters such as beam speed and beam power have been studied, in order to explore their effect on porosity formation. However, the relationship between different forms of porosity is not very clear and further studies need to be conducted.

Balling or melt ball formation refers to the solidification of material into spheres instead of layers, wetted onto the part. Balling occurs when the process temperature becomes too high, which limits the liquid phase formation in the molten pool. Balling is related to various mechanisms, such as molten pool behavior, wettability, Marangoni convection and surface tension [85]. Energy density and material features affect mostly these mechanisms [86, 87]. The phenomenon of balling is very unwanted, since it forms rough and spherical structures on the surface of the printed part, degrading the quality of the final structures.

Balling is mostly attributed to poor wettability and droplet splashing. The molten pool consists of an upper and a lower part (**Figure 3.11**) [88]. The balling phenomenon is mainly promoted by the gas-liquid interface of the upper molten pool. On the other hand, the lower melt pool in the molten substrate material prevents the balling trend of the upper part. The balling of the upper melt pool can be completely prevented by enough melt in the lower molten pool [88]. In order to obtain sufficient liquid metal in the upper melt pool, energy density should be high. However, the laser energy should be adjusted in way that the energy density is high enough to enable sufficient liquid but not too high, which will cause balling and deformations [89, 90].

In order to minimize porosity and balling phenomena in metal AM, process parameters should be adjusted so that optimum energy density is obtained, which is the main factor that determines the level of such defects in the printed parts. PBF and DED processes have been studied, in order to define an optimum combination of process parameters for different kind of metals and metal alloys [91-95]. These studies conclude that high energy density levels, which means a combination of high energy power and low scan speed (low h and d) result in minimum porosity and balling phenomena. Another factor that can contribute in reducing balling, is lowering the oxygen level during the SLM process [96]. Oxygen is forming oxide films in the surface of each layer and obstructs interlayer bonding, which leads to balling. An oxygen level

at 0.1%, applying a combination of high laser power and low scanning speed could reduce significantly the phenomenon of balling.

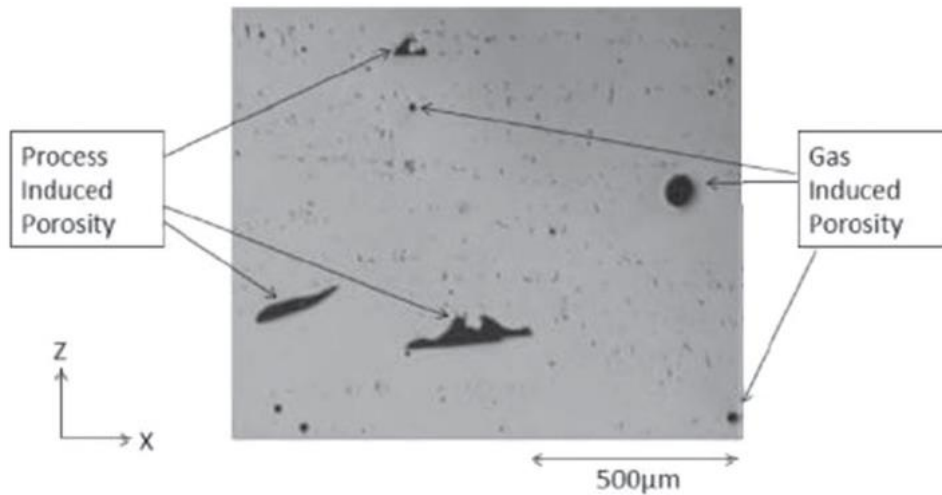


Figure 3.10. Process induced porosity vs. Gas induced porosity [80].

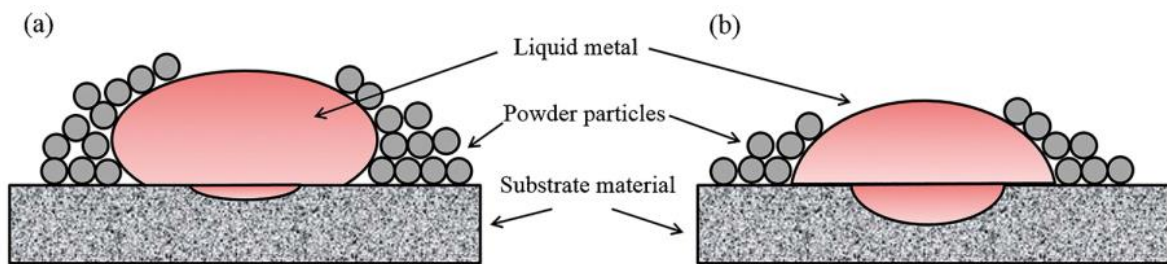


Figure 3.11. Illustration of balling phenomenon. **a)** Less molten substrate material and **b)** more molten substrate material [97].

Residual stresses and cracks

Residual stress is a common effect that occurs during metal AM processes due to continuous thermal cycling, which is characterized by rapid heating and solidification, high cooling rates and temperature gradients. This results in an inhomogeneous heat distribution that generates thermal expansion and contraction to the solidified structures [98]. Residual stress is a very critical issue in metal AM parts, since the steep residual stress gradients formed around the molten pool could lead to cracking, delamination, fatigue failure and thermal deformation [99, 100].

Stresses are formed during mechanical and thermal processes and are mainly divided in two types, thermal and structural stresses [100]. When heating produced by the energy source (laser, electron, and arc) is uneven, then different amounts of thermal expansion and shrinkage deformation between the regions near to and away from the molten pool are formed and causing thermal stresses [101,102]. On the other hand, structural stresses are mainly caused due to material phase transformation during the process [103]. The different specific volume of phases causes volume expansions and contractions to the material and results in structural stresses. Residual stresses affect the functionality and strength of the produced parts by causing cracks or even plastic deformation. Cracking is a common effect in metal AM produced parts and is caused by thermal stresses. Thus, it is essential to predict the distribution and evolution of residual stresses with respect to the process parameters.

In order to reduce residual stresses, process parameters should be adjusted in a way that optimal energy density is obtained. Low energy density causes not uniform solidification of liquid metal, usually results in balling which leads to cracks formation. On the other hand, very high energy density implies low liquid viscosity and long liquid lifetime and is increasing the possibility of thermal stress formation. Another factor that should be taken into account is the level of cooling rate. If it is high, it increases the development of thermal stresses and therefore the formation of cracks. The cooling rate could be reduced by laser re-melting and substrate preheating, and reduce the formation of residual stresses.

3.5 Post-processing

After the process of producing metal parts via AM is completed, several steps of post-processing are recommended, in order to turn the produced part into a final product. The initial steps, after printing include excess powder and support structures removal, as well as separation of the printed part from the build platform. After these steps, a heat treatment should be performed, in order to improve mechanical properties and minimize surface defects such as porosity and cracks.

The first step after the fabrication of a part, is to remove the excess powder. In parts that are produced by PBF processes, the excess powder is vacuumed out or blasted off the part. A saw that may be electrical is used to separate the produced part from the build substrate, which is adhered to the part. Supports structures are usually removed mechanically by cutting or applied force.

Metal parts usually require a type of thermal treatment, in order to achieve a proper microstructure and enhance mechanical properties. Thermal post processing of metal AM fabricated parts, is required to obtain an optimum microstructure and enhance mechanical properties. A heat treatment process is recommended, in order to increase surface quality, reduce residual stresses, close pores and improve mechanical properties of the produced part. These treatments are performed under vacuum or an inert gas is used, so that chemical reactions at high temperature are avoided.

Laser process is a treatment mainly used to improve the surface of metal AM parts, in terms of roughness, porosity and wear resistance [104]. The surface is improved and becomes smoother, when a low powered laser is applied and melts a region of the surface and relocates the liquid phase of metal. Another method that uses laser power is called ablation, where the laser is used for the evaporation of materials and therefore defected layers can be removed.

Hot isostatic pressing (HIP) is a very common method of post-processing, applied in metal AM produced parts, in order to close pores and cracks, reduce stresses and overall improve mechanical properties [105]. HIP applies high temperature and pressure to the fabricated part in an inert environment, to close pores. This is achieved mainly by high pressure, which causes plastic deformation of the pores and brings the surfaces of the pores into contact. Furthermore, the combination of high temperature and pressure applied for a sufficient period of time, provides bonding of the material by creep and diffusion mechanisms. According to

the literature, HIP process reduces effectively internal pores and tensile strength, due to microstructure changes [106, 107]. AM method, material properties of powders and process parameters should be taken into account, in order to obtain the desired results. After HIP a heat treatment is recommended, in order to enhance the effectiveness of the process [108, 109].

Parts that are fabricated via DED methods are usually treated in a different way than PBF produced parts. The reason is basically the large scale dimensions that are achieved via DED. Large parts produced by DED processes have higher ratio between length and width than PBF produced parts. Heat treatments could induce residual stresses, which may cause deformation that affects the functionality of the produced part. Cold post-processing [110] with a roller is applied directly to the produced part via DED process after deposition, so that porosity is reduced and microstructure is improved. Different rolling methods are tested [111], in order to study the effect of the cold rolling treatment on large produced metal AM parts. Two different types of rollers are tested (**Figure 3.12**), one profiled with a 3.6mm radius and another one with a 10*5.2mm slot. This study [111] proved that cold rolling is a method that improves effectively the microstructure and mechanical properties of Titanium and Aluminum produced parts.

A common feature in metal AM fabricated parts, is the high surface roughness, therefore machining is required, to obtain smoother surfaces. An easy way of machining metal AM parts is by subtractive manufacturing with CNC machines. Polishing or grinding can be applied, in order to minimize roughness and achieve smooth finish surfaces. However, this approach is not so effective for high-quality parts, which require a different treatment such as electrochemical polishing. In addition, surface finishing operations such as machining, chemical etching and vibrating are performed to ensure dimensional accuracy of produced parts that can be affected by other post-processing operations [112].

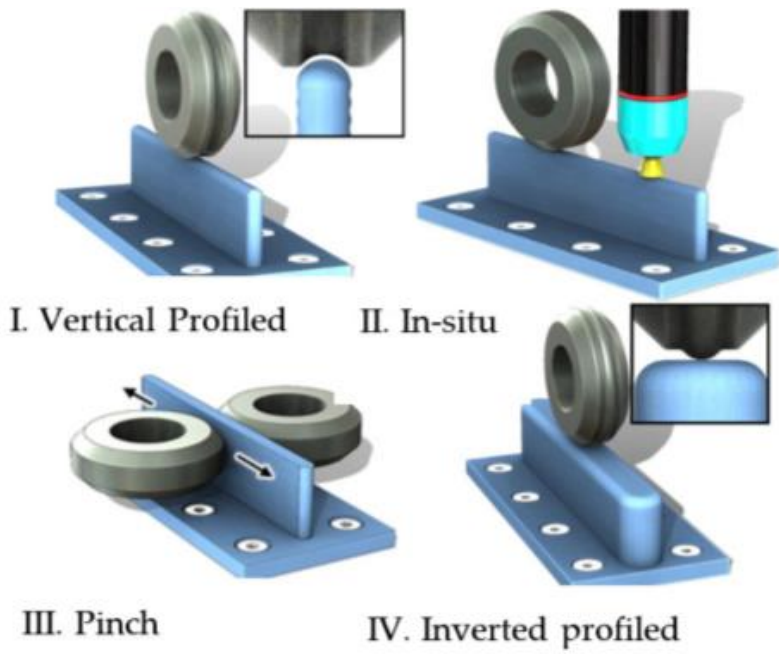


Figure 3.12. Common cold rolling processes [111].

3.6 Applications

Aerospace, automotive, oil and gas, and medical industry are the main fields of metal AM application. This technology opens up new opportunities to improve manufacturing capability. Plenty are the advantages of metal AM, such as complex geometries fabrication, lead times reduction and material waste reduction. These are key factors to encourage different types of industry to adopt metal AM technology to the production. Example applications of metal AM in different industries are presented in the section.

3.6.1 Aerospace

The aerospace field was one of the main industries to employ metal AM. The aerospace industry benefits from the continuously evolved techniques and materials in metal AM, that are capable of producing components with specific properties for applications with high demands. Lightweight components with extremely good mechanical properties can be successfully produced via metal AM. In addition, complex parts can be simplified in one single component, eliminating the need for assembly and reducing the risk of failures. These are some of the AM features that are suitable for high demanded production in aerospace field.

The Italian aerospace company Avio Aero, part of the General Electric (GE) Aviation group used Electron Beam Melting (EBM) to produce Titanium Aluminide (TiAl) low pressure turbine blades for GE Aviation's GE9X jet engine (**Figure 3.13**), which powers the Boeing 777X jet [113]. TiAl is a lightweight alloy, suitable for such applications but its processing with conventional techniques was very expensive and it also prone to crack. An alternative used material is Nickel Alloy 718 but has double weight, which increased fuel consumption. The group managed to produce TiAl components via EBM, which is a cost-effectively and suitable solution for turbine blades.

The first successful effort by GE, to produce fuel nozzles (**Figure 3.14**) for LEAP jet engines via Selective Laser Melting (SLM) completed in 2012 [114]. According to GE, the SLM technology is beneficial, in terms of shortened production cycles, reduced production cost and reliability. The printed fuel nozzle is 25% lighter and stronger than the original one and it increases the fuel efficiency of the engine up to 15% [115]. In 2018 GE celebrated the successful production of 30,000 3D printed fuel nozzles.

Airbus employs metal AM for the production of several parts of its aircraft, such as brackets and bleed pipes. For the production of small-scale parts, Airbus mainly uses EOS and Concept Laser machines but for large-scale components collaborates with Arconic [114]. A wing bracket for the next generation Airbus A350 XWB jets, produced by Concept Laser AM machines. Another example is the one of a lightweight Titanium Ti64 turbine cover door hinge, used on Airbus A380 that it was printed via laser sintering. Both aerospace metal additive manufactured components are presented in **Figure 3.15**.

DED technologies are particularly attractive for the aerospace industry, not only for the fabrication of components but also for repairing damages. In particular the method of LMD has been used for the fabrication of impeller blades of turbomachinery and also for the repair of damaged areas on the blades [116]. LENS was also employed to repair defective voids in turbine airfoils. The repaired airfoil matched the geometry of the original one and it also increased the total energy saving by up to 36% [117]. In general, DED technologies can be used in the aerospace field to repair turbine airfoils, engine combustion chambers and blisks, providing 'Near-Net-Shape' geometry [114].

The security and aerospace company Lockheed Martin produced and tested the quality of a giant 3-D printed titanium dome for satellite fuel tanks, in the frame of a multi-year development program to create giant, high-pressure tanks that carry fuel on board satellites [118]. The titanium 46inch (1.16m) diameter vessel produced by the Sciaky's Electron Beam Additive Manufacturing (EBAM) process [119] and it is the largest part (**Figure 3.16**) produced by Additive Manufacturing in space. In July 2018, the final round of quality tests completed by Lockheed Martin, which was the end of the development program. The use of Siacky's EBAM technology reduced the production time and the material waste during manufacturing of domes. According to Lockheed Martin, satellites can be produced twice as fast and with the half cost. In particular, the total delivery time was reduced from two years to just three months, shaving off 87% of the process for the production of domes.



Figure 3.13. TiAl low pressure turbine blades for GE Aviation's GE9X jet engine produced by EBM



Figure 3.14. Fuel nozzles for LEAP jet engines via Selective Laser Melting (SLM)

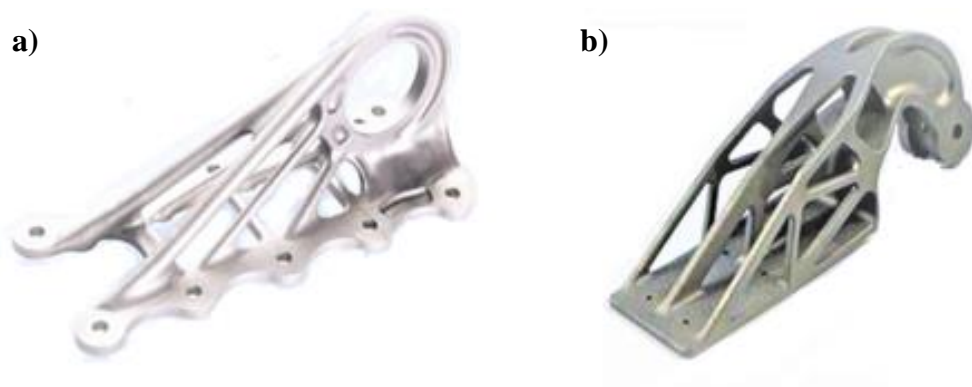


Figure 3.15. a) Airbus A350 XWB jet wing bracket and b) Titanium turbine cover door hinge.



Figure 3.16. An LM worker (for scale) next to their EBM printer and satellite tank dome at the LM space hardware manufacturing facility in Colorado, US.

3.6.2 Automotive

Besides the aerospace industry, one of the leading industries of AM in the recent years is the automotive, with an average growth of 3.6% [120]. Different automotive companies started to adopt metal AM, in order to produce more flexible, lighter, stronger, safer and optimized components.

Bugatti is a French car manufacturer that employs metal AM for the fabrication of several components. An example is the car brake caliper (**Figure 3.17.a**), produced by SLM with Ti6Al4V powder, which is one of the largest calipers in the world [121]. Brake caliper's bracket (**Figure 3.17.b**) are made of AlSi10Mg with integrated water cooling and weights 2.9 kg, 40% lighter than the original Aluminum bracket of 4.9 kg. This is an optimized bracket that has been used in all series of Bugatti Chiron cars.

The BMW Group uses a different AM techniques for the production of automotive components. The BMW i8 Roadster consists of a window guide rail [122] and a fixture for the soft top attachment, both produced by metal AM. The fixture is made from aluminium alloy and it is 44% lighter than the injection-moulded plastic attachment [123]. The BMW S55 engine is replaced by an innovative engine with several consolidated components, including a 3D printed cylinder head, produced by a PBF printer [124].

Audi is another car manufacturer that uses SLM processes, in corporation with SLM Solutions Group AG to manufacture prototypes and spare parts on demand [125]. Water adapters for the Audi W12 engine have been successfully produced by utilizing SLM, as shown in **Figure 3.18**.

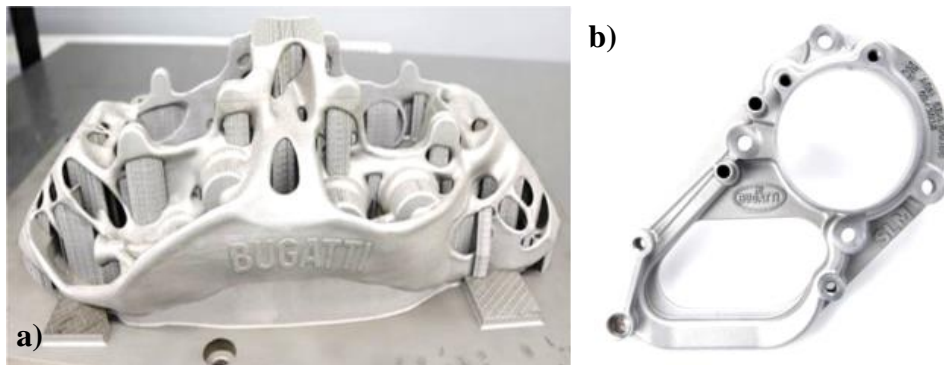


Figure 3.17. a) Bugatti Ti6Al4V brake caliper and b) Bugatti AlSi10Mg bracket.



Figure 3.18. Metal 3D printed water connectors for AUDI W12 engine.

3.6.3 Oil and gas

The adoption of metal AM processes in the oil and gas industry seems very beneficial, in terms of cost and supply chain efficiency. According to world economic forum, metal AM could save costs in the range of \$30 billion [126]. Furthermore, the supply chain in oil and gas industry can be improved by reduced lead times, provided by AM technology [127]. Some example applications of metal AM in oil and gas industry for use end products, are presented below.

Gateway manifolds for pipelines consist of many channels of complex geometry. The production of such parts with traditional manufacturing methods is very difficult or almost impossible [128]. PBF system was employed and gateway manifold of Titanium was successfully printed for pipelines (**Figure 3.19**). Siemens is a company that has integrated metal AM in its manufacturing processes of oil and gas components. A number of products such as fuel nozzles, turbine blades impellers and swirlers are produced by metal AM in Siemens. Some of these examples include an advanced burner swirl for the SGT-750 gas turbine (**Figure 3.19**), a water pump impeller of the fire protection system at Slovenia power station and sealing rings of SST-300 steam turbines (**Figure 3.20**).

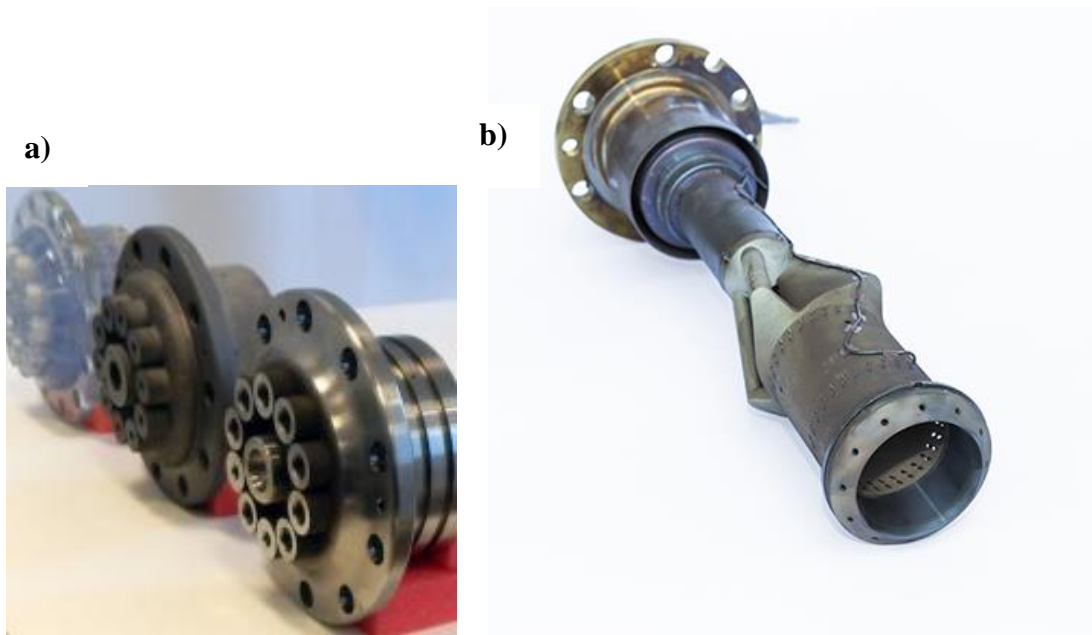


Figure 3.19. a) Certified 3D Printed Gateway Manifold and b) Siemens' 3D printed gas burner for the SGT-700 gas turbine

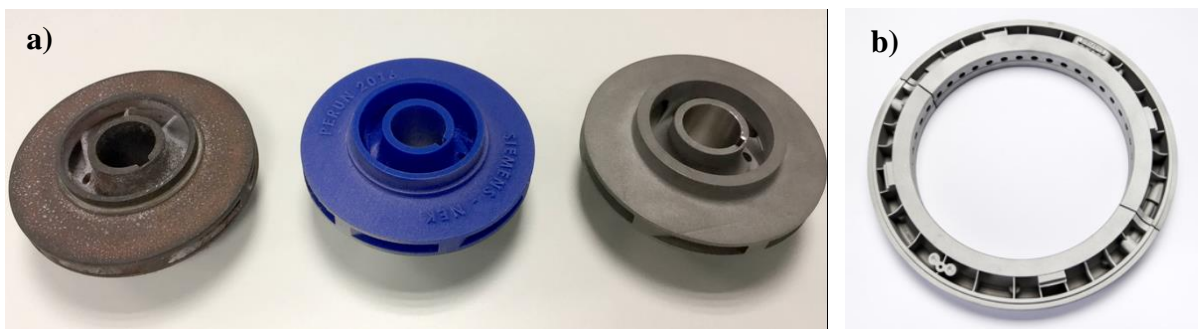


Figure 3.20. a) The original, obsolete water impeller (left), Siemens' 3D printed prototype (blue) and the resulting 3D-printed replacement (right) now operating in Krško NPP in Slovenia and b) An oil sealing ring for an industrial steam turbine, designed and produced by Siemens using metal AM

CHAPTER 4

AEROSOL JET PRINTING

4.1 Introduction

The history of Aerosol Jet Printing (AJP) started in the late 1990s, in the frame of a project, called MICE (Mesoscale Integrated Conformal Electronics), which was funded by DARPA [129]. The project's aim was to develop a manufacturing process, so that a range of materials can be deposited in almost any substrate directly from CAD models. Thus, they developed the technology of AJP, which was afterwards commercialized by the company OPTOMECH. The AJP technique belongs to the family of Additive Manufacturing (AM) technology and finds a wide range of application in the field of electronic and biological devices production.

AJP utilizes a focused aerosol stream, which is deposited on substrates with a nozzle-substrate height of 1–5 mm [130]. Materials have an initial form of an ink, which is suspended within an aerosol that is generated by a pneumatic or ultrasonic atomizer. AJP systems enable printing of inks with viscosity ranges from 1 to 1000 cp [130], unlike other direct write methods that are limited to viscosities below 20cp. Any material that can be dispensed in a gas phase is compatible with AJP systems that support a wide range of inks such as metals, semiconductors, ceramics and even biological matter.

AJP is an innovative, digital, non-contact, maskless method of fabrication that enables aerosol deposition on both 2D and 3D substrates of ceramic, plastic and metal to produce high performance electronic and biologic devices. AJP is used in a wide range of applications for the production of passive and active electronics, sensors, fuel cells and photovoltaics. Particular examples of AJP produced electronic components include interconnects, resistors, capacitors, antennas and thin film transistors. Multi-layer interconnects can be created on a single layer on 2D substrates, due to the fact that materials can be switched or blended during the printing process. On 3D substrates, conformal interconnects can be printed on a surface, eliminating the need of wire bonding. Regarding the reliability and performance of AJP parts, a recent study by Global defense company Northrop Grumman [132] concludes that the AJP technology can be competitive to existing semiconductor technologies.

On this chapter, an overview of the AJP technology is presented. The first section presents the AJP working principle, the AJP system and sub-systems and the printing process. Characteristics of different type of inks used for the deposition on different kind of substrates are presented in the second section. Post-processing, which is required after the deposition is explained in section 4.3. Common parameters that affect the geometry, quality and resolution of printed patterns are surveyed, according to the literature. The final section of this chapter concentrates on AJP applications, including some state-of the art examples.

4.2 The Aerosol Jet System

The Aerosol Jet Printing technology is a non-contact and digital additive manufacturing technique based on aerosol (spray) deposition. The AJP process utilizes a pneumatic or an ultrasonic atomizer for the aerosol generation. Then the aerosol is carried by a gas flow – carrier gas to the deposition head, where it is aerodynamically focused by a gas flow – sheath gas and deposited into a substrate. Before analyzing further the AJP system, it would be useful to clarify the AJP terminology.

Aerosol: A solid particle or a liquid droplet that is dispensed in a gas phase, is defined as aerosol. Almost all kind of inks are capable of forming an aerosol and therefore a wide range of materials can be used in AJP systems.

Carrier gas: It refers to a gas flow of compressed air or Nitrogen. The carrier gas flow is the primary flow that carries the aerosol from the atomizer module onto the nozzle head.

Sheath gas: It refers to a gas flow of compressed air or Nitrogen. The sheath gas flow is the secondary flow that enters in the deposition head and coaxially surrounds the aerosol stream, as an annular ring.

Aerodynamic focusing: It is the focusing technique that AJP system use by utilizing two gas flows, the carrier and the sheath gas flow. The combination of the two flows form the aerosol stream at the deposition head and transport it to the nozzle. Pressure variations of both gas flows, determine the aerosol beam collimation, which results in the aerodynamic focusing.

Non-contact: A non-contact deposition means that there is a distance between the nozzle and the substrate surface, during deposition of the aerosol. This is very beneficial for printing electronic devices, which usually consists of multiple layers. Multilayer deposition requires subsequent layers deposition into printed layers and every slight contact could affect or damage the underlying layers. Therefore, non-contact deposition with a distance of 2-5mm between nozzle and substrate surface, is a great advantage for AJ P technology.

Digital: The pattern of the printed ink is designed digitally on a computer (usually by AutoCAD). The drawing file is then converted into tool paths using VMTTools (VMT) or similar software. The tool path VMT file translates the vectorial drawing into the machine code, generating the commands that instruct the printer's software how to deposit material to achieve

the designed pattern. The substrate x-y-(z) stage moves according to the desired path by the printer's software.

The working principle of Aerosol Jet Printing is based on the atomization of inks. The atomization process generates an aerosol with liquid droplets of 1-5 μm . AJP has the advantage that a wide variety of materials can be used for printing, based on the fact that almost all kind of inks are capable of forming an aerosol. The atomization method can be either pneumatic or ultrasonic (**Figure 4.1**), depending on viscosity's ink. Once the aerosol is generated, it is then transported by a carrier gas flow to the deposition head. The focusing of the aerosol occurs in the deposition head by two gas flows and then is non-contact deposited to a substrate surface. The AJ process can be divided in four steps, which are a) atomization – aerosol generation, b) aerosol transportation, c) aerosol focusing, and d) aerosol deposition.

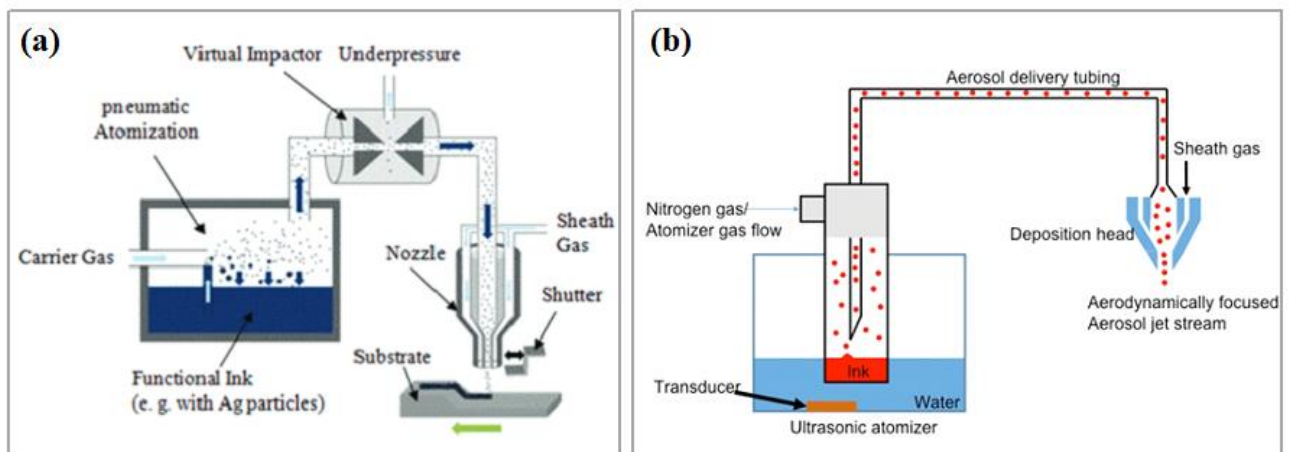


Figure 4.1. Schematic of a) pneumatic [133], b) ultrasonic Aerosol Jet Printing system [134].

a) Atomization – aerosol generation

An aerosol is generated when the liquid ink is dispensed in a gas phase. The ink is placed in an atomizer, where a dense mist of material droplets – aerosol is generated. Atomizers are distinguished in pneumatic and ultrasonic, depending on materials viscosity. The pneumatic atomizer (PA) is used for low and high viscosity materials, in the range of 1 to 1000cP. On the other hand, the ultrasonic atomizer (UA) is able to atomize liquids with low viscosity of 1 to 5cP (maximum). The PA requires fluid volume of 30ml, while the UA is able to operate with just 0.5 ml.

The *pneumatic atomizer* employs a closed chamber, where the ink is placed inside (Figure 4.2). The chamber is supplied with gas (pressured air or Ni), called the carrier gas. The gas enters the chamber and is accelerated across the top surface of the ink. A high velocity carrier gas enters the chamber that contains the ink through the atomizer's nozzle. Reduced pressure due to Venturi effect, causes the ink to be drawn out of the atomizer's nozzle, reaching the carrier gas flow level and subsequently breaks it into droplets. The droplets diameter is essential and should be no greater than 5 microns. Large droplets of high inertia are impacted on the chamber walls and finally return to the ink. Smaller and lower inertia droplets remain within the gas flow and can be transferred [135]. The generated droplets ranging from 1 to 5 microns. The mass mean diameter of generated droplets can be estimated as follows:

$$d_p = d_t \cdot \left(\frac{2\sigma}{\rho V^2 d_t} \right)^{45} \quad (4.1)$$

Where d_t is the diameter of the liquid flow tube, σ the surface tension, ρ the fluid density and V the relative velocity between carrier gas and liquid.

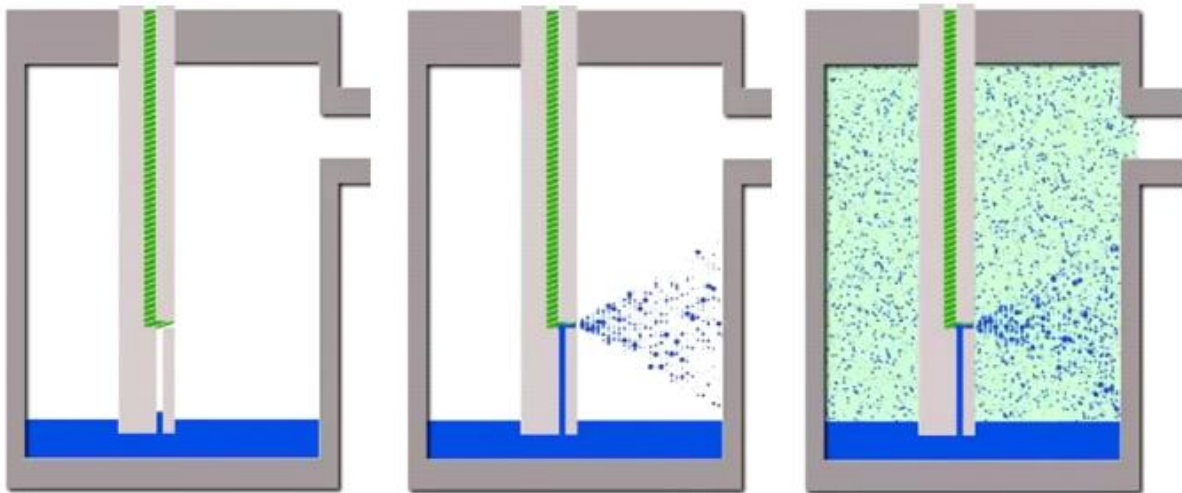


Figure 4.2. Aerosol generation inside the pneumatic atomizer [136].

The *ultrasonic atomizer* utilizes an ultrasonic bath for atomization (Figure 4.3). The ink is placed inside a vial, which is positioned in a tank that contains a fluid (typically water) and an ultrasonic transducer. The ink inside the vial is subjected to ultrasonic field of high frequency, which induce a capillary wave in the ink and causes the atomization [137]. Thus, a

dense mist of droplets is generated. The droplet diameter is influenced by parameters such as fluid density, surface tension and excitation frequency of the transducer. The mean diameter should not exceed 5 microns and can be estimated by the following formula [138]:

$$d_p = 0.34 \cdot \left(\frac{8\pi\sigma}{\rho f^2} \right)^{\frac{1}{3}} \quad (4.2)$$

Where σ is surface tension, ρ fluid density and f the excitation frequency of transducer.

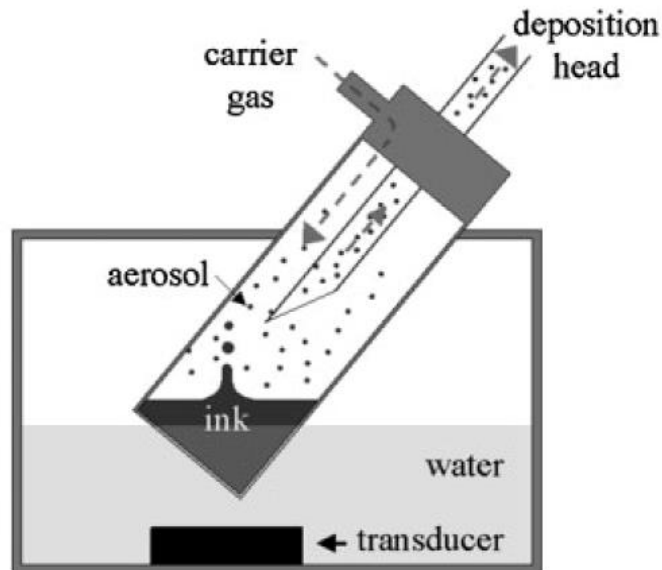


Figure 4.3. Aerosol generation inside the ultrasonic atomizer [135].

b) Transport of the generated aerosol

Once the aerosol mist is generated, then is transported by the carrier gas, through a tube to a virtual impactor (**Figure 4.4**). There, an area of stagnant flow causes the separation of droplets, based on their inertia [135]. Small droplets cannot overcome the stagnation point and are usually vented to the atmosphere, while large and high inertia droplets pass through the point and move to the deposition head. Systems with ultrasonic atomizer does not use a virtual impactor, instead the aerosol is transferred by the carrier gas flow directly to the deposition head.

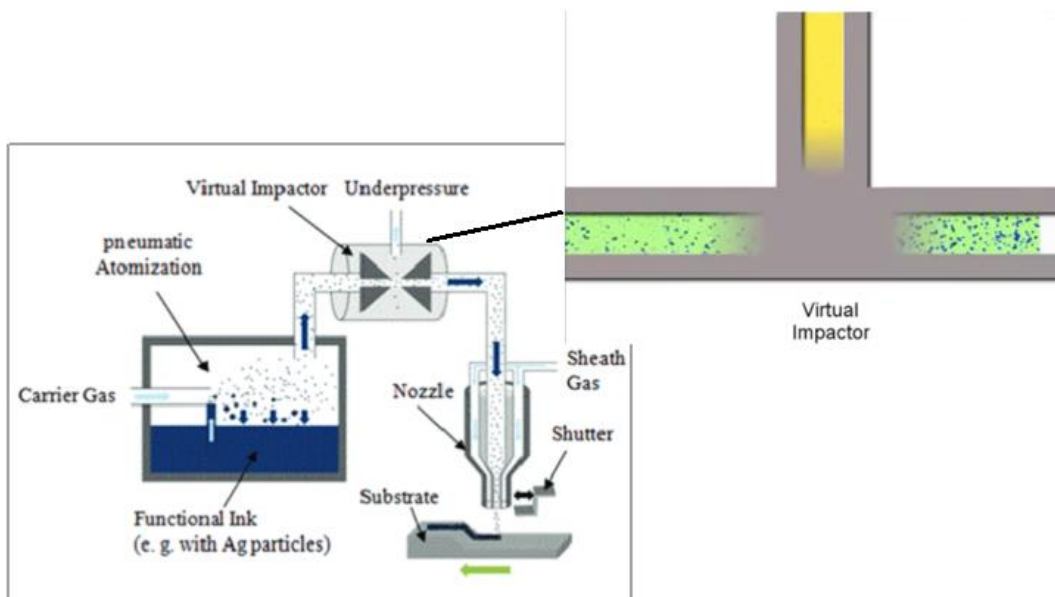


Figure 4.4. Illustration of the aerosol stream entering and exiting the virtual impactor [133, 136].

c) *Focusing and deposition*

The generated aerosol is transferred to the deposition head by the carrier gas flow, where it is focused. A secondary flow of sheath gas enters in the deposition head and surrounds coaxially the aerosol, as an annular ring (**Figure 4.5**). As a result, the aerosol stream is constricted by the sheath gas flow, which also creates an interlayer between the aerosol and the machine's components. The application of the sheath gas results in concentrating the aerosol flow in a focused and collimated beam, which enables constant deposition at a 1–5 mm distance. Additionally, the sheath gas and its formed interlayer, prevent the phenomenon of clogging. The aerosol and the sheath gas are further focused through the nozzle before being deposited on to the substrate. When the aerosol and the sheath gas pass through the nozzle, they accelerate due to the decreased nozzle diameter and remain focused towards the substrate surface. The flow ratio of the sheath and carrier gas determine the aerosol beam diameter that impacts the substrate surface (**Figure 4.6**). When the sheath gas to the carrier gas ratio increases, the aerosol beam decreases and vice versa. However, the nozzle orifice diameter should be taken into account for an accurate estimation of the aerosol beam diameter.

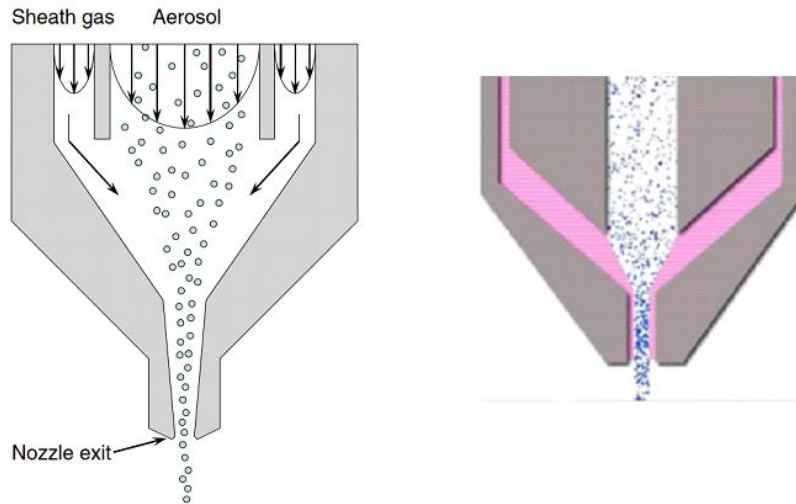


Figure 4.5. Illustration of the sheath gas flow that surrounds the aerosol stream [139, 136].

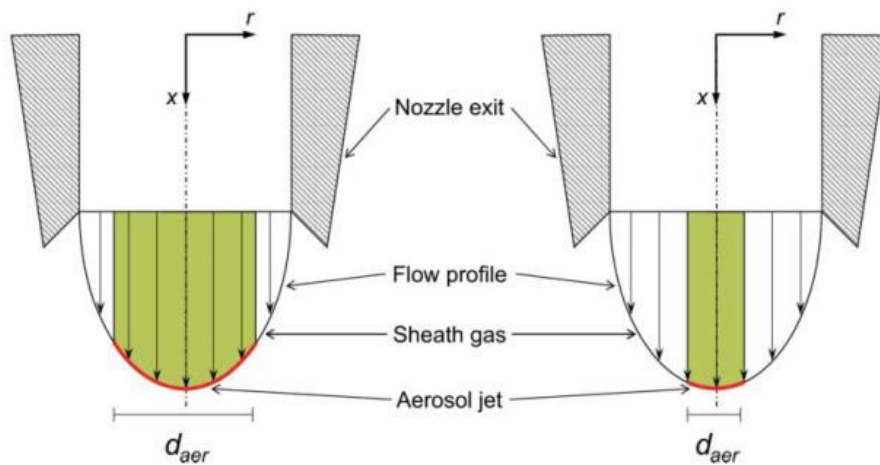


Figure 4.6. Schematic of the nozzle flow profile with contributions of the sheath and carrier gas flows. Small flow ratio (**left**) and high flow ratio (**right**) [139].

The deposition process is contactless, keeping a constant distance of 1 to 5 mm between the substrate, and the nozzle and it is CED driven. The substrate is placed below the nozzle exit with the surface perpendicular to the aerosol stream. The aerosol stream, due to its high velocity particles, is remaining focused during deposition.

4.3 Inks and substrates

Aerosol Jet Printing systems are very flexible, in terms of materials. Based on the fact that almost any type of material is capable of forming an aerosol, AJP has broadened the range of printed materials, compared to other methods. Aerosol Jet systems can deposit a wide variety of materials, including metals, conductors, insulators, ferrites, polymers, adhesives, and biological materials. The functionality of these materials is enabled by various post-processing methods, such as thermal sintering that will be discussed further in the next section. Deposition of inks can be made on almost any substrate material, with the most common to be polymers, silicon, glass, metals and ceramics.

Selecting an ink that forms aerosol droplets is essential for the properties and performance of the printed structures. AJP inks are not made of pure materials but they are constituted of: a) solvent, b) functional material, c) binder and d) additives [140].

- a) **Solvents** disperse the other three constituents and determine the ink viscosity. Typical solvents for AJP inks are: Water, isopropyl alcohol, DMF, and cyclohexanone.
- b) **Functional** are the materials that determine the electrical properties of the ink and can be divided in: metal, polymer, ceramic and carbon-based inks. Nanoparticles are prone to agglomeration and sedimentation, which may affect the desired properties.
- c) **Binders** are unusually added polymers that eliminate intermolecular interactions between nanoparticles.
- d) **Additives** increase the stability and performance of the ink and are used in small quantities (<4%). Typical additives for AJP inks are: Dispersing agents (surfactants), rheology modifiers, deformers, plasticizers, and biocides.

Functional materials of inks can be divided in: metal, polymer, ceramic and carbon-based inks. The metal inks (silver, gold and platinum) are printed at temperatures almost well below their melting temperature point. They easily become conductive at the temperature of 120 for one hour, when a sintering method is performed. A wide variety of polymer inks, conjugated or electroactive has been developed, with the most promising to be poly (3,4-ethylenedioxythiophene):polystyrene sulfonate (PEDOT:PSS), due to its high conductivity. Ceramics include ruthenates and ferrite based inks that can also be printed but require higher temperature firing. Carbon-based inks refer to carbon nanotubes (CNT) that are either single

wall (SWCNT) or multiwall carbon nanotubes (MWCNT). Single wall (SWCNT) consist of one tubular layer of sp^2 carbons, while multi-wall (MWCNT) have a number of concentric tubes, one inside the others. Last but not least, biomaterials such as proteins and DNA have been printed without denaturing or loss of bio-activity. Commercially available inks can be classified in main categories, as **Table 4.1** presents, according to OPTOMECC categorization [130].

<i>Particle size (nm)</i>	300 – 500	
<i>Viscosity (cP)</i>	0.1–1000 (at ambient temperature)	
<i>Minimum line width (μm)</i>	10	
<i>Nozzle diameter (μm)</i>	100–300	
METAL	RESISTOR	NON-METALLIC
Gold Platinum Silver Nickel Copper Aluminum	Carbon Ruthenate	Single Wall Carbon Nanotubes Multi Wall Carbon Nanotubes PEDOT:PSS
DIELECTRIC & ADHESIVE	SEMICONDUCTORS	OTHER
Polyimide Polyvinylpyrrolidone (PVP) Teflon AF SU-8 Adhesives Opaque coatings UV adhesives UV acrylics	Organic semiconductors SWCNT	General solvents, acids & bases Photo and etch resists DNA, Proteins, Enzymes

Table 4.1. AJP commercially available inks [130].

Impressive is the fact that AJP supports printing of combined materials layer-by-layer within a single system, which makes it an attractive solution for the production of many devices of electronics. A good example of multilayer printing of combined materials is the case of a capacitor, which consists of a dielectric layer and then a silver layer on a copper board pad (**Figure 4.7**). Multi-layer deposition has also been applied for the generation of biosensor structures.

Inks can be deposited on a wide variety of substrates including polyester, polyimide, glass, C-Si, ceramic, FR4 and metal materials. Several parameters should be consider before selecting substrate materials, as they can affect the performance of the printed patterns and the overall device. Such parameters include chemical composition, roughness, thermal resistance and surface energy. These parameters mainly determine the behavior of inks and the suitable sintering method. The most commonly used material in printed electronics is plastic, due to low cost, simple manufacturing and high flexibility. Plastic substrates are usually made of polyimide, polyethylene terephthalate (PET) and polydimethylsiloxane (PDMS). Polyimide is also known as Kapton and is one of the most popular plastic substrates, due to its high thermal stability, high chemical resistance, dielectric strength and good mechanical properties.

As it was mentioned, the substrate material determines the post-processing method (sintering) of the printed ink. Several substrates have low melting point and therefore typical thermal sintering in a conventional oven, where materials are exposed in high temperature ranges, it is not a suitable option. Such materials should be treated in a way that no damage is caused to the substrate. Other than the typical thermal sintering, there are other sintering techniques that will be revised on the next section, protecting substrates from damage. However, AJP systems have an integrated laser module that sinters selectively the deposited ink while leaving the substrate unharmed.

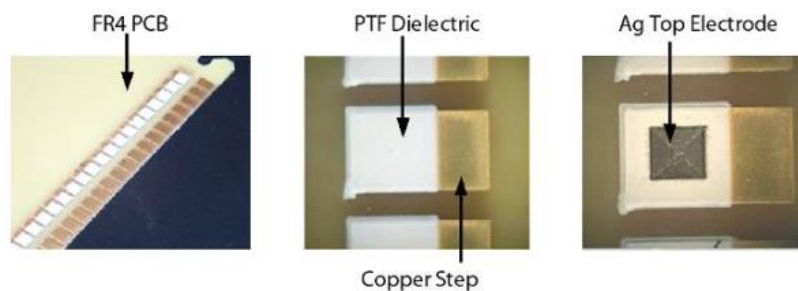


Figure 4.7. Simple capacitor made by multi-layer deposition, Polyimide dielectric and Ag deposited onto Cu pads [141].

4.4 Post – processing

After deposition, post-processing is required to turn the printed ink into a functional structure. Inks are composed of additives and binders, mostly organic, to stabilize dispersion and inhibit aggregation. Therefore, post-processing is required to obtain good electron conduction and a uniform structure. This type of treatment is called sintering and is applied on the printed inks of nanoparticles, in order to: a) evaporate the solvent, b) degrade and remove organic additives, and c) fuse the nanoparticles for better electron transport. The applied technique of sintering depends on ink and substrate materials. Of high importance is the consideration of substrate material, because some sintering methods may damage the substrate or the printed pattern is affected by material flows, coming from the substrate. Post-processing is required to achieve optimal material properties, mechanical and electrical behavior, and adhesion between the printed ink the substrate. Some of the commonly used methods of sintering AJP inks are present below.

Thermal sintering is the most commonly used method of post-processing. A conventional oven is used to heat the printed pattern at 200-350 °C for 10-30 minutes, in order to degrade organic polymer binders and surfactants from the nanoparticles and to reach sufficient level of conductivity. This treatment is basically applied to metal inks, and rarely to polymer inks. This method provides high conductivity and good adhesion. Due to the high processing temperature ranges, the choice of used substrates is limited to materials with high melting point, such as: Glass, polyimide, polytetrafluoroethylene (PTFE), fluorine-doped tin oxide (FTO) and indium tin oxide (ITO).

Photonic sintering utilizes an energy source that is either laser, flash pulsed light or lamps to heat selectively the printed pattern. A beam of light is focused, scans and heats selectively the surface to be sintered. Due to local thermal control that the method provides, substrate thermal damage is minimized and therefore it is a proper treatment for substrates with low T_g. Laser sintering uses Nd:YAG or Argon ion energy sources and has been successfully used to sinter silver, gold and copper nanoparticles [142, 143, 144]. Intense pulsed light (IPL) belongs to photonic sintering that was first developed by NovaCentrix, in 2005. In this process, the ink is exposed to a high-intensity pulsed light from a flash light in short duration. The key advantage of this method is that moreover the temperature is high enough to cure properly the ink, the substrate stays relatively cool, due to the short exposure time (~1ms) [145]. This allows the deposition on a wide variety of substrate materials.

Electrical Sintering is based on the Joule heating. This method relies on electric field, applying a current (AC or DC) to the printed pattern and sintering the nanoparticles through Joule heating. Materials need to be already slightly conductive, so that electrical current can be transferred to the printed pattern. It is possible that another sintering treatment should be performed before electrical sintering, to increase the conductivity. Electrical sintering is a fast process but proper only for conductive inks.

Plasma sintering utilizes a flow of low-pressure Argon plasma. A flow of plasma is applied on the top surface of a printed pattern, penetrates the structure and causes the evaporation of the organic material coating within the ink. Basically, this process is based on plasma etching of polymer shell of ink nanoparticles. Once the coating is removed, the nanoparticles are being sintered in few minutes at low temperature ranges. The method provides lower conductivity, due to low sintering temperature. Sometimes, bad adhesion is observed between the printed pattern and the substrate, because the bottom layer is not sintered, enough. Plasma sintering is inappropriate for plastic substrates, due to etching that affects the substrate materials [146].

4.5 Parameters

Aerosol Jet Printing is a very valuable method of producing electronics, minimizing production time and materials compared to traditional methods. Although AJP is a very fast process with printing time to count few minutes, the process includes several stages. Therefore, several factors could affect the printing quality of a produced part. Process parameters should be considered and adjusted in a way that improving performance and quality. Besides this, other factors that influence the deposition and should be taken into account are the material, the substrate and the environment.

Process parameters are also related with path design (e.g. number of layers, geometry) and AJP machine (e.g. atomizer, nozzle orifice diameter), factors that are configurable. On the other hand, factors such as ink and substrate material and a proper combination of them, seems to be more challenging. In addition to that, environmental conditions (humidity, temperature) play important role and affect instantly the material state. The parameters that affect the geometry and quality of a printed line are presented in **Figure 4.8**.

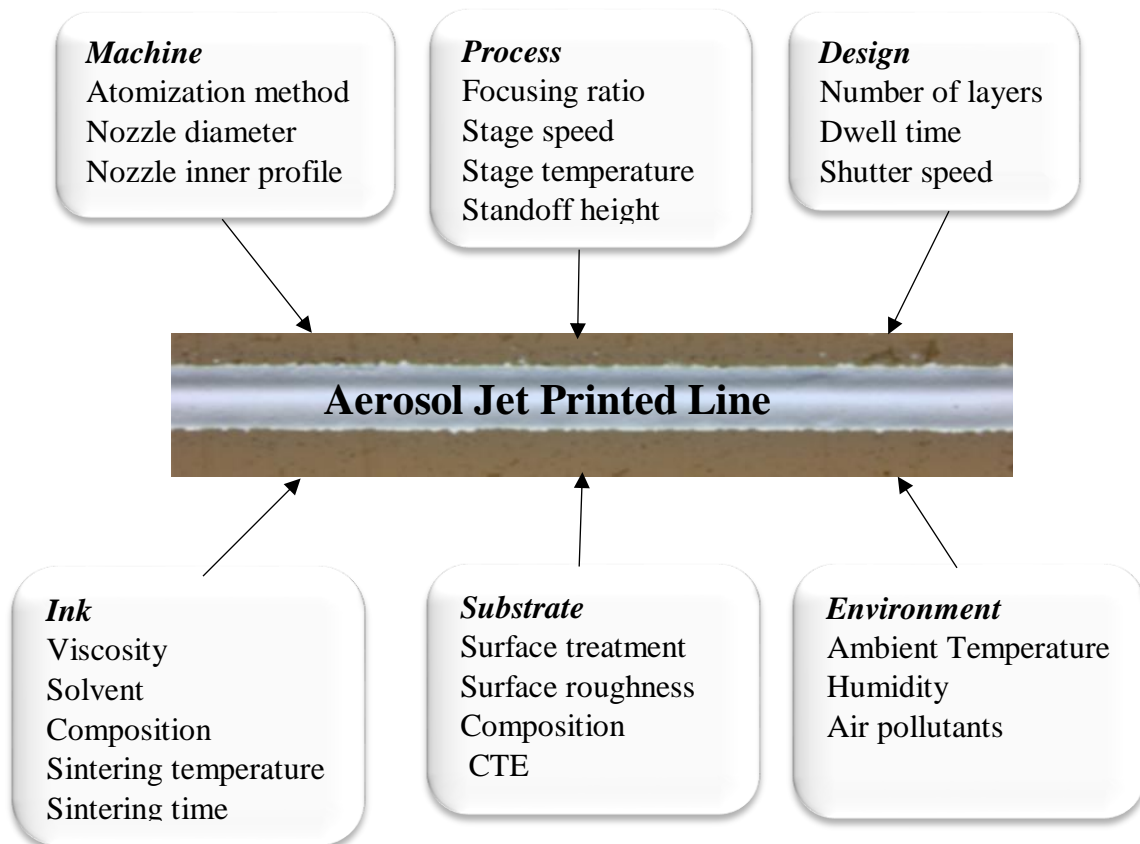


Figure 4.8. Different types of parameters, affecting the geometry and quality of an AJP deposited line.

Focusing ratio

The geometry of a printed line depends on various process parameters and determines the quality and resolutions of printed patterns of electronic networks. Optimal line widths should be narrow, in order to achieve high density circuitry. On the other hand, sufficient thickness is required for high current carrying capacity. The ratio of thickness to the width of a line, is defined as aspect ratio. To achieve high resolution and good quality of printed lines, low line width and high aspect ratio are recommended.

One of the earliest studies [147] investigated and defined the process parameters that affect the geometry of printed lines of ultrasonic atomized silver ink (40% silver and viscosity of below 5 cP). It was found that the carrier gas and the sheath gas flow rates, the stage speed and the nozzle diameter determine the geometry of printed lines. In the case of a pneumatic atomizer, the carrier gas flow is equivalent to the difference between atomizer and impactor gas flow. In the AJP systems with ultrasonic atomizer, there is no impactor and therefore the carrier gas flow is as the same as the atomizer gas flow [148]. The key parameter that affects the printed lines is called focusing ratio and is defined as:

$$FR = \frac{\textit{sheath gas flow rate}}{\textit{carrier gas flow rate}} \quad (4.3)$$

The focusing ratio varies with either adjusting the sheath gas or the carrier gas flow rate. Mahajan et al studied the variations in geometry by increasing and decreasing the focusing ratio, for a constant carrier gas flow. For constant stage speed, a fixed nozzle diameter, and constant carrier gas flow rate, they found that: when the focusing ratio increases, the line width decreases while the thickness line increases.

Considering the parameter of the nozzle size, a test with different nozzle diameters proved that finer lines are produced from smaller nozzles. However, as the focusing ratio increases, pressure is accumulated in the nozzle and leads to lower FR for smaller diameter nozzle. A decrease in the nozzle diameter results in decreased width and increased thickness. The nozzle size and the FR can give us a useful information, regarding the aerosol beam diameter. The ratio of the aerosol beam diameter to the nozzle diameter is defined as follows [149]:

$$\frac{D_a}{D_n} = \sqrt{1 - \sqrt{\frac{FR}{1 + FR}}} \quad (4.4)$$

Where D_a is the aerosol beam diameter, D_n is the nozzle diameter, and FR the focusing ratio. Finally the stage speed seems to have also an influence to the lines geometry. It is observed that as stage speed increases, both the line width and thickness decrease.

Binder et al [139] developed an analytical model to calculate the aerosol droplet distribution entering and exiting the capillary and with this the printed line width. The model assumes that the aerosol beam diameter equals to the printed line width. This assumption is valid only for planar substrates and small distance between nozzle and substrate. Smith et al [150] also studied the effect of the focusing ratio to lines geometry and investigated the influence of substrate temperature on the morphology of silver lines. It was found that the line width decreases with increasing temperature.

In a recent study [151], a different approach of adjusting the focusing ratio was investigated. Mahajan increased or decreased the focusing ratio by adjusting the sheath gas flow rate for a constant carrier gas flow rate. However, the focusing ratio (**Eq. 4.5**) varies when there is a change either in the sheath gas or the carrier gas flow rate. In this study, the focusing ratio was increased by i) increasing the sheath gas flow rate or ii) decreasing the carrier gas flow rate. The second approach results in decreased width and increased thickness, as it was already proved by Mahajan. However, decreasing the carrier gas flow for a constant sheath gas flow rate, different results were obtained. It was found that when the focusing ratio is increased by decreasing the carrier gas flow rate, the width decreases but the thickness decreases too. This is a reasonable outcome, since the carrier gas flow rate is decreased and therefore the quantity of matter deposited on the substrate is reduced. This study presents the importance of both flow rates and the different effect on the printed lines geometry.

Overspray

The phenomenon of overspray appears, while the aerosol is deposited on a substrate. Some droplets of ink within the aerosol are not able to impact to the concentrated aerosol center line, due to insufficient inertia. This leads to overspray deposition that causes an increase to

the line width, as the edges become not well defined (**Figure 4.9**). The inertia of droplets depend mainly on the ink composition, atomization and virtual impaction parameters, factors that can cause variations in the volume of the droplets. Overspray should be minimized, in order to improve quality and resolution of printed lines. Minimizing overspray is usually achieved by trial and error. This is not a valid approach and therefore overspray is considered to be a challenge and an open issue for AJP deposition.

However, analytical models are developed, in order to understand better the deposition mechanism and the physics behind the overspray phenomenon. The aim is to define and determine parameters that create such phenomena, to eliminate them and increase printing quality. In a recent study [152], a three-dimensional (3-D) computational fluid dynamics (CFD) model was developed, in order to define how the aerosol particle size and the gas flow rate affect the deposition location of each individual aerosol droplet. It was found that nozzle exit diameter, size distribution of droplets within the aerosol and focusing ratio are the key parameters that affect the quality of printed lines. If these parameters are optimal could lead to high resolution printing. Finally, it is concluded that the atomization should be in a manner that the carrier gas mainly consists of ink particles with proper sizes to ensure a reduction in the overspray.

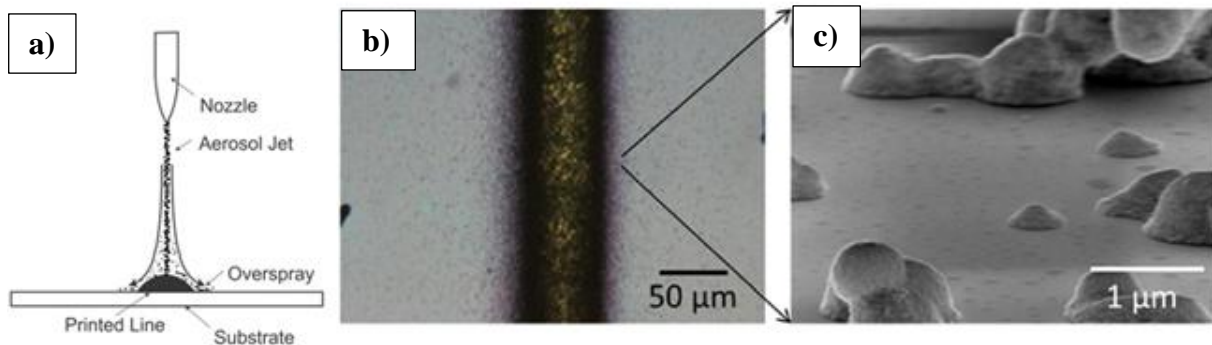


Figure 4.9. Phenomenon of overspray: **a)** Schematic of overspray during deposition, **b)** optical microscope image of overspray on either side of a printed and sintered silver line, and **c)** SEM image of the same region showing overspray [147].

Ink formulation

Among the process parameters that are linked mainly with the geometry of printed lines, the formulation of AJP inks seems to be a key parameter for the morphology of a printed line. In section 4.3, a wide variety of inks together with ink characteristics (viscosity, particle size,

etc.) was presented, but nothing regarding the composition of inks. However, the initial ink composition can affect the generated aerosol and therefore optimizations are considerable for optimized morphologies.

Evaporation is a common phenomenon that occurs during atomization, transportation and deposition. Solvents with low boiling point evaporate easily during the AJP process, which results in the deposition of drier particles that increase the roughness and porosity of the printed surface. Additionally, the evaporation results in droplets with low inertia, unable to impact the substrate surface which leads to non-homogenous lines or lines with less conductive material [149].

In order to avoid pure quality lines, as a result of evaporation, a combination of high and low volatility solvents is required. High volatility solvents are evaporated shortly after atomization of the ink, the carrier gas is saturated and a stable droplet volume achieved during transportation, before the interaction with the sheath gas. At this point, evaporation of the low volatility solvent will begin. Including ~ 10% of low volatility co-solvent within the in, prevents total drying of the particles [149].

Sintering

The sintering method, temperature and time are factors that mainly affect the electrical and mechanical properties of printed patterns. Electrical properties refer to electrical resistance and electrical resistivity, which should be low for electronic applications. Regarding the mechanical properties, elastic modulus and shear load to failure should be considered after sintering. The most commonly used method of sintering is the thermal sintering with a conventional oven, due to its simplicity. Some examples of the thermal sintering effects on AJP patterns are presented here.

An early study [153] investigated the performance of Intense Pulse Light (IPL) sintering, also called photonic curing, compared to thermal and laser sintering. The thermal sintering of the silver samples performed at 500 °C for two hours. The samples were sintered with a laser fluency of 2800 J/cm². The photonic curing (IPL) used a lamp voltage of 1200 volts with a pulse length of 900 μs. the results proved that the surface resistivity is comparable for the three methods, validating that sufficient conductivity is obtained with photonic curing, which is a suitable method for sensitive to high temperature substrates.

Lall et al [154] studied the effect of sintering temperature and time on the mechanical and electrical properties of silver printed lines. Tests performed for different sintering temperatures and time, in order to characterize the electric resistivity, elastic modulus and shear load to failure. It was found that the resistivity decreases with an increase in temperature at a constant sintering time. The increased temperature increasing melting of the particles and results in less porous, more uniform lines and therefore the resistivity is decreased. When the sintering time increases at a constant temperature, the resistance first decreases but after increases, which leads to higher resistivity. It was concluded that for decreased resistivity, the sintering temperature should be increased but not the sintering time. Another observation is that the long sintering time causes cracks on the printed line, due to high evaporation of the solvent. The shear load to failure decreases with increased sintering temperature and time. Increased sintering temperature deteriorates the elastic modulus, possibly due to degradation of grain boundaries.

In another study [155] the effect of water vapor sintering on silver ink was presented. A measured amount of water (10grams) was placed inside a thermal oven (18-L) for the sintering of the samples. A comparison between thermal sintering with and without water vapor, proved that the presence of water vapor reduces significantly the electrical resistivity. Water vapor sintering at 120 °C for 1 hour, resulted in less resistivity than dry sintering at 200 °C. This opens new possibilities, in terms of sintering with lower temperature ranges in ovens. Scanning electron microscopy (SEM) images, presented that the water vapor enhances nanoparticle coalescence to form much large connected regions of silver. Adhesion between the printed - sintered silver ink and the polycarbonate substrate was fine. Future research is recommended in the domain of thermal sintering with integrated vapor solvent systems.

4.6 Applications

The field, where AJP is mostly employed is in the printing of electronics. In general, 3D printing of electronics has become an attractive method, alternative to traditional methods, which provides production of smart structures. In particular, the technology of AJP technology is a viable technique that provides miniaturized and flexible products. However, AJP has been successfully applied for the fabrication of biological devices for the medical industry. This chapter focuses on applications that use AJP for the production of electronics. Electronic devices or components are typically categorized into three types; passives, actives and sensors (**Table 4.2**). Here, the applications are presented, according to the different type of electronics.

ELECTRONICS	
Passives	Interconnects
	Antennas
	Capacitors
	Inductors
Actives	Transistors
	Solar cells
	Fuel cells
Sensors	Strain gauges
	Capacitive sensors
	Photodetectors
	Temperature sensors

Table 4.2. The three different types, produced by AJP.

4.6.1 Passive devices

Passive devices are components that they can only receive energy and they can either dissipate, absorb or store it in an electric field or a magnetic field. Such components include

resistors, capacitors (and supercapacitors), inductors, interconnects, transformers, and antennas. Most of them can be successfully printed via AJP, as it is presented with some examples from the literature, on this section.

Antennas

Traditional methods of producing conformal antennas, such as chemical etching, print the antenna elements on a Kapton sheet, which is then glued on a composite layer. In this approach, only planer surfaces can be used and multiple bonding is required. AJP is capable of direct printing the antenna element not only on planar but also on curved surfaces and eliminating extra bonding and alignment steps. The location, the geometry, and the thickness of the deposited antenna are accurately controlled by the printer, providing optimal performance to the printed element. Conformal antennas produced by AJP are usually made of silver nanoparticle inks and printed on dielectric substrates.

Silver-based ink is used to produce conductive single-layer antennas on a planar dielectric substrate. However, a new possibility of entirely three dimensional printed antennas on no-planar substrates was presented by Rahman et al [156]. First, a dielectric ink is employed to form pillars and cylinders and then a silver ink to deposit the antenna on the vertical walls of the dielectric structures, as it is presented in **Figure 4.10**.

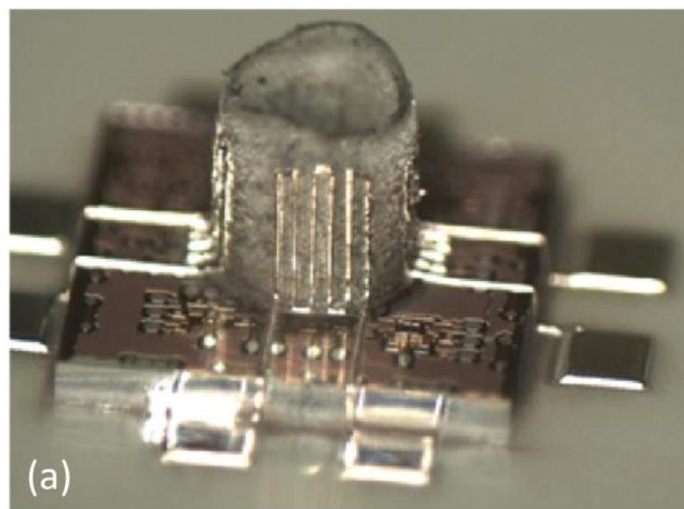


Figure 4.10. Vertical metal antenna on a dielectric pillar [156].

Capacitors

AJP is a multi-layer technique that is capable of depositing conductive, insulating, and adhesive materials layer-by-layer within a single system. Therefore, this method is attractive for producing passive devices that consists of several material layers, such as capacitors.

Gupta et al. [157] presented printed multi-layered passive components prototypes that include capacitors, resistors and inductors. The capacitor is fully printed and consists of two electrodes made of silver and PEDOT:PSS and a layer of SU-8, which is placed between them. A linear increase in capacitance was observed by increasing the area of overlap on the printed structures. Ceramic capacitors produced by the combination of AJP and selective laser sintering (SLS) [158]. The challenge was to develop an ink that could be compatible with both processes. The problem was that ceramic binders inhibit the sintering process. Finally, AJP was employed for the printing of barium titanate ink, before using SLS to form a continuous film. Functional devices with silver electrodes either side of the ceramic along with a PMMA interlayer, were produced with a capacitance of 17.5 pF at 1 MHz.

Interconnects

Producing interconnects of electronics using methods such as chemical etching and screen printing require masks and several steps to produce the conductive traces on planar surfaces. AJP simplifies the process and enables vertical printing along terraced steps of stacked dies connecting the dies on different levels. Wire bonding often cause the problem of cross talk at high frequencies (GHz). Shortened distance printed interconnects do not suffer from this problem and they increase the speed of the signal processing time [159].

Early studies [160] used silver ink to produce interconnects within silicon solar cells, providing higher conductivity for more efficient charge transfer. Interconnects between LEDs have been produced by the deposition of silver ink on glass, providing functional circuitry [161]. AJP's capability of vertical printing has been successfully applied on the production of silver vertical interconnects for multi-layer circuitry and stacked componentry [162]. Silver lines were deposited on PCB substrates to produce interconnections with stacked components, enabling the production of compact packaging [163].

Besides silver ink, other unconventional materials have been tested for the fabrication of interconnects. One of the first attempts of depositing non-silver inks, used graphene-based

ink, which resulted in low conductivity due to the low concentration of graphene, which is required to avoid nozzle clogging [164]. Instead of using graphene ink, a combination of graphene and silver inks achieved to increase the conductivity [165].

4.6.2 Active devices

Active devices are components that either supply energy to an electronic circuit or require energy, in order to operate. Such devices are transistors, switches, current/voltage sources, and solar cells. Active devices consist of multi-material structures. Therefore, AJP is an attractive fabrication method for such devices, due to its capability of printing different materials, at once. Furthermore, AJP enables the deposition of conductive inks into non-standard substrates, such as paper and fabric, which is also a benefit for such applications.

Transistors

AJP technology has been focused on research and development of printed transistors, due to their wide application in electronic systems. Studies in the literature concentrated on the deposition of semiconducting single-walled carbon nanotubes (SWCNTs) inks, to produce thin film transistors. A silver ink was first printed on a Kapton substrate, as source and drain electrodes [166]. After the sintering of the silver ink, SWCNT aqueous solution was printed on the electrodes to form the carrier transport active layer. The printed flexible thin film transistors were characterized to have an operation frequency of greater than 5 GHz. In another study [167], a semiconducting SWCNTs ink was deposited on SiO₂/Si substrates with pre patterned gold electrodes by AJP and drop-casting methods to produce thin-film transistors (TFTs).

Xu et al [168] presented a method to convert the polarity of thin-film transistors by employing AJP. Ethanolamine ink was deposited on printed SWCNT thin film transistor, which resulted in changing the polarity of the transistor from p-type to n-type. Through this approach, a complementary metal oxide semiconductor (CMOS) could be produced. A flexible H-bridge integrated with a polymer electrochromic pixel were printed on polyester (PET) foil [169]. The entire circuit includes 23 transistors, 12 capacitors, 20 resistors and nine crossovers, all of them printed with AJP (**Figure 4.11**). Only interconnects were produced by other mean,

photolithography and electron beam evaporation. This work not only presents the capability of printing transistors and electronic devices individually, but also proves that AJP can be used successfully for the production of more complex circuits.

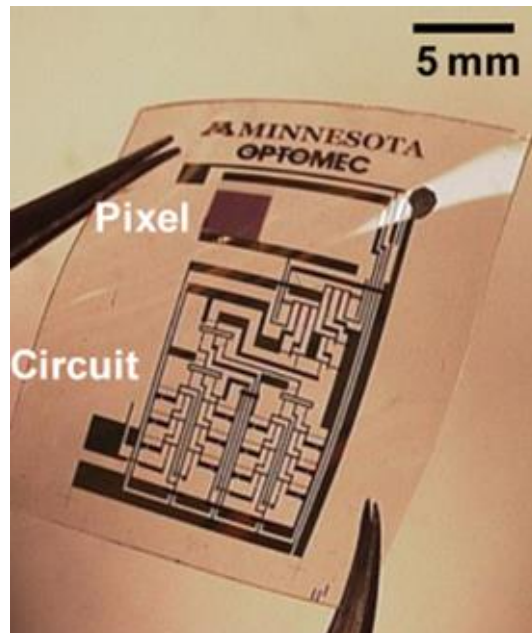


Figure 4.11. The printed circuit with EC display pixel on a flexible PET substrate [169].

Solar cells

Optomech together with the Fraunhofer Institute of Solar Energy Systems (ISE) were the firsts that worked on developing higher efficiency solar cells with AJP. In order to increase the efficiency, their aim was to reduce the width of collector lines, which would increase the conductivity and reduce the shadow effect. Narrow collector lines with widths between $18\mu\text{m}$ and $60\mu\text{m}$ (unlike screen printed line $\sim 100\mu\text{m}$) were printed on crystalline silicon solar cells. High reflectivity was observed in the shape of the printed line, which leads to an optical width that is $<50\%$ of their geometric width and reduces the shadowing [170]. Achieving higher conductivity and reduced shadow effect has proven higher efficiency. Finally, solar cells achieved 20% efficiency. More details can be found in the study by ICE [171].

Early studies [172, 173] focused on the metallization of silicon cells by printing, in order to minimize shadow effect, obtain high conductivity and finally improve the efficiency. However, other than metal inks, earth-abundant materials (perovskite, kesterite) started to be

attractive for the production of photovoltaics, due to easy processing and low cost. Perovskite films were deposited as part of a functional solar cell and achieved 15.4% efficiency [174]. This study was extended to the deposition of perovskite on an array of curved stripes, on a hemispherical surface, indicating the capability of deposition in non-flat surfaces (**Figure 4.12**).

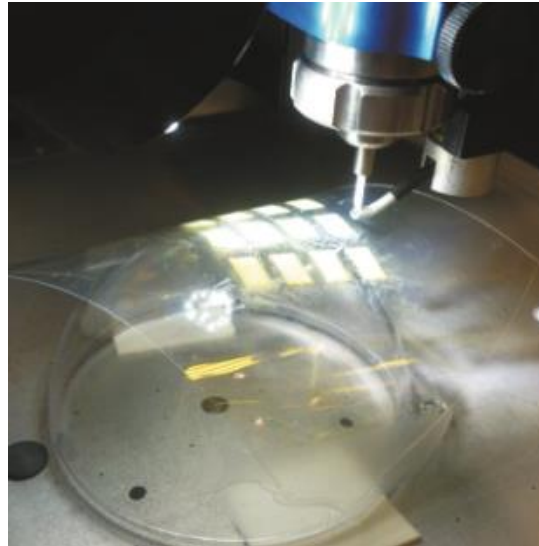


Figure 4.12. Direct AJP deposition of perovskite semiconductor on a hemispherical surface [174].

Fuel cells

AJP is considered to be a cost and functional effective method for the production of solid oxide fuel cells (SOFC). Solid oxide fuel cells are ceramic electrochemical devices that generate power from hydrogen (**Figure 4.13**). They consist of two electrodes (anode and cathode) and an oxide-ion conducting electrolyte in between. The most commonly used electrolyte is yttria stabilized zirconia (YSZ). The anode electrode is usually made of cermet of Ni-YSZ. For the cathode electrode, La-based perovskites, such as strontium-doped lanthanum manganate (LSM) and lanthanum strontium cobalt ferrite (LSCF) are used.

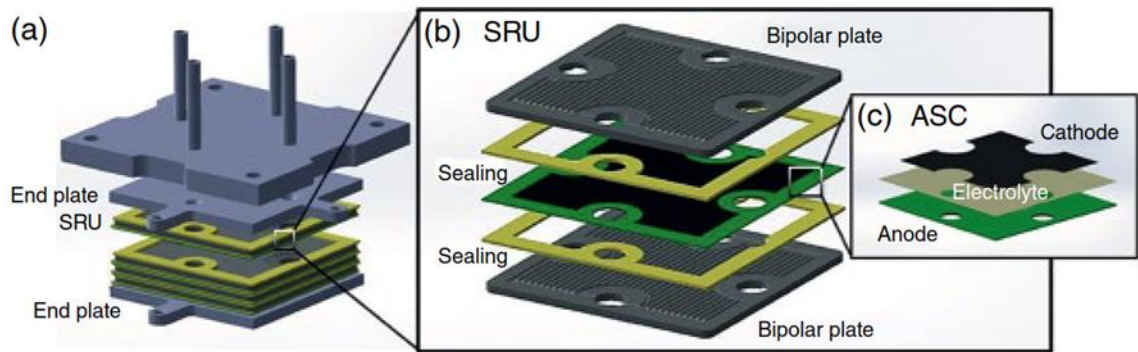


Figure 4.13. Scheme of a 5-cells SOFC stack, with components of a SOFC single repeating unit (SRU), and (c) components of an anode-supported SOFC cell (ASC) [175].

AJP creates smooth transitions between the layers of solid oxide fuel cells, since the printer is capable of mixing multiple materials during deposition, providing increased functional zones. Compared to AJP, traditional methods create more abrupt and unstable interfaces, which may lead to mismatches in thermal expansion coefficients between different materials and finally results in delamination. AJP produces smoother transitions and provides better mechanical stability, preventing delamination between the layers.

In the literature, studies [176, 177] concentrate on the deposition of functionality graded interlayers for SOFC. They basically focused on the deposition of an YSZ electrolyte, a LSM cathode and an YSZ/LSM composite interlayer. The interlayer material printing uses a dual atomization that combined two aerosol streams before deposition. The initial performance of the developed cell was low and therefore additional researcher performed to find out the parameters that affect the performance. It was found that controlling the process parameters, in order to produce optimized geometry and microstructures could increase the performance. Simply by controlling the process parameters, power density of 235 mW/cm² at 850°C in anode supported cells is achieved.

4.6.3 Sensors

A sensor is an input device, which provides an output (signal) with respect to a specific physical quantity (input). It is a device used to measure a property, such as pressure, position,

temperature, or acceleration, and respond with feedback. AJP has been proved a promising and effective method of producing small-scaled, high-resolution sensors of high resolution. Such sensors can be integrated and embedded in several structures, without affecting mechanical properties. There are no limitations of material substrates, since AJP is capable of printing on even soft surfaces that used in robotics. Packing more functionality into less space, is achieved by the micro printed patterns that provide sensing capabilities into devices. Plenty of examples can be found on the literature and some of them will be revised on this section.

Strain gauges

A simple strain gauge sensor consists of conductive traces. When mechanical strain is applied, results in deformation, which causes a change to electrical resistance. Such devices are fabricated as part of a film and afterwards are attached on a substrate surface. However, AJP is capable of producing and deposit strain gauges directly to the surface of the component, eliminating the need for bonding. Printable and flexible strain gauges offer distinct advantages over conventional rigid sensors, such as mechanical flexibility, smaller dimensions, and higher sensitivity.

Maiwald et al [178] produced strain gauges, consisted of three layers (**Figure 4.14**). The sensing element has the form of meander and it is deposited on a printed polymer layer, which is used for isolation between the sensor and the metal substrate. Afterwards, the sensor was encapsulated. All the layers are produced with AJP. The printed sensor was then compared with commercial reference foil strain gauges sensor. The results show that the printed sensor has a reliable output for a 500 N load over 1000 cycles at 0.5 Hz.

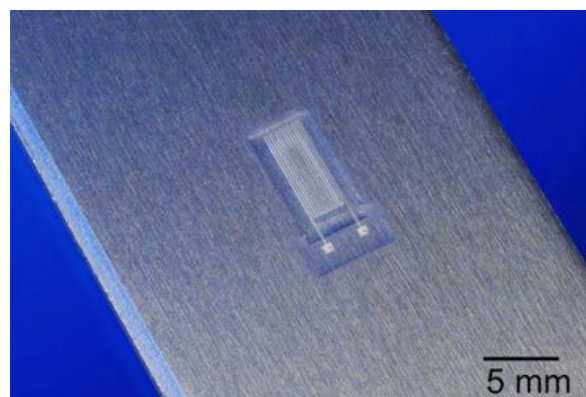


Figure 4.14. AJP strain gauge on aluminium surface with isolation layer and encapsulation. [178].

Embedding sensors inside composite structures with traditional methods, results in degradation of mechanical properties, especially of the interlinear shear strength of the composite. In order to produce multifunctional composite structures with no effect on the composite's properties, smaller volume electronics and less invasive methods should be considered. Zhao et al [179] employed AJP, to print strain gauges and interconnects inside composite structures, without degrading the composite's mechanical properties. Silver-based strain gauges were printed onto carbon fiber prepregs substrate, including an epoxy resin film in between. The challenge of this work was to achieve both good printing quality and mechanical integrity of multifunctional composites. To achieve this, critical factor found to be the degree of pre-cure of the carbon fiber prepreg. If pre-curing was not performed, the resin flow would induce sensor deformation. Finally, it was found that 10% degree of cure of the prepreg is required to avoid such phenomena. For the characterization of strain gauges sensors, resistance changes were measured under cyclic loading and were compared with commercial foil metal strain gauges. The results showed a reliable mean strain gauge factor of 2.2 ± 0.06 .

Printing sensors via AJP requires post processing steps to fuse particles and achieve final properties. It is observed that sintering or curing methods affect or even damage substrates, made of materials with low melting point (T_g). However, a variety of low-cost plastics with low T_g used in a wide range of industrial and commercial applications and therefore would be used as substrates, reducing the cost of the entire process. A recent study [180] focused on the deposition of strain gauge on commonly used plastic materials with low T_g , as the substrate of the sensor. Silver-based strain sensors were directly printed on curved surfaces of different types of plastic. Specifically, the sensor was deposited on the following types of plastic: Polyethylene terephthalate (PET), polyethylene, polyvinyl chloride (PVC), thermoplastic polymer polylactic acid (PLA) and polyimide. Then the samples was cured, using the photonic curing method. The silver ink presented a good adhesion with all different types of plastic and damage of the plastics was not observed after curing. Finally, a PVC conduit was selected as the substrate of the printed sensor (**Figure 4.15**), in order to examine and evaluate the electrical properties and the performance of the strain sensors. The strain gauge was printed on a PVC conduit and was sintered by photonic curing. The sensor was characterized by evaluating the gauge factor, compared to commercial foil strain. The results present similar gauge factors but due to a protective layer of rubber silicon, the factor was reduced to 30%. The conclusion of this study is that the combination of AJP and photonic sintering is an effective method of producing strain sensors on non-conventional surfaces.

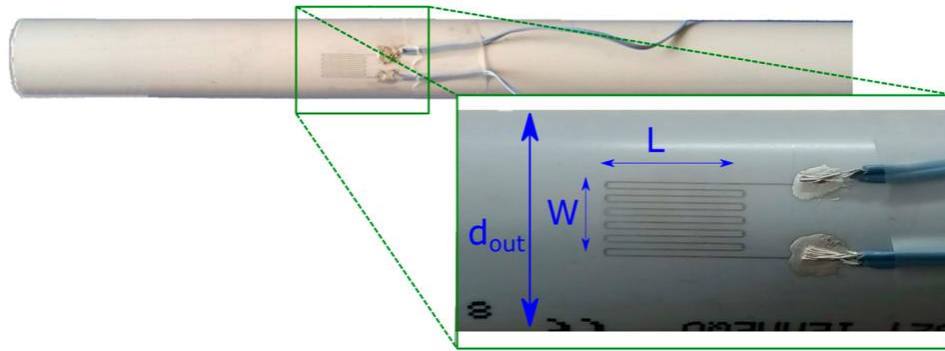


Figure 4.15. AJP strain gauge deposited on a PVC conduit, $d=20\text{mm}$, $L=10\text{mm}$ and $W=5.5\text{mm}$ [180].

A recent study [181] conducted to evaluate aerosol jet printed capacitive strain gauge for soft structural materials that are used for structural health monitoring systems (SHM) in space applications. A silver-based capacitive strain gauge sensor (CSG) was developed via AJP, having an interdigitated electrode design and deposited on a flexible polymer substrate of Kapton (**Figure 4.16**). The sensor was then compared with a commercial high elongation resistance-based strain gauge (HE-RSG), in order to test their capability of monitoring military grade Kevlar webbing under high load (26.7 kN). For the characterization of both sensors, performed tests with dynamic, static and cyclic loads. The comparison between two sensors proved that the printed CSGs has superior performance for high elongation strain measurements. Additionally, when the electrode arrangement was perpendicular to the direction of strain, they operate with a gauge factor of 5.2.

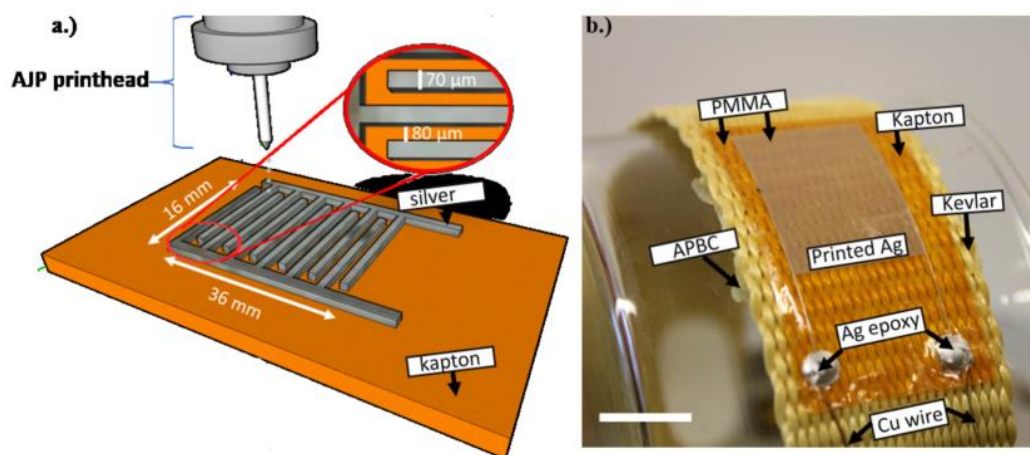


Figure 4.16. a) Sensor configuration with interdigitated electrode structure, and b) capacitive strain gauge on Kapton substrate attached to Kevlar [181].

Temperature sensors

Several types of temperature sensors, such as thermocouples, thermistors and Resistance Temperature Detectors (RTDs) are commercially available and find a wide range of applications. Three dimensional printed sensors can be more advantageous, compared to commercial sensors, due to the capability of deposition on a wider range of substrates. Additionally, printed sensors can fit the surface topography of measurement situation and demand less space of installation. AJP enables the fabrication of temperature sensing arrays and therefore temperature distribution of a system can be measured.

Miniaturized thermistors were developed, to be integrated in tiny cutting tools that are types of turning inserts [182]. Printing thermistors on turning inserts, requires an insulation layer, in order to avoid short-circuiting. Turning inserts were coated with an Al₂O₃ layer by physical vapor deposition and then silver (Ag) and nickel oxide (NiO) were deposited on the insulated inserts (**Figure 4.17**). First, silver lines were deposited on the Al₂O₃ insulated layer and then NiO thin films were deposited on the silver lines. The printed thermistors showed high temperature sensitivity without hysteretic effects, and the response time was almost as fast as that of reference thermocouples.

A common method of sensing temperature is by measuring thermoelectric voltage generated by two different metal/metal alloy junctions under a temperature gradient. A Cu and CuNi ink was deposited on flexible Kapton substrates (**Figure 4.18**) and afterwards was laser sintered at low powers, to avoid substrate damage [183]. Producing temperature sensors by AJP involves minimal process steps when compared to traditional methods of lithography or MEMS. The aim of this study was first the fabrication of high performance deformable temperature sensor by employing AJP, which can be used for soft robotics, biomedical, energy, industrial, and defense requirements. The sensors showed a highly linear response as a function of the temperature and high sensitivity. Flexibility tests showed a stable device performance (variation of Seebeck coefficient within 2.5%) after 200 bending cycles and 200 twisting cycles.

Silver-based ink was used for the fabrication of Resistance Temperature Detectors (RTDs) that were deposited on polyimide foils in three different length configurations (**Figure 4.19**) [184]. After thermal sintering of the printed silver ink, the sensors were coated with a protective layer to resist temperature in the range of 450 °C. Thermal cycling tests were performed in a controlled thermal oven, using a reference sensor (PT100), in order to characterize the printed RTDs and define the temperature coefficients. It was found that the

resistance value measured after the thermal cycles decreased by 40% on average to that after the printing process. However, the sensors showed a similar behavior with the reference PT100 sensor with sensitivity (α coefficient) of 0.00315 K^{-1} similar to commercial PT100 ($\alpha=0.00380 \text{ K}^{-1}$) and linear response.

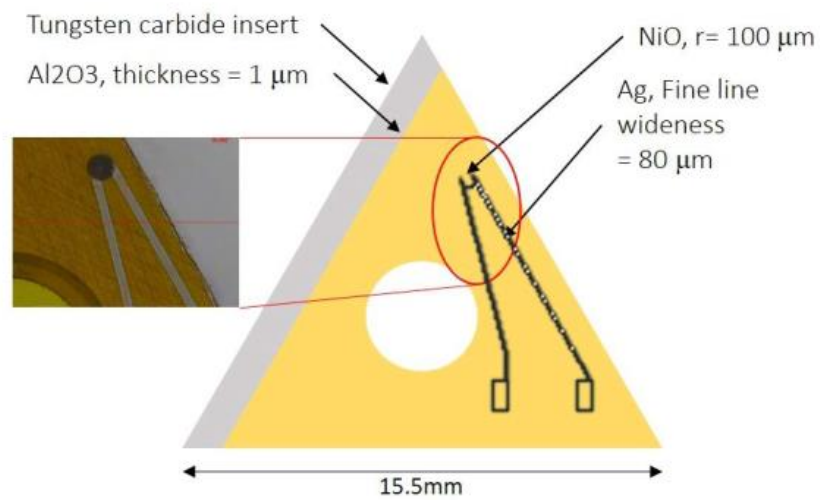


Figure 4.17. The AJP printed thermistor [182].



Figure 4.18. AJP flexible temperature sensors deposited on Kapton [183].

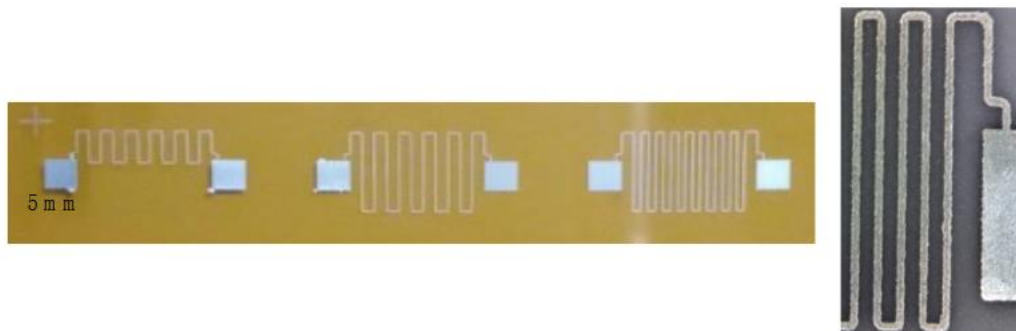


Figure 4.19. RTD in three different configurations (33, 66, 99 mm in length) deposited via AJP on Kapton [184].

Photodetectors

AJP has been successfully integrated in the process chain of fabricating photodetectors, together with other methods. AJP, inkjet printing and drop casting have been employed to develop photodetectors on paper substrates. Aga et al [185] applied a combination of the above fabrication methods to produce a photodetector. AJP deposited PEDOT:PSS and P3HT:PCBM layers were deposited by AJP (**Figure 4.20**), silver bottom electrodes used inkjet printing and DNA biopolymer was fabricated by drop casting.

However, photodetectors can be fully printed by AJP [186]. Fully printed by AJP flexible organic photodiodes (OPDs) were produced and compared with devices that are fabricated on rigid substrates by conventional methods. First, OPDs were deposited on the top surface of an ITO covered PET foil. Then, the ITO was replaced by PEDOT:PSS electrodes. It was found that the performance of the AJP sensor is equivalent to devices, fabricated by conventional methods.

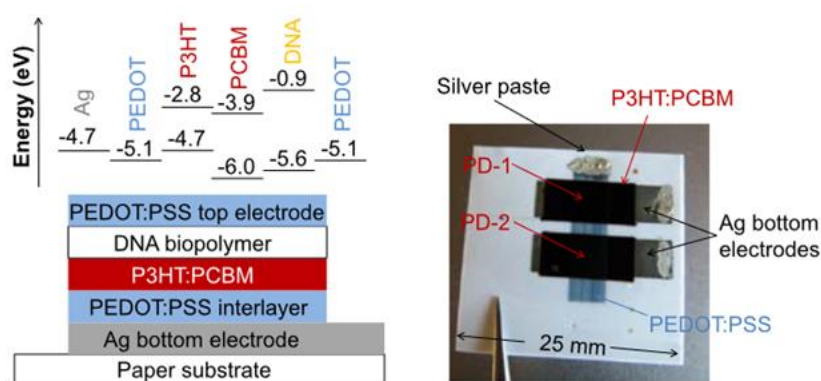


Figure 4.20. Two AJP printed photodetectors on a single paper substrate (left) and P3HT:PCBM surface after printing PEDOT:PSS (right) [185].

CHAPTER 5

DESIGN & FABRICATION OF THE SWaP PROTOTYPE

5.1 Introduction

The breakthrough character and aim of the SWaP project is the combination of advanced manufacturing methods, in the form of Selective Laser Melting (SLM) and Aerosol Jet Printing (AJP), to create a new generation of smart fluidic elements for cooling systems. These smart fluidic elements are designed with the following attributes [12]:

- Compatibility with existing standard hydraulic circuits.
- Capability to sense fundamental fluidic properties.
- Negligible addition of mass and volume to the cooling system while being a single component part produced at an affordable cost.
- Direct integration in the fluid flow to allow for multiple measurement points of fluid properties in the cooling system.

To create the smart fluidic devices (**Figure 5.1**), the fabrication relies on the combination of different advanced manufacturing technologies with the following steps [12]:

1. 3D digital model design of the smart pipe and generation of the printing file
2. Fabrication of the pipe, the electrical wires, electrical connectors, and fluidic interfaces by SLM
3. Complete removal of the un-melted powder
4. Epoxy casting for the insulation layer
5. Separation of the 3D printed part from the build platform
6. Removal of the supporting materials
7. Electropolishing
8. Thermal treatment of the UV curable epoxy
9. Digital model design of the sensors and generation of the printing file
10. Sensor deposition by AJP
11. Thermal treatment of the 3D printed sensor

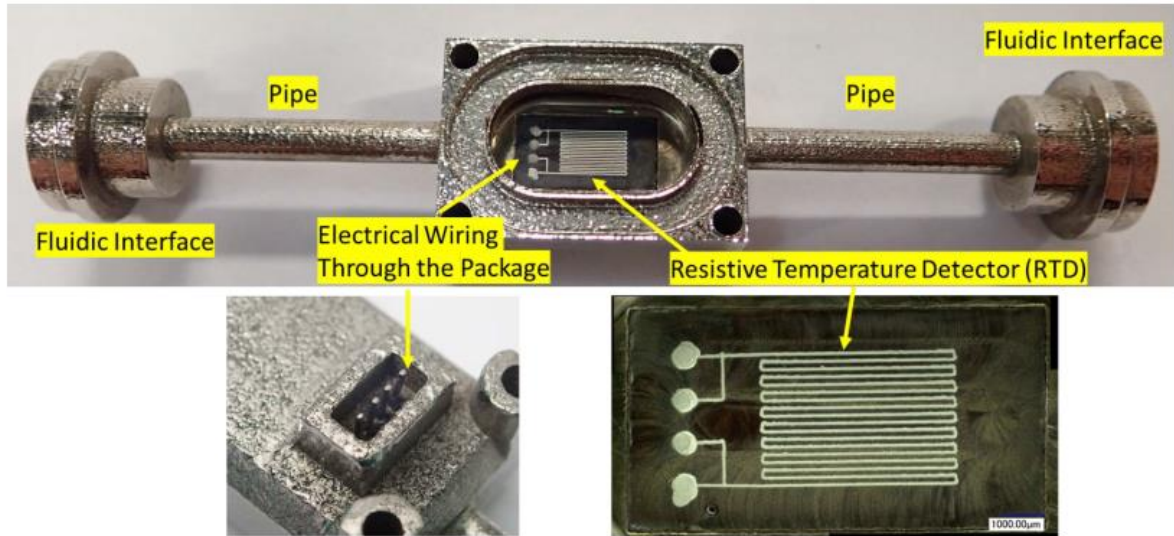


Figure 5.1. AM constructed pipe from SLM with AJP patterned RTD embedded. [12]

This chapter presents the steps for the fabrication of the smart pipes with embedded temperature sensors. The first section concentrates on the fabrication of the smart pipe via SLM, and the evolution of its design during the project. Then, it follows an introduction to the types of temperature sensors with an emphasis on Resistance Temperature Detectors (RTDs), which is the type of the patterned sensor deposited by AJP. The deposition process of the sensor on the pipe's substrate is then described. The last part of this chapter focuses on the importance of embedding a sensor in the inner wall of the pipe, by presenting the conventional methods of fluid temperature sensing.

5.2 The smart pipe – SLM

The idea and the aim of the SWaP project is to design and fabricate a pipe that can include sensors/s on its inner wall. A cavity in the pipe's profile is required, in order to deposit the sensor in the inner wall. To receive the signal of the sensor, electrical connectors should be also included in the pipes design. However, the first step was to produce a simple pipe without the cavity and the connectors, in order to verify that a pipe can be successfully produced via metal additive manufacturing. A set of pipes produced via Selective Laser Melting (SLM), in various diameters. Each pipe was then connected via standard hydraulic connectors (**Figure 5.2**) to a circuit, tested for leaks.

Since, the fabrication of a pipe via SLM is efficient and the tightness of the pipe was verified, the next stage involves the design and fabrication of a pipe with cavity and pins (**Figure 5.3**). This is one single component that has been printed in one step by the SLM printer. Testing the produced pipes, requires hydraulic components, in order to connect the pipe in a circuit, used for leak tests. Standard nuts are placed on both sides of the pipe and then ferrules are attached and glued on both sides, ensuring tightness in connecting the part. To fix the position of the ferrules on the pipe by glue, it is a process that requires time for the glue to dry. Furthermore, the nuts cannot be reused for other pipes to be tested, because their placement is permanent. To overcome these problems, the idea was to fabricate a pipe with integrated fluidic interfaces (**Figure 5.4**). The final design of the SWaP prototype is presented in **Figure 5.5**.

Every different design of the pipe that was presented above, employs the method of Selective Laser Sintering, to produce single components with embedded features. The SLM is a Powder Based Fusion (PBF) method of metal Additive Manufacturing (AM), in which a very thin layer of powder is spread on a build platform and a laser beam scans and melts an area of the powder. This process is repeated layer-by-layer until the part is finished. The 3D printing process conducted by CSEM, using advanced 3D printing industrial machines. In particular, the TruPrint1000 by TRUMPF (**Figure 5.6**) was employed with 17-4PH Stainless Steel powder, for the fabrication of the prototype. The process of producing the final SWaP prototype is described in the following paragraph.

The first step is to create a digital model of the prototype by a CAD software, which is then used to generate the printing file. After the printing file is introduced to the printer's software, printing parameters can be adjusted and determined. Then the 3D printing process

starts and fabricates the part, according to the digital model. The fabrication of the part includes the pipe with the cavity, the electrical connectors and the fluidic interfaces. This is one single component that is being produced with a single step. Once the printing is finished, the excess and unmelted powder is being removed from the part. Then, UV curable epoxy is casted around the electrical connectors (pins), to hold them in a fixed position, as well as to create an electrical insulation layer on the inside of the cavity, where the sensor is printed. The produced prototype is removed from the build platform of the printer by wire saw cutting and then supporting structures are removed. As post –processing, electropolishing is applied to obtain a surface finishing, proper to ensure the tightness of the fluidic interfaces, when they are connected to a circuit. The last step is the thermal treatment of the UV curable epoxy.

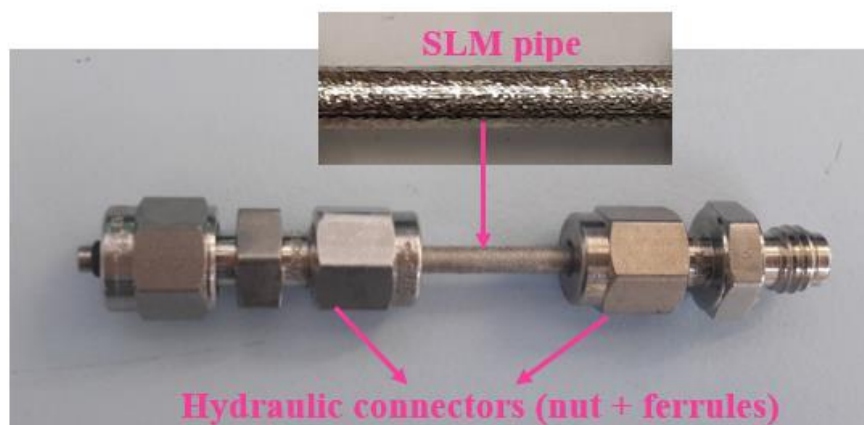


Figure 5.2. Simple SLM pipe with connected nuts and ferrules.

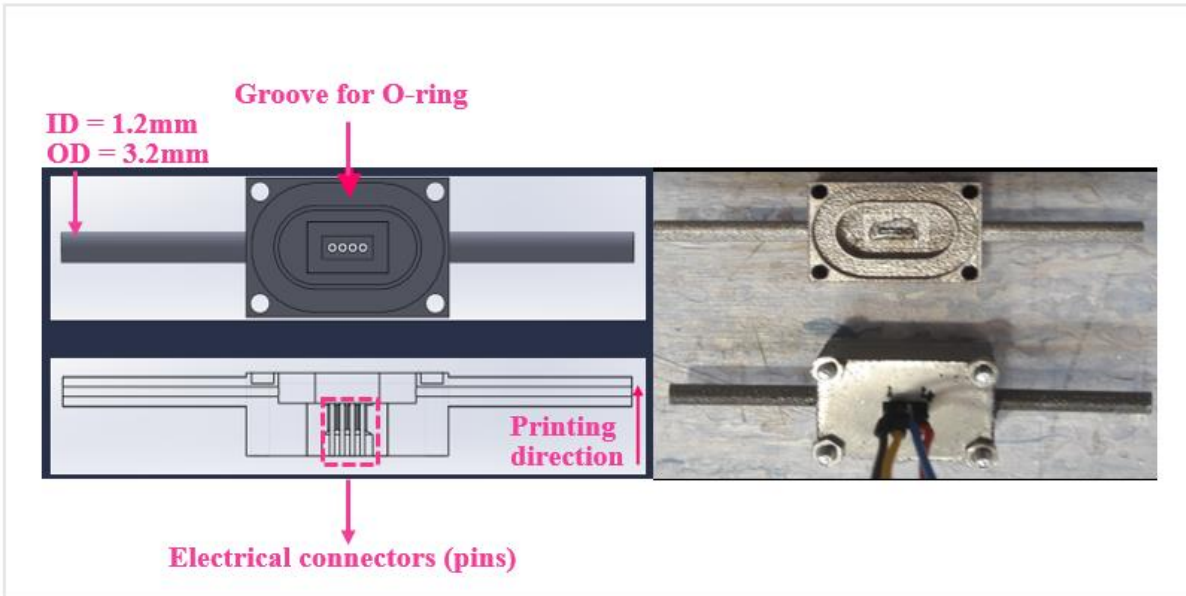


Figure 5.3. The design of the pipe with the cavity and the electrical connectors (**left**) and the 3D –printed pipe with cavity and with 3D-printed electrical connectors (**right**).



Figure 5.4. The 3D-printed pipe (ID=2mm, OD=3mm) with fluidic connectors (VCR) (**left**) and the 3D-printed pipe with 3D-printed casing, electrical and fluidic connectors (**right**).

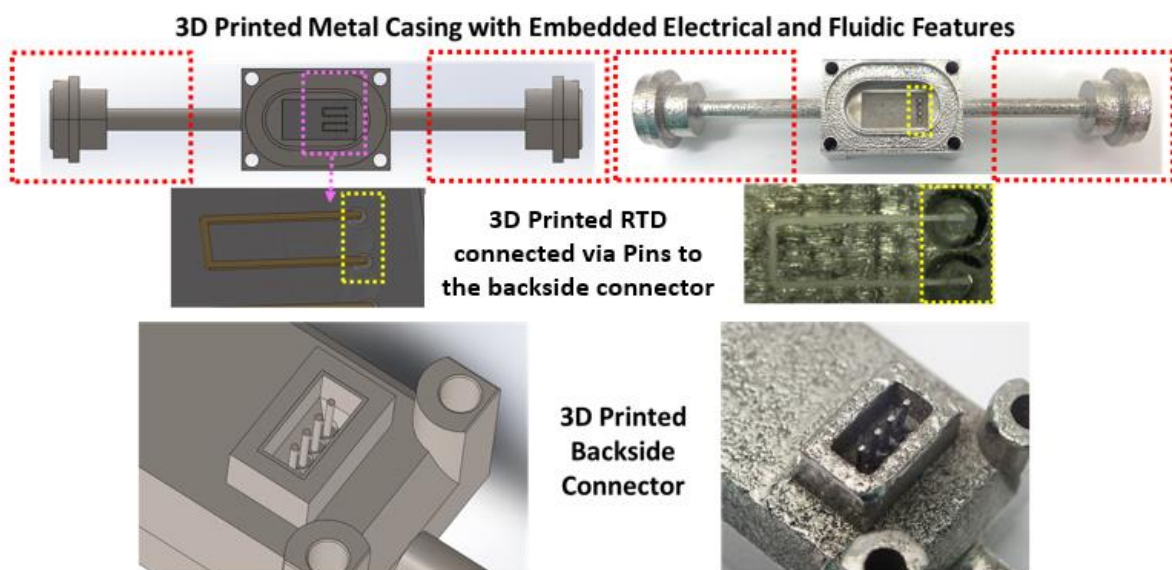


Figure 5.5. The final design of the 3D printed SWaP prototype: 3D printed pipe with metal casing with embedded electrical and fluidic connectors.

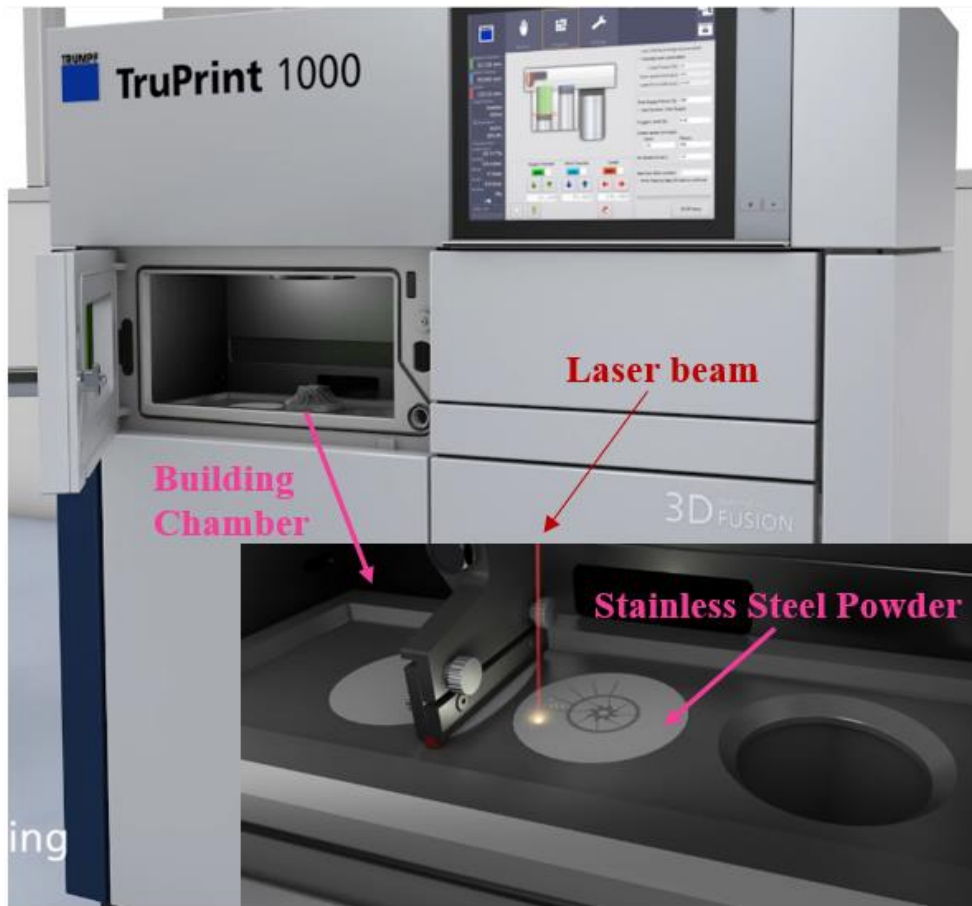


Figure 5.6. The TruPrint 1000 SLM printer by TRUMPF.

5.3 The embedded sensors – AJP

Once the SLM and the post processing are finished, the deposition of the temperature can be performed on the electrical pins of the insulated cavity of the smart pipe. The method, used for the fabrication of the 3D printed sensors is the Aerosol Jet Printing, which was presented in the fourth chapter of this work. However, before the description of the AJP deposition begins, it is important to present the type of temperature sensor that is fabricated via 3D printing, in the frame of the SWaP project. This chapter begins with an introduction on temperature sensing and the most commonly used types of temperature sensors and focuses on the type of Resistance Temperature Detectors (RTDs), which are the produced via AJP pattern embedded sensors. In addition, RTDs are the sensors, used as reference temperature for the evaluation of the SWaP prototype, as it is presented in the following chapters. Then, the following section of this chapter focuses on the steps of the AJP process for the fabrication of the 3D printed embedded RTD. The last section concentrates on the conventional methods for fluid temperature sensing, including an example of the laboratory for detector cooling at CERN.

5.3.1 Introduction to temperature sensing

Temperature sensors are part of our everyday life. They are used in buildings, vehicles, HVAC systems, household electrical appliances (refrigerator, thermostat, oven, etc.) as well as computers [186]. Industry requires several sensors to monitor production condition. Temperature sensors are widely in industrial applications, such as manufacturing, chemical engineering, renewable energy, oil mining, etc. Control and monitor of the process temperature is essential to the normal operation and efficiency of such systems. In order to meet the need of temperature sensing in a large number of application, many different types of temperature sensors have been developed and the most commonly used ones are present in this chapter. Before the review in types of sensors, it is advisable to understand the operation principle of temperature sensing.

According to thermodynamics, the movement of molecules and atoms produces heat (kinetic energy). When heat is added to a system, causes an increased motion of the molecules, which increases the temperature of the system. Therefore, temperature changes as the average

heat energy of molecular movement. However, temperature sensors cannot measure directly this energy, and therefore another property that changes with temperature is utilized for the calibration of the sensor. Temperature sensors are used for the measurement of medium temperature.

Temperature sensors are a simple device that measures the degree of hotness or coolness and converts it into a readable form through an electrical signal. Temperature sensing is based on voltage changes across the diode. If the voltage increases, the temperature and resistance will rise and vice versa. The electrical resistance can be measured and converted in a readable unit of temperature. There are many different types of temperature sensors and are divided in two main groups; contact and non-contact sensors.

Contact temperature sensors require a physical contact with object being sensed. This method assumes that there is no heat flow between the sensor the sensed object and therefore both are in thermal equilibrium. This type of sensors can be used to detect the temperature of an object in the form of solid, liquid and gas. Resistance Temperature Detectors (RTDs), thermocouples, and thermometers are the main and most commonly used temperature sensors and they belong to the group of contact sensors. They measure a physical property (i.e. volume of a liquid, current or resistance of a wire, etc.), which changes as a function of temperature.

On the other hand, non-contact temperature sensors detect the temperature from a distance by measuring the thermal radiation emitted by an object or heat source. They are mainly used, when a safe distance away from the object is required, due to dangerous conditions, such as high voltages and temperatures or hazardous environments. Pyrometers, thermal imaging sensors and infrared sensors are the most common type of non-contact temperature sensors. These sensors can be used to detect the temperature of solids, liquids and gases.

Besides the contact and non-contact sensors categories, the main types of temperature sensors that are mostly used are Resistance Temperature Detectors (RTDs), thermocouples and thermistors. The need for sensing and monitoring the temperature in different application fields, increased the range of temperature sensors, which are available in different forms and types, providing various functions. There are three types of contact temperature sensors that have gain the interest in main applications, due to their simplicity, ease of use and accuracy.

Thermocouples (**Figure 5.7.a**) are electromechanical elements that generate a voltage difference caused by a temperature differential between junctions of dissimilar metals. The

operation of thermocouples is based on the Seebeck effect [187]. Thermistors (**Figure 5.7.b**) are resistive ceramic or polymer elements that change their physical resistance in response to temperature changes. Unlike metals that increase their resistance with an increase in temperature, semiconductors resistance is decreased with temperature increases [188]. Therefore, thermistors have typically a negative temperature coefficient (NTC). However, few thermistors operate like RTDs, having a positive temperature coefficient (PTC) and their resistance increases with temperature rises (Figure 5.6). NTC thermistors are commonly used as inrush current limiters, while PTCs are typically used as overcurrent protectors. Resistance Temperature Detectors (RTDs) (**Figure 5.7.c**) are also resistors, made of metal that change the resistance with respect to temperature variations [189].

All of these sensors are designed to respond to temperature in a measurable way. They are connected to electrical circuits that are usually built from analog-to-digital converters (ADCs) and other components (amplifiers, active and passive components, etc.). When the sensor is connected to these circuits, the sensor signal is converted into a usable analog or digital value that can be translated in temperature units.

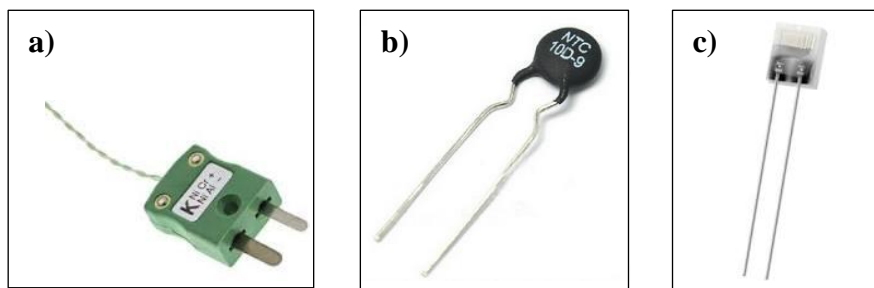


Figure 5.7. a) Thermocouple type K, b) NTC Thermistor, and c) Pt100 RTD

5.3.2 Resistance Temperature Detectors (RTDs)

Resistance Temperature Detectors (RTDs) measure the temperature based on the electrical resistivity of metals, which varies with temperature changes. The operating principle of RTDs is based on changes in electrical resistance of pure metals that is characterized by relatively linear positive change in resistance with temperature. RTDs are made from high purity conducting metals such as platinum, copper and nickel. The most commonly used material is platinum, due to its chemical stability, linear response and high accuracy.

RTD operation is based on a linear relationship between resistance and temperature, where the resistance increases with respect to temperature. As the temperature of the metallic sensing element increases, increased random molecular movement impedes the flow of electrons. The electrical resistance is related to temperature, following the Callendar- Van Dusen equation [190]:

$$\text{For } T < 0^{\circ}\text{C} \rightarrow R(T) = R_0(1 + aT + bT_2 + cT_3(T - 100)) \quad (5.1)$$

$$\text{For } T > 0^{\circ}\text{C} \rightarrow R(T) = R_0(1 + aT + bT_2) \quad (5.2)$$

Where, $R(T)$ is the resistance at temperature T , R_0 the nominal resistance, and a , b and c the temperature coefficient values.

This section reviews the different types of RTDs according to their structure, the different materials used in RTDs, as well as the influence of the resistance ratio. The last part of the section focuses on the different methods of RTD connections to devices, used for temperature measurements.

RTDs can be constructed in three ways; thin film, wire wound and coiled RTDs [191]. The later structure is a type of wire wound RTD.

a. Thin film RTDs

Thin film RTDs consists of a thin film of platinum (sensing element) deposited on a ceramic chip and then laser cutting or chemical etching is applied to form a resistance path in the platinum film (**Figure 5.8**). The entire element is coated with a thin layer of glass, which protects it from harmful conditions. Lead wires are bonded to the chip and are covered with epoxy, providing secure connection. Typically, a laser beam is employed that opens parallel shunts in the pathway, in order to adjust the resistance at 0°C . With an increased number of opened shunts, higher resistance is obtained.

Thin film RTDs are the most commonly used and they have lower cost, as compared to wire wound RTDs. Furthermore, they are smaller in size and they also have faster response time. However, they less accurate than other types, due to a number of reasons. One of the

reasons is that the resistance cannot be adjusted as precisely as in the other types. When they are exposed at higher temperature, a strain error is caused by different expansion rates of ceramic and platinum. The phenomenon of self-heating occurs mainly because of their small size and can cause an error to the temperature measurement.

b. Wire wound RTDs

Wire wound RTDs consists of a resistive wire, which is wound around a core (mandrill) that is usually made from a ceramic material (**Figure 5.9**). The length of the wire determines the sensors resistance (R_0) at 0°C. Lead wires are welded to the winding wire and are coated with glass or ceramic, providing a protection layer. The length of the resistance wire increases slightly with a rise in temperature. If the resistance wire is twisted deforms with temperature increases due to change in wire's resistance, caused by mechanical strain.

c. Coiled RTDs

Coiled RTD consists of a resistance wire, rolled into small coils that loosely fit into ceramic form, filled with non-conductive powder (**Figure 5.10**). Basically, the powder is used to increase the rate of heat transfer in the coils, providing improved response time. The loosely fit of the coils allows the wire to expand and contract as temperature changes. Therefore, errors caused by mechanical strain are minimized for this type of wound wire RTDs. A metal sheath can be used to protect the sensing element and it also forms the RTD in temperature probes.

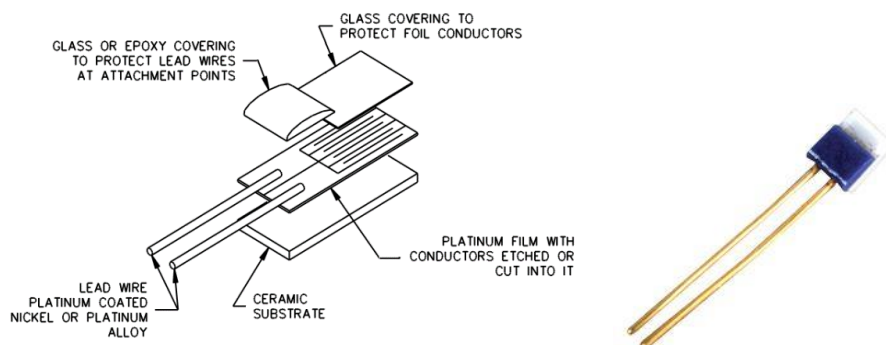


Figure 5.8. Schematic of a thin film RTD configuration.

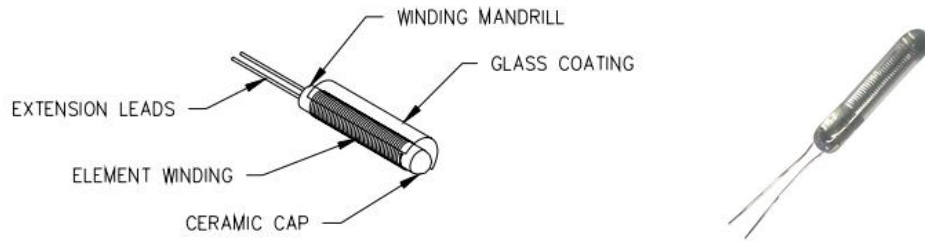


Figure 5.9. Schematic of a wire wound RTD configuration.



Figure 5.10. Schematic of a coiled RTD configuration.

RTDs are made from high purity conducting metals such as platinum, copper and nickel. Nickel is cheaper than platinum, it has good corrosion resistance but lowers its accuracy at higher temperatures and also ages relatively faster than the other two materials. Nickel's temperature range is limited to -80 to $+260^{\circ}\text{C}$. On the other hand, copper is a low cost material that presents extremely linear temperature-resistance relationship but when it is exposed to higher temperatures oxidizes. Copper's temperature range is limited to -200 to $+260^{\circ}\text{C}$. The most commonly used material is platinum, due to its chemical stability, linear response and high accuracy.

Platinum RTDs are the most commonly used sensors of its kind and find a wide range of applications in industry, instruments and process control. Platinum has excellent corrosion resistance, long-term chemical stability, linear temperature-resistance relationship and wide temperature range of -200 to $+850^{\circ}\text{C}$. However, they are the most expensive, as compared with nickel and copper RTDs.

Platinum RTDs are categorized in Pt100 and Pt1000, according to their nominal resistance value (R_0) at 0°C . Pt indicates the sensor's material, which is Platinum, while 100 or 1000 is the nominal resistance value (Ohm), measured at the temperature of 0°C .

Material types and properties are important, in order to fulfill properly the needs of each application. The type and purity of materials affect the resistance ratio. The average slope of

temperature-resistance for the temperature range of 0 to +100°C is described by the resistance ratio and is expressed as following [192]:

$$\text{Resistance ratio} = (R_{100} - R_0) / R_0 \quad (5.3)$$

Where, R_{100} is the RTD resistance at 100°C and R_0 at 0°C, respectively.

A high resistance ratio can improve the measurement accuracy but features of material used in the wires affect also the accuracy and should be taken into account. However, it is noted that high resistance ratios are achieved by higher resistance values at 0°C. **Figure 5.11** illustrates the resistance-temperature curves for the three different materials used in RTDs, together with the resistance ratios and resistance R_0 .

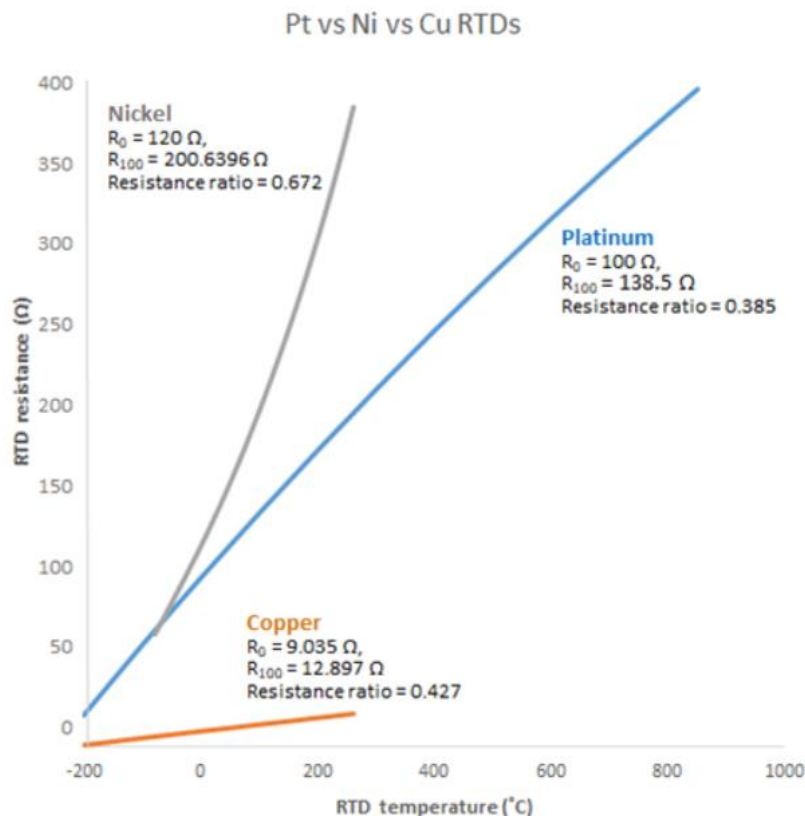


Figure 5.11. Resistance- Temperature relationship of RTDs, made from different metals.

Signal conditioning plays an important role in RTD temperature measurement. RTDs require an equipment such monitoring devices, in which they can be connected to generate a signal. They also require an excitation current flow to generate and read the voltage across the RTD terminals. A simple algorithm is applied to calculate the resistance for a given excitation current and measured voltage. Then, this reading can be easily transformed to temperature units. In order to avoid self-heating phenomenon, the excitation current should be minimized.

The connection of an RTD to the reading device requires wiring of the sensor. The resistance of the wires, should be taken into account, since they could change the sensors resistance and consequently they add an error to the temperature measurement. In case that the wires is not negligible, a wire-RTD configuration that reduces such effects should be selected. There are three basic wiring RTD configurations that are separated, according to the number of wires in 2-wire, 3-wire and 4-wire RTD configurations [190].

a) 2-wire RTD configuration

The 2-wire RTD configuration is the simplest but the least accurate among the three circuit designs. In this configuration, each end of the RTD sensor is connected via a lead wire to a monitoring device. The total resistance of the circuit includes RTD resistance, as well as the resistance of the wires and connectors. In this case, there will be always a degree of error, since eliminating the lead wire resistance is not possible. Therefore, 2-wire configuration is used with short wires or in application with limited demands in accuracy.

b) 3-wire RTD configuration

The 3-wire RTD configuration is one of the most commonly used methods in industrial and monitoring applications. A pair of wires is connected to the one end of the sensing element and one wire to the other end. The third wire provides a method for removing the average lead wire resistance from the sensor measurement. This method assumes that that three wires have the same resistance, which is not a problem for short length wires but not if the wires are extended and the length is increased. This configuration measures the resistance between two wires (1 and 2) and subtracts the resistance of the pair of wires (2 and 3), which results in the total resistance of the RTD.

c) 4-wire RTD configuration

This configuration provides the most accurate and precise temperature measurements, as compared with the previous ones. Two wires are connected to each side of the RTD and are

linked to the monitoring device. One pair of wires (1 and 4) is used to power the circuit with current, while the other pair (2 and 3) measures the voltage drop and is used for reading. The resistance of the lead wires does not contribute to the RTD resistance, due to the bridge-configuration, which compensates any differences in lead wire resistances. When current passes through the sensor along the lead wires, generating voltage across the sensor, which is measured by the potential lead wires. The resistance of the sensor is calculated by the Ohm's law, as a function of the measured voltage divided by the current. The value of the current is equal at any point in the circuit and it does not depend on the lead wires resistance. A 4-wire RTD configuration is mainly used in laboratories or other applications, where great accuracy is required.

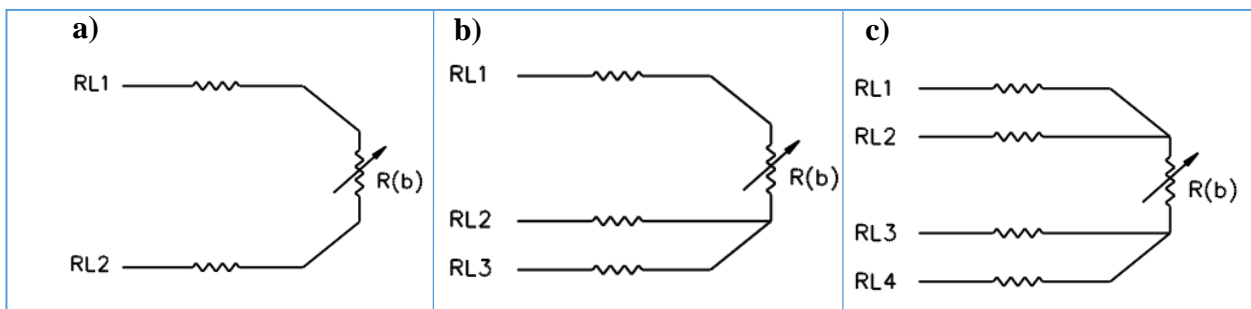


Figure 5.12. Methods of wire-RTD signal connections a) 2-wire, b) 3-wire, and c) 4-wire.

5.3.3 The embedded RTDs

Once the 3D printing process of the SWaP prototype fabrication is finished and the insulated layer of epoxy is completely cured, the deposition of the sensor can begin. The Aerosol Jet Printing (AJP) method is employed for the fabrication of the temperature sensor. This process is held also at CSEM, using an innovative AJP system “AEROSOL JET FLEX SYSTEM” by OPTOMECA (Figure 5.13). The ink, used for the deposition is the silver-based nanoparticles ink HPS-108AE1 by NovaCentrix. Due to its high viscosity, the atomization performed with the pneumatic atomizer. The shield gas that transfers the generated aerosol in the deposition head, is Nitrogen. The nozzle diameter is 100 μ m and the nozzle-substrate

distance was set at 2mm. The process of the sensor fabrication via AJP is described in the following paragraph.

Prior to printing, an important step is the cleaning of the AJP system's components. The cleaning process is quite simple and it can be made with Alcohol and dry Nitrogen. The deposition nozzle can be cleaned with a wire and Alcohol. In order to ensure that there is no residual ink in the nozzle, an optical reflective microscope can be utilized and it shows if the nozzle hole is open and clean. Then vortex is performed to the ink for few minutes (e.g. 5min) to induce ink homogenization. The clean components can be now assembled to the AJP system. The printing file with the digital model is introduced to the printer's software and printing parameters can be set. Before the deposition starts, a leak test is conducted in the pipe circuit of the system for approximately 5 minutes. Then, the prototype can be placed on the AJP system platform. The deposition process is very fast and it takes only few minutes. The printed pattern is then subjected to incident plasma via a plasma pen, which increases the surface energy. The last step is the thermal treatment, which is performed to sinter the silver nanoparticles together, in order to enhance electrical properties.

Once the deposition and thermal process of the sensor are completed, the sensor resistance can be measured and compared it with the goal resistance. The sensor's resistance depends on the volume resistivity, the length and the cross-sectional area (width \times thickness) of the sensor (**Eq. (5.4)**). The volume resistivity depends on the type of the used ink and its values are listed on the Technical Datasheet, measured at room temperature after thermal processing. The electrical properties of the printed ink change after the thermal processing, because most of the ink are water-based and change their state proportionally to temperature.

$$R = \rho \frac{L}{A} \quad (5.4)$$

Where r is the volume resistivity, L the length of the sensor and $A = \text{width} \times \text{thickness}$ is the cross-sectional area of the sensor.

A number of sensors of different patterns have been deposited and tested on different substrates, before the deposition on the pipes wall. The initial pattern design is a simple line, printed on the electrical pins of 3D printed electrically insulated stainless steel substrate (**Figure 5.14**). Another pattern has been tested, that first was deposited on glass and insulated

stainless steel substrates (without electrical connectors), in order to observe the influence of the epoxy layer on the sensor (**Figure 5.15**). This pattern was finally deposited inside the smart pipe, integrating two sensors on the same pipe. The final sensor has a pattern of Meander, which increased the reliability of on measurements (**Figure 5.16**).

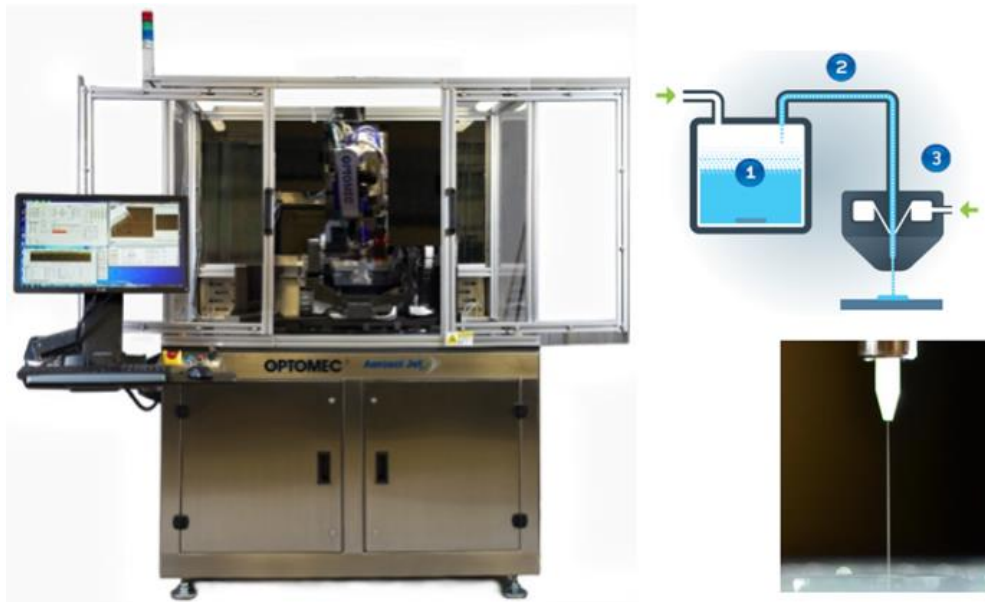


Figure 5.13. The Aerosol Jet Flex System by OPTOMECH.

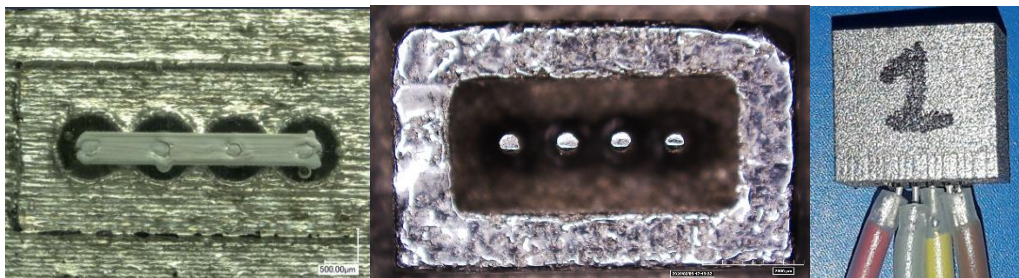


Figure 5.14. Line pattern deposited on the pins of insulated stainless-steel substrate.

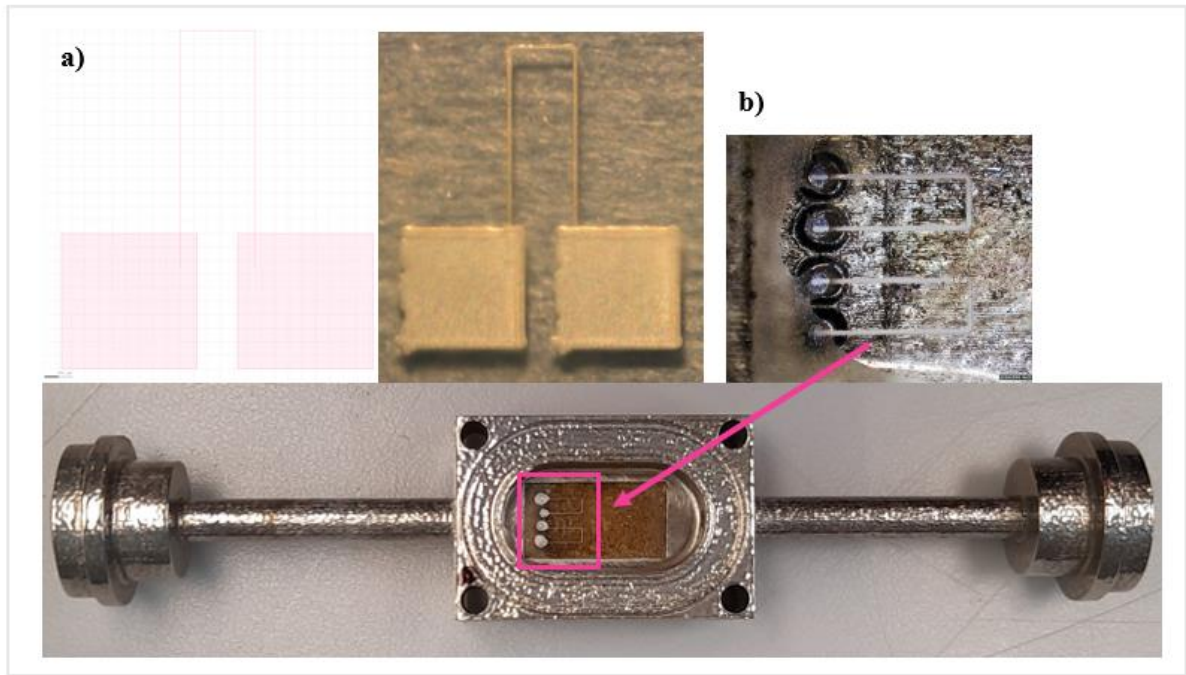


Figure 5.15. a) Design and deposition on glass and insulated stainless steel substrate, and b) the same pattern deposited on the smart pipe, integrating two sensors in one pipe.

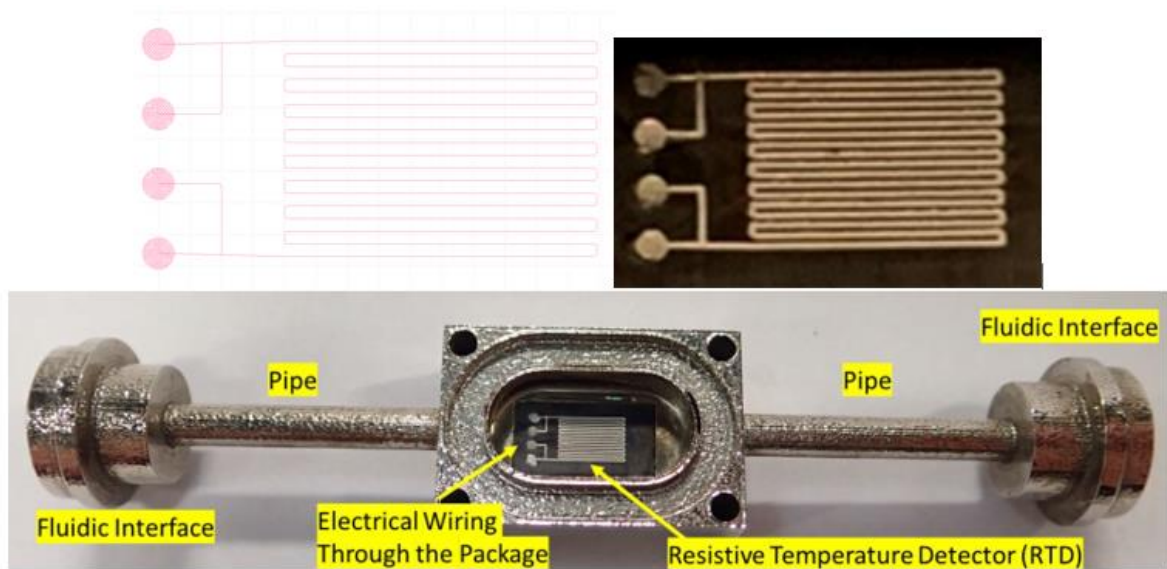


Figure 5.16. The final version of the SWaP prototype with embedded sensor with a meander pattern.

5.4 Fluid temperature sensing

Temperature sensing provides valuable data in process systems. Temperature measurements are essential for monitoring, protection and compensation in industrial and medical applications. Ambient and fluid temperature, as well as the entire temperature of a system can be monitored and measured by the integration of temperature sensors in a process system. These sensors provide feedback for the system conditions. Temperature variations below or above functional temperature thresholds can be detected by sensors, in order to prevent systems damage or failure. Therefore, temperature sensing ensures the normal operation and improves the performance of a system.

The temperature of fluids, flowing in pipes is essential to energy management and process control systems. Traditional methods of measuring the temperature of fluids flowing in pipes use probe-style sensors and thermowells, immersed into the fluid stream, and surface sensors, mounted on the outer surface of the pipe. These methods are mainly categorized as invasive and non-invasive; an introduction to them and their limitations, were presented in Chapter1, in the introduction (1.1.). In this section, these methods will be further analyzed and compared with the SWaP developed technology.

5.4.1 Immersed sensors and thermowells

Immersed sensors are directly exposed to the fluid stream, providing accurate and fast response fluid temperature measurements. Integrating an immersed a sensor in a pipe is an intrusive process that requires either drilling of the pipe or extra components element (elbow, tee union, etc.) to connect the sensor. Immersing sensors in the flow stream is pretty invasive and it requires a well-defined planning before the installation, since several factors can affect the system's operation and increase the risk of failures. Several parameters, such as fluid properties, pipe's material and diameter, and immersion depth should be taken into account. In addition, the replacement of immersed sensors is a time-consuming process that requires draining the system and reintroducing the fluid into the piping system. To simplify the process of replacing immersed sensors, thermowells are established as the main method of fluid temperature measuring in pipe systems.

Thermowells are widely used in many applications, with large or small pipe diameters, due to the fact that accurate measurements with fast response time are obtained. Here, the sensor is not directly exposed to the fluid, but only the thermowell. The sensor is placed inside the thermowell and a layer of thermal paste can be applied between the sensor and the inner wall of the thermowell, in order to achieve thermal conductivity. This means that the replacement of the sensor is pretty simple by removing the sensor of the thermowell which is fixed on the pipe, eliminating the process of draining. However, as in the case of the immersed sensors, the same parameters should be taken into account (fluid properties, pipe's material and diameter, and immersion depth). Another important factor concerns the method of inserting the thermowell in a pipeline (**Figure 5.17**), perpendicular or with an angle to the flow or at a pipe elbow [3]. Selecting the method of integrating the thermowell in the pipe, depends on the conditions of each application. In general, fluid, flow rate, temperature distribution, and fluid (state, viscosity, etc.) are essential factors that can affect the fluid flow.

Both methods are intrusive, which increases the risk of disturbance to the flow and pressure drops. The disturbance is created on the downstream side that oscillates back and forth. As the flow rate increases, the oscillation frequency increases, too. Here, there is the risk of sensor's failure, due to thermowell's vibrations. If the resonant frequency of the thermowell matches the vortexes frequency, induces vibration to the thermowell, which causes a damage to the sensor [193]. Another common effect is the stem conduction errors. The immersed sensors are probe-styles sensors, like thermometers. The thermowell has a cylindrical shape like a tube, in which the sensor is installed. In both cases, part of the sensor is exposed to ambient airflow and it induces these errors on the temperature measurement. In order to minimize stem conduction errors in thermowells, there is a rule of thumb for a minimum immersion length, which is 10 times the probe diameter plus the sensitive length of the probe [193]. However, this rule cannot be usually applied in small diameter pipe, where the immersion length is limited. In this case, a specific type of thermowell should be selected.

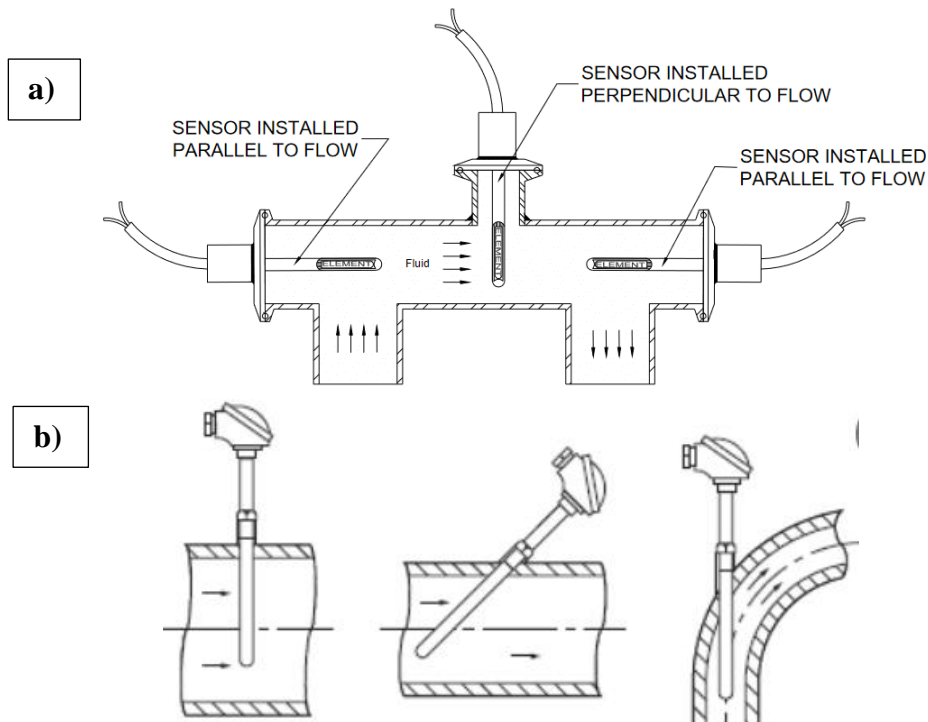


Figure 5.17. Different options of installation: **a)** immersed sensors perpendicular or parallel to flow and **b)** thermowells perpendicular or diagonal to flow or inside an elbow.

5.4.2 Surface sensors

Measuring the temperature with a surface sensor is a non-intrusive approach, since immersion of the sensor in the fluid stream is not required. On the contrary, the sensor is placed on the outside surface of the pipe either by gluing or clamping. The commonly used surface sensors for fluid temperature measurements are types of resistance temperature detectors (RTDs), thermistors and thermocouples (TCs). To ensure or improve the heat transfer, conductive adhesive can be applied between the sensor and the pipe surfaces. Insulation can be added over the sensor or the entire pipe, in order to avoid and minimize the effect of ambient airflow. This installation process is simple, fast and low-cost method for fluid temperature sensing that eliminates any possibility for leaks. However, accuracy and response time are usually lower, compared to intrusive methods. Another problem is the temperature difference between the real fluid temperature and the measurement point on the pipe surface. Common readout errors are caused by lack of contact between the sensor and the pipe surface due to bad mounting of the sensor on the pipe. Improving the heat transfer can provide more accurate and faster responding measurements.

Eliminating the above problems, the company Emerson developed an instrument “Rosemount Pipe Clamp Sensor”, which optimizes surface contact by spring loaded sensor and calculates the fluid temperature via a thermal conductivity algorithm **Figure 5.18.b**. Therefore, this instrument increases the accuracy and the reliability of temperature measurements by considering thermal conductive properties of the pipe and assembly. However, temperature differences are also possible to occur, due to the geometry of the instruments structure which creates a heat flow path around the pipe. Gorman et al. [4] developed a numerical model considering a number of parameters and use cases, to characterize and simulate the behavior of such systems. The simulation results indicated that for well specified use cases the surface sensors were able to provide adequate temperature measurements. However, these instruments are not a proper solution for small diameter pipes, due its volume and weight. This is a factor that limits their use, in pipe circuits, where the space is enough.

Besides the typical sensors that are mounted on the surface pipe as shown in **Figure 5.18.a**, another solution of surface mounted sensors is the one of thin, flexible sensing elements, the thermal ribbons. The sensing element is an RTD or thermocouple and has a form of a flat wire, laminated in electrical insulation layers **Figure 5.18.c**. These ribbons can be easily and tightly mounted on the outer surface of a pipe, by various methods such as silicone rubber tape, polyimide tape and shrink band. In any case, good insulation should be applied. According to the white paper by MINCO [194], the use of thermal ribbons is particularly attractive for pipe surface sensing, since the accuracy and response time of a Thermal-Ribbon is comparable to an immersed thermowell.

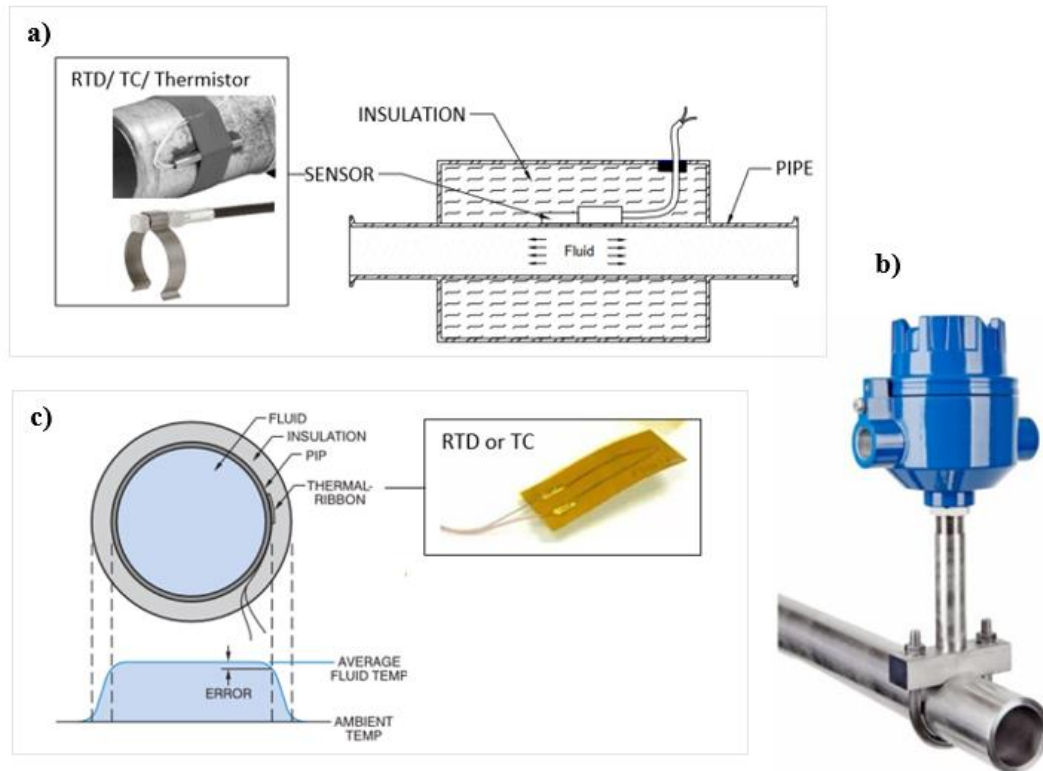


Figure 5.18. Surface sensors: a) typical RTDs, TCs, and thermistors clamped on the outer surface, b) fluid temperature sensing via thermal conductivity algorithm, and c) thin film thermal ribbons.

In order to present the limitations of the traditional methods for fluid properties measurements and note the positive impact of SWaP technology on this field, a real application of a hydraulic circuit, used for Detector Cooling testing at CERN, is presented below. The test setup that is illustrated in **Figure 5.19**, consists of a hydraulic circuit of very small diameter pipes with immersed and surface sensors and it is connected to a vacuum chamber. Here, the lack of space due to the vacuum chamber size, limits the number and the type of sensors that can be placed on it. For example, the pressure transducers that can be founded on the market, are bulky (massive) and cannot be placed inside or close to the piping system. On the other hand, the integration of the temperature sensors inside the pipe is a process that consists of several steps, which are described in the next chapter. The only other measurement that can be conducted in this system is the local temperature on the outer surface of the pipe by mounting a sensor to the pipe.

SWaP can provide solutions and optimizations to the current situation by combining AM techniques, to produce smart structures. Embedding a sensor in the inner wall of the pipe is a non-invasive method that provides direct contact with fluid, which means faster response

time. Fluid disturbance, pressure drop are eliminated, due to the very small geometry of the 3D printed sensor. Stem conduction errors are eliminated, since none of the area of the sensor is exposed to ambient airflow. Furthermore, the small size of the sensor, allows for an increased number of sensors that can be deposited along the pipe. SWaP is aiming at the development of revolutionary components for the next generation of cooling systems, directly embedded sensors in a hydraulic circuit element by the combination of Additive Manufacturing (AM) technologies. Last but not least, different types of sensors (pressure, flow mass rate) can be printed and embedded in the same pipe (**Figure 5.20**), providing a complete monitoring of the system operation.

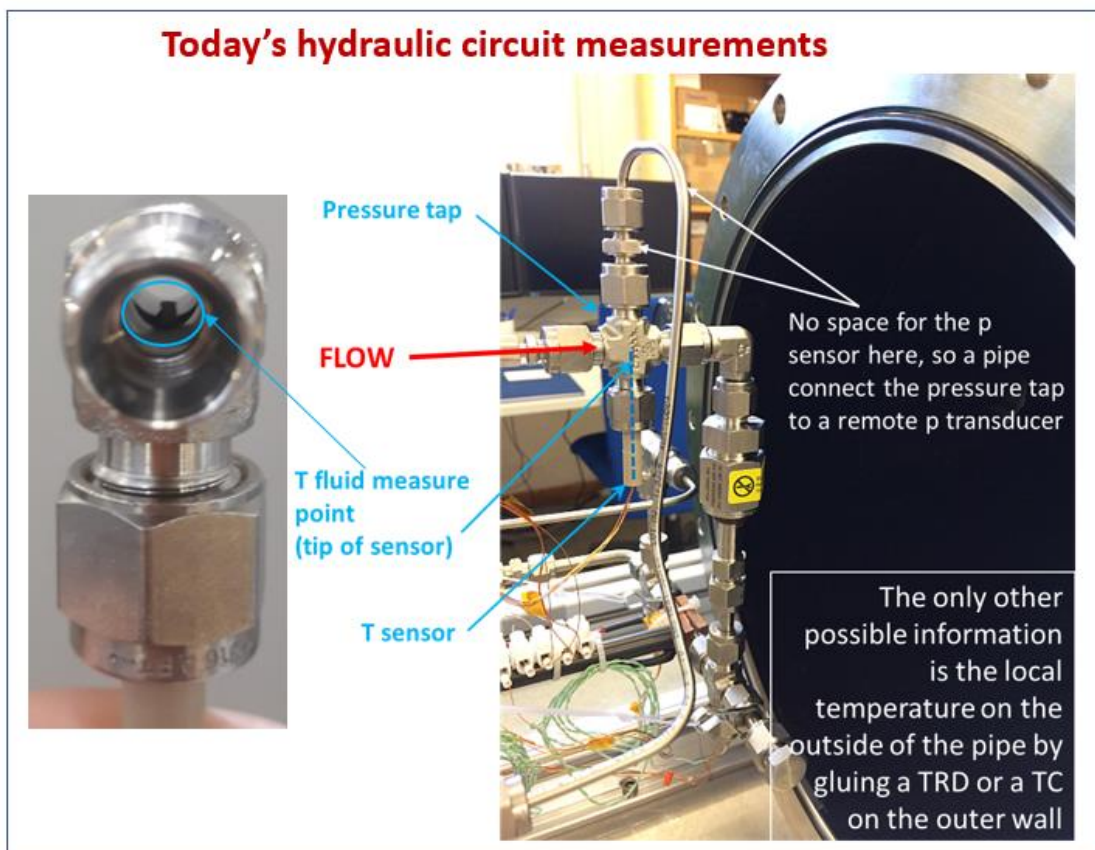
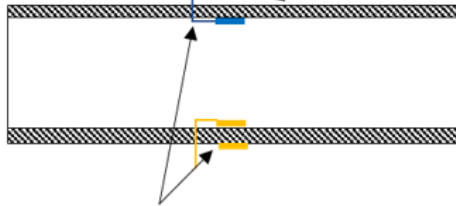


Figure 5.19. Test setup for Detector Cooling applications at CERN.

The dream for any hydraulic circuit

3D printed segment of pipe with interfaces for connectors at the ends



Ink printed Temperature and Pressure sensor inside the wall (T outside too) with electrical contacts ready outside

Figure 5.20. SWaP's technology illustration.

5.5 Applications of SWaP

The SWaP prototype can be integrated in almost any hydraulic/ piping circuit. In the first chapter one application of SWaP was presented, for the thermal management of silicon tracker detectors of CERN. However, the SWaP technology could be used not only for cooling systems but for any other piping system. Exploring other applications, we concentrate on the points, presented in following table:

	Current Prototype	Future Prototypes
Fluid	Coolant (C6F14, CO2)	Any liquid or gas
Sensor	Temperature, Pressure	Any type of sensor (pressure, flow, etc.)
Data transfer	Wired	Wired or wireless
Purpose	Cooling system	Any kind of pipe or duct

Table 5.1. Questions on how to find new applications.

Taking advantage of 3D printing technologies, SWaP can find applications in various fields due to the ability to produce on demand products that fit applications individually. The aim is either to improve existing systems or to create new smart sustainable systems while being conscience of industrial and societal challenges. Some example applications are listed below:

- Pipe segments in cooling plants with embedded measurement of refrigerant temperature, pressure, and flow rate.
- Chemical synthesis with multiple reactors.
- Fuel injection systems (monitoring pressure and temperature among multiple injectors, control of fuel pump efficiency).
- Aerospace piping systems (water, fuel, coolant).

CHAPTER 6

LABORATORY TEST SETUP

6.1 Laboratory test-setup upgrade

Testing the SWaP prototype requires a proper laboratory equipment, in order to validate the SWaP technology and to compare it with current fluid temperature sensing methods. The idea was to create a hydraulic circuit that consists of commercial temperature sensors (immersed and on the outer surface) and the SWaP prototype with embedded sensors. This circuit is then connected to a chiller that circulates the coolant and it is placed inside a vacuum chamber. First, this test setup is used for the calibration of the AJP embedded sensor for a reference temperature, recorded by the commercial immersed sensors. Afterwards, temperature measurements are recorded by the AJP sensor, in order to validate the sensor response and compare it with commercial ones.

The experimental work of the SWaP project took place in the Crystal Palace; a facility in the Fluidic Systems (FS) section of the Detector Technologies (DT) group in the Experimental Physics (EP) department at CERN. The setup in Crystal Palace was entirely upgraded, in order to meet the requirements of testing the SWaP technology. The upgrade process includes several steps that can be described as follows:

- a. Preparation of the commercial RTDs
- b. Integration of the RTDs in the hydraulic circuit
- c. Leak, pressure and safety tests
- d. Connect the RTDs to the data acquisition system
- e. Calibration of the RTDs

Each one of these steps is presented in this section.

a. Preparation of the commercial RTDs

The first step was to select the type of temperature sensor that is suitable for this application. Since, the SWaP prototype is a pipe with very small inner diameter and wall thickness, the hydraulic circuit in which the prototype is connected, it uses also pipes with similar geometry. Therefore, commercial sensors should have a small size, so that they can be

immersed and fit in the pipe. Commercial RTDs, PT100, class A, in form of small thin films (1.2 x 1.6 mm) (**Figure 6.1.a**) were selected due to their small size, and reliability and accuracy in measurements.

In order to perform four-wire measurements, soldering two wires in each end of the RTDs is mandatory. The soldered junction was then coated with a protective layer of silicon, in order to ensure electrical insulation. The length of the wires was determined, with respect to the distance between the chiller's piping system inlet and the position of the sensors in the tested hydraulic circuit. Two RTDs are attached on the outer surface of the pipe and two are integrated, as probes in the fluid stream. Further modification is required, to create probes that can be immersed in the hydraulic circuit.

A rod made of PEEK was used and machined in a way that it fits properly the hydraulic circuit. The RTDs were then integrated inside the PEEK tube and placed in a fixed position by epoxy injection (**Figure 6.1.b**). The epoxy covers totally the inner area of the PEEK tube, including the inlet and outlet of the tube but not the tip of the sensor. The required time for the epoxy curing is usually 1-2 days, depending on the type and quantity of epoxy that has been applied. This process is not driven by a machine and therefore several failures may occur, such as trapped air in the epoxy, insufficient or too much epoxy or even detachment of the wires. Furthermore, the total process requires an average time of 3-5 days, if failures does not occur. However, these probes provide an accurate and reliable method for fluid temperature sensing.

b. Integration of the RTDs in the hydraulic circuit

Once the probes and the surface sensors are completed, the next step is to integrate both types of sensors in the hydraulic circuit. The surface sensors can be easily placed and attached on the outer surface of the pipe, where modification of the piping circuit is not required. Thermal conductive paste, Kapton tape and tire-ups are the materials, used for the surface sensor attachment on a fixed position in the circuit. On the other hand, the probes should be placed inside a union (tee, cross, etc.), taking into account the immersion depth. In this case, the probes were placed inside tee unions (**Figure 6.1.c**), which were connected to the hydraulic circuit.

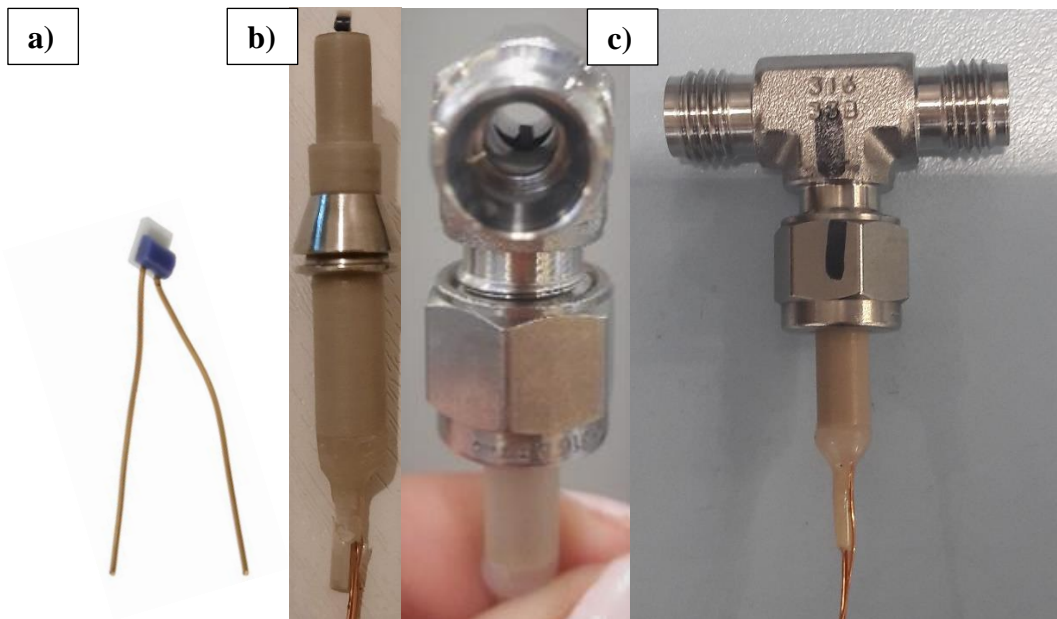


Figure 6.1. a) The PT100 RTD, used as surface and immersed sensor, b) the PT100 RTD placed at a fixed position inside the PEEK tube, and c) the temperature probe (RTD inside the tube) placed in a tee union.

c. Leak, pressure and safety tests

Before the circulation of a fluid in any hydraulic circuit, a mandatory step is the leak test. The circuit was connected to a helium leak detector (**Figure 6.2**), following the spray testing method. In this method, the circuit is connected to an evacuation line, where air is removed from the tested circuit and then helium is dispersed over the outer surface of the circuit. The detector measures the flow of helium, penetrating the part.

Another important test before fluid circulation is the pressure test, which indicates if the hydraulic circuit leaks for a maximum pressure of operation. In this test, the hydraulic circuit is filled with gas carbon dioxide (CO₂), which's pressure is adjusted via a pressure regulator. Leaks are detected by A CO₂ sniffer. However, since the probes are made in the lab and are not certified, a safety test is required. The safety test can be performed in a facility at CERN that uses specific equipment. The hydraulic circuit was tested under a maximum pressure, continuously for two hours.



Figure 6.2. Leak test: The hydraulic circuit, connected to the helium leak detector.

d. Connect the RTDs to the data acquisition system

The data acquisition system that was employed for temperature measurements, consists of NI 9219 C Series Universal Analog Input Modules by National Instruments. Since the hydraulic circuit will be tested inside a vacuum chamber, the sensors wires cannot be directly connected to the module. A feedthrough is placed on the lid of the vacuum chamber and two plugs are connected on its both sides (**Figure 6.3**). The sensors wires are soldered in the pins of a female plug, which is connected to the inner side of the feedthrough (inside the vacuum chamber). Then, wires are soldered in the corresponding pins of a male plug (outside the chamber) and are connected to the pins of the input module.

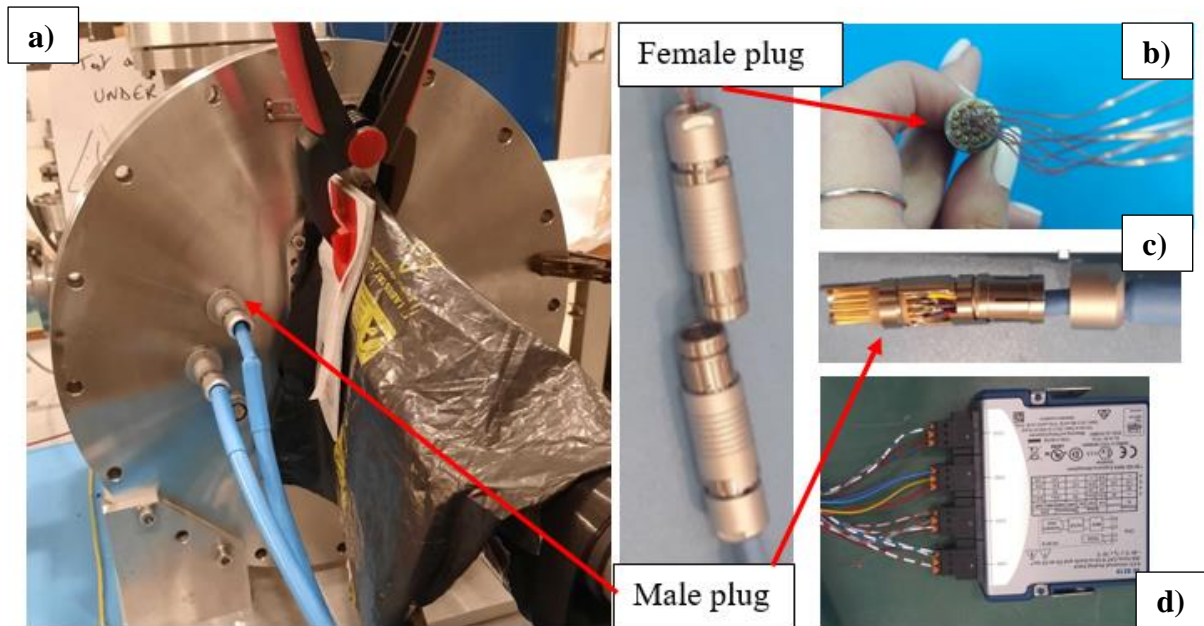


Figure 6.3. a) The male plugs connected to the feedthrough, placed in the chamber's lid, b) the sensors wires, soldered to the female plug pins, c) the module wires, soldered to the male plug pins, and d) the input module NI 9219 with the connected wires.

e. Calibration of the RTDs

The calibration procedure uses a chiller filled with a mixture of glycol and deionized water, and a reference probe by FLUKE that measures accurately the temperature. The immersed (probes) and the surface sensors were placed as close together as practical. The sensors to be calibrated should be placed in a radial pattern with the reference probe in the center of the circle (**Figure 6.4**). This ensures an equal distance from the reference probe to each of the sensors under test. Furthermore, the sensors should be on the same horizontal plane. Sufficient immersion must be achieved so that stem losses do not occur. A general rule for sufficient immersion estimates the immersion depth as 20 times the probe diameter plus the length of the sensing element [196].

The calibration performed with a ramp up, from $-25\text{ }^{\circ}\text{C}$ to $+20\text{ }^{\circ}\text{C}$ and a ramp down from $+20\text{ }^{\circ}\text{C}$ to $-25\text{ }^{\circ}\text{C}$, with a step of $5\text{ }^{\circ}\text{C}$. Data was recorded as soon as temperature was stabilized. The sample size was 120 measurements for each temperature group, with a sampling rate of 1Hz. The calibration coefficients were calculated, using the polynomial equation:

$$T(R) = a + bR + cR^2 + \dots + nR^{n+1} \quad (6.1)$$

Where T is the temperature of the reference probe, R is the resistance of the sensors to be calibrated and a, b, c are the calibration coefficients.

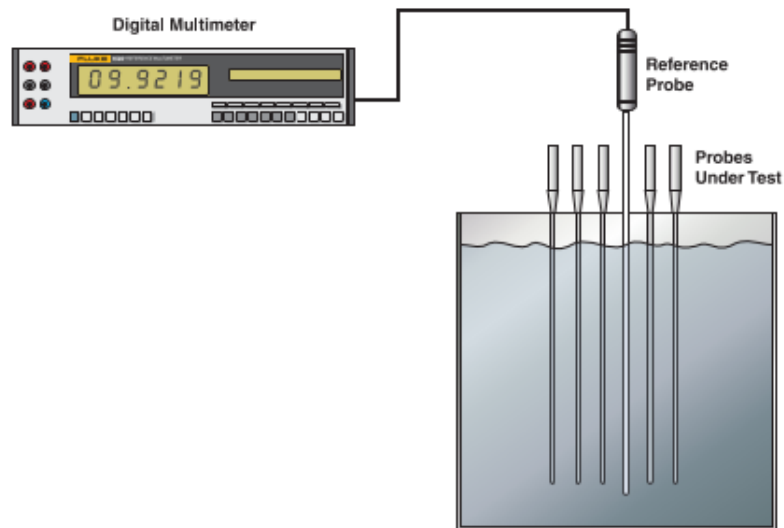


Figure 6.4. Calibration setup: Sensors under test, placed around the reference probe.

6.2 Integration of the prototype to the test setup

The previous section presents the procedure of creating a hydraulic circuit with calibrated immersed and surface temperature sensors, suitable for testing the SWaP prototype. Tests performed to ensure the tightness of the hydraulic circuit and the response of the temperature sensors. After these tests, the next step is to connect the SWaP prototype in the hydraulic circuit. A great advantage of the prototype's design is that it consists of hydraulic interfaces and electrical pins. This makes the assembly easy and fast, eliminating the need for further modifications. The pipe is simply connected to the hydraulic circuit via standard VCR nuts and metal gaskets. The AJP sensor is connected to the DAQ system via PCB connectors (**Figure 6.5.b**) with wires, following the four-wire configuration.

Since a new component is added to the circuit, before starting the circulation of the fluid in the hydraulic circuit, leak and pressure tests should be conducted. The circuit is first connected to the helium leak detector and afterwards it is filled with gas CO₂, as it was described in the previous section. The hydraulic circuit has been tested for leaks and the sensors response is tested by recording temperature. The maximum pressure of the test setup is set at 6 bars. It is advisable to test the circuit for a higher than the set pressure, which in this case was a pressure of 10 bars. Both tests resulted in extremely good, very low leak rate ($< 2 \times 10^{-10} \text{mbar} \cdot \text{L} \cdot \text{s}^{-1}$) which is within the permissible range.

Once, the procedure of assembly and testing is completed, the hydraulic circuit can be connected to the inlet and outlet pipes of a chiller and placed inside the vacuum chamber. Finally, the completed hydraulic circuit consists of the following (**Figure 6.6**):

- **TS1**: surface sensor, placed close to the inlet of the coolant, just before the probe 1
- **Probe 1**: immersed sensor, placed close to the inlet of the coolant
- **AJP sensor**: embedded in the inner wall of the SLM pipe, placed between probe1 and probe2
- **Probe 2**: immersed sensor, placed after the AJP sensor
- **TS2**: surface sensor, placed just after the probe 2

The test setup, in which the hydraulic is connected is illustrated in **Figure 6.7** and it consists of the following:

- Vacuum pump
- Booster
- Chiller
- Flowmeter
- DAQ system
- Computer

Before starting with any test, the first step is to turn on the vacuum pump. The pressure inside the vacuum chamber is displayed via a pressure gauge. As soon as the pressure reaches an order of magnitude of 10^{-2} bars, the booster can start operating. If the pressure is higher or close to atmospheric, it indicates that there is a leak in the circuit and the test should stop immediately, in order to check and detect the leak. The booster is a more powerful pump that accelerates the process of reducing the pressure inside the chamber. When the pressure is stabilized within the value range of 10^{-4} to 10^{-5} bar, the circulation of the fluid can begin. The mass flow can be adjusted by the flow-mass meter, which is connected in the inlet pipe of the chiller. Consequently, the fluid pressure changes with variations in the mass flow. The fluid pressure increases for higher mass flow and decreases for lower. The fluid temperature is recorder by the DAQ system, which transfers the sensors signals via USB plug to a computer. The computer communicates with the DAQ system by the LabVIEW software. The programming in LabVIEW, provides measurements with various sampling rates and sizes. Finally, data can be recorded and saved in the computer as typical file formats (ASCII, Excel, etc.).

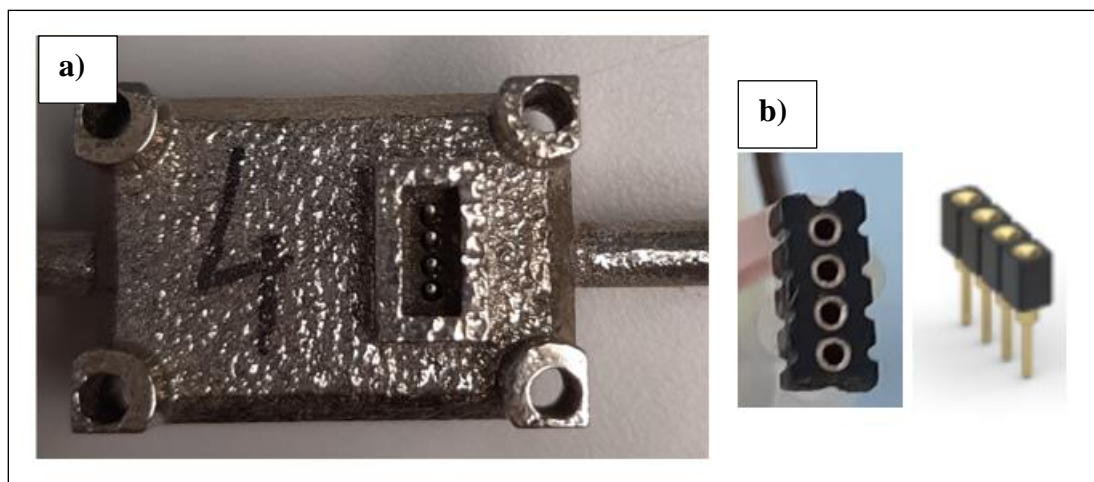


Figure 6.5. a) The 3D printed electrical pins and b) the PCB connector that can be plugged on the pins.

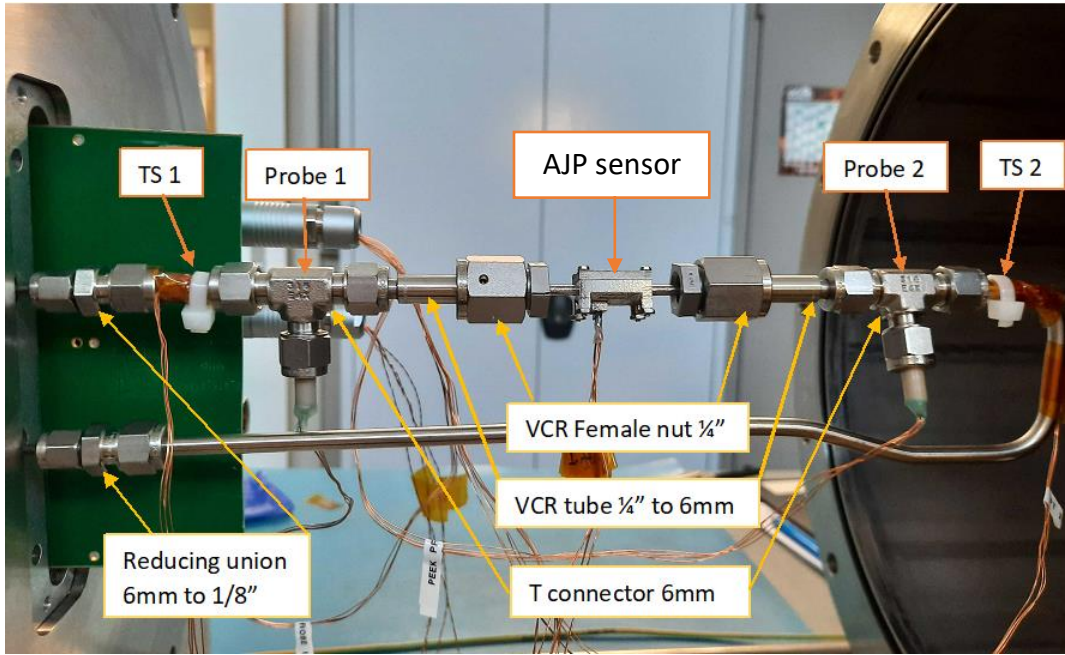


Figure 6.6. The hydraulic circuit with the SWaP prototype.

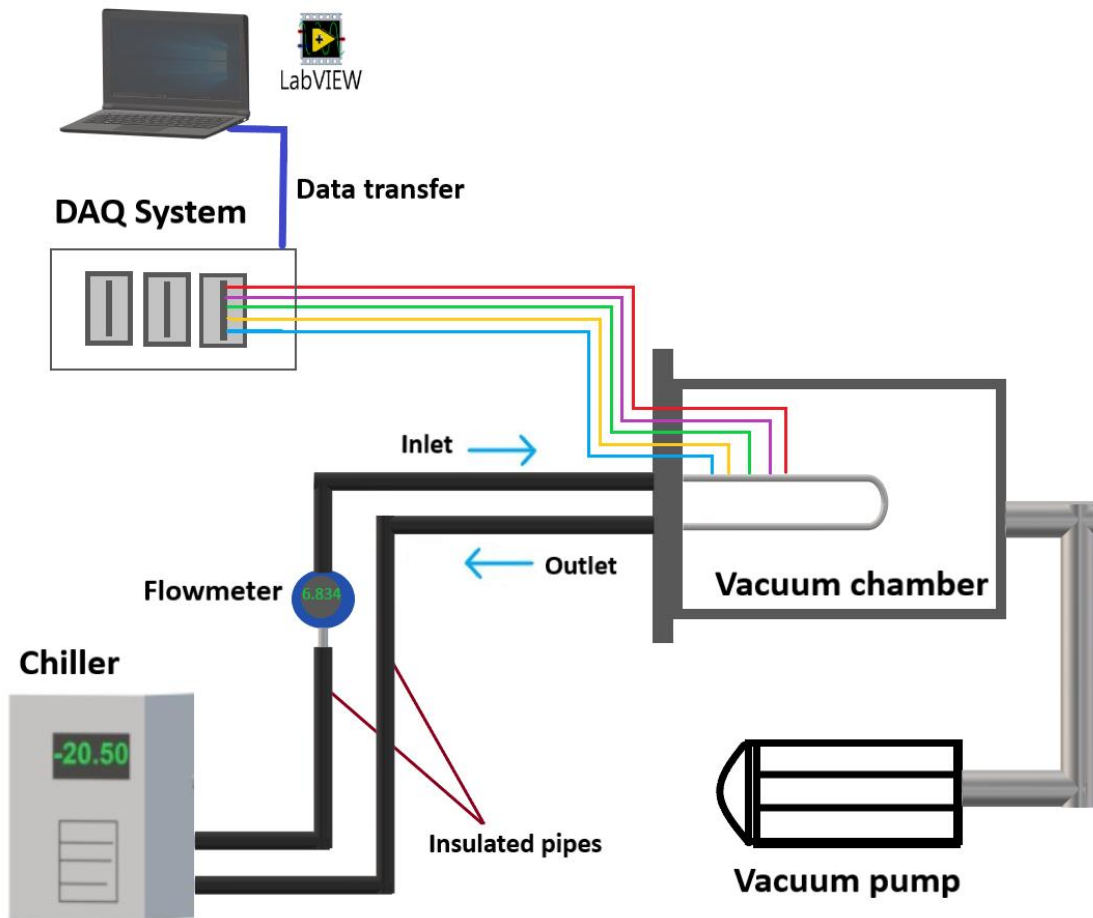


Figure 6.7. The test setup of the hydraulic circuit.

6.3 Calibration of the AJP sensor

The calibration process was performed under vacuum. The C6F14 coolant enters the hydraulic circuit, when the fluid temperature was the same as room temperature (+18°C). Then the temperature is decreased until it reaches the value of approximately -20°C, which is followed by a warm up at 5°C. The PT100 RTDs measure the fluid temperature before and after the AJP sensor, while the resistance of the AJP sensor is recorded for each temperature measurement (**Figure 6.8**). The mass flow rate was set at 8.15 *gr/s* and the fluid pressure at 2.83 *bar*. Data was recorded for approximately 1 hour with a sampling rate of 0.1Hz.

The temperature measurements are presented in **Figure 6.9**. It is observed that there are some temperature variations among the sensors for the minimum and relatively constant temperature of approximately -20°C. The temperature difference between the immersed probes is less than 0.3°C and could be caused due to their different position in the hydraulic circuit. The probe 1 is closer to the inlet of the chiller and detects faster the maximum negative temperature. However, the temperature difference between the probe 1 and the TS1 is very high, almost 1.3°C. A possible explanation is that the surface sensor has been moved and it is not completely attached to the pipe surface. This means that this gap between the two surfaces, causes readout errors. On the other hand, the TS2 presents a lower temperature difference with the probe 2.

The obtained calibration curve line of the AJP sensor with the corresponding Positive Temperature Coefficients (PTCs) is presented in **Figure 6.10**. The calibration coefficients calculated by applying a linear equation to the acquired temperature-resistance data.

$$T (R) = a + bR$$

Where T is the reference temperature (mean value of Probe 1 and Probe 2), R the resistance of AJP sensor and a , b the linear calibration coefficients.

The AJP patterned sensor presents a linear behavior. The common for most of the sensor's effect of hysteresis is illustrated for a data area inside the main plot. The low hysteresis of the AJP patterned RTDs indicates that the sensor could provide reliable measurements.

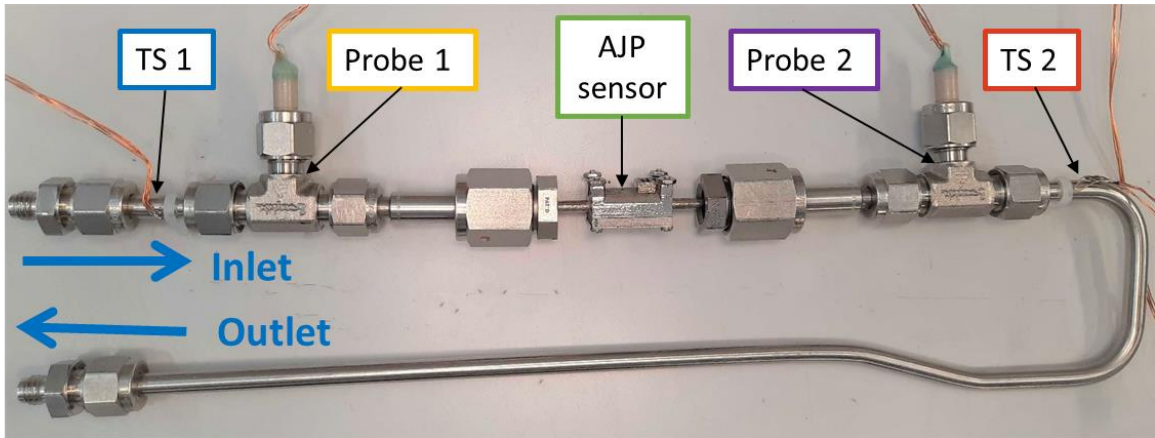


Figure 6.8. The position of the temperature sensors in the hydraulic circuit.

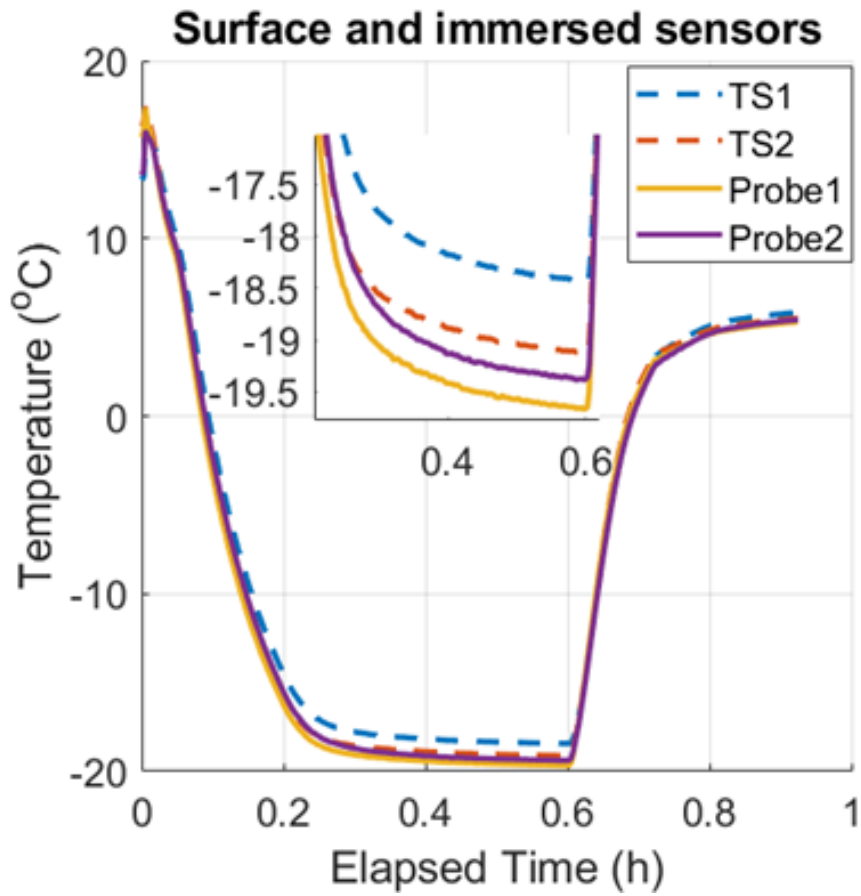


Figure 6.9. Temperature measurements with immersed and surface sensors.

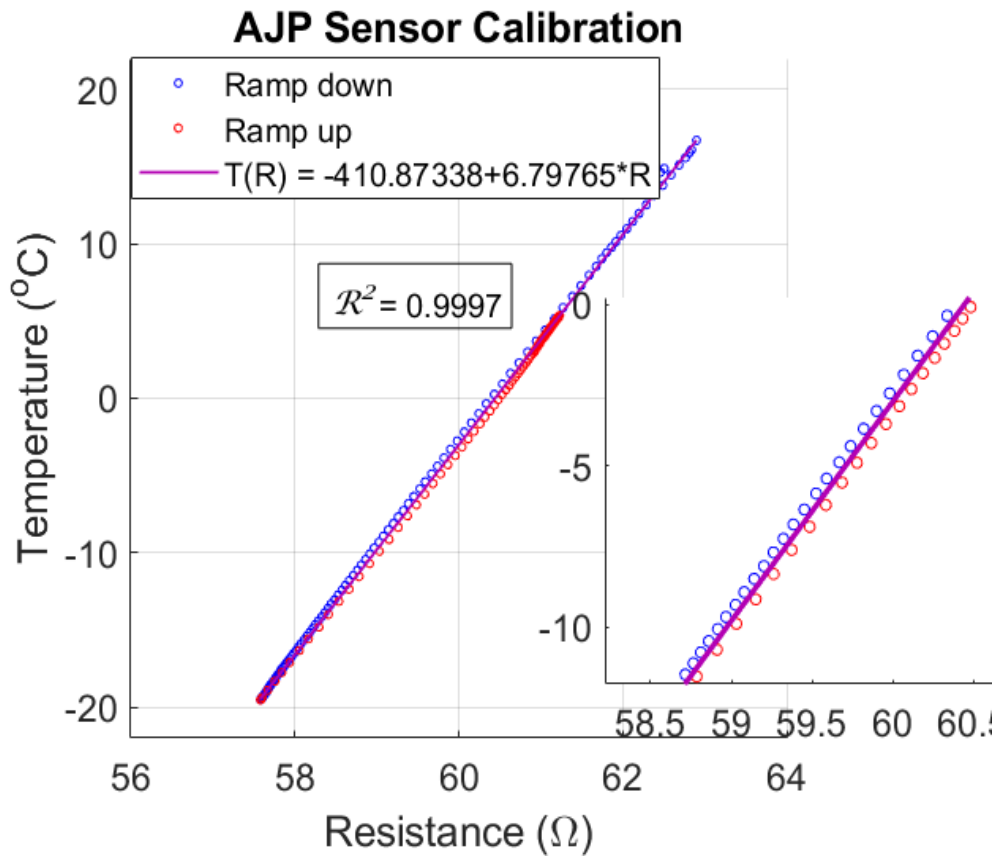


Figure 6.10. The linear response and PTC of the AJP sensor.

CHAPTER 7

EVALUATION OF THE SWaP PROTOTYPE SENSOR

7.1 Tests under vacuum

The aim of these tests is to evaluate the 3D printed patterned sensor, produced via Aerosol Jet Printing (AJP) and compare it with the commercial PT100 RRDs (immersed and surface sensors). Initially, the sensor is tested under vacuum, in order to observe its behavior under controlled conditions, in which the sensor is not affected by heat losses, as in environmental conditions. Therefore, first it is essential to ensure that the sensor has a repeated behavior under different tests. Afterwards, we can examine if and how much the sensor is affected, when it is exposed to real conditions.

The aim of the first test is to estimate the sensor's precision, by testing the sensor in different temperature groups. The second test performed for a constant temperature with the first execution at 1Hz and the second at 100Hz. The noise of the AJP sensor can be calculated and compared it with the commercial sensors noise. The last test, examines the AJP sensor response under fast and repeated temperature changes. The results of the above tests are presented in this section, including all the corresponding plots.

7.1.1 TEST 1: Temperature Groups

The first test performed under vacuum for seven temperature groups of constant temperature. The data recording starts, as soon as the temperature is stabilized. Data was recorded with a sampling rate of 1Hz for a sample size of 120 measurements per temperature group. Then, the mean temperature value of each group is calculated and plotted on a temperature-time graph (**Figure 7.1** and **Figure 7.2**). The purpose of this test is to evaluate the sensor's precision. The precision of a sensor is calculated as follows:

- Calculation of the mean of the measured values
- Calculation of the standard deviation
- The result reports as mean \pm standard deviation

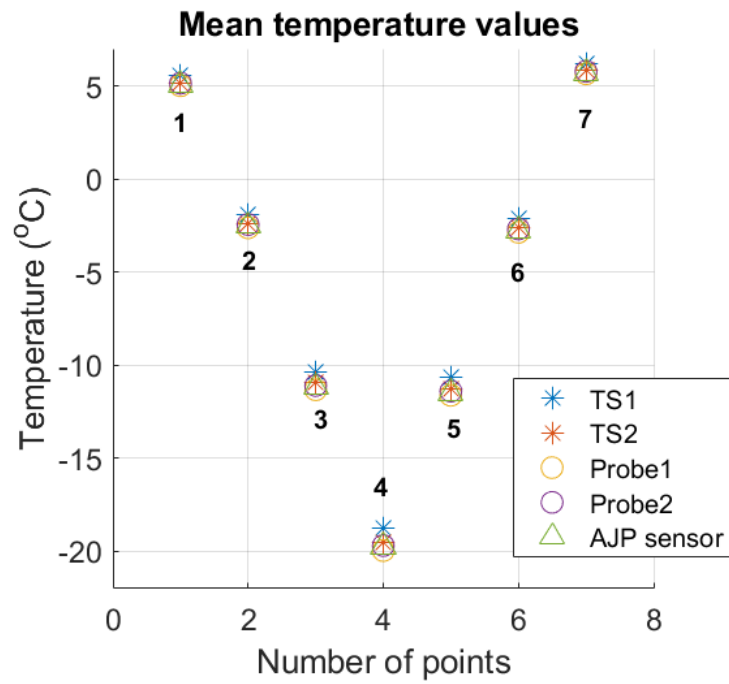


Figure 7.1. Mean value of temperature for each group.

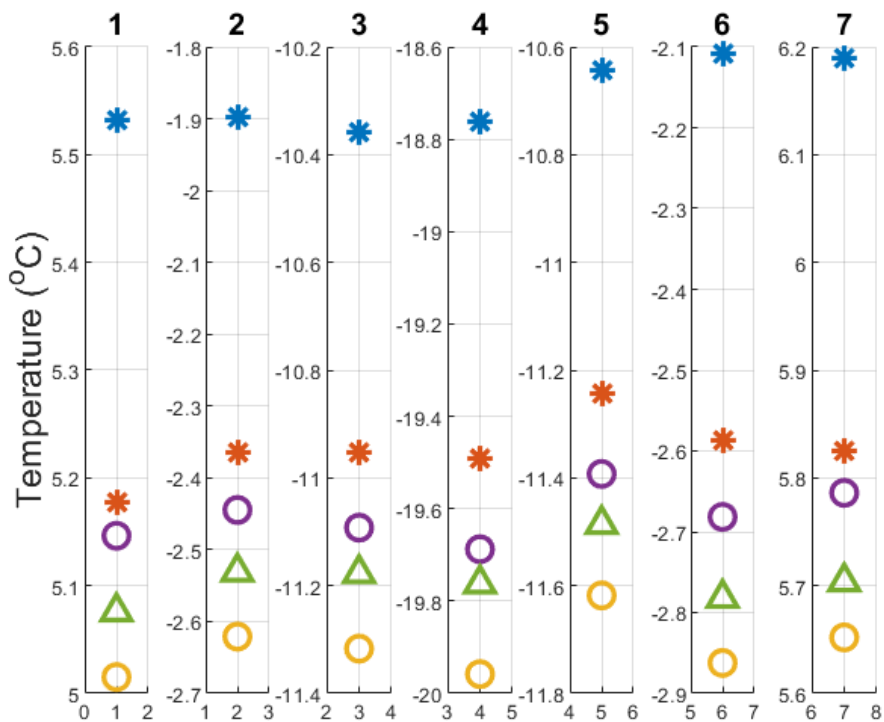
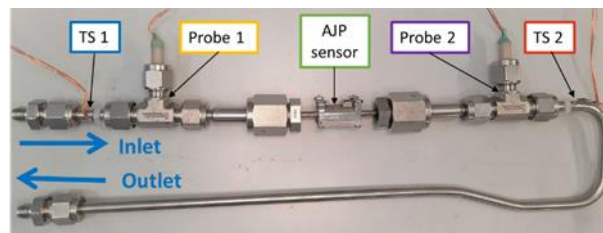


Figure 7.2. Mean value of temperature for each group (zoom).

Temperature differences are observed among the sensors and are presented in **Table 7.1**. The temperature values of the AJP lie almost between the values of the immersed sensors. However, as the temperature drops and reaches the maximum negative value, the AJP sensor temperature measurement is getting closer to the probe 2. The temperature difference between the immersed sensors is low and quite constant but it also increases for lower temperatures. The TS1 presents again the highest temperature with probe 1. This could happen, due to some kind of detachment of the surface pipe. The TS2 values are close to the values of probe 2.

In general, the minimum temperature difference is observed between the AJP sensor and the immersed probes. The maximum difference is the one between the TS1 surface sensor and the probe 1. All the sensors tend to increase the temperature difference among them for lower temperature ranges.

ΔT	1	2	3	4	5	6	7
TS1 – Probe1	0.517	0.723	0.958	1.197	0.974	0.754	0.537
TS2 – Probe2	0.032	0.079	0.138	0.195	0.148	0.094	0.038
Probe1 – Probe2	-0.131	-0.176	-0.225	-0.270	-0.225	-0.181	-0.134
AJP – Probe1	0.061	0.09	0.140	0.196	0.132	0.080	0.052
AJP – Probe2	-0.070	-0.086	-0.085	-0.075	-0.093	-0.101	-0.082

Table 7.1. Temperature differences.

The precision of each sensor for each temperature group is presented in **Table 7.2**. The precision of PT100s has an order of magnitude of about 10^{-3} degrees, while the precision of AJP has an order of 10^{-2} degrees.

	AJP Sensor	
1	5.08	± 0.0141
2	-2.53	± 0.0137
3	-11.18	± 0.0173
4	-19.76	± 0.0151
5	-11.49	± 0.0162
6	-2.78	± 0.0145
7	5.70	± 0.0125

Table 7.2. Precision of each sensor for each temperature group.

	TS 1	TS 2	Probe 1	Probe 2
1	5.53 ± 0.0046	5.18 ± 0.0050	5.02 ± 0.0047	5.146 ± 0.0049
2	-1.90 ± 0.0059	-2.37 ± 0.0060	-2.62 ± 0.0063	-2.45 ± 0.0061
3	-10.36 ± 0.0093	-10.95 ± 0.0114	-11.31 ± 0.0128	-11.09 ± 0.0107
4	-18.76 ± 0.0053	-19.49 ± 0.0049	-19.96 ± 0.0070	-19.69 ± 0.0064
5	-10.64 ± 0.0074	-11.25 ± 0.0085	-11.62 ± 0.0098	-11.39 ± 0.0086
6	-2.11 ± 0.0051	-2.59 ± 0.0055	-2.86 ± 0.0058	-2.68 ± 0.0055
7	6.19 ± 0.0056	5.82 ± 0.0051	5.65 ± 0.0055	5.79 ± 0.0052

Table 7.2. Precision of each sensor for each temperature group.

7.1.2 TEST 2: Constant Temperature

Testing the temperature sensors at constant temperature aims at observing the sensor's response with respect to time (drift, noise). Two types of tests were performed, both under vacuum at constant temperature, mass flow rate and pressure of the coolant (C6F14). In the first execution, data was recorded for 10 hours with a sampling rate of 1Hz. A new set of data recorded with a different sampling rate of 100Hz for 15mins, in the second execution. The results of both tests are presented below.

A. Long duration test (1Hz, 10h)

In the long duration test, the temperature is stabilized at around +12°C and data was recorded with a sampling rate of 1Hz, for a sample size of 3615 measurements for 10 hours. The general plot for a duration of 10 hours (**Figure 7.3**) shows that the sensors have a very similar response with constant temperature differences. However, it is noted that the temperature is not absolutely constant for the entire period of time but it is slightly increased. In order to take a closer look to the sensors behavior, the period of time is separated in shorter periods of 1 or 2 hours.

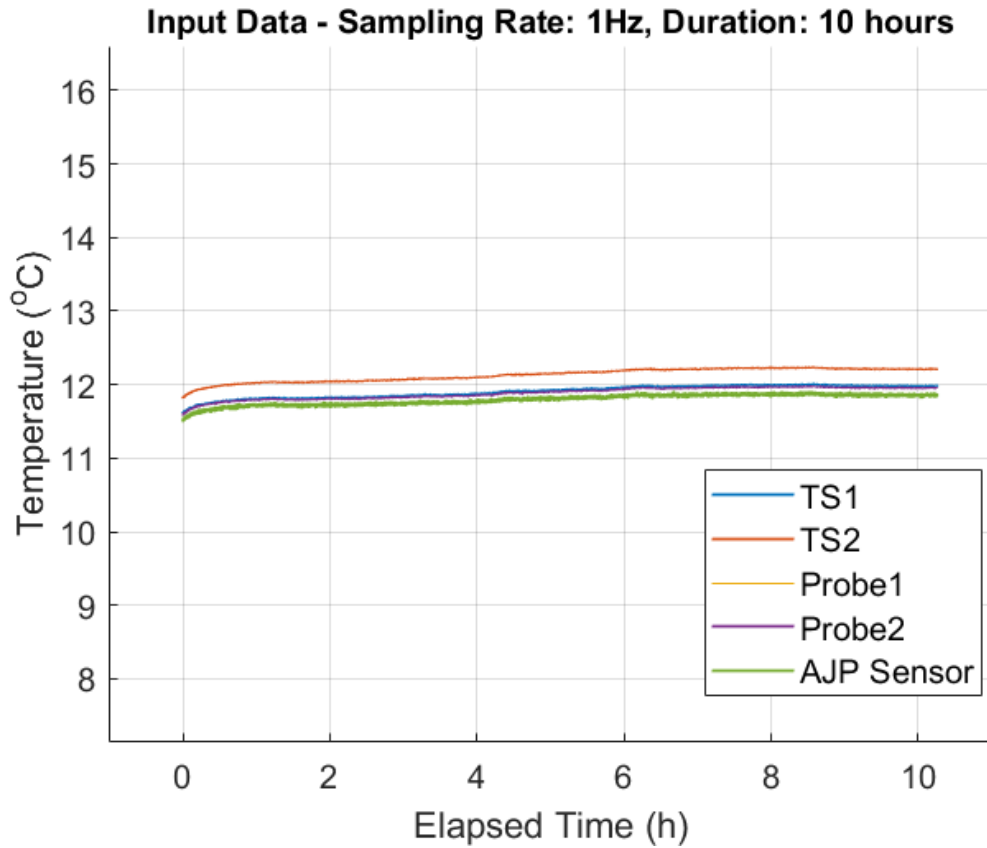


Figure 7.3. Long duration test for 10 hours

The plot in **Figure 7.4** represents the data acquired within the last hour of the test (from 9th to 10th). This time period was selected, due to the fact that at this moment the temperature was very stable. First, we observe that the AJP sensor is noisier than the commercial PT100s, which's noise is identical. Second, the temperature difference among the sensors, is higher for the surface sensor TS2 and is lower for the AJP sensor, which's value is very close to probe 1.

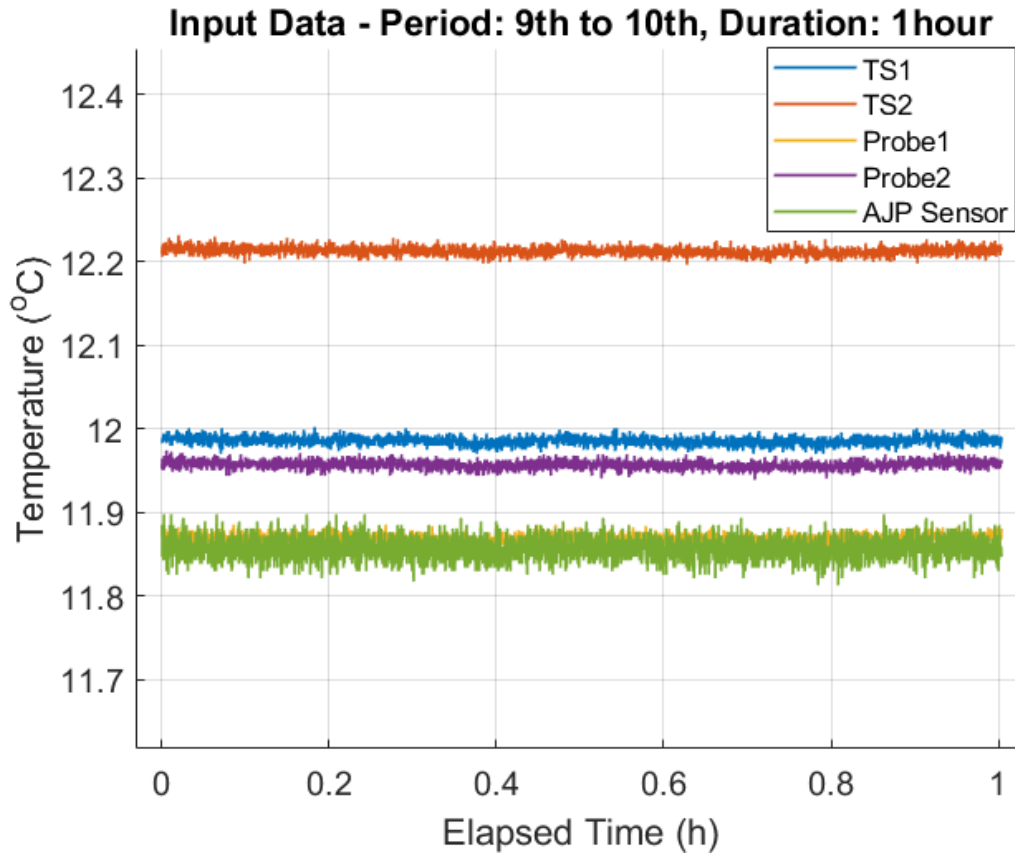
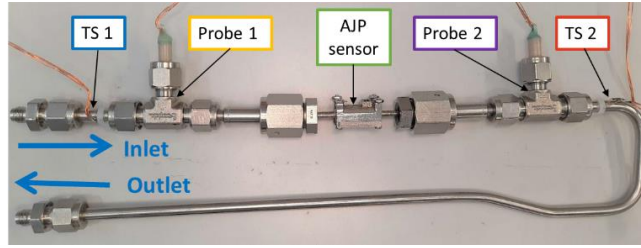


Figure 7.4. Constant temperature within the last one hour of the test

In order to estimate the sensors noise, the first step is to ensure that the fluid temperature was really constant for the selected period of time. The rate of temperature change can be calculated by the polynomial equation. The coefficient of t indicates the rate of temperature change with time. When this coefficient is close to zero, it means that the temperature is constant. The following equation, presents the temperature stability of the AJP sensor. This equation was applied for all the sensors, which have also constant temperature.

$$T(t) = 11.857 - 0.000655t \tag{7.1}$$

Once, the temperature is constant, the next step is the statistical process of the raw data. We assume that the data are normally distributed. However, there are few factors that ensure the normal distribution. These are the characteristic bell curve, the Skewness and Kurtosis. First the data was plotted in a form of histogram, which creates the characteristic bell curve of the normal distribution (**Figure 7.5**). Then, Skewness and Kurtosis were calculated by MATLAB functions, proving also a normal distribution.

Skewness measures the symmetry of the distributed data [197]:

- A positively skewed distribution has scores clustered to the left, with the tail extending to the right.
- A negatively skewed distribution has scores clustered to the right, with the tail extending to the left.
- Skewness is 0 in a normal distribution, so the farther away from 0, the more non-normal the distribution.

Kurtosis is a measure of how outlier-prone a distribution is [198]:

- The kurtosis of the normal distribution is 3.
- Distributions that are more outlier-prone than the normal distribution have kurtosis greater than 3.
- Distributions that are less outlier-prone have kurtosis less than 3.

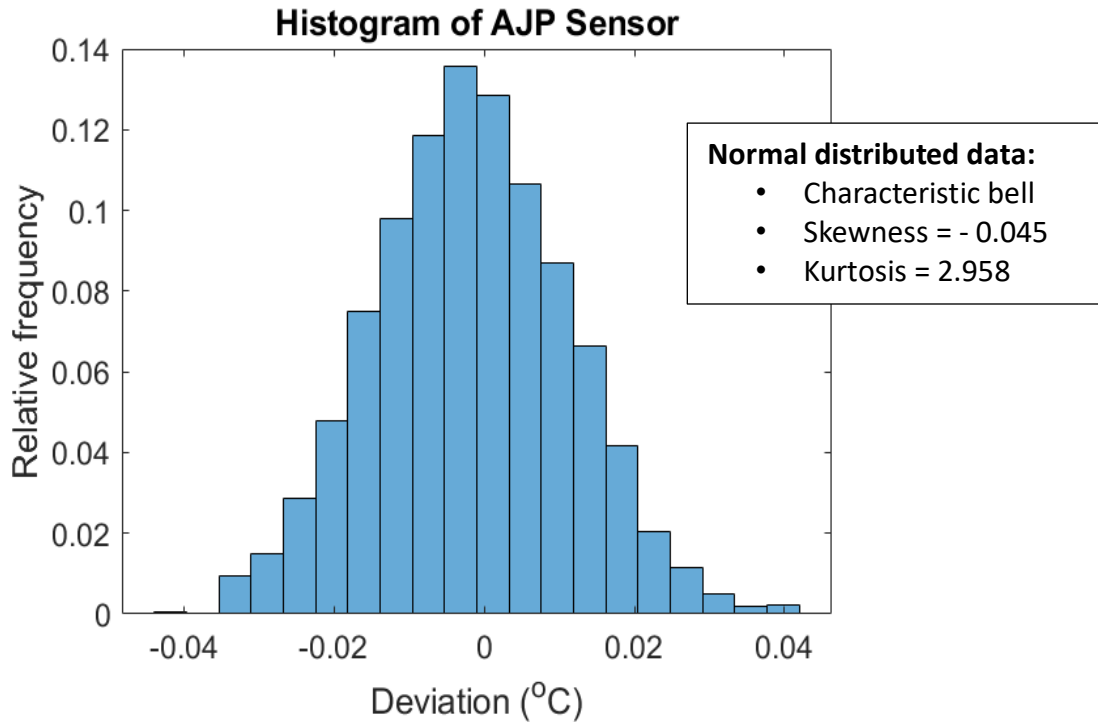


Figure 7.5. Normally distributed temperature data.

In order to measure the degree of uncertainty or certainty of the test sampling method, we take into account the confidence interval. The following table (**Table 7.3**) presents the mean value, the standard deviation and the confidence level of the AJP sensor temperature measurements.

<i>Sample Size (n)</i>	3615
<i>Sample Mean (μ)</i>	11.856744
<i>Population Stdv (σ)</i>	0.0128532
<i>Conf Level (1-a)</i>	0.95
<i>Significance Level (a)</i>	0.05

Table 7.3. Normal distribution parameters.

95% Confidence Interval: 11.856744 ± 0.000419 or $11.8563 \leq \mu \leq 11.8572$

Finally, the noise of the AJP sensor can be calculated as follows:

$$noise = \pm 3\sigma = \pm 0.038560 \quad (7.2)$$

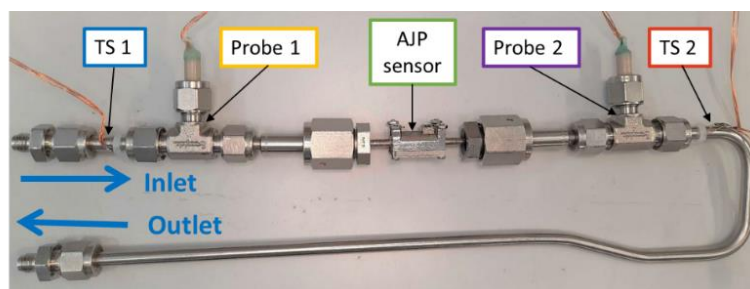
The temperature stability, the distribution of the data, and the certainty of the test sampling method were evaluated for each one the sensors. The results proved that all the sensors recorded a constant temperature, and the data was normally distributed. The noise of each sensor is presented in **Table 7.4**. It is observed that the AJP sensor noise is 2.6 times greater than the PT100s noise. However, the noise can be reduced by optimized ink deposition in the Aerosol Jet Printing process.

	μ	σ	<i>95% Confidence Interval</i>	<i>Noise</i>
TS1	11.986	0.00497	11.985628 \pm 0.000159	\pm 0.014660
TS2	12.213	0.00494	12.212703 \pm 0.000161	\pm 0.0148098
Probe 1	11.869	0.00496	11.869092 \pm 0.000162	\pm 0.0148740
Probe 2	11.957	0.00490	11.957054 \pm 0.000160	\pm 0.0147062
AJP Sensor	11.857	0.01285	11.856744 \pm 0.000419	\pm 0.0385600

Table 7.4. Normal distributed parameters and sensors noise.

B. Short duration test (100Hz, 15min)

In the long duration test, the temperature is stabilized at around +12°C and data was recorded with a sampling rate of 100Hz and with a sample size of 43829 measurements for 15 minutes. The general plot for a duration of 15 minutes (**Figure 7.6**) shows that the sensors have a very similar response with constant temperature differences. In order to ensure that the temperature was constant and the data is normally distributed (**Figure 7.7**), the previous process is applied in this set of data. The level of certainty of the test sample, as well as the noise of each sensor are presented in **Table 7.5**.



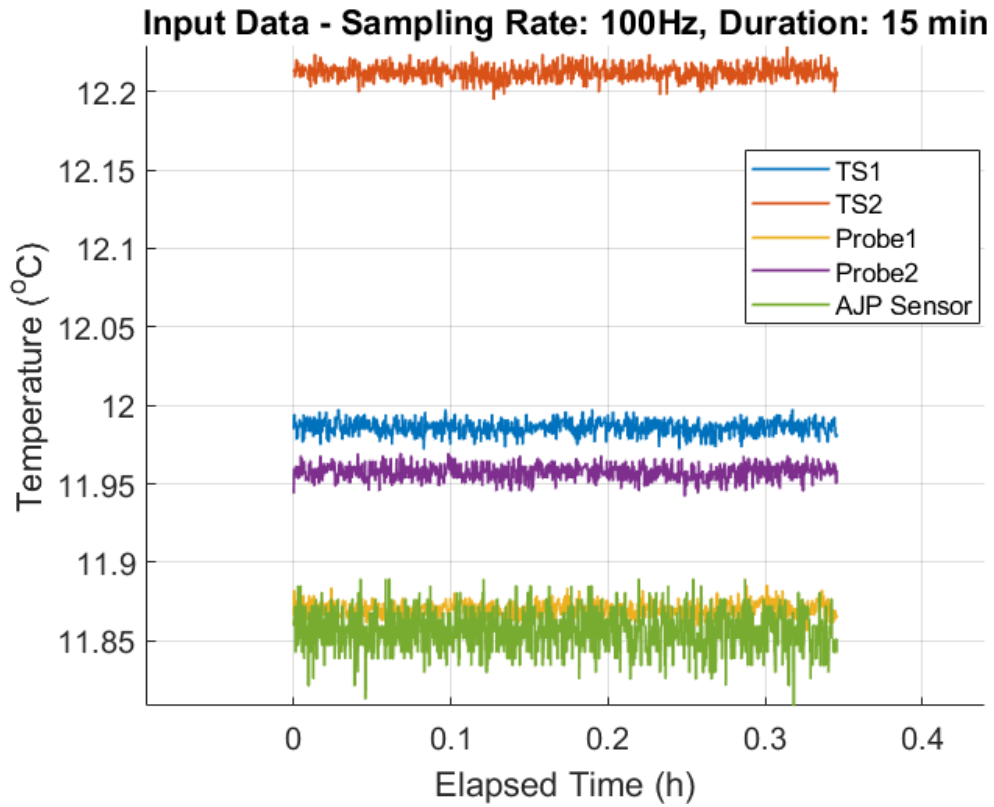


Figure 7.6. Constant temperature, recorder for 15min.

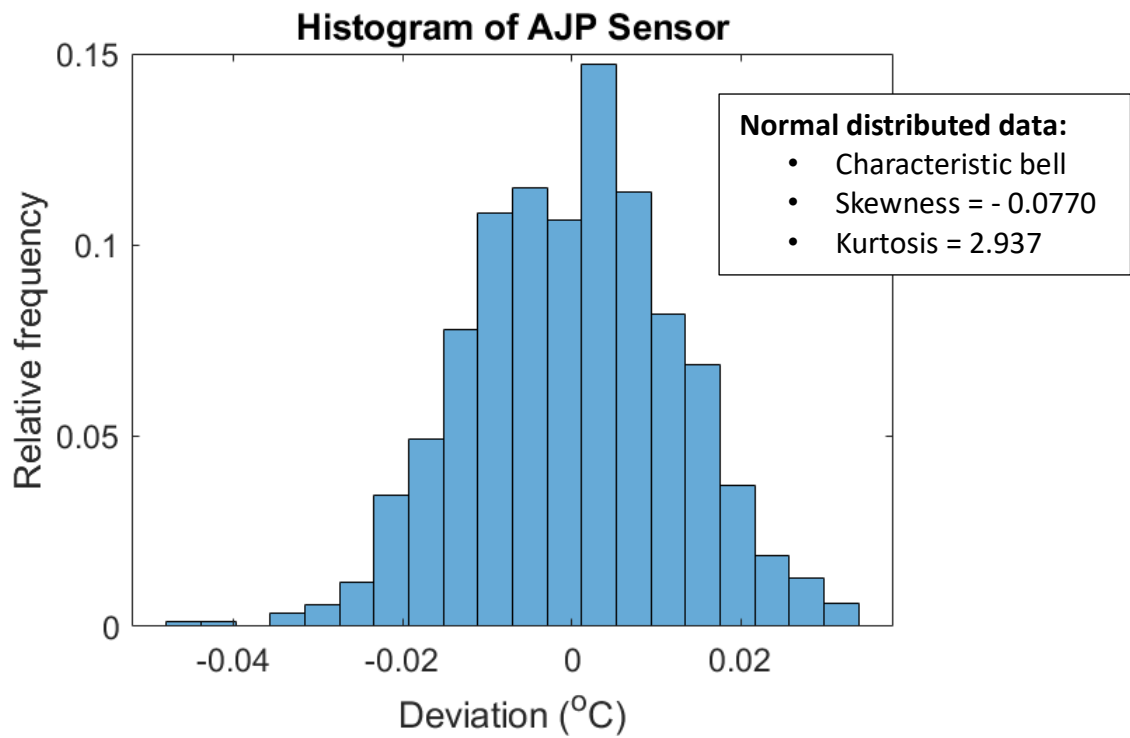


Figure 7.7. Normally distributed temperature data.

	μ	σ	<i>95% Confidence Interval</i>	<i>Noise</i>
TS1	11.986	0.00437	11.985784 \pm 0.000041	\pm 0.013132
TS2	12.212	0.00470	12.212088 \pm 0.000044	\pm 0.013132
Probe 1	11.870	0.00467	11.869869 \pm 0.000044	\pm 0.014009
Probe 2	11.957	0.00481	11.957285 \pm 0.000045	\pm 0.014430
AJP Sensor	11.856	0.01280	11.856382 \pm 0.000120	\pm 0.038396

Table 7.5. Normal distributed parameters and sensors noise.

Although, the frequency of the sampling rate increased from 1Hz to 100Hz, the noise for all the sensors is constant and variations are not observed.

7.1.3 TEST 3: Fast Cycling

The last test performed for repeated temperature changes. In the beginning of each cycle the temperature has a value of around +6°C, which is decreased as fast as possible, to reach the temperature of -23°C, followed by a fast warm up to +6°C. This process of fast cooling-heating is executed continuously with a sampling rate of 0.1Hz and it is repeated for five cycles (**Figure 7.8**). The aim is to testify if the AJP sensor response is affected from quick and repeated temperature changes.

The sensors have a constant response and they follow the fast temperature changes in a very similar way, as it is presented in **Figure 7.8**. However, it is essential to observe closer their response, at both extreme temperatures, as it shown in **Figure 7.9**. and **Figure 7.10**. In the warmer temperatures, the sensors have a constant response for each cycle and the temperature difference between them is stable. The AJP sensor value is very close to the one of the immersed sensors (almost between them), while the surface sensor TS1 has the maximum temperature difference with the probe 1. In addition, the sensors have similar response for the coldest temperatures.

The AJP sensor has a linear response, similar with the commercial RTDs, for fast and repeated temperature changes. This means that the 3D printed sensor is capable of detecting temperature in more extreme conditions, providing reliable measurements.

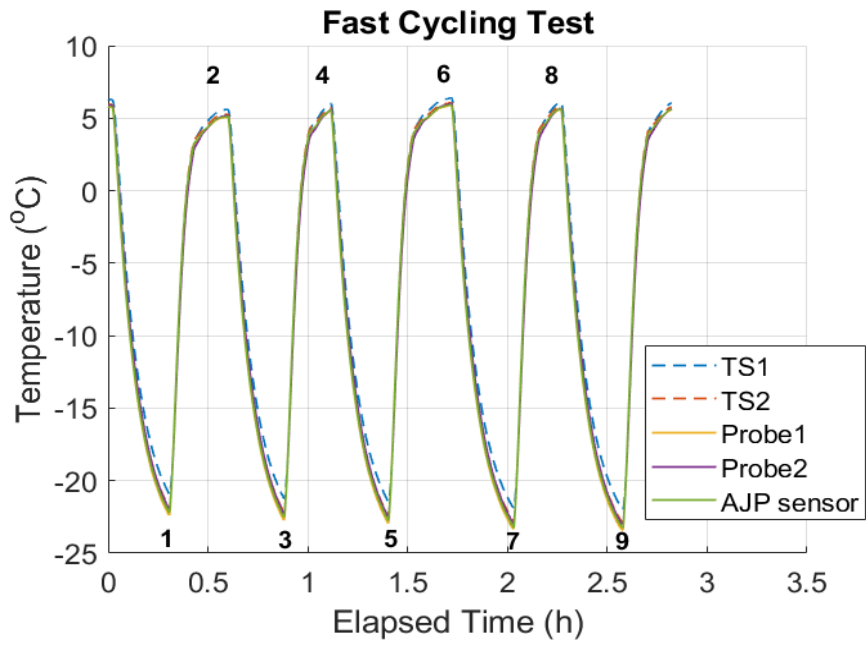


Figure 7.8. The fast heating – cooling process.

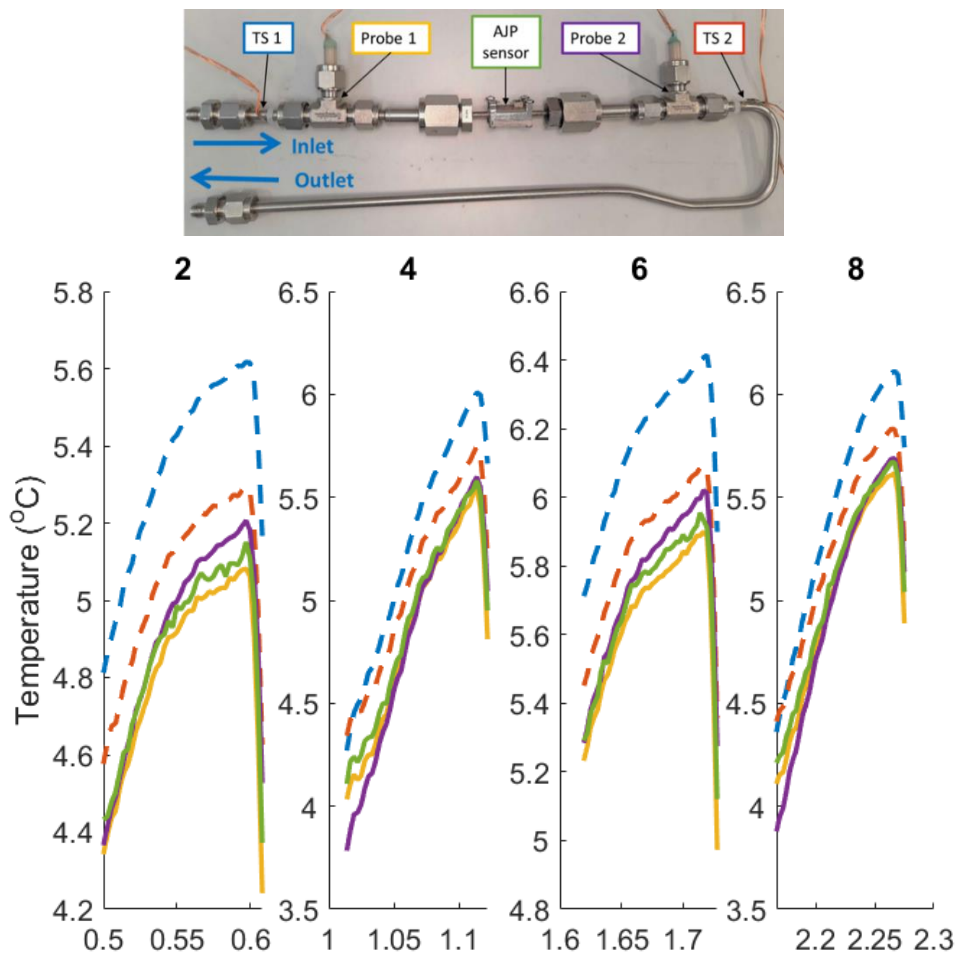


Figure 7.9. Sensors response after fast heating for each cycle.

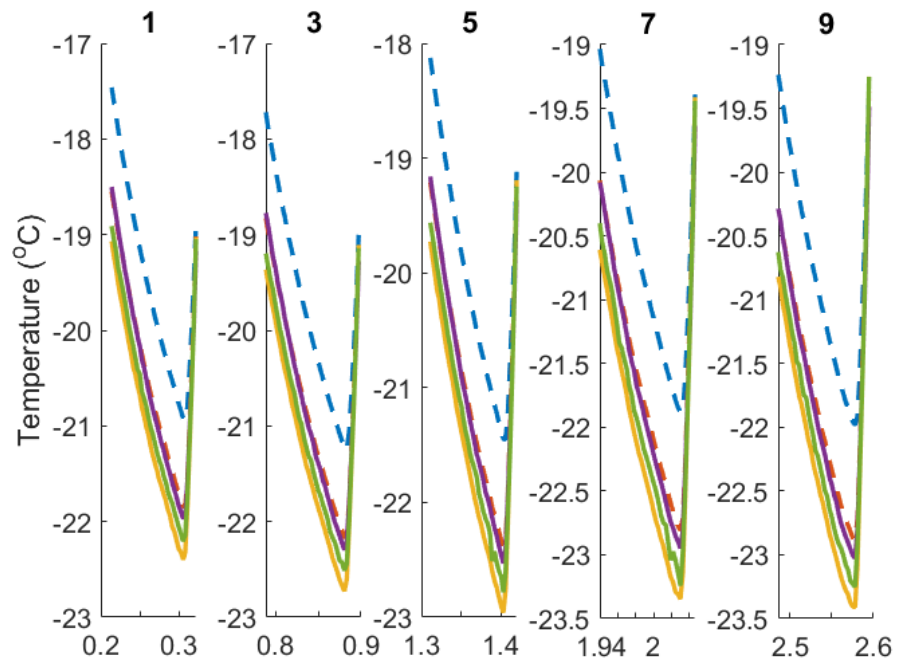


Figure 7.10. Sensors response after cooling for each cycle.

7.2 Tests under real conditions

Tests under real conditions are essential, to define if the AJP sensor can be efficient under uncontrolled and not only laboratory conditions. In real conditions the temperature and the pressure are not controlled. This is particularly important, in terms of environmental temperature, which could affect the fluid temperature reading, due to energy losses.

These tests were executed in two ways. In the first execution the hydraulic circuit was insulated, sandwiched in 30 mm thick foam insulation. Two metal plates used to compress the insulation plates, so that no air passes through the circuit and the system is fully insulated (**Figure 7.11**). This approach is applied for any cooling system in real-world applications. However, the second test executed without insulation (**Figure 7.12**), in order to observe potential heat influence on both types of sensors, the 3D printed as well as the commercial ones.

In both cases, two types of tests performed. The first test performed for one cycle, starting from room temperature, going down to $-22\text{ }^{\circ}\text{C}$ (a pause for approximately 15min) and going up again to a positive temperature of $+8\text{ }^{\circ}\text{C}$. The second test performed for repeated temperature changes. Each cycle starts in a positive temperature (around $+5\text{ }^{\circ}\text{C}$), goes down to a minimum temperature (around $-22\text{ }^{\circ}\text{C}$) as fast as possible and returns to the same positive temperature. Each cycle is repeated five times (non-stop) and the aim is to test the sensor's response under repeated temperature changes.

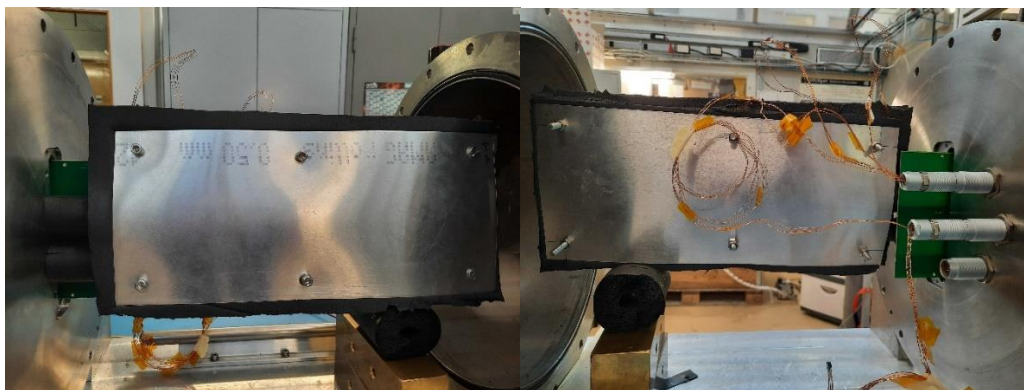


Figure 7.11. The hydraulic circuit, sandwiched in in 30 mm thick foam insulation.

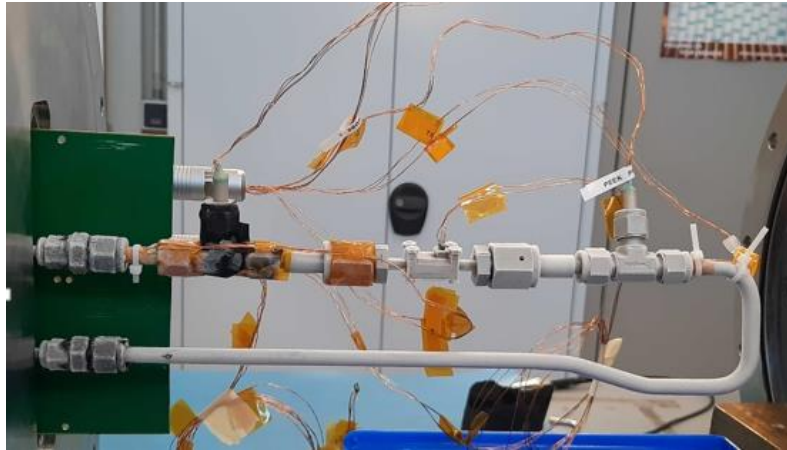


Figure 7.12. The uninsulated hydraulic circuit with ice on the surface.

7.2.1 Insulated test section

The first test performed with a sampling rate of 0.1 Hz for approximately 2 hours (**Figure 7.13**). Temperature differences are observed among the sensors and are presented in **Table 7.6**. The temperature values of the AJP lie almost between the values of the immersed sensors. However, as the temperature increases, the AJP sensor temperature is getting closer to the probe 1. The temperature difference between the immersed sensors is low and quite constant. The TS1 presents again the highest temperature difference with probe 1. This could happen, due to some kind of detachment of the surface pipe. The TS2 values are very close to the values of probe 2. In general, the minimum temperature difference is observed between the AJP sensor and the immersed probes. The maximum difference is the one between the TS1 surface sensor and the probe2.

ΔT	at -22 °C	at 8 °C
TS1 – Probe1	1.08	0.36
TS2 – Probe2	-0.12	-0.10
Probe1 – Probe2	-0.39	-0.14
AJP – Probe1	0.15	0.03
AJP – Probe2	-0.25	-0.12

Table 7.6. Temperature differences among the sensors of the *insulated* hydraulic circuit.

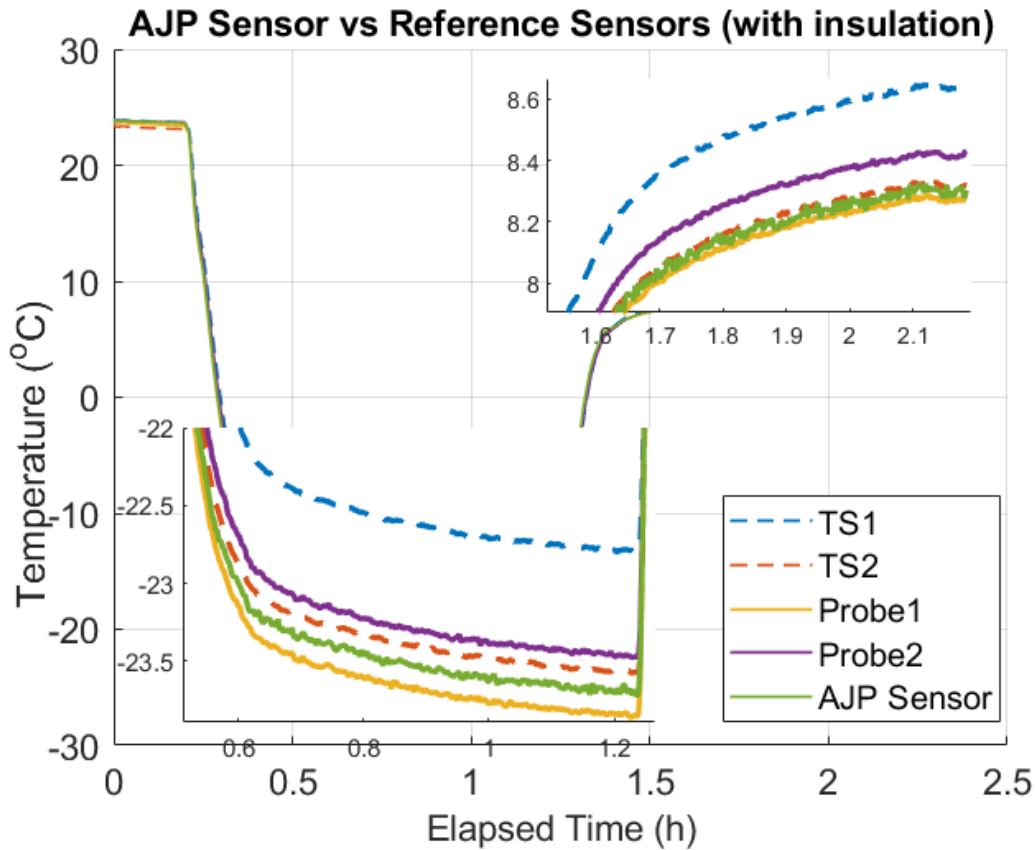
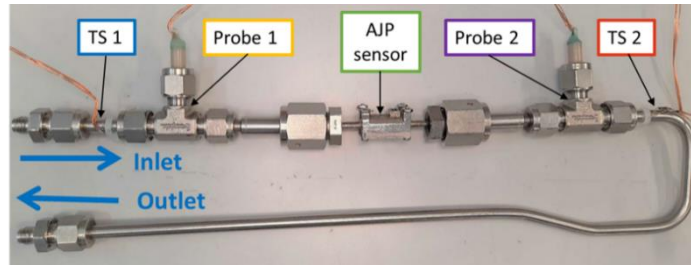


Figure 7.13. The sensors temperature response for the *insulated* hydraulic circuit.

The fast-cycling test performed with a sampling rate of 0.1 Hz. The sensors have a constant response and they follow the fast temperature changes in a very similar way, as it is presented in **Figure 7.14**. However, it is essential to observe their response closer, at both extreme temperatures, as it shown in **Figure 7.15** and **Figure 7.16**. In the warmer temperatures, the sensors have a constant response for each cycle and the temperature differences between them are stable. The AJP sensor value is very close to the one of the immersed sensors (closer to probe 1, close to the inlet), while the surface sensor TS1 has the maximum temperature difference with the probe1. In addition, the sensors have similar response for the coldest temperatures. The AJP sensor has a linear response, similar with the commercial RTDs, for

fast and repeated temperature changes. This means that the 3D printed sensor is capable of detecting temperature in more extreme conditions, providing reliable measurements.

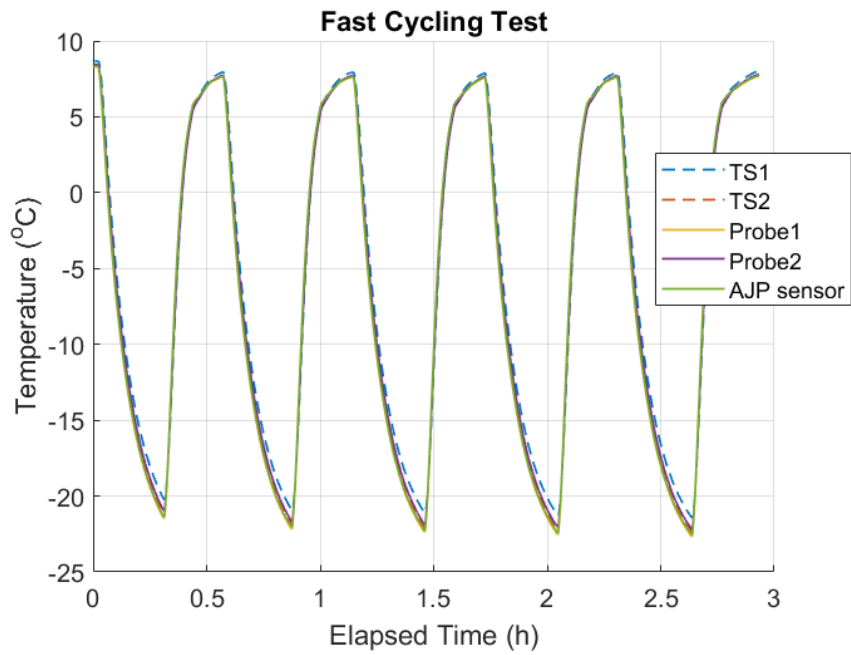


Figure 7.14. The fast heating – cooling process of the *insulated* hydraulic circuit.

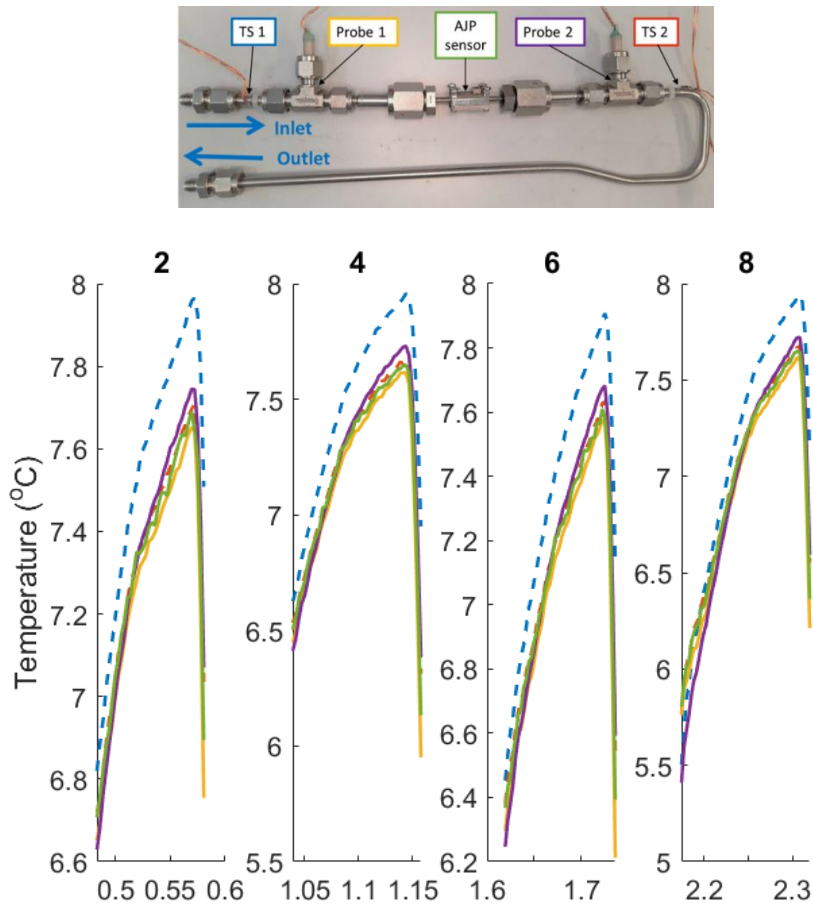


Figure 7.15. Sensors response after fast heating for each cycle.

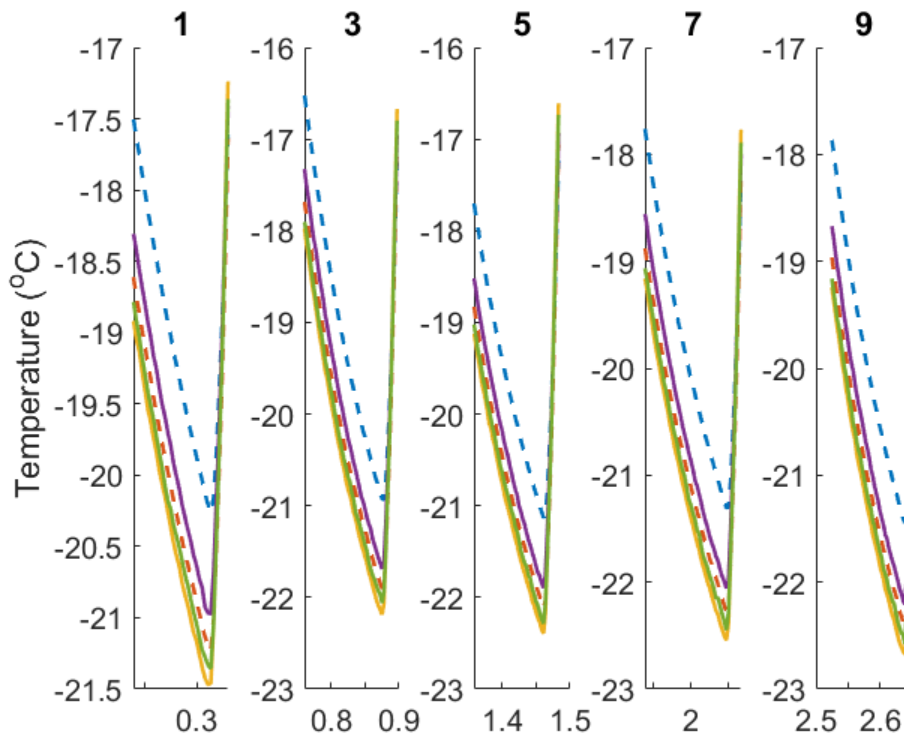


Figure 7.16. Sensors response after fast cooling for each cycle.

7.2.2 Uninsulated test section

The uninsulated hydraulic circuit was tested in a way, as described above for the insulated test section. In the beginning, one cycle test performed and afterwards the fast-cycling test. In the first test, temperature differences are observed among the sensors (**Figure 7.17**) and are presented in **Table 7.6**. The temperature values of the AJP lie almost between the values of the immersed sensors but closer to the probe 1. The temperature difference between the immersed sensors increased, as compared to the insulated test section. The TS1 presents again a high temperature difference with probe 1. However, the highest temperature difference is observed between the TS2 and probe 2. In the previous test, the TS2 temperature was very close to probe 2. This means that the surface sensor is extremely affected by ambient temperature and heat losses. In general, the minimum temperature difference is observed between the AJP sensor and the immersed probes. The fact the AJP sensor's temperature is closer to probe 1, which is closer to the inlet of the chiller's hydraulic circuit, indicates that the ambient temperature has a very low or even no effect on the sensor.

ΔT	at -22 °C	at 8 °C
TS1 – Probe1	1.55	0.26
TS2 – Probe2	2.56	0.57
Probe1 – Probe2	-1.36	-0.31
AJP – Probe1	0.41	0.06
AJP – Probe2	-0.95	-0.25

Table 7.7. Temperature differences among the sensors of the *uninsulated* hydraulic circuit.

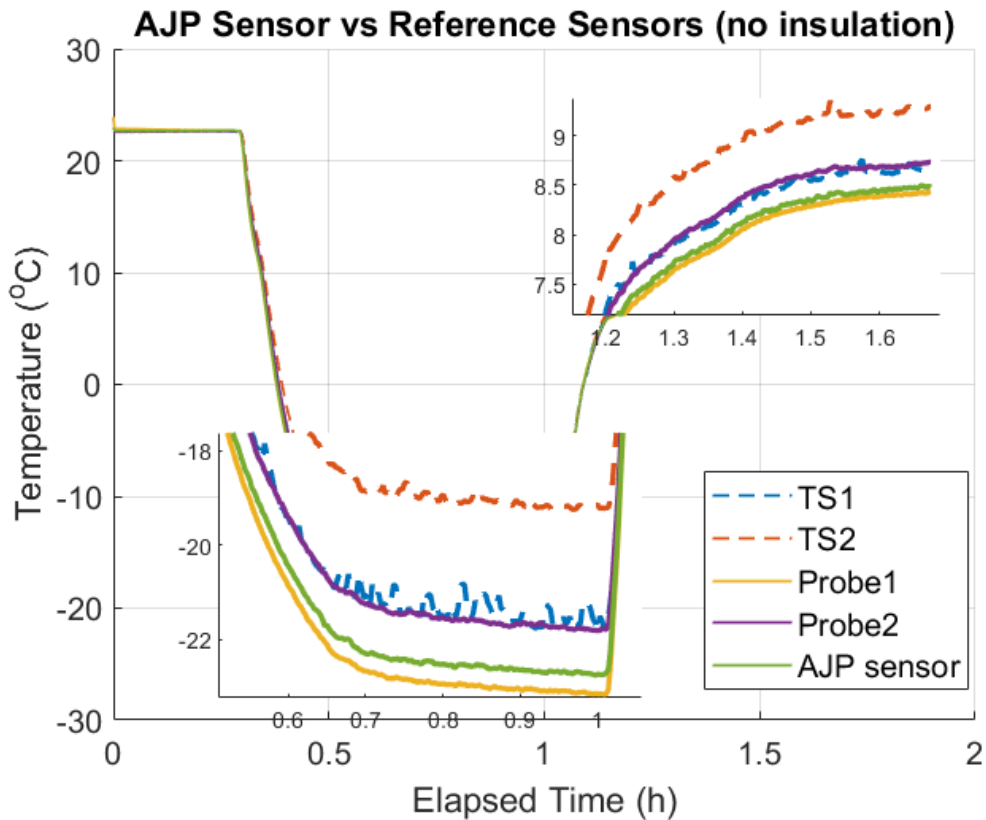
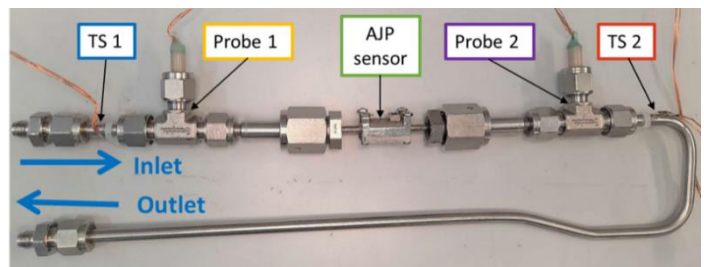


Figure 7.17. The sensors temperature response for the *uninsulated* hydraulic circuit.

In the fast-cycling test, the sensors have a constant response and they follow the fast temperature changes in a very similar way, as it is presented in **Figure 7.18**. However, it is

essential to observe their response closer, at both extreme temperatures, as it shown in **Figure 7.19** and **Figure 7.20**. In the warmer temperatures, the sensors have a constant response for each cycle and the temperature differences between them are quite stable. The AJP sensor value is very close to the one of the immersed sensors (closer to probe 1, close to the inlet). The surface sensors present the maximum temperature difference with the immersed probes. The AJP sensor has a linear response, similar with the commercial RTDs, for fast and repeated temperature changes. This means that the 3D printed sensor is capable of detecting temperature in more extreme conditions, providing reliable measurements.

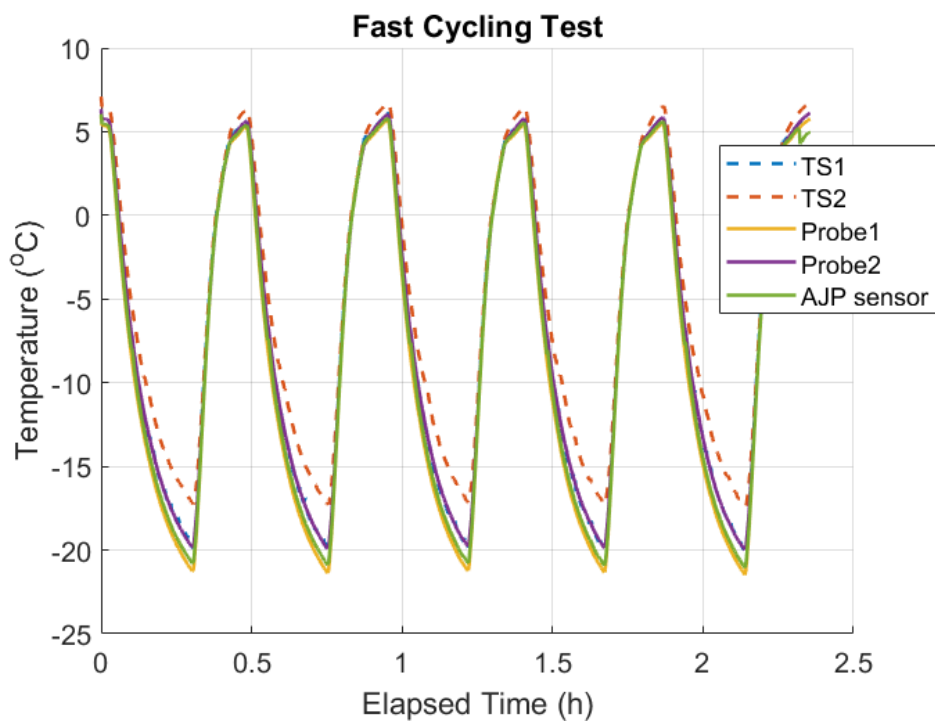
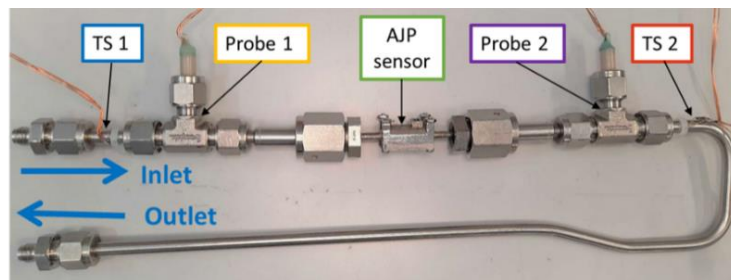


Figure 7.18. The fast heating – cooling process of the *insulated* hydraulic circuit.



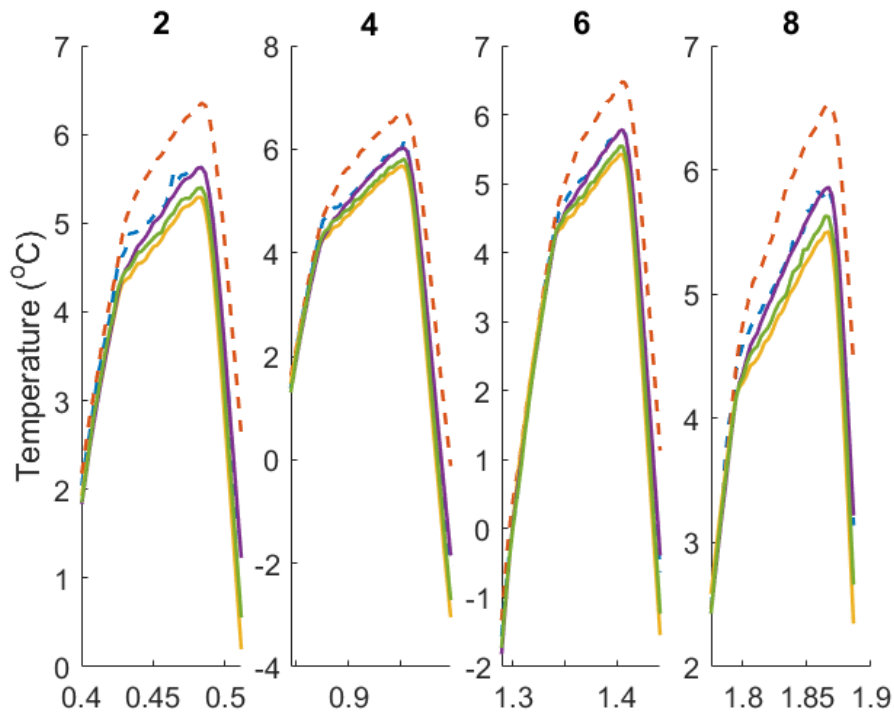


Figure 7.19. Sensors response after fast heating for each cycle.

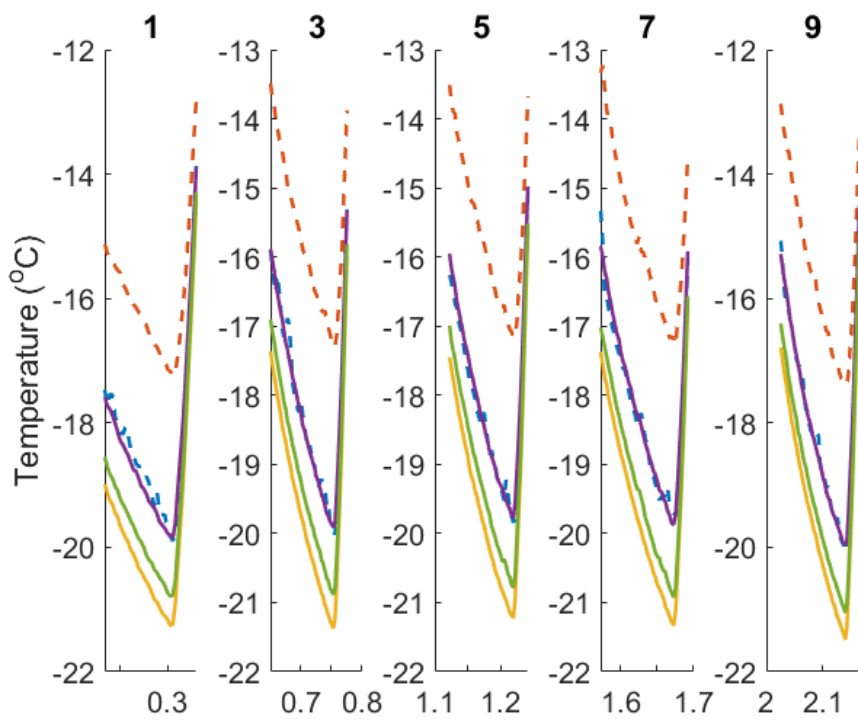


Figure 7.20. Sensors response after fast cooling for each cycle.

7.3 Discussion - Obtained Results & Comments

Temperature differences among the sensors are observed in all the different methods of testing. It is sinful to compare first the temperature variations between the surface and the immersed sensors, since it is expected to differ and it is important to measure this difference. The variations between the immersed sensors, and between the AJP sensor and each one the immersed sensors, are listed below.

TS1 – Probe 1

- The minimum temperature difference ($\Delta T = 0.12$) is presented in the test under vacuum with a constant temperature of 11°C.
- The maximum temperature difference ($\Delta T = 1.55$) is observed in the test under real conditions without insulation at the coldest temperature.

TS2 – Probe2

- The minimum temperature difference ($\Delta T = 0.03$) is presented in the test under vacuum, for group temperature testing at 5°C.
- The maximum temperature difference ($\Delta T = 2.56$) is observed in the test under real conditions without insulation at the coldest temperature.

Probe 1 – Probe 2

- The minimum temperature difference ($\Delta T = -0.09$) is presented in the test under vacuum with a constant temperature of 11°C.
- The maximum temperature difference ($\Delta T = -1.36$) is observed in the test under real conditions without insulation at the coldest temperature.

AJP sensor – Probe 1

- The minimum temperature difference ($\Delta T = 0.01$) is presented in the test under vacuum, for group temperature testing at 5°C.
- The maximum temperature difference ($\Delta T = 0.41$) is observed in the test under real conditions without insulation at the coldest temperature.

AJP sensor – Probe 2

- The minimum temperature difference ($\Delta T = -0.07$) is presented in the test under vacuum with a constant temperature of 11°C.
- The maximum temperature difference ($\Delta T = -0.95$) is observed in the test under real conditions without insulation at the coldest temperature.

In general, the behavior of the sensors, subjected to different testing conditions is very similar. However, there is a variation in the value of the temperature differences. The temperature reading of the surface sensors is highest than the immersed sensors, in most of the cases. This proves that although the installation of such sensors is simple, the measurements are not reliable. These errors on the measurement usually occur, due to slower response time and disconnections between the sensor and the pipe surface. Furthermore, their behavior is not very predictable, since the same sensor, which had a high temperature difference with the immersed sensor, afterwards reduced this difference. On the other hand, the immersed sensors provide more reliable measurements, and their temperature variations are mainly caused by their different position in the hydraulic circuit. However, the preparation of such sensors and the pipe's modification, required for their installation, make this method pretty intrusive and time-consuming.

The AJP sensor, which is embedded in the inner wall of the pipe presents the lowest temperature variation with the commercial immersed sensors. Even in the case of the uninsulated circuit, the maximum ΔT is less than 1°C. This proves the high importance of embedding a sensor in the inner wall of pipe, providing direct contact with the fluid and minimizing heat losses. The comparison of the AJP sensor with commercial PT100 RTDs shows that the AJP sensor response is very similar, presenting the same characteristics of linearity and low hysteresis. On the other hand, the AJP sensor is noisier and has a precision of one order higher than the PT100s. However, both can be improved by optimized AJP deposition parameters.

7.4 Conclusions and future work

This study concludes that the smart pipe with embedded electrical and fluidic connectors, and sensing capabilities can increase the efficiency of a cooling system, in terms of tightness and fluid temperature sensing. The SWaP approach provides an innovative, compact and low-cost solution to problems that immersed and surface sensors face. In particular:

- Clamping a sensor on the outer wall of a pipe can provide a rough measurement of the fluid temperature, but it is prone to errors, in particular if the circuit cannot be properly insulated from the environment.
- Inserting in the circuit a sensor with the tip directly immersed in the fluid provide a reliable measurement but:
 - a. It requires space around the circuit; and
 - b. introduce a disturbance to the flow (invasive measurement).
- The SWaP prototype is a hydraulic component with sensing capabilities, fully produced by AM:
 - a. It does not leak even at high pressure.
 - b. It can be integrated in ANY hydraulic circuit.
 - c. Potentially fast and cheap production.
 - d. Provides reliable fluid temperature measurements, comparable with immersed commercial PT100 RTDs
 - e. It does not induce disturbance to the flow (no-invasive measurement).

The future work concentrates on the closure of the casing by a second SLM step. The casing will not be separated (cap and O-ring) and its size can be reduced. CSEM has already started to work on this new design and fabrication. Another idea focuses on the encapsulation of the AJP sensor, probably by the method of Atomic Layer Deposition. This could protect the sensor from harmful and/or humid fluids. Therefore, the field of applications can be even more expanded (e.g. chemical industry). Regarding the AJP sensor, new materials other than silver nanoparticles could be tested, in order to examine which material provides the optimum electrical properties. A reliability study is one of the priorities, in order to test the smart pipe under different condition and verify its repeatability and reliability. Last but not least, a new study on design and fabrication of new sensors for fluid pressure and flow-mass measurements, has always been part of our next plans. These steps will result in increasing the TRL (5 – 6).

REFERENCES

1. Public Summary: SWaP, Smart wall pipes and ducts. ATTRACT Showroom. <https://phase1.attract-eu.com/showroom/project/smart-wall-pipes-and-ducts-swap/>
2. P. R. N. Childs, J. R. Greenwood, and C. A. Long. Review of temperature measurement. *Rev. Sci. Instrum.* 71, 2959, 2000.
3. P. Klason, M. Holmsten, A. Andersson, P. Lau, and G. J. P. Kok. Temperature Measurement in Flow Pipes: Comparison with Single Pt-100 and Multisensors. *AIP Conference Proceedings 1552*, 987, 2013.
4. J.M. Gorman, E.M. Sparrow, J.P. Abraham. Differences between measured pipe wall surface temperatures and internal fluid temperatures. *Case Studies in Thermal Engineering 1*, 13–16, 2013.
5. Rosemount™ 0085 Pipe Clamp Sensor. *Product Data Sheet*, 00813-0100-4952, Rev IA May, 2021. <https://www.emerson.com/documents/automation/product-data-sheet-rosemount-0085-pipe-clamp-sensor-en-73338.pdf>
6. Jörg Gebhardt, Guruprasad Sosale, and Subhashish Dasgupta. Non-invasive temperature measurement of turbulent flows of aqueous solutions and gases in pipes. *tm – Technisches Messen* 87(9): 553–563, 2020.
7. Paolo Petagna, Bart Verlaat and Andrea Francescon. Two-Phase Thermal Management of Silicon Detectors for High Energy Physics. *Encyclopedia of Two-Phase Heat Transfer and Flow III, Ch.5*, pp. 335-412, 2018.
8. Paolo Petagna. Past Experiences and Future Trends on Vertex Detector Cooling at LHC. *Proceedings, 22nd International Workshop on Vertex Detectors (Vertex 2013): Lake Starnberg, Germany, September 16-20, 2013*.
9. Mead O'Brien. Industrial Thermowells: Sometimes Taken for Granted, but Critically Important. <https://blog.meadobrien.com/2018/09/>
10. Temperature Transmitter Installation General Guidelines. <https://rmsengineering.freshdesk.com/support/solutions/articles/19000030871-temperature-transmitter-installation-general-guidelines>
11. Clamp on Temperature Sensors. <https://fluidic-ltd.co.uk/product/clamp-on-temperature-sensor/>
12. Chrysoula Manoli, Nicholas R. Hendricks, Jérôme Noël, Paolo Petagna, and Sébastien Lani. Smart Wall Pipes and ducts (SWaP). *Public deliverable for the ATTRACT Final Conference*, 2020.
13. Paolo Petagna. Detector cooling: which perspectives for future detectors? *AIDA-2020 Topical Workshop on Future of Tracking*, 2019.
14. The Project. <https://phase1.attract-eu.com/the-project/>
15. Detection & Imaging Technologies as key enablers for breakthrough innovation. THE ATTRACT PROGRAMME. *ATTRACT CONSORTIUM ©2018*.
16. <https://www.csem.ch/about/History>
17. <https://www.csem.ch/Solutions/ByExpertise>
18. <https://www.csem.ch/Solutions/ByIndustry>
19. <https://home.cern/about/who-we-are/our-people>
20. <https://home.cern/about/key-achievements>
21. <https://home.cern/science/accelerators/large-hadron-collider>

22. <https://home.cern/science/experiments/atlas>
23. <https://home.cern/science/experiments/cms>
24. <https://home.cern/science/experiments/alice>
25. <https://home.cern/science/experiments/lhcb>
26. <https://ep-dep-dt.web.cern.ch/detector-cooling-service>
27. IdeaSquare Licence to dream. Progress Report 2017-2018.
28. Carlos A. Gonzalez Lengua. History of Rapid Prototyping. *Rapid Prototyping in Cardiac Disease*, pp 3-7, 2017.
29. Mark Vitale, Mark Cotteleer and Jonathan Holdowsky. An Overview of Additive Manufacturing. *Defense AT&L*, 2016.
30. Ferry P.W. Melchels, Jan Feijen and Dirk W. Grijpm. A review on stereolithography and its applications in biomedical engineering. *Biomaterials* 31(24):6121–30, 2010.
31. G. Gerbino, E. Zavattero, F. Zenga, F.A. Bianchi, P. Garzino-Demo, S. Berrone. Primary and secondary reconstruction of complex craniofacial defects using polyetheretherketone custom-made implants. *J. Cranio-Maxillofac, Surg.* 43 (8), 1356–1363, 2015.
32. Hu Jing. Study on stl-based slicing process for 3d printing. *Solid Freeform Fabrication 2017 Proceedings of the 28th Annual International Solid Freeform Fabrication Symposium – An Additive Manufacturing Conference*, 2017.
33. D. Ding, Z. Pan, et al. Multi-direction slicing of STL models for robotic wire-feed additive manufacturing. *Annual international solid freeform fabrication symposium*, pp. 1059–1069, 2015.
34. 3D PRINTING G-CODE TUTORIAL, SIMPLIFY 3D. <https://www.simplify3d.com/support/articles/3d-printing-gcode-tutorial/>
35. Perry Cain. Selecting the optimal shell and infill parameters for FDM 3D printing. <https://www.hubs.com/knowledge-base/selecting-optimal-shell-and-infill-parameters-fdm-3d-printing/>
36. Standard Terminology for Additive Manufacturing Technologies. Designation, *Designation: F2792–12a*, 2012. <https://web.mit.edu/2.810/www/files/readings/AdditiveManufacturingTerminology.pdf>
37. Xin Wang, Man Jiang, Zuowan Zhou, Jihua Gou and David Hui. 3D printing of polymer matrix composites: A review and prospective. *Compos B Eng* 110:442–58, 2017.
38. The History of 3D Printing: 3D Printing Technologies from the 80s to Today. Sculpteo. <https://www.sculpteo.com/en/3d-learning-hub/basics-of-3d-printing/the-history-of-3d-printing/>
39. Guide to Stereolithography (SLA) 3D Printing. Formlab Guides. <https://formlabs.com/blog/ultimate-guide-to-stereolithography-sla-3d-printing/>
40. Goldy Katal, Nelofar Tyagi and Ashish Joshi. Digital light processing and its future applications. *International Journal of Scientific and Research Publications*, 3(1):2250-3153, 2013.
41. Christina Schmidleithner and Deepak M. Kalaskar. Stereolithography. *Intechopen*.78147, Ch.1, 2018.

42. Fused Deposition Modeling: Everything You Need To Know About FDM 3D Printing. 3D Printing Technologies / Guides. <https://www.3dsourced.com/guides/fused-deposition-modeling-fdm/>
43. Ludmila Novakova-Marcincinova, Ivan Kuric, Basic and Advanced Materials for Fused Deposition Modeling. *Rapid Prototyping Technology, Manuf. and Ind. Eng.* 11(1), 2012.
44. Ala'aldin Alafaghani, Ala Qattawi, Muhammad Ali Ablat. Design Consideration for Additive Manufacturing: Fused Deposition Modelling. *Open Journal of Applied Sciences*, 7, 291-318, 2017.
45. Ala'aldin Alafaghani, Ala Qattawia, Buraaq Alrawia and Arturo Guzman. Experimental Optimization of Fused Deposition Modelling Processing Parameters: a Design-for-Manufacturing Approach. *Procedia Manufacturing* 10: 79 – 803, 2017.
46. About Additive Manufacturing: Material Jetting. Additive Manufacturing Research Group, Loughborough University. <https://www.lboro.ac.uk/research/amrg/about/the7categoriesofadditivemanufacturing/materialjetting/>
47. E. Sachs, M. Cima, J. Cornie. Three-dimensional printing: Rapid tooling and prototypes directly from a CAD model. *CIRP Ann. Manuf. Technol.* 39, 201–204, 1990.
48. Simon Meteyer, Xin Xu, Nicolas Perry, Yaoyao Fiona Zhao. Energy and material flow analysis of binder-jetting additive manufacturing processes. *Procedia CIRP* 15, 19–25, 2014.
49. Xin Xu, Simon Meteyer, Nicolas Perry & Yaoyao Fiona Zhao. Energy consumption model of binder-jetting additive manufacturing processes. *Int. J. Prod. Res.* 53, 7005–7015, 2014.
50. Kaufui V. Wong, Aldo Hernandez. A review of additive manufacturing. *ISRN Mech. Eng.* 208760, 2012.
51. Prashanth Konda Gokuldoss, Sri Kolla and Jürgen Eckert. Additive Manufacturing Processes: Selective Laser Melting, Electron Beam Melting and Binder Jetting—Selection Guidelines. *Materials* 10, 672, 2017.
52. Ian Gibson, David Rosen, Brent Stucker. Sheet lamination processes. Additive manufacturing technologies: 3D printing, rapid prototyping, and direct digital manufacturing. *New York, NY: Springer New York; 2015. p. 219–44*, 2015.
53. Ganzi Suresh, K.L.Narayana and M. Kedar Mallik. A Review on Development of Medical Implants by Rapid Prototyping Technology. *International Journal of Pure and Applied Mathematics*, 2017.
54. Mohsen Attaran. The rise of 3-D printing: The advantages of additive manufacturing over traditional manufacturing. *Business Horizons* 60, 5, September–October 2017, pp. 677-688, 2017.
55. Tanisha Pereira, John V Kennedy, Johan Potgieter. A comparison of traditional manufacturing vs additive manufacturing, the best method for the job. *Procedia Manufacturing* 30, 11–18, 2019.
56. D. Chen, S. Heyer, S. Ibbotson, K. Salonitis, J.G. Steingrímsson, S. Thiede. Direct digital manufacturing: definition, evolution, and sustainability implications. *J. Clean. Prod.*, 107 pp. 615-625, 2015.
57. Mike Gayette. Top Ten Advantages of Additive Manufacturing. December 13, 2019. <https://www.ptc.com/en/blogs/cad/10-additive-manufacturing-advantages>

58. Megan Kreiger and Joshua M. Pearce. Environmental Life Cycle Analysis of Distributed Three-Dimensional Printing and Conventional Manufacturing of Polymer Products. *ACS Sustainable Chem. Eng.* 1, 12, 1511–1519, 2013.
59. Energy Consumption in Metal Additive Manufacturing. *Digital Alloys' Guide to Metal Additive Manufacturing, Part 7*, 28 March, 2019.
60. Cherdo, L. The Best Metal 3D Printers in 2020. <https://www.aniwaa.com/best-of/3d-printers/best-metal-3d-printer/>
61. Ana Vafadar, Ferdinando Guzzomi, Alexander Rassau and Kevin Hayward. Advances in Metal Additive Manufacturing: A Review of Common Processes, Industrial Applications, and Current Challenges. *Appl. Sci.*, 11, 1213, 2021.
62. Kaufui V. Wong and Aldo Hernandez. A Review of Additive Manufacturing. *ISRN Mech. Eng.* 1–10, 2012.
63. EMPA, Swiss Federal Laboratories for Materials Science and Technology, <https://www.empa.ch/web/coating-competence-center/selective-laser-melting>
64. Welcome to Manufacturing UNBOUND, <http://www.arcam.com/wp-content/uploads/arcamebm-corp.pdf>
65. Leo Gregurić. History of 3D Printing: When Was 3D Printing Invented? Dec 10, 2018. <https://all3dp.com/2/history-of-3d-printing-when-was-3d-printing-invented/>
66. K.R. Bakshi, A. V. Mulay. A Review on Selective Laser Sintering: A Rapid Prototyping Technology. *IOSR Journal of Mechanical & Civil Engineering*, 2278-1684, 53-57, 2016.
67. Gordon Jones. Direct Metal Laser Sintering (DMLS) – Simply Explained. Updated Apr 15, 2021. <https://all3dp.com/2/direct-metal-laser-sintering-dmls-simply-explained/>
68. Sarah Goehrke. The SLM Solutions Story. July 10, 2019. <https://www.fabbaloo.com/blog/2019/7/10/the-slm-solutions-story>
69. Swee Leong Sing, Jia An, Wai Yee Yeong, Florencia Edith Wiria. Laser and Electron-Beam Powder-Bed Additive Manufacturing of Metallic Implants: A Review on Processes, Materials and Designs. *Journal of Orthopaedic Research*, October 2015.
70. Laser metal fusion for complex, metallic components (TruPrint100, TRUMPF). https://www.trumpf.com/en_INT/products/machines-systems/additive-production-systems/truprint-1000/
71. An Introduction to Electron Beam Melting. May 16, 2018. <https://amfg.ai/2018/05/16/electron-beam-melting-introduction/>
72. S. Biamino, A. Penna, U. Ackelid, S. Sabbadini, O. Tassa, P. Fino, M. Pavese, P. Gennaro, C. Badini. Electron beam melting of Ti-48Al-2Cr-2Nb alloy: microstructure and mechanical properties investigation. *Intermetallics* 19 (6) 776–781, 2011.
73. C. Körner. Additive manufacturing of metallic components by selective electron beam melting—a review. *International Materials Reviews*, 61:5, 361-377, 2016.
74. W. J. Sames, F. A. List, S. Pannala, R. R. Dehoff, and S. S. Babu. The metallurgy and processing science of metal additive manufacturing. *Int. Mater. Rev.* 61, 1–46, 2016.
75. Shahir Mohd Yusuf, Samuel Cutler and Nong Gao. Review: The Impact of Metal Additive Manufacturing on the Aerospace Industry. *Metals* 9, 1286, 2019.
76. Anthony R. McAndrew, Marta Alvarez Rosales, Paul A. Colegrove, Jan R. Hönnige, Alistair Ho, Romain Fayolle, Kamal Eyitayo, Ioan Stan, Punyawee Sukrongpang, Antoine Crochemore, Zsolt Pinter. Interpass rolling of Ti-6Al-4V wire + arc additively

- manufactured features for microstructural refinement. *Addit. Manuf.* 21, 340–349, 2018.
77. Eytayo Olatunde Olakanmi, Kenneth W. Dalgarno, and Robert F. Cochrane. Laser sintering of blended Al-Si powders. *Rapid Prototyp. J.*, 18, 109–119, 2012.
 78. Chao Guoa, Wenjun Gea, Feng Lin. Effects of scanning parameters on material deposition during Electron Beam Selective Melting of Ti-6Al-4V powder. *Journal of Materials Processing Technology* 217, 148–157, 2015.
 79. C. Y. Yap, C. K. Chua, Z. L. Dong, Z. H. Liu, D. Q. Zhang, L. E. Loh, and S. L. Sing. Review of selective laser melting: Materials and applications. *APPLIED PHYSICS REVIEWS* 2, 041101, 2015.
 80. W. J. Sames, F. Medina, W. H. Peter, S. S. Babu and R. R. Dehoff. Effect of process control and powder quality on Inconel 718 produced using electron beam melting. *Superalloy 718 and derivatives, Pittsburgh, PA*, 2014.
 81. E. Yasa and J.P. Kruth. Microstructural investigation of Selective Laser Melting 316L stainless steel parts exposed to laser re-melting. *Procedia Eng.* 19, 389–395, 2011.
 82. S. Dadbakhsh and L. Hao. Effect of Al alloys on selective laser melting behaviour and microstructure of in situ formed particle reinforced composites. *J. Alloys Compd.* 541, 328–334, 2012.
 83. A. Simchi. Direct laser sintering of metal powders: Mechanism, kinetics and microstructural features. *Mater. Sci. Eng. A*, 428, (1–2), 148–158, 2006.
 84. D. Clark, M. R. Bache, and M. T. Whittaker. Shaped metal deposition of a nickel alloy for aero engine applications. *J. Mater. Process. Technol.* 203, (1–3), 439–448, 2008.
 85. J. P. Kruth, L. Froyen, J. Van Vaerenbergh, P. Mercelis, M. Rombouts, and B. Lauwers. Selective laser melting of iron-based powder. *J. Mater. Process. Technol.* 149, (1–3), 616–622, 2004.
 86. N. K. Tolochko, T. Laoui, Y. V. Khlopokov, S. E. Mozzharov, V. I. Titov, and M. B. Ignatiev. Absorptance of powder materials suitable for laser sintering. *Rapid Prototyp. J.* 6, 155–161, 2000.
 87. W. Shifeng, L. Shuai, W. Qingsong, C. Yan, Z. Sheng, and S. Yusheng. Effect of molten pool boundaries on the mechanical properties of selective laser melting parts. *J. Mater. Process. Technol.* 214, 2660–2667, 2014.
 88. Xuesong Zhang, Hanwu Lei, Gayatri Yadavalli, Lei Zhu, Yi Wei, Yupeng Liu. Gasoline-range hydrocarbons produced from microwave-induced pyrolysis of low-density polyethylene over ZSM-5. *Mater. Process. Tech.* 222, 33–42, 2015.
 89. M. Shiomi, K. Osakada, K. Nakamura, T. Yamashita, F. Abe. Residual Stress within Metallic Model Made by Selective Laser Melting Process. *CIRP Ann. Manuf. Techn.* 53, 195–198, 2004.
 90. Xuezhi Shi, Shuyuan Ma, Changmeng Liu, Qianru Wu. Parameter optimization for Ti-47Al-2Cr-2Nb in selective laser melting based on geometric characteristics of single scan tracks. *Opt. Laser Technol.* 90, 71–79, 2017.
 91. H. Attar, M. Calin, L. C. Zhang, S. Scudino, and J. Eckert. Manufacture by selective laser melting and mechanical behavior of commercially pure titanium. *Mater. Sci. Eng. A* 593, 170–177, 2014.
 92. D. Gu, Y.C. Hagedorn, W. Meiners, G. Meng, R. J. S. Batista, K. Wissenbach, and R. Poprawe. Densification behavior, microstructure evolution, and wear performance of

- selective laser melting processed commercially pure titanium. *Acta Mater.*, 60, 3849–3860, 2012.
93. N. T. Aboulkhair, N. M. Everitt, I. Ashcroft, and C. Tuck. Reducing porosity in AlSi10Mg parts processed by selective laser melting. *Addit. Manuf.* 1-4, 77–86, 2014.
 94. D. Dai and D. Gu. Thermal behavior and densification mechanism during selective laser melting of copper matrix composites: Simulation and experiments. *Mater. Des.* 55, 482–491, 2014.
 95. Ruidi Li, Jinhui Liu, Yusheng Shi, Li Wang and Wei Jiang. Balling behavior of stainless steel and nickel powder during selective laser melting process. *Metall. Mater. Trans. A* 46, 3864–3875, 2015.
 96. Jinliang Zhang, Bo Song, Qingsong Wei, Dave Bourell, Yusheng Shi. A review of selective laser melting of aluminum alloys: Processing, microstructure, property and developing trends. *Journal of Materials Science & Technology*, 35, 270–284, 2019.
 97. D D Gu, W Meiners, K Wissenbach and R Poprawe. Laser additive manufacturing of metallic components: materials, processes and mechanisms. *Int. Mater. Rev.* 57, 133–164, 2012.
 98. Ahmed Hussein, Liang Hao, Chunze Yan, Richard Everson. Finite element simulation of the temperature and stress fields in single layers built without-support in selective laser melting. *Mater. Des.* 52, 638–647, 2013.
 99. C. Li, C. H. Fu, Y. B. Guo, F. Z. Fang. A multiscale modeling approach for fast prediction of part distortion in selective laser melting. *J. Mater. Process. Tech.* 229, 703–712, 2016.
 100. C.M. Chen, R. Kovacevic. Finite element modeling of friction stir welding—thermal and thermomechanical analysis. *Int. J. Mach. Tool Manu.* 43, 1319–1326, 2003.
 101. Dean Deng, Hidekazu Murakawa. Numerical simulation of temperature field and residual stress in multi-pass welds in stainless steel pipe and comparison with experimental measurements. *Mater. Sci.* 37, 269–277, 2006.
 102. Peter Mercelis, Jean-Pierre Kruth. Residual stresses in selective laser sintering and selective laser melting. *Rapid Prototyp. J.* 12, 254–265, 2006.
 103. Dong-Kyu Kim, Ji-Hyun Hwang, Eun-Young Kim, Yoon-Uk Heo, Wanchuck Woo, Shi-Hoon Choi. Evaluation of the stress-strain relationship of constituent phases in AlSi10Mg alloy produced by selective laser melting using crystal plasticity FEM. *J. Alloy Compd.* 714, 687–697, 2017.
 104. Fang Zhihao, Lu Libin, Chen Longfei, GuanYingchun. Laser polishing of additive manufactured superalloy. *Procedia CIRP* 71, 150–154, 2018.
 105. Dirk Herzog, Vanessa Seyda, Eric Wycisk, Claus Emmelmann. Additive manufacturing of metals. *Acta Mater.* 117, 371–392, 2016.
 106. Tomotake Hirata, Takahiro Kimura, Takayuki Nakamoto. Effects of hot isostatic pressing and internal porosity on the performance of selective laser melted AlSi10Mg alloys. *Mater. Sci. Eng. A* 772, 138713, 2020.
 107. Chaoyue Chen, Yingchun Xie, Xingchen Yan, Shuo Yin, Hirotaka Fukanuma, Renzhong Huang, Ruixin Zhao, Jiang Wang, Zhongming Ren, Min Liu, Hanlin Liao. Effect of hot isostatic pressing (HIP) on microstructure and mechanical properties of Ti6Al4V alloy fabricated by cold spray additive manufacturing. *Addit. Manuf.* 27, 595–605, 2019.

108. Chao Cai, Bo Song, Pengju Xue, Qingsong Wei, Jia-min Wu, Wei Li, Yusheng Shi. Effect of hot isostatic pressing procedure on performance of Ti6Al4V: Surface qualities, microstructure and mechanical properties. *J. Alloy. Compd.* 686, 55–63, 2016.
109. Samuel Tamas-Williams, Philip J. Withers, Iain Todd & Philip B. Prangnell. The effectiveness of hot isostatic pressing for closing porosity in titanium parts manufactured by selective electron beam melting. *Metall. Mater. Trans. A* 47, 1939–1946, 2016.
110. Jianglong Gu, Jialuo Ding, Stewart W. Williams, Huimin Gu, Jing Bai, Yuchun Zhai, Peihua Ma. The strengthening effect of inter-layer cold working and post-deposition heat treatment on the additively manufactured Al–6.3 Cu alloy. *Mater. Sci. Eng. A* 651, 18–26, 2016.
111. Paul A. Colegrove, Jack Donoghue, Filomeno Martina, Jianglong Gu, Philip Prangnell, Jan Hönnige. Application of bulk deformation methods for microstructural and material property improvement and residual stress and distortion control in additively manufactured components. *Scr. Mater.* 135, 111–118, 2017.
112. Olusola Oyelola, Peter Crawforth, Rachid M’Saubic, Adam T. Clare. Machining of additively manufactured parts: Implications for surface integrity. *Procedia CIRP* 45, 119–122, 2016.
113. Tomas Kellner. The Blade Runners: This Factory Is 3D Printing Turbine Parts For The World's Largest Jet Engine. March 20, 2018. <https://www.ge.com/news/reports/future-manufacturing-take-look-inside-factory-3d-printing-jet-engine-parts>
114. Joel C. Najmon, Sajjad Raeisi, Andres Tovar. Review of additive manufacturing technologies and applications in the aerospace industry. *In Additive Manufacturing for the Aerospace Industry; Elsevier: Amsterdam, The Netherlands*, pp. 7–31, 2019.
115. Tomas Kellner. 3D-Printed ‘Bionic’ Parts Could Revolutionize Aerospace Design. *General Electric Reports: Boston, MA, USA*, 2017. <https://www.ge.com/news/reports/3d-printed-bionic-parts-revolutionize-aerospace-design>
116. Haizea González-Barrio, Amaia Calleja-Ochoa, A. Lamikiz and L. N. López de Lacalle. Manufacturing Processes of Integral Blade Rotors for Turbomachinery, Processes and New Approaches. *Appl. Sci.* 10, 3063, 2020.
117. J. Michael Wilson, Cecil Piya Yung, C. Shin, Fu Zhao, Karthik Ramani. Remanufacturing of turbine blades by laser direct deposition with its energy and environmental impact analysis. *J. Clean. Prod* 80, 170–178, 2014.
118. Giant Satellite Fuel Tank Sets New Record for 3-D Printed Space Parts. <https://news.lockheedmartin.com/2018-07-11-Giant-Satellite-Fuel-Tank-Sets-New-Record-for-3-D-Printed-Space-Parts>
119. Metal 3D Printing with Electron Beam Additive Manufacturing (EBAM®). <https://www.sciaky.com/additive-manufacturing/electron-beam-additive-manufacturing-technology>
120. T. Wohlers, I. Campbell, O. Diegel, R. Huff, J. Kowen, 3D Printing and Additive Manufacturing State of the Industry: *Annual Worldwide Progress Report, Lund University: Lund, Sweden*, 2017.
121. Tim Marten Wischeropp, Helge Hoch, Frank Beckmann, C. Emmelmann. Opportunities for Braking Technology Due to Additive Manufacturing Through the

- Example of a Bugatti Brake Caliper. *Internationales μ -Symposium 2018 Bremsen-Fachtagung, Bad Neuenahr, Germany, pp. 181–193.*, 2018.
122. Michael Tyrrell. Use of 3D Printed Components at BMW Jumps 42% Annually. January 8, 2019. <https://www.pesmedia.com/3d-printing-components-bmw-group/>
 123. James Bakewell. Customising Production. April 10, 2019. <https://www.automotivemanufacturingsolutions.com/customising-production/31218.article>
 124. Victor Anusci. BMW's New S58 Engine Features Cylinder Head Made with 3D Printing. February 16, 2019. <https://www.3dprintingmedia.network/bmw-s58-engine-3d-printed-cylinder/>
 125. Michael Petch. AUDI gives update on use of SLM metal 3D printing for the automotive industry. February 22, 2018. <https://3dprintingindustry.com/news/audi-gives-update-use-slm-metal-3d-printing-automotive-industry-129376/>
 126. Davide Sher. New SmarTech Analysis report on AM in the oil and gas industry finds \$1B+ AM hardware opportunity. May 30, 2019. <https://www.3dprintingmedia.network/new-smartech-analysis-report-on-am-in-the-oil-and-gas-industry-finds-1b-opportunity-am-hardware/>
 127. Madison Burns, Christoph Wangenheim. Metal 3D Printing Applications in the Oil & Gas Industry. In *Proceedings of the SPE Middle East Oil and Gas Show and Conference, Manama, Bahrain*, 18–21 March 2019.
 128. Lloyd's. First Additively Manufactured Part for Oil and Gas Certified. <https://www.lr.org/en/latest-news/first-additively-manufactured-part-for-oil-and-gas-certified-by-lr/>
 129. Michael Maher, Adrien Smith, Jesse Margiotta. A synopsis of the Defense Advanced Research Projects Agency (DARPA) investment in additive manufacture and what challenges remain. *Proc. SPIE 8970, Laser 3D Manufacturing*, 897002, 2014.
 130. Jeffrey G. Tait, Ewelina Witkowska, Masaya Hirade, Tung-Huei Ke, Pawel E. Malinowski, Soeren Steudel, Chihaya Adachi and Paul Heremans. Uniform Aerosol Jet printed polymer lines with 30 μm width for 140 ppi resolution RGB organic light emitting diodes. *Organic Electronics*, 22: 40-43, 2015.
 131. AEROSOLJET MATERIALS DATASHEET, https://optomec.com/wp-content/uploads/2014/04/AJ_MATERIALS_FAQs-Web0417.pdf
 132. Xing Lan, Xuejun Lu, Maggie Yihong Chen, Dan Scherrer, Thomas Chung, Evan Nguyen, Rich Lai and Jesse Tice. Direct On-Chip 3-D Aerosol Jet Printing With High Reliability. *IEEE Transactions on Components, Packaging and Manufacturing Technology*, 2017.
 133. K. Schuetz, J. Hoerber and J. Franke. Selective Light Sintering of Aerosol-Jet Printed Silver Nanoparticle Inks on Polymer Substrates. *AIP Conf. Proc.* 1593, 732-735, 2014.
 134. Shweta Agarwala, Guo Liang Goh and Wai Yee Yeong. Optimizing Aerosol Jet Printing Process of Silver Ink for Printed Electronics. *International Conference on Materials Engineering and Nano Sciences (ICMENS 2017)*, 2017.
 135. N. J. Wilkinson, M. A. A. Smith, R. W. Kay1 and R. A. Harris. A review of aerosol jet printing—a non-traditional hybrid process for micro-manufacturing. *The International Journal of Advanced Manufacturing Technology*, 105:4599–4619, 2019.
 136. How Aerosol Jet Technology Works by OPTOMECC. <https://optomec.com/printed-electronics/aerosol-jet-technology/>

137. Robert J Lang. Ultrasonic atomization of liquids. *The Journal of the Acoustical Society of America* 34, 6, 1962.
138. R. Rajan and A.B. Pandit. Correlations to predict droplet size in ultrasonic atomisation. *Ultrasonics* 39, 235 – 255, 2001.
139. Sebastian Binder, Markus Glatthaar and Edda Rädlein. Analytical Investigation of Aerosol Jet Printing. *Aerosol Science and Technology*, 48:924–929, 2014.
140. Hamed Abdolmaleki, Preben Kidmose, Shweta Agarwala. Droplet-Based Techniques for Printing of Functional Inks for Flexible Physical Sensors. *Adv. Mater.* 2006792, 2021.
141. AEROSOL JET® PRINTED ELECTRONICS OVERVIEW, OPTOMECC.
142. Sukjoon Hong, Junyeob Yeo, Gunho Kim, Dongkyu Kim, Habeom Lee, Jinhyeong Kwon, Hyungman Lee, Phillip Lee, and Seung Hwan Ko. Nonvacuum, Maskless Fabrication of a Flexible Metal Grid Transparent Conductor by Low-Temperature Selective Laser Sintering of Nanoparticle Ink. *ACS Nano* 7, 6, 5024–5031, 2013.
143. Myungo Joo, Byoungyoon Lee, Sooncheol Jeong, Myeongkyu Lee. Laser sintering of Cu paste film printed on polyimide substrate. *Applied Surface Science*, 258(1):521–524, 2011.
144. Dapeng Li, David Sutton, Andrew Burgess, Derek Graham, Paul D. Calvert. Conductive copper and nickel lines via reactive inkjet printing. *Journal of Materials Chemistry*, 19:3719–3724, 2009.
145. K. A. Schroder. Mechanisms of Photonic Curing™: Processing High Temperature Films on Low Temperature Substrates. *Nanotechnology 2011: Electronics, Devices, Fabrication, MEMS, Fluidics and Computational*, 2:220 – 223, 2011.
146. Sebastian Wunscher, Steffi Stumpf, Jolke Perelaer, Ulrich S. Schubert. Towards single-pass plasma sintering: temperature influence of atmospheric pressure plasma sintering of silver nanoparticle ink. *Journal of Materials Chemistry C*, 2:1642–1649, 2014.
147. Ankit Mahajan, C. Daniel Frisbie, Lorraine F. Francis. Optimization of Aerosol Jet Printing for High-Resolution, High-Aspect Ratio Silver Lines. *Appl. Mater. Interfaces* 5:4856–4864, 2013.
148. Anubha A Gupta, Antoine Bolduc, Sylvain G. Cloutier and Ricardo Izquierdo. Aerosol Jet Printing For Printed Electronics. *Rapid Prototyping IEEE*, 2016.
149. Ethan B. Secor. Principles of Aerosol Jet Printing. *Flex. Print. Electron.* 3 035002, 2018.
150. Michael Smith, Yeon Sik Choi, Chess Boughey and Sohini Kar-Narayan. Controlling and assessing the quality of aerosol jet printed features for large area and flexible electronics. *Flex. Print. Electron.* 2, 2017.
151. Pavel V. Arsenov, Alexey A. Efimov and Victor V. Ivanov. Effect of Methods of Changing in Focusing Ratio on Line Geometry in Aerosol Jet Printing. *Key Engineering Materials*, 2018.
152. Guang Chen, Yuan Gu, Harvey Tsang, Daniel R. Hines, and Siddhartha Das. The Effect of Droplet Sizes on Overspray in Aerosol-Jet Printing. *Adv. Eng. Mater.*, 2018.
153. J. West, J. W. Sears, S. Smith and M. Carter. Photonic sintering – an example: photonic curing of silver nanoparticles. *Sintering of Advanced Materials Woodhead Publishing Series in Metals and Surface Engineering*, Pages 275-288, 2010.
154. Pradeep Lall, Nakul Kothari, Amrit Abrol, Sudan Ahmed, Jift Suhling, Ben Leever, Scott Miller. Effect of Sintering Time and Sintering Temperature on the Mechanical

- and Electrical Properties of Aerosol-Jet Additively Printed Electronics. *18th IEEE Intersociety Conference on Thermal and Thermomechanical Phenomena in Electronic Systems (ITherm)*, 2019.
155. Justin Bourassa, Alex Ramm, James Q. Feng, Michael J. Renn. Water vapor-assisted sintering of silver nanoparticle inks for printed electronics. *SN Applied Sciences*, 2019.
 156. Md Taibur Rahman, Rahul Panat, Deuk Heo. 3-D antenna structures using novel direct-write additive manufacturing method. In: *Volume 3: Advanced fabrication and manufacturing; emerging technology frontiers; energy, health and water-applications of nano-, micro-and mini-scale devices; MEMS and NEMS; technology update talks; thermal management using micro channels, jets, sprays*. ASME, 2015.
 157. Anubha A Gupta, Antoine Bolduc, Sylvain G. Cloutier, Ricardo Izquierdo. Aerosol jet printing for printed electronics rapid prototyping. In: *2016 IEEE International Symposium on Circuits and Systems (ISCAS)*. IEEE, pp 866–869, 2016.
 158. Christian E. Folgar, Carlos Suchicital, Shashank Priya. Solution-based aerosol deposition process for synthesis of multilayer structures. *Mater Lett* 65:1302–1307, 2011.
 159. Martin Hedges and Aaron Borrás Marin. 3D Aerosol Jet® Printing - Adding Electronics Functionality to RP/RM. *DDMC 2012 Conference, Berlin*, 2012.
 160. A. Mette, P. L. Richter, M. Hoerteis and S. W. Glunz. Metal aerosol jet printing for solar cell metallization. *Prog Photovolt Res Appl* 15:621–627, 2017.
 161. S. Padovani, S. Sinesi, S. Priante, M. Antonipieri, A. Del Negro, V. Zoellmer, M. Maiwald, M. Hedges. New method for head-up display realization by mean of chip on board and aerosol jet process. In: *3rd Electronics System Integration Technology Conference (ESTC)*. IEEE, pp 1–3, 2010.
 162. Zhan Zhan, Lingke Yu, Jin Wei, Cheng Zheng, Daoheng Sun, Lingyun Wang. Application of aerosol jet technology in through-via interconnection for MEMS wafer-level packaging. *Microsyst Technol* 21:451–455, 2014.
 163. Tobias Seifert, Mario Baum, Frank Roscher, Maik Wiemer, Thomas Gessner. Aerosol jet printing of nano particle based electrical chip interconnects. *Mater Today Proc* 2:4262–4271, 2015.
 164. Elahe Jabari, Ehsan Toyserkani. Micro-scale aerosol-jet printing of graphene interconnects. *Carbon N Y* 91:321–329, 2015.
 165. Elahe Jabari, Ehsan Toyserkani. Aerosol-jet printing of highly flexible and conductive graphene/silver patterns. *Mater Lett* 174:40–43, 2016.
 166. Carissa S. Jones, Xuejun Lu, Mike Renn, Mike Stroder, Wu-Sheng Shih. Aerosol-jet-printed, high-speed, flexible thin-film transistor made using single-walled carbon nanotube solution. *Microelectron Eng* 87:434–437, 2010.
 167. Long Qian, Wenya Xu, XiaoFeng Fan, Chao Wang, Jianhui Zhang, Jianwen Zhao, and Zheng Cui. Electrical and photoresponse properties of printed thin-film transistors based on poly (9,9-dioctylfluorene-co-bithiophene) sorted large-diameter semiconducting carbon nanotubes. *J Phys Chem C* 117:18243–18250, 2013.
 168. Qiqi Xu, Jianwen Zhao Orcid, Vincenzo Pecunia, Wenya Xu, Chunshan Zhou, Junyan Dou, Weibing Gu, Jian Lin, Lixin Mo, Yanfei Zhao, and Zheng Cui. Selective conversion from p-type to n-type of printed bottom-gate carbon nanotube thin-film transistors and application in complementary metal–oxide–semiconductor inverters. *ACS Appl Mater Interfaces* 9:12750–12758, 2017.

169. Mingjing Ha, Wei Zhang, Daniele Braga, Michael J. Renn, Chris H. Kim, and C. Daniel Frisbie. Aerosol-jet-printed, 1 volt H-bridge drive circuit on plastic with integrated electrochromic pixel. *ACS Appl Mater Interfaces* 5:13198–13206, 2013.
170. <https://optomec.com/printed-electronics/aerosol-jet-emerging-applications/alternative-energy/>
171. M. Hoerteis and S.W. Glunz. Fine Line Printed Silicon Solar Cells Exceeding 20% Efficiency. *Prog. Photovolt: Res. Appl.*; 16:555–560, 2008.
172. Maikel F.A.M. van Hest, Susan E. Habas, Jason M. Underwood, Robert M Pasquarelli, Peter A. Hersh, Alex Miedaner, Calvin J. Curtis, David S. Ginley. Direct write metallization for photovoltaic cells and scaling thereof. *In: 2010 35th IEEE Photovoltaic Specialists Conference. IEEE, pp 003626–003628, 2010.*
173. Heather A.S. Platt, Yunjun Li, James P. Novak, Maikel F.A.M. van Hest. Non-contact printed aluminum metallization of Si photovoltaic devices. *In: 2012 38th IEEE Photovoltaic Specialists Conference. IEEE, pp002244–002246, 2012.*
174. Santanu Bag, James R. Deneault, Michael F. Durstock. Aerosol-Jet-Assisted Thin-Film Growth of CH₃NH₃PbI₃Perovskites—A Means to Achieve High Quality, Defect-Free Films for Efficient Solar Cells. *Adv. Energy Mater.* 1701151, 2017.
175. A. Hornés, A. Pesce, L. Hernández-Afonso, A. Morata, M. Torrell, and Albert Tarancón. 3D Printing of Fuel Cells and Electrolyzers. *3D Printing for Energy Applications, First Edition. Edited by Albert Tarancón and Vincenzo Esposito, Ch.11, 2021.*
176. A. M. Sukeshini, Thomas Jenkins, Paul Gardner, Ryan Miller, Thomas L. Reitz. Investigation of aerosol jet deposition parameters for printing SOFC layers. *ASME 2010 8th International Fuel Cell Science, Engineering and Technology Conference: Volume 1. ASME, pp 325–332, 2010.*
177. A. M. Sukeshini, Paul Gardner, Frederick Meisenkothen, Thomas Jenkins, Ryan Miller, Michael Rottmayer, Thomas L. Reitz. Aerosol jet printing and microstructure of SOFC electrolyte and cathode layers. *ECS Trans.* 35 2151, 2011.
178. Marcus Maiwald, Christian Werner, Volker Zoellmer, Matthias Busse. INKtelligent printed strain gauges. *Sensors and Actuators A* 162:198–201, 2010.
179. Da Zhao, Tao Liu, Mei Zhang, Richard Liang, Ben Wang. Fabrication and characterization of aerosol-jet printed strain sensors for multifunctional composite structures. *Smart Mater Struct* 21:115008, 2012.
180. Michela Borghetti, Mauro Serpelloni, Emilio Sardini. Printed strain gauge on 3D and low-melting point plastic surface by aerosol jet printing and photonic curing. *Sensors* 19, 4220, 2019.
181. Kiyoo T. Fujimoto, Jennifer K. Watkins, Timothy Phero, Doug Litteken, Kevin Tsai, Takoda Bingham, Kshama Lakshmi Ranganatha, Benjamin C. Johnson, Zhangxian Deng, Brian Jaques, David Estrada. Aerosol jet printed capacitive strain gauge for soft structural materials. *Flexible Electronics* 4:32, 2020.
182. Chia Wang, Guan-Yi Hong, Kuan-Ming Li, Hong-Tsu Young. A Miniaturized Nickel Oxide Thermistor via Aerosol Jet Technology. *Sensors* 17, 2602, 2017.
183. Md Taibur Rahman, Chih-Yang Cheng, Burcu Karagoz, Mike Renn, Matthew Schrandt, Andrew Gellman, Rahul Panat. High Performance Flexible Temperature Sensors via Nanoparticle Printing. *ACS Appl. Nano Mater.*, 2, 3280–3291, 2019.

184. Michela Borghetti, Edoardo Cantù, Emilio Sardini, Mauro Serpellon. Future Sensors for Smart Objects by Printing Technologies in Industry 4.0 Scenario. *Energies*, 13, 5916, 2020.
185. Roberto S. Aga, Jack P. Lombardi, Carrie M. Bartsch, Emily M. Heckman. Performance of a printed photodetector on a paper substrate. *IEEE Photon Technol Lett* 26:305–308, 2014.
186. Ralph Eckstein, Tobias Rödlmeier, Tobias Glaser, Sebastian Valouch, Ralf Mauer, Uli Lemmer, Gerardo Hernandez-Sosa. Aerosol-jet printed flexible organic photodiodes: semi-transparent, color neutral, and highly efficient. *Adv Electron Mater* 1:1500101, 2015.
187. Temperature Sensor Tutorial by *maxim integrated*.
188. Joseph Wu. A Basic Guide to Thermocouple Measurements. TEXAS INSTRUMENTS Application Report, SBAA274, September, 2018.
189. Thermistor Basics. WAVELENGTH ELECTRONICS: Application Note AN-TC11 Rev. A, May, 2013.
190. Temperature sensing fundamentals. TEXAS INSTRUMENTS, SNOAA25, January, 2019.
https://www.ti.com/lit/an/snoaa25/snoaa25.pdf?ts=1625821771338&ref_url=https%2F%2Fwww.google.com%2F
191. Taking Temperature Measurements with RTDs: How-To Guide. National Instruments knowledge article.
<https://knowledge.ni.com/KnowledgeArticleDetails?id=kA03q000000x1rnCAA&l=en-GR>
192. RTD Theory by *Pyromation Training*.
193. The fundamentals of RTD temperature sensors by *PR electronics*.
<https://www.prelectronics.com/the-fundamentals-of-rtd-temperature-sensors/>
194. Bill Bergquist, Jeff Wigen. Thermowell Selection and Application. © Burns Engineering.
195. Sensing Fluid Temperature with Thermal-Ribbons. Copyright 2008, Minco.
196. How to calibrate an RTD or Platinum Resistance Thermometer (PRT). Application Note. From the Fluke Calibration Digital Library @ www.flukecal.com/library
197. Skewness. MathWorks Documentation.
<https://ch.mathworks.com/help/stats/skewness.html>
198. Kurtosis. MathWorks Documentation.
https://ch.mathworks.com/help/stats/kurtosis.html?s_tid=doc_ta